GROWTH AND CHARACTERIZATION OF PURE AND Sn DOPED COPPER OXIDE THIN FILMS FOR HYDROGEN SULFIDE SENSING

Thesis Submitted for the Award of the Degree of

DOCTOR OF PHILOSOPHY

in

Physics

By

Jyoti

Registration Number: 41900076

Supervised By

Dr. Rajesh Kumar (12236)

Department of Physics

Professor. & HOL

LOVELY PROFESSIONAL UNIVERSITY, PUNJAB

2024

DECLARATION

I, hereby declared that the presented work in the thesis entitled "Growth and characterization of pure and Sn doped copper oxide thin films for hydrogen sulfide sensing" in fulfilment of degree of **Doctor of Philosophy (Ph. D.)** is outcome of research work carried out by me under the supervision of Dr. Rajesh Kumar, working as Professor & HOL in the school of chemical engineering and physical sciences of Lovely Professional University, Punjab, India. In keeping with general practice of reporting scientific observations, due acknowledgements have been made whenever work described here has been based on findings of other investigator. This work has not been submitted in part or full to any other University or Institute for the award of any degree.

(Signature of Scholar)
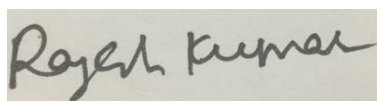
Jyoti

Registration No.: 41900076

Department/school: Physics

Lovely Professional University,

Punjab, India

CERTIFICATE

This is to certify that the work reported in the Ph. D. thesis entitled **"Growth and characterization of pure and Sn doped copper oxide thin films for hydrogen sulfide sensing "** submitted in fulfillment of the requirement for the reward of degree of **Doctor of Philosophy (Ph.D.)** in the Physics is a research work carried out by Jyoti, (Registration No.) 41900076, is bonafide record of his/her original work carried out under my supervision and that no part of thesis has been submitted for any other degree, diploma or equivalent course.

(Signature of Supervisor)

Dr. Rajesh Kumar

Professor & HOL

Department of physics

School of Chemical Engineering and Physical Sciences

Lovely Professional University

Phagwara, Punjab

ABSTRACT

Nanofilms fabricated from semiconducting metal oxide have been used up to a great extent for transparent electrode, absorber layer in solar cell and especially for gas sensor. The primary member of metal oxide family is CuO that has been broadly explored in field of nanotechnology. Because of the incomparable properties, CuO became a promising candidate for gas sensing applications.

The title of this thesis is "Growth and characterization of pure and Sn doped copper oxide thin films for hydrogen sulphide sensing". Sol-gel spin coating synthesizes pure and doped copper oxide films. The various features of prepared samples were examined by using XRD, two probe set-up, UV spectrometer and field emission scanning electron microscope respectively. The main focus of this work is to improve optical properties and porosity of CuO films for solar cell and gas sensing applications.

CuO films deposits on glass substrate and annealed at 400ºC temperature for 1hr. The effect of dopant concentration and spinning speed is investigated on properties of synthesized films. Initially, pure CuO films of different molar concentrations of 0.75M and 1M deposited on glass substrate. To investigate effect of spinning speed on various properties of CuO thin films, spinning speed vary between 1500rpm to 4500rpm. Cross sectional SEM was used to obtained the thickness of films. It was found that as rpms increases from 3000 to 4500, thickness decreased from 239 nm to 75 nm respectively. Films deposited at 3000-4500 rpm shows range of band gap from 0.98eV to 1.46eV, consequently these films used for solar cell applications. For all of the produced films of varying thickness, the diffract-grams reveal notable (200) and (111) atomic planes situated at 2 theta values of 36° and 38.6°. It was observed from the graph that obtained peaks are sharp and peak intensity is large at (111) plane which confirm that obtained films have good crystallinity. Other copper oxide films of 0.75M concentration have been prepared by varying spinning speed 1500 rpm to 2500 rpm at 30s spinning time. These films used as sensing element for gas sensor to monitor H_2S gas. Various concentration of gas passed to the sample at operating temperature in range of 25ºC to 150ºC and found from the obtained data that at a lower usage temperature of 25 °C, CuO-based sensor displays good sensitivity. Pure thin films of CuO of thickness 75 nm are explored supersensitive to H_2S gas at 25ºC temperature and shows a comparatively lower response time towards the gas at higher operating temperatures.

Later on, tin doped CuO films with different mole percentage of 3%, 5% and 7% deposits on glass substrate. The doping of tin chloride into CuO increase conduction of electron, improve

porosity and decrease crystallite size of prepared thin films. All samples' electrical characteristics were examined using a two-probe setup. It was found that current linearly increase on increasing the voltage which reveals that prepared films were of ohmic in nature. It was found that sample prepare from 3% Sn doping with 0.75M concentration have resistivity in range of 6.04 Ω-m to 1.86 Ω-m as the thickness reduced from 570nm to 165nm respectively. The value of conductivity noted from the doped sample of 1M concentration are 0.1105 (Ω-m)$^{-1}$ and 0.0947 (Ω-m)$^{-1}$ as the thickness reduced from 582nm to 181 nm respectively.

The structural properties of Sn doped films show that all of samples have (111) and (200) atomic planes. As the molarity increase from 0.75 M to 1M, these dominant peaks became finer and more intense. Debye- Scherrer formula was used to calculated crystallite size from the data obtained by XRD diffraction and found that it goes increases from 14.33nm to 43.79 nm as the molarity increases from 0.75M to 1M. This was perhaps caused by the fact that an enhancement in molarity raises the concentration of copper, which causes a higher condensation of copper atoms with a quicker nucleation to create larger crystallites. Investigations show that homogeneous grains form in CuO films, and all synthesized samples are discovered to be relatively oxygen-enriched. At 400°C of calcination temperature, obtained films are more crystallize and shows high sensitivity for H_2S gas.

To obtain the optical band gap of prepared samples, tauc plot was used. It was noted from the obtained data that band gap gets reduces from 3.28 eV to 1.45 eV on increasing the thickness from 165 nm to 528 nm. The obtained optical band gap of prepared Sn doped CuO films is appropriate as a material for a selective absorber in solar cell cells.

Fabricated films with various dopant concentration have been applied for fabrication of gas sensor. At room temperature, number of gases such as NH_3, SO_2, CO and H_2S of 100 ppm concentration exposed on gas sensor and noted the response. It has been found that CuO films was highly selective toward H_2S gas. It is observed from gas sensing results that sensitivity of films increases by doping of $SnCl_2$. The films prepare from the 3% doping of Sn with 0.75M concentration exhibit a high response of 74.63 toward 4 ppm concentration of hydrogen sulphide at room temperature. The gas sensing research done on the films also demonstrates that Sn doped CuO films with a thickness of 181 nm deposited at substrate of temperature of 400°C are highly sensitive to hydrogen sulphide and exhibit a high response of 1036. It was also noticed that response time and recovery time also be reduced by doing doping of $SnCl_2$. As the Sn doping increases from 3% to 7% then sensitivity increase up to a point and then became saturate. The doping of tin into copper oxide can affect the sensitivity of the thin films,

particularly in gas sensing applications. The effect on sensitivity can vary depending on the dopant concentration. We observed that a moderate concentration of tin doping (5%) could further enhance the sensitivity of the CuO thin film. At this level of doping, the film's surface potentially leading to improved gas interaction and greater sensitivity to hydrogen sulphide gas. This is due to reason that the presence of Sn atoms increases the molecules of gas adhering and increase the sensitivity to target gas. The minimum response time obtained for sample 0.75MD1 of thickness 165 nm was 5 seconds. It was analysed that recovery time decreases as the operating temperature increases.

The detection mechanism of CuO films is depend on the change in electrical resistivity and conductivity on exposing H_2S gas due to absorption and desorption. The response and recovery time also improve by using 3% doping concentration. Any gas sensor must have long-term stability in its gas sensing characteristics. To determine the reproducibility of prepared thin films, we have noticed the response of H_2S gas over a period of 1-3 years and found it stable. Hence, the present work is suitable for hydrogen sulphide gas sensing applications.

.

ACKNOWLEDGEMENTS

express my gratitude to my lovely daughter – Nivika for being there for me at the end of the day. Your love is what has gotten me through when I wanted to give up.

(JYOTI)

Date:

TABLE OF CONTENTS

List of tables

List of figures

List of abbreviations

List of symbols

Chapter 1. Introduction

List of tables

List of figures

List of Symbols

Symbol	Full name
Å	Angstrom
μm	Micro-meter
%	Percentage
ω	Frequency
t	Thickness
°C	Degree Celsius
g	Gram
cm	Centi-meter
eV	Electron volt
d	Inter planer spacing
Θ	Bragg's angle
λ	Wavelength
β	Full width at half maxima
ħ	Planck constant
υ	Frequency of radiation
ε	Strain
α	Absorption coefficient
E_g	Band gap
ρ	Resistivity
Li	Lithium
G	Conductance
I	Current
V	Voltage
K	Kelvin
D	Dipole moment
mA	Milli- ampere
nm	Nano-meter
S/m	Simen per meter
Ω	ohm
σ	Conductivity
ρ	Density of Copper Oxide
δ	Dislocation density

CHAPTER 1

1. INTRODUCTION

1.1 Introduction of thin films

One of the oldest forms of art as well as one of the most recent fields of science are both thin-film technology. Thin films have been used since the ancient metal eras. Think of the age-old art of beating gold, which has been performed for at least four millennia. Gold can be hammered into very thin sheets of leaves because to its high malleability, and its beauty and chemical resistance make it ideal for use in enduring adornment and protection. The process of beating and gilding gold seems to have been first practiced by the Egyptians. The advancement of contemporary science has been significantly aided by thin film and their devices. In 1852, Bunsen and Grove achieved the first thin metal films in a system based on vacuum. Depending on the application, the thickness restriction might range from a few nano-meters to a few micro-meters.

In the beginning, research on thin films was done out of pure scientific curiosity, especially given how radically different those characteristics were from the same material's bulk properties. Hard disk read heads based on the GMR effect are a well-known example of this situation since they can only function because of the unique properties of a mix of magnetic and insulating thin layers. However, when the capacity to regulate thin film qualities was developed throughout time, it greatly aided the use of thin films in electronic devices along with other devices. As a consequence, the electronics sector has benefited most from thin film technology. Beside this, on decreasing the size of semiconductor devices up to two dimensions, technology of thin films used in development of microelectronics. The distinguishing feature of thin film technology is outstanding stability and precision together with a degree of accuracy (which is not commercially attainable in comparable to other technologies) of the electronic devices.

Thin film systems that serve as laser mirrors, anti-reflex coatings, and other optically responsive surface modifications make up a significant portion of further instances. They are put down on substrates in the optical sector that provide mechanical stability and other particular qualities. The change in features of thin films can be due to the rising surface-to-volume ratios at thinner films, as well as microscopic structures that rely on the deposition factors. Optical interferences, an increment in electrical resistance, reduction of the electrical

resistance of temperature coefficient, a rise in the temperature and magnetic induction that is critical for superconductivity and Josephson effect are all possible effects of a thin film [1].

1.2. History of thin films

For the interest of completeness, a short history of the technology of thin films is provided below:

- In 1650: interference pattern (e.g. oil on water) was observed and interpreted by R.Boyle, I.Newton and R.Hooke.

- In 1850: Commercial electrochemistry for gold plating of standardized accessories introduced by Galvanics, thickness measurement's method given by Wiener, Arago, Fizeau; Wernicke; and invention of the first deposition method given by W.Grove; M.Faraday; T.A.Edison.

- In 1940: Manufacturing on an industrial scale of coatings for various applications (primarily in the military).

- In 1965: In the semiconductor and optical industries, thin film technology has evolved into a crucial component of mass production processes.

- In 1990: High Tc-Superconductors films.

- In 2000: Making nanocrystalline materials with a known structure and makeup that can be used as protective layers and in tribology. The deposition of highly organized 2D and 3D objects with dimensions on the nanometer scale.

- In 2004: Increasing the capacity of sophisticated methods for reactive coatings for use in industrial applications (such as coatings on glass and thermal management). An inquiry into the combinatorial possibilities of ternary and materials pertaining to the quarternary systems.

- In 2006: The research that was done on organic coatings eventually led to the development of organic electronics.

- In 2010: Synthesis and study of its properties of the prototype two-dimensional material. The foundation of solid-state touch displays (Smartphones) into the realm of communication devices.

- In 2015: Creation of heterostructures using two-dimensional materials. Methods for producing ultrathin materials that can be shaped into flexible electrical devices.

- In 2018: Scientists developed a revolutionary method to produce ultra-thin films with unprecedented precision and durability. This breakthrough opened doors for advancements in flexible displays, solar panels, and electronic devices, revolutionizing industries and paving the way for a sleeker and more efficient future.

➢ In 2020: A remarkable breakthrough in thin film technology revolutionized the industry. Researchers introduced a novel method for producing ultra-thin films that boasted enhanced conductivity, transparency, and flexibility. This game-changing innovation spurred advancements in wearable electronics, foldable displays, and energy-efficient devices, shaping a future with sleeker, more versatile technology.

1.3 Definition of thin films

The thin film is a two-dimensional solid substance whose thickness is the only dimension that is significantly less than the other two. They generally have thicknesses of a few microns or less.
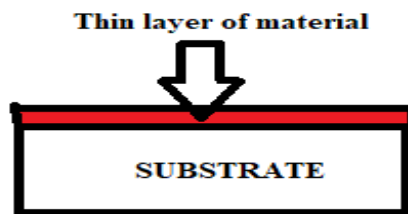
Figure1.1 Thin films of a material

Based on the magnitude, type of films is given as:

- Ultra-thin films having size of 50-100 Å.
- Thin films having size of 100- 1000 Å.
- Thick films having size of greater than 1000 Å.

Although literature sometimes uses the arbitrary figure of 1 µm, the boundary between "thin" and "thick" films is not something that can typically be defined. In general, a film is said to be "thin" when its characteristics vary greatly from those of the bulk. Films may be mathematically characterized as homogeneous solid material between two planes and stretched in two directions, but constrained in third direction perpendicular to XY plane. Thin films can be classified in three basic categories:
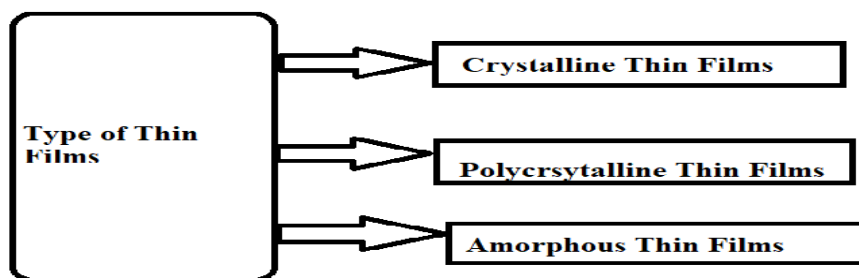
Figure 1.2 The types of films

1.3.1 Crystalline thin films

The crystal lattice of crystalline thin films is regular and free of grain boundaries. It can be difficult to create these kinds of thin films in the lab. Controlled conditions are a fundamental need for the fabrication of these thin films since the existence of grain boundaries has a substantial effect on their electrical and physical characteristics. A clean glass substrate is necessary for the manufacture of these kinds of thin films, and a high temperature is the primary need for the mobility of the growing species.

1.3.2 Polycrystalline thin films

The creation of polycrystalline thin films necessitates the use of materials with altered crystal size and orientation. The tiny polycrystalline grains result in the production of powder grains. Grain boundaries exist in polycrystalline thin films between two grains. For the creation of these kinds of thin films, a moderate deposition temperature is required. All substances, including ceramics and common metals, may be combined to make polycrystalline thin films.

1.3.3 Amorphous thin films

In the amorphous phase of thin films, which are deposited as solid layers on substrates with thicknesses of one to thousands of nm, atom positions are constrained to small ranges. Low temperature is required for production and there is insufficient surface transportation of the growth species [2].

1.4 CuO thin films

A number of highly referenced research publications on CuO sparked interest in the field of research in the middle of the 1980s. Several deposition methods, including as plasma and thermal evaporation, spray pyrolysis, dc magnetron sputtering, electrodeposition and sol-gel have proven successful in depositing CuO thin films. Early research in the 2000s was primarily concerned with the factors that drive growth and its mechanics [3].

CuO absorbs significantly throughout the visible spectrum and has a black appearance, whereas Cu_2O oxide films are said to have great transparency, a somewhat yellowish appearance, and to absorb primarily at wavelengths below 600 nm. Currently, solar cells and electro-chromic devices are two promising applications for copper oxide thin films [4-5]. Band gap energy values of copper oxide films have been found to be such that they can be used as windows for conversion of solar energy [6]. Richardson [7] has also emphasized the possibility of copper oxide films for use in aeronautical and architectural applications as spectrally specific variable reflectance coatings for luminescence management. It is necessary for materials to have both

low electrical resistivity and good transmittance in the visible range in order to be employed as solar cell windows.

The literature contains numerous attempts to create substitute production techniques that yield Cu_2O films with reduced resistivities. Reactive sputtering has been used by Drobny, Pulfrey, and other researchers in the literature [8] to try and generate copper oxide films. By adjusting the deposition settings, this technique might yield a variety of films with stoichiometries ranging from Cu-rich Cu_2O to Cu_2O and ultimately CuO. They discovered that they could alter the resistivity of the produced films by adjusting the oxygen partial pressure after producing copper oxide films using both D.C. and RF reactive sputtering. These authors reported on copper oxide coatings with resistivities that were as low as 25 cm [8].

The kinetics of the formation of oxides of copper during thin film deposition is dependent on a number of factors [9-11]

1) Cu, Cu_2O, and CuO nucleation rates during the deposition process.

2) The chance of the particles sticking to the substrate, or the sticking coefficient

3) Re-evaporation and migration caused by the oxygen and copper species that are encroaching

4) The nucleated species' disparate growth rates

1.4.1 Choice of copper oxide

Because of their distinct characteristics, copper oxides earned the most interest across all metal oxides. +1 and +2 are two oxidation states of copper under specific conditions, trivalent compounds have also been found. It has been demonstrated that this trivalent copper only lives for a brief period of time. Due to their stability, cupric oxide (CuO) and cuprous oxide (Cu_2O) are two significant copper oxide compounds. They exhibit a fascinating range of characteristics that can be fully utilized in catalysts, gas sensors, magnetic storage devices, solar cells, and other devices [12-16]. The only phase reported to be gas-sensitive is cupric oxide (CuO), which also demonstrates a variety of intriguing characteristics. CuO or tenorite oxide has monoclinic structure which makes it different from the transition metal monoxides. Among the family of copper compound, CuO has attracted particular attention because it has a number of potentially useful physical properties, including as spin dynamics and electron correlation effects. In the second part of the 20th century, this resulted in a rapid development of theoretical study, production, characterization, and applications of CuO-based devices [17-18].

1.4.2 Physical and Chemical Properties of CuO

Table 1.1 The physical properties of CuO.

Cupric oxide (CuO)	
Melting point of CuO	1134 °C
Boiling point of CuO	2000 °C
Density	6.32 g/cm^3
Appearance	Black powder
Solublity	In-soluble
Dielectric constant	12
Lattice parameters	a=4.69Å, b=3.42Å, c=5.13Å and β=99.54º
Energy band gap	1.2eV-1.9eV
Molecular mass	79.55 g/mol
Odour	Odourless
Type of material	Semiconductor

- **Structure and bonding**

Copper oxide is a molecular compound, and the copper atoms are coordinated by four oxygen atoms in a square planar configuration. The copper-oxygen bonds are ionic, with a partial charge of +1 on the copper atom and a partial charge of -2 on each oxygen atom.
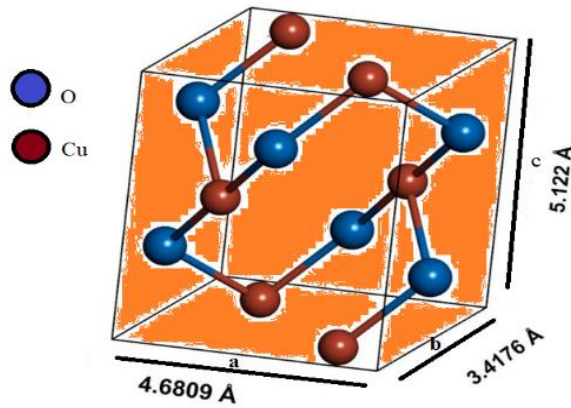
Figure 1.3 The structure of CuO.

- **Electrical Properties**

At the center of the Brillouin zone, CuO, a p-type semiconductor, has the narrowest band gap. CuO's electrical structure in its monoclinic form is depicted in figure I.16. Determined energy gap of 1.251 eV agrees with experimental observations i.e. 1.2 eV to 1.9 eV reported at room temperature [19]. Typically, CuO has a low conductivity. Both non-stoichiometry and grain boundary conduction have been implicated in the reported wide fluctuations in resistivity readings as well as the significant method-dependent relationship of resistivity. The conductivity evolution, on the other hand, demonstrates a novel behaviour that can be utilized as a crucial element for semiconductors-based gas detectors. The little quantity of contaminant in this material and its thermal stability in an environment with low oxygen partial pressure are two potential explanations for the behaviour of CuO [20].
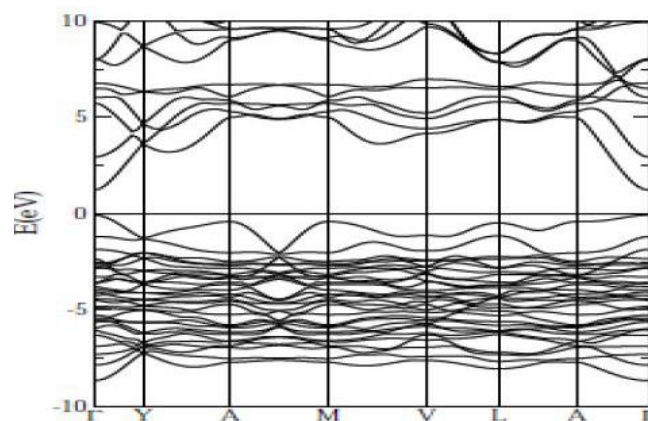
Figure 1.4 The CuO band structure computed by DFT+U method.

- **Optical Properties**

The grain size, temperature of substrate, thickness, concentration of doping, strain, structural characteristics, and disorder, as well as type of method used for deposition, all affect the optical properties of CuO [21-23]. Copper oxide emits photons in response to an energetic light beam or an electron bombardment. This occurrence is comparable to luminescence. Different luminescence bands were seen depending on the elaboration circumstances. Due to inter-band emission or near-band-edge emission as well as other defect states, the UV and visible luminescence is produced.

1.5 Experimental Methods for synthesis of Thin Films

Thin films are necessary in modern technology for a variety of purposes. Thin films are often used in contemporary technologies. The criteria for better and more affordable deposition systems, as well as for in-situ process controls and monitors for monitoring film parameters, have been successfully satisfied by equipment makers. There isn't a standard deposition method that can be used in every circumstance. Some particular qualities are needed for every application [24]. To meet the growing industrial needs, deposition methods have been greatly varied.

When an individual atom, ion or molecule species are manipulated to condense onto a solid substrate either physically or by chemical processes, the solid substance is said to be thin films. There are several deposition processes available for the creation of materials. Depending on how the thin-film deposition process is carried out, several ways may be used. Number of methods may be combined into two categories to accomplish the deposition of thin films:

1. Physical Vapor Deposition [25-27]   **2.** Chemical Vapor Deposition [28-29]

Three fundamental stages may be distinguished in the deposition of a film:

1. Preparation of the atoms, molecules, and clusters that compose films
2. Particle movement via source to the target.
3. Particle adsorption on the surface and film development
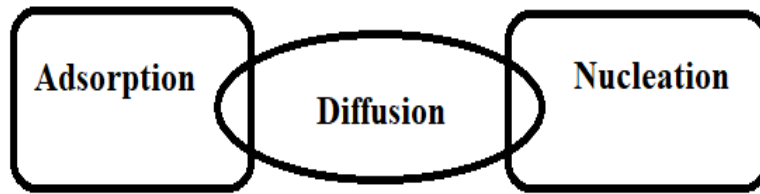
Figure 1.5 The stages of deposition of thin films.

1.5.1 Physical vapor deposition method

It is a deposition method in which films are prepared on substrate by condensation of entering species. The goal of PVD operations is to precisely transport atoms from a source to a substrate, allowing atomistic film development and growth to take place. In this instance, we have a solid source. Atoms are extracted from the solid target by thermal approaches in evaporation, but by the collision of gaseous ions on source surfaces in sputtering. Various of techniques used in PVD are shown by given table:

Table 1.2 Various techniques of PVD.

Physical Approach	
Evaporation	Sputtering
1. Electron beam evaporation	1. DC and magnetron sputtering
2.Inductive evaporation	2. Triode and getter sputtering
3. Resistive evaporation	3. Ion beam sputtering
4. Thermal evaporation	4. RF sputtering
5. Vacuum evaporation	5. A.C sputtering

1.5.2 Chemical Vapor Deposition method

Using CVD techniques, films are created on the substrate by chemical reactions between entering species. To fabricate solid state electronics devices, thin films are produced by using

chemical vapor deposition at high temperature. In this process non-volatile solid produced by chemical reaction of volatile compound.

Table 1.3. Various CVD techniques.

Chemical Approach	
Gaseous Phase	Liquid Phase
1. Chemical Vapor deposition	1. Electro and electro less deposition
2.Photo chemical deposition 3. Plasma enhanced vapor deposition	2. Chemical bath deposition 3. Epitaxy 4. Sol-Gel
4. Polymer assisted deposition	5. Polymer assisted deposition
5. Laser chemical vapor deposition	6. Spray pyrolysis 7. Spin coating

1.5.3 Deposition Parameters

Any deposition process may be described and recognized by the following five factors:

1. Type of source.

2.Type of medium for growth occurrence.

3. Method used (either CVD or PVD) to introduce the coating species in the medium.

4. Particles with coatings that are either molecules or may be other.

Thin films may be deposited using two or three different sequences, depending on the deposition process and the source of the material to be deposit. The deposition steps of various sources are described in new section.

1.5.4 Deposition steps using solid source

The liquid source approach primarily consists of three phases.

➢ The generation of gaseous particles from the source using energetic species via the process of evaporation or sputtering

➢ Atomic movement from the source to the substrate. For this stage to decrease film contamination and generate higher-quality films, a rather high vacuum medium is required. In this medium, reactive gas atom may be added to create composite films.

➢ Species condensing at the substrate.

Figure 1.6 The preparation of films using solid source

1.5.5 Deposition steps using liquid source

The liquid source approach primarily consists of two phases.

➢ Direct contact between the liquid and the substrate, such as submerging it completely, or solution application, such as spraying it on.

➢ Films are created when distinct species in a liquid interact chemically. In this phase, the substrate's temperature is crucial.
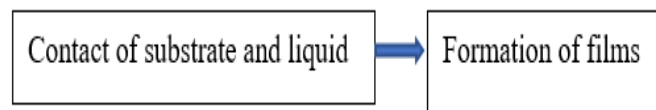
Figure 1.7 The preparation of films using liquid source.

1.5.6 Deposition steps using gaseous source

The gas source approach primarily consists of three phases.
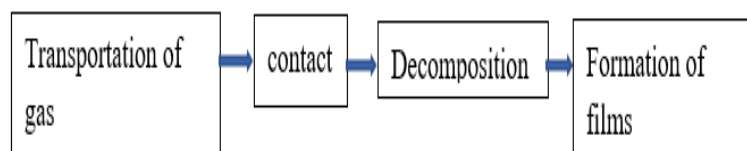
Figure 1.8 The preparation of films using gaseous source.

➢ The gas is transported into the deposition chamber by interaction among the source and the substrate.

➢ Thermal breakdown or electrical discharge converts gas into ions and molecules. Composed alloys are created by adding reactive gases. Vacuum is required, much as with solid sources, to prevent film contamination.

➢ The substrate temperature often starts or regulates chemical processes involving a variety of species at the site where films are to be formed.

The ability to create a wide range of films, semiconductors and compound in crystalline form with a high degree of purity and desired qualities, is one of the factors contributing to the increased acceptance of CVD technologies. Furthermore, CVD stands out from other deposition processes due to its capacity to controllably produce films with a broad range of stoichiometry. However, there isn't a perfect way to make thin films that can meet every need. But we confine ourselves to the methodology used in this investigation: spin coating.

1.5.7 Sol-gel Spin Coating

• **Sol- gel**

For material science, the wet-chemical sol-gel process has been used extensively. It is generally used to create materials, usually metal oxides, starting with precursor for making gel. With the use of the sol-gel technology, materials can be developed that can be used to create glasses, and ceramics from solution-based precursors. It creates thin layers made up of stacks of metal oxide nanoparticles. When compared to traditional synthetic pathways, this procedure is carried out at substantially lower temperatures under "mild chemistry" conditions.

The metal centers (M) are linked together by a sequence of hydrolysis and polycondensation processes in the sol gel process to create metal oxo and hydroxo polymers in solution. Metal chlorides, nitrates, and alkoxides are frequently employed as precursors in combination with aqueous or organic solvents. The chemical structure, surface polarity, surface acidity, and crystalline structure of the generated product are determined by the reagents, additives, and drying conditions that are used. The final microstructure can be affected in a way that improves selectivity and catalytic characteristics, by carefully varying the desired parameters at each stage of the process.

An appropriate solvent, frequently ethanol, is used to dissolve a metal alkoxide as the starting material. The substance is hydrolyzed when a small amount of water is added, and this process is typically aided with help of somewhat acidic solution. The end product is a loose gel with pores containing liquid that can be spin or coated to a surface. The materials created with this

method have various intriguing morphologies and are very porous, nanocrystalline, or amorphous [30-32].
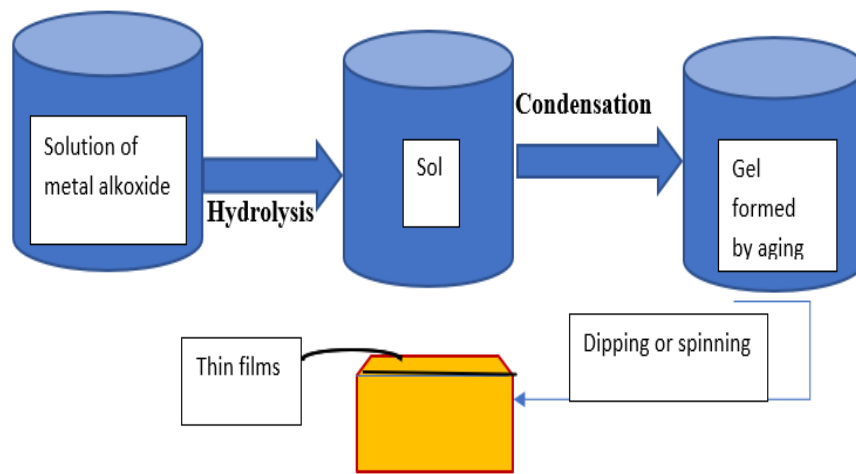
Figure 1.9 The sol-gel method for synthesize thin films.

- **Spin coating**

The spin coating process is the most prevalent chemical procedure used today since it can produce a homogeneous conducting and semi-conducting thin films. It is also well-liked for its ease of use and affordability. It is an easy and inexpensive process that can create uniformly thick, high-quality adhesive films. In a typical procedure, a small drop of fluid resin is applied to substrate and it begins to spin rapidly (usually at a speed of roughly 3000 rpm). Due to centripetal acceleration, finally a resin films produce at top of substrates.

The procedure of spin coating is used to deposit thin layers on metal substrates. This method is preferred for covering planar surfaces with thin layers of material. The substrate spins during the spin coating process about an axis which is perpendicular to coating area. The spin coating differs from dip coating because deposited films from spin coating are thin due to centrifugal draining and tends to be uniform due to the balance between the centrifugal force and the viscous force (friction)

The process of spin coating is divided in four stages as depicted in Figure 1.8. The processes of deposition, spin up and spin off take place in order, while evaporation happens at various points and eventually takes over as the main method of thinning near the conclusion.
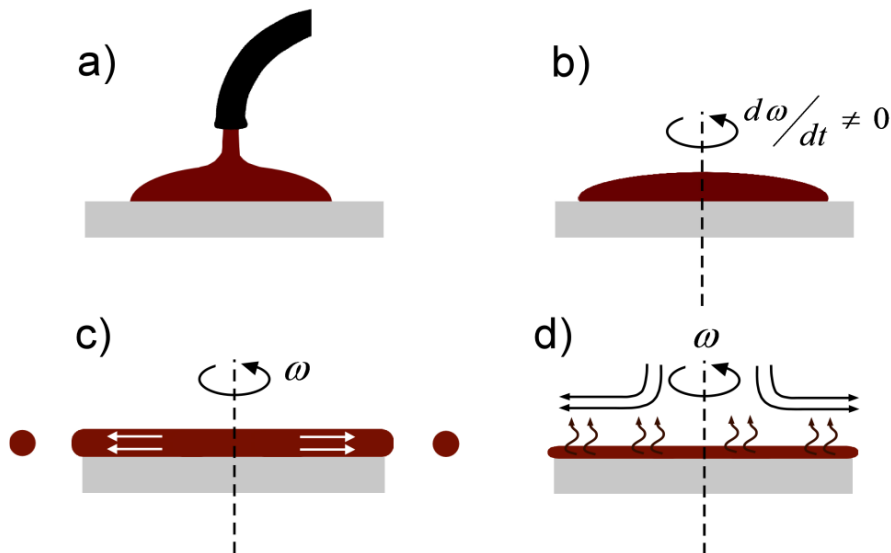
Figure 1.10 The different stages of deposition.

- **Deposition of sol**

An excessive volume of fluid is dispensed during the deposition process onto a still substrate. The fluid is applied through a nozzle to center of wafer. To avoid coating discontinuities brought on by the fluid front evaporating before it reaches the substrate edge, a lot of fluid is required throughout the coating process.

- **Spin up**

The substrate is speeded up to its required spin sped during the spin up phase. This stage sees the formation of a wave front as rotating forces are carried upwardly through the fluid that uses centrifugal force to flow to the substrate's edge and leave a largely homogeneous fluid layer there.

- **Spin off**

The surplus solvent is thrown off the substrate surface as the substrate rotates to higher spinning speed during the spin off step. Centrifugal forces are the main means of thinning the fluid until sufficient solvent is withdrawn to raise viscosity to a point where flow is stopped. After spin up, the spin off stage lasts for around 10 seconds [33].

- **Solvent evaporation**

A portion of the extra solvent is absorbed in the surrounding environment through the complicated process of evaporation. Premature substantial produces a solid skin on the fluid surface, which hinders the evaporation of solvent trapped beneath it and leads to coating flaws

when exposed to the centrifugal forces of the spinning substrate. Although present during the spin coating process, the main way to thin films is by evaporation after fluid flow stops. Due to the fact that film thickness is roughly inversely related to the spin speed square root. It gets more difficult to develop a solution that won't dry up before reaching the substrate edge as coating thicknesses rise. This is why thick films can occasionally be created by spinning together several thinner, more dependable coatings.

- **Advantages of spin coating**

This method provides several benefits in operations of coating, with the absence of connected process variables serving as its primary advantage. Spinning speed and fluid viscosity are the degrees of freedom which makes this process exceedingly reliable. Therefore, altering the spin speed or using a fluid with a different viscosity can quickly change the thickness of films. Many of the alternative coating processes that are later detailed include multiple coupled factors, which complicates coating control.

Another benefit of spin coating is that the film can become even more uniform as it thins, and if it ever does so throughout the process of coating, it will remain uniform the entire time. The maturity of spin coating implies that numerous spin coating-related issues have been researched and that a wealth of information is available [34].

1.6 Experimental Methods for Characterization of Thin Films

In the process of creating unusual materials, characterization is an essential stage. Structural, compositional and microstructural characterization and analysis of phase are all essential components of a material's comprehensive characterization and have a deep impact on its attributes. In the field of materials science, this has caused the birth of numerous cutting-edge approaches. Below are descriptions of various instrumentation techniques for characterizing thin films along with pertinent operating and functioning principles.

1.6.1 X-ray Diffraction technique

Effective and appropriate method for determining the microstructure of samples is X-ray diffraction. It gives helpful details of the existence and composition of the phases, size of grains and thickness of films without causing damage or requiring physical contact. The textbooks by Buerger [35] and Tayler [36] contain the fundamentals of X-ray diffraction. Diffraction generally takes place when the repetition spacing among scattering centers and the wave

motion's wavelength are of the same order of magnitude, which is Bragg's law. The Bragg's condition is given as equation (1.1), [37]:

$$2d \sin \theta = n\lambda \quad (1.1)$$

Where λ is stand for wavelength of X-ray, d denote the interplanar spacing, Θ for diffraction and n is stand for order of diffraction. In Laue Method, Bragg's angle remains fixed and vary the wavelength of X-ray to determine the orientation of crystal. In Rotating crystal Method, wavelength remains fixed and vary the Bragg's angle to determine the type of crystal structure. In the powder approach, the crystal under investigation is ground into a fine powder and exposed to a monochromatic x-ray beam. Each powder particle is a tiny crystal, or an assembly of smaller crystals, that is orientated arbitrarily in relation to the incident beam. In line with Bragg's law, the constructive x-ray interference should happen at a specific d value or Bragg's angle destructive interference for other values of interplanar spacing at which became lowest. The schematic of an X-ray diffractometer is shown by given figure
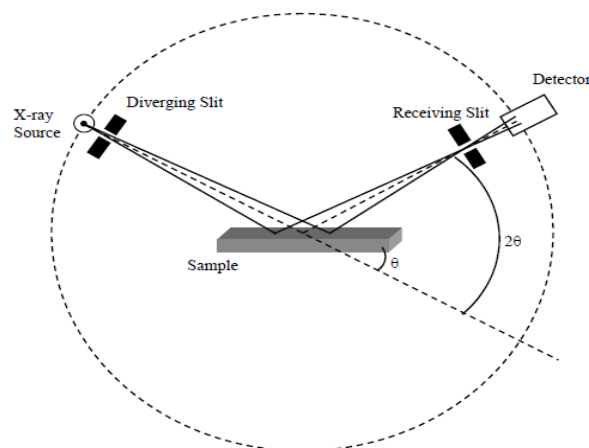
Figure 1.11 The X-ray diffractometer.

The best gratings for x-ray diffraction are crystals due to comparable interatomic distance to x-ray wavelength. Studies using x-ray diffraction can confirm the crystal structure and phase development because information of arrangements of atoms reveal by directions of diffracted x-rays. The method for fulfilling Bragg's condition has been developed, and it involves continuously changing either during the experiment. On the basis of variation in wavelength and Bragg's angle, three diffraction method was introduced to identify phase, orientation and type of crystal.

In Laue Method, Bragg's angle remains fixed and vary the wavelength of X-ray to determine the orientation of crystal. In Rotating crystal Method, wavelength remains fixed and vary the Bragg's angle to determine the type of crystal structure. In the powder approach, the crystal under investigation is ground into a fine powder and exposed to a monochromatic x-ray beam. Each powder particle is a tiny crystal, or an assembly of smaller crystals, that is orientated arbitrarily in relation to the incident beam. The standard JCPDS powder diffraction file can be used to determine the phases in a film from the d-spacings, and Miller indices can be used to index the reflections. From X-ray diffraction particle size was calculated with the help of Debye Scherrer formula [38].

$$D = 0.9\lambda/\beta cos\Theta \quad (1.2)$$

Where D denote size of crystallite, Ɵ denotes Bragg's angle, λ used for X-ray wavelength and β is stand for full width at half maxima.

1.6.2 Scanning Electron Microscopy (SEM)

In comparison to an optical microscope, SEM is a which examine morphology of the material with good resolution and high magnification. This technique is a practical approach for determining size of grains and researching microstructural elements. The only extra preparation needed for metal items for SEM is cleaning and mounting on a specimen stub. Gold, platinum, tungsten, and chromium are conductive materials now used for specimen coating. During electron irradiation, coating prevents the object from accumulating static electric charge. Even when the specimen conductivity is sufficient to prevent charging, coating is nevertheless recommended in order to boost signal and surface resolution, especially with materials with low atomic number (Z) [39].
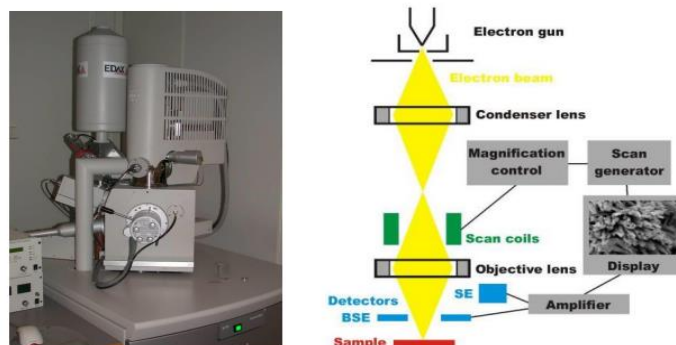
Figure 1.12 The schematic diagram of SEM

The usage of these numerous products to gather the various types of information about the sample is dipcted in Fig. 1.12

The characterization of materials has made considerable use of electron interaction with elements. When primary electrons have enough energy, they can remove the electron from an atom's inner shells, which allows Auger electrons or X-ray photons to escape and allow the excited atom to relax. Secondary and backscattered electrons are produced by the electrons of the atom scattering. These scattered electrons produce a picture that contains data about the sample's microstructure. Both the secondary electron image and the backscattered electron image are terms used to describe these pictures. Numerous interaction products are created when an electron collides with an atom.

Backscattered electrons, secondary electrons, and transmitted electrons of these all reveal details about the sample's microstructure. The auger electron, ejected electrons, and x-rays' energy is unique to its element. Backscattering and SE emission at the surface are intensified, increasing resolution and creating a surface image. [40].

1.6.3 Fourier Transform Infrared Spectroscopy (FTIR)

A tool for both qualitative and quantitative investigation of the various chemical groups present in the material is FT-IR spectroscopy. The infrared (IR) light is directed through an interferometer rather of being measured for energy absorption as the IR light's frequency changes (using a monochromator). After applying the Fourier transform to this interferometer data, a spectrum resembling to infrared spectrometer is produced. The fundamental concept behind infrared spectroscopy is that chemical bonds vibrate at specific frequencies. The masses of the atoms at its two ends as well as the bond's length affect its resonant frequencies. The schematic illustration is given as below
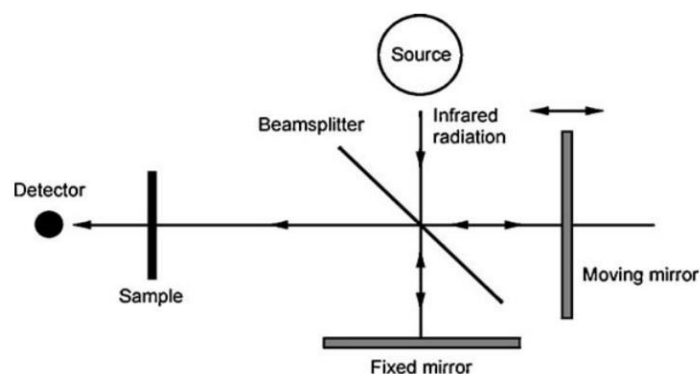
Figure 1.13 The schematic representation of FTIR spectroscopy.

A sample is subjected to electromagnetic radiation in a traditional IR spectrometer, and the amount of radiation that is transmitted is measured. The response is shown as a frequency function and the radiation energy is changed over the appropriate range. The radiation will be absorbed at specific resonance frequencies that are unique to the particular sample, producing a series of peaks in the spectrum that can be used to identify the sample. The majority of spectroscopic research is done in a comparatively limited region of the spectrum that is near to visible light. This zone, which is often defined as having between wavelengths of 10^{-6} cm and 10^{-3} cm, comprises the UV, visible, and IR regions. A molecule's vibrational spectrum is regarded as both a characteristic and a special physical property. To support XRD technique for characterization, the infrared spectrum can therefore be employed as a fingerprint for identification [41].

1.6.4 UV-VIS Spectroscopy

The measurement of the broad range of light absorbed by a sample in the ultraviolet-visible region, absorbed energy distribute electronic structure of molecules, atoms or ions is known as ultraviolet-visible spectroscopy (UV-Vis). This energy is absorbed by electrons, allowing them to move from a valance band to conduction band. This method provides information on the material's optical properties, including estimates of absorption coefficient, refractive index and band gap. The electromagnetic radiation source, cell (where sample and reference put down), and the detector are the three basic components of the UV-visible spectrophotometer.

The ability of a molecule to absorb light in the UV-visible area of electromagnetic radiation changes as a result of energy absorbed in the UV or visible region, which changes the electronic excitation of the molecule. Colour transition results from this. The following equation describes the association between the frequency, wavelength, and wave number of the radiation that caused the electronic transition and the energy absorbed in the transition:

$E = \hbar \upsilon$ (1.3)

Where E is used for photon energy, υ is frequency and $\hbar$ is planck constant.

The absorbance is given by beer's lambert's law which is state by given equation (1.4)

$A = -\log_{10} (I_T / I_o)$ (1.4)

Where A is absorbance, I_T and I_o are transmitted and incident light respectively [42].

The band gap in the absorption spectrum represents the least amount of energy necessary for a photon to drive an electron across the band gap and be absorbed in the semiconductor material, hence it corresponds to the point at which absorption starts to increase from the baseline. The local density of states at the valence band maximum and conduction band minimum, as well as excitonic effects, are reflected in a nonlinear increase in absorption in real spectra. The absorption coefficient α can be created by normalizing the absorbance A to the light's path length l through the material [43].

$\alpha = \ln(10) \times A / l$ (1.5)

According to Tauc's plot, the optical band gap (E_g) of the films was determined by the following relationship

$(\alpha \hbar \upsilon)^n = A(E_g - \hbar \upsilon)$ (1.6)

Depending on the type of electrical transition, we can choose value of "n" as 2, 1/2, 2/3 and 1/3 for direct-allowed, indirect-allowed, direct-prohibited and indirect forbidden respectively [44].

1.6.5 Two-Probe

For determining resistivity of high resistivity specimens, such as polymer films/sheets, two probe approach is appropriate.
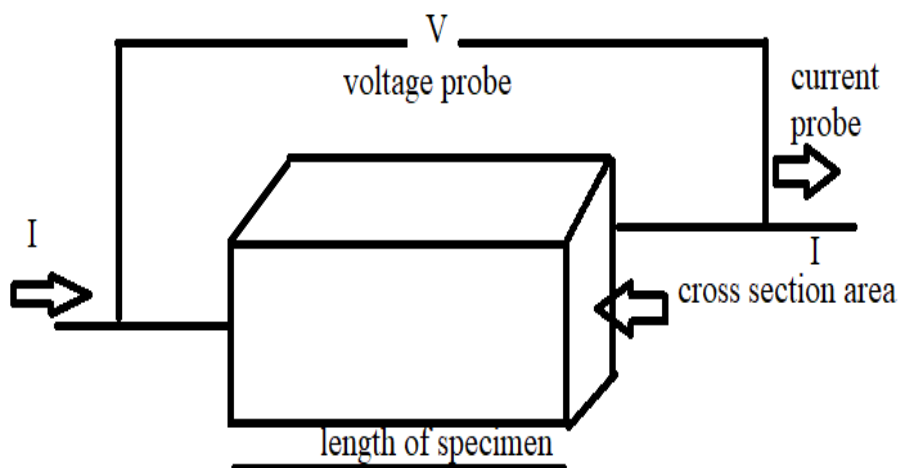
Figure 1.14 The measurement of electrical resistivity by two-probe method.

The resistivity is determined using the voltage drop (V) and current (I), as shown follows:

$$\rho = \frac{V \times A}{I \times L} \quad (1.7)$$

Where ρ is resistivity of sample, V is applied voltage, I is obtained current, A used for cross-section area of films and L stand for the sample's length [45].

In two-probe set-up two independently spring-loaded probes on it. The probe assembly is supported by alumina stand and sample plate. The thermocouple connection is inserted in the sample plate directly beneath the sample to guarantee accurate measurement of sample temperature. This stand doubles as the oven's lid and supports the weight of the oven. To connect to a capacitance meter and a temperature controller, the appropriate leads are provided. There is a superior oven with temperature control. High grade Kanthal-D is employed as the heating element. In order to prevent any heating wire slipping, it is set atop a specially constructed grooved, sintered alumina fixture. To reduce outer cover heating, a shield of heat is provided. To meet the safety standard, the top half is also adequately covered. The controller performs better since the oven is built for quick heating and cooling rates.

An excellent PID controller is used in a two-probe setup to simply set and manage temperature. The user may change the P, I, and D parameters for particular applications and to automatically tune the oven as needed. The user handbook provides instructions for these. However, with the current setup, only the large oven is to be utilized, even though controller works with ovens of 200°C and 600°C temperatures. The thermocouple is used by the controller as a temperature sensor.
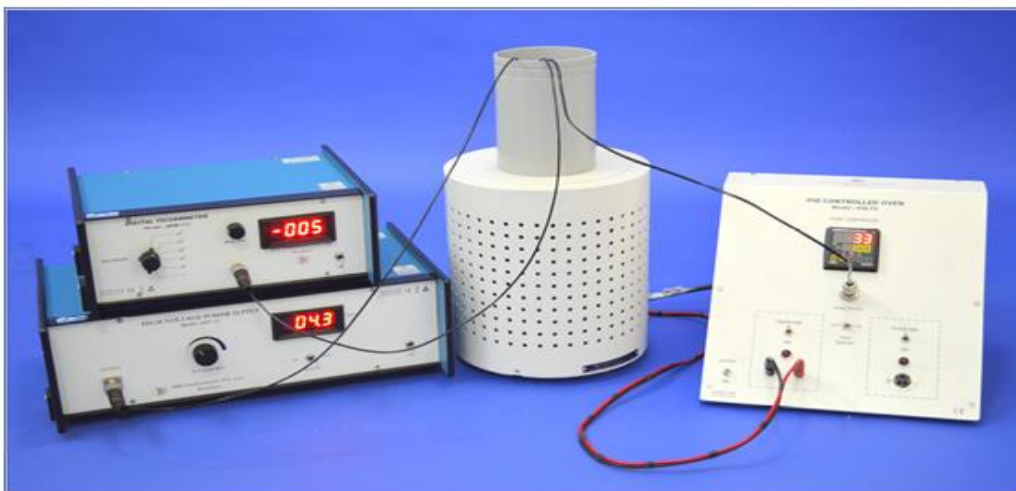
Figure 1.15 The two-probe set-up.

1.7 Applications of Thin Films

Thin films synthesized from semiconducting materials preferred for gas sensors [22], superconductors, magnetic portable devices [46-48], solar cells [23] photoelectrochemical cell and Li batteries [49-50].

1.7.1 Thin Films As Solar cells

First-generation solar cells account for around 89% of the worldwide solar cell market, making solar energy the most accessible, reliable, and affordable renewable energy source. It is necessary to increase the production processes' efficiency in order to produce thin-film solar cells [51]. In order to effectively activate surface plasmon polaritons (SPPs), the periodicity of the grating device was selected. Their insertion in this layer is meant to boost solar energy absorption by condensing plasmon resonators on the surface [52-53].

Plasmonic gratings, when inserted onto the surface of a solar cell, enhance absorption, minimize losses with remarkable efficiency, and facilitate light power transmission for optoelectronic devices [54]. Light is diffracted by the grating surface, which lengthens the path the light takes when reflected. The absorber layer of a solar cell can absorb more light with greater efficiency if surface plasmon resonance and effective light trapping are both used [55]. Different models that fall into two categories are employed to create solar energy monitoring circuits and systems with great efficiency.

To configure the primary PV parameters, which require low processing times even with reduced precision, the first approach is based on the inclusion of simple, compact models [56]. Less precision and longer computation durations are needed for the second, which is based on the inclusion of complex models [57]. The two varieties of those models suffer from a dearth of knowledge regarding semiconductor physics outside of a few research publications [58-59], and they are both employed for various objectives contingent on the design specifications. It is possible to build the Si solar cell in an n-i-p sequence in addition to its initial p-i-n configuration [60].

The intermediate band solar cells (IBSCs) proposed by Luque and Marti [61]can be utilized to increase power conversion efficiency. The maximum efficiency value that other forms of solar cells have managed to accomplish is less than this enhancement's potential 63.2% value [61]. Quantum dots (QDs) can increase the efficiency of solar cells by being incorporated into their active layers, according to numerous theoretical and practical investigations [62]. Of all the IBSC types that have been reported in the literature on science to date, quantum dot intermediate band solar cells (QDIBSCs) have the highest efficiency [63]. At the surface, there are numerous reflections that lengthen the optical path of the light wave path and cause

absorption [64]. Research has demonstrated that maximizing a solar cell's efficiency can be achieved by using a surface grating with a triangle or pyramid form [65].

The layers of solar cells with thin films are made up of diverse materials. CuO thin film is a prospective absorber layer due to its 1.4eV band gap, low manufacturing cost, p-type conduction, stability, high visible absorption coefficient and non-toxicity. CuO-based solar cells have a maximum theoretical conversion efficiency of about 31%. Various deposition processes, including sol-gel spin coating, electrodeposition, evaporation and sputtering used for making solar cells with CuO as a active layer.

The kind of window layer, such as ZnO, CuO and sn doped ZnO utilized also has an impact on the solar cells' efficiency. Several experiments involve controlling buffer layer optical and chemical features to improve solar cell efficiency.

Table 1.4 The efficiency of solar cell year wise.

Year	Efficiency of solar cell based on CuO
2010	0.02%
2014	2.88%
2018	4.19%
2022	19.65%

Bhaumik et al. reported the greatest photovoltaic performance for hydrothermally produced CuO nanostructure thin films. In 2018, J.sultana deposit CuO and ZnO nanowire on silicon substrate and increase the efficiency of solar cell up-to 4.19%. Y. Ait- Wahmane shows that the efficiency of solar cell formed by using CuO thin films improve upto 19.65% in 2020 year [66].

1.7.2 Thin Films as Gas Sensors

There are numerous metal oxides that can be used to conduct measurements to find flammable, reducing, or oxidizing gases. Numerous metal oxides have been effectively employed as for gas sensors sensitive layers [67]. However, up until now, huge research efforts in the field of metal oxide gas sensors have been focused on n-type semiconductors and little attention paid p-type oxide for sensor characteristics.

Gas sensors based on CuO have been produced using a variety of manufacturing techniques. Purity of films, morphology of surface, performance and repeatability are aspects that must be

considered when choosing the production procedure. Selectivity, low operating temperature, high sensitivity, low detection limits, stability, less response time and a long-life cycle are all desirable characteristics of a chemical sensor. CuO thin films have been utilized to detect flammable, poisonous, and polluting gases such as ethanol, NO_2, methanol, CO, H_2, acetone vapor, CO_2, organic vapor and H_2S gas [23].

Table 1.5 The sensitivity analysis by gas sensors fabricate from various processes [68-72].

Type of gas	Concentration of gas (ppm)	Applied method to fabricate gas sensor	Operating temperature	Response time(s)	Sensitivity
NO_2	200	Rf sputtering (CuO sensor)	180	6	26
Ethanol	2500	Spray pyrolysis (CuO sensor)	350	247	29
H_2S	100	Sol-gel (CuO sensor)	200	25	24
Methanol	2500	Spray pyrolysis (CuO sensor)	400	235	15
H_2	3000	Sol-gel (CuO-ZnO sensor)	200	250	60

Table 1.5 provides an overview of the performances of sensors made by CuO using different deposition processes and for different gases. Sensitivity has now gained greater prominence as one of the crucial gas sensor properties, and work has been done to increase gas sensors' sensitivity. There is a claim that sensors based on the combined use of the two components are more sensitive than the use of the individual components separately. Because of this, more recent research has concentrated on composite materials such ZnO-CuO, SnO_2-ZnO and CuO-TiO and found a good increment in sensitivity.

1.7.3 Other Applications

Thin layers of cupric oxide (CuO) have played a crucial role in the field of superconducting material of high temperature. Thin films made of CuO have demonstrated superconducting properties above the temperature of liquid nitrogen. Numerous studies and reports have been published, and work is still being done to enhance CuO-based high-temperature superconductors. Researchers have looked at the antibacterial properties and found that CuO are quite useful in this area.

Nanoparticle of metal oxides has recently gained popularity and has shown to be quite effective. Additionally, frequently investigated as a potential material for nanofluids is cupric oxide (CuO). According to reports, adding 4 vol% of CuO nanoparticles improved thermal conductivity by 35% in flowing water at a temperature of 51 °C. The thermal properties of water were said to be improved by up to 46% with the addition of 0.1 vol% CuO nanoparticles. The thin layers applied to lenses and mirrors as anti-reflection coatings, for corrosion protection, in magnetism and magnetic fields. Electronic devices such as piezoelectric detectors, transistors, diodes, and integrated circuits are all made of thin films. For a long time, researchers have searched for suitable alternatives to graphite electrodes. The usage of CuO nanoparticles as an anode material in Li-ion batteries with a large capacity and superior persistence has been confirmed in numerous papers [73].

1.8 Gas sensors and their various types

The International Union of Pure and Applied Chemistry (IUPAC) defines a gas sensor as a device that converts chemical data into an analytically relevant signal [74].
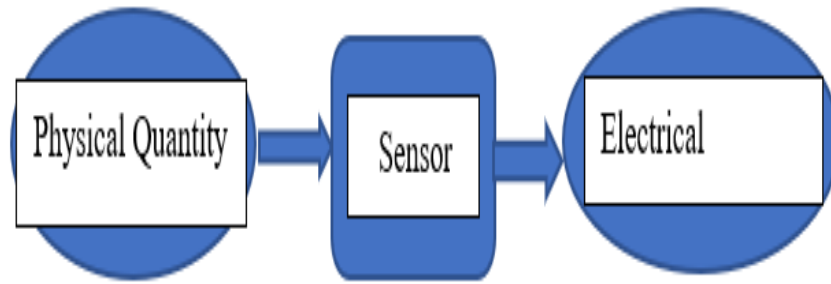
Figure 1.16 The block diagram of sensor.

Chemical sensors typically include two primary components: a transducer and a receptor. Chemical information is converted by the receptor into an energy form that the transducer can measure. This energy is transformed by the transducer into an analytical signal that is helpful and often electrical. In another words a gas sensor transforms chemical species, such as the gas concentration, into a consistently measurable signal. It then changes this signal into a useful analytical and observable signal. The surface of metal oxide worked as the receptor in sensor made by using metal oxide.

Chemical sensors may be categorized in a variety of ways, one of which is based on the receptor's working principle. Using this concept, it's possible to distinguish between physical sensors, chemical sensors, and biochemical sensors. The signal from physical sensors is produced by a physical process, such as a change in mass, absorbance, refractive index, temperature, or conductivity, rather than by a chemical reaction, which would typically occur at the receptor. Chemical interactions between the molecules of analyte and the receptor are the foundation of chemical sensors. Chemical sensors are under the category of biochemical sensors since they measure biological reactions. A gas sensor is an excellent example, where gas adsorption produces the signal. Various of gas sensors have been characterized as follows based on reception and transducer principles [75]:

1. Optical gas sensor
2. Acoustic gas sensor
3. Amperometric gas sensor
4. Potentiometric gas sensor
5. Metal oxide-based sensor

1.8.1 Optical gas sensor

The optical gas sensor is a common device in the gas detecting sector; it is just a wave-guide sensor built with optical fibres. These optical fibres are called optodes which provide change in optical properties. The mechanism of optical sensor based on transduction method in which gas molecules are detected by using absorption and emission of gas species. Butler [76] invented first optical gas sensor in 1984 using a Palladium and Titanium-coated optical fiber. S. Okazaki et al. [77] made a tungsten trioxide fiber optic gas sensor. The sensor detected hydrogen gas at room temperature using platinic acid at 500°C.

Most commonly used optical gas sensor is infrared gas sensor. The detector used in infrared sensors transforms the electromagnetic radiation energy into electrical impulses. Additionally, it has an infrared source that may be used to detect CO_2, CO, and other hydrocarbons. This source might be an ordinary incandescent lamp or a heated wire filament. Dispersive and non-dispersive are two types of an optical fibre.

Time and space double beams are used in infrared CO_2 gas sensors. The space double beam and cone-shaped air chamber improve construction in this design. The optical probe in this illustration 1.17 contains two sapphire windows, an air chamber, an infrared source and a reception mechanism. With CO_2 gas concentration 0–3%, the sensor had an accuracy of 0.026 %. A carbon infrared emitter and infrared camera system for propane detection was tried by Naoya Kasai and colleagues. [78].
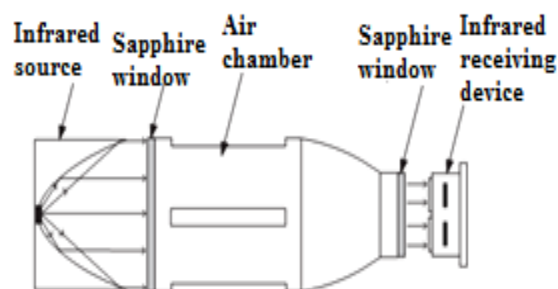
Figure 1.17 The optical probe structure [79].

1.8.2 Acoustic gas sensor

Because acoustic wave serves as its sensing mechanism, acoustic wave sensors get their name. Any modifications to the properties of the propagation, the velocity or amplitude of the wave gets change as it travels through or over the surface of the material. The phase properties of the sensor may be used to monitor changes in velocity for relevant physical quantity being

measured. Depending on how the waves propagate, types of acoustic wave sensors cab be described. The particular kind of SAW wave used in gas sensing applications depends on the piezoelectric substrate selected. The material of the substrate, how crystallized it is, and the operating frequency all affect the wave's speed of propagation.

Wireless, little power usage and high sensitivity are the ability to be used in hazardous environments and on moving or rotating parts are the key benefits of adopting SAW technology. Due to the SAW device's fabrication method being comparable to that of other microelectronic devices, it is also technologically compatible [80]. An acoustic wave sensor consists of a transducer, or component to produce an electrical signal, and a receptor, or component that is sensitive to an analyte. The first acoustic gas sensor was created by King in 1964 [81]. It worked by detecting bulk acoustic waves in a quartz crystal resonator constructed of piezoelectric material, which is sensitive to mass changes.
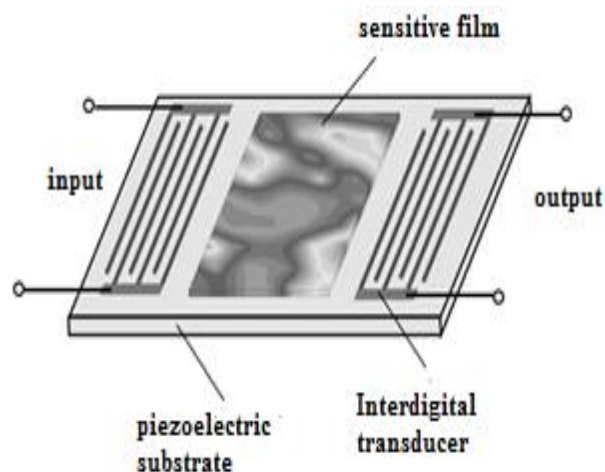
Figure 1.18 The surface acoustic wave gas sensor [82].

Chemical detectors for industrial air pollutants were created in the middle of the 1960s after extensive research investigations. These sensors are known as quartz microbalances (QMB) because they make use of piezoelectric quartz resonators. Applications for acoustic wave sensors include measuring temperature, pressure, mass, and chemicals.

1.8.3 Amperometric gas sensor

The sensor signal from amperometric sensors is a diffusion-limited current that operates at a constant applied voltage. As illustrated in below figure, it comprises of a reference electrode, a working electrode, and a counter electrode and a potentio stat which is a device for maintaining constant voltage.

A three-electrode design is used to construct amperometric sensors, which are typically constructed using two-electrode design due to the limitations of concentration of reactant gas. When using three electrodes, the current at the detecting electrode may be monitored at a fixed potential, providing potential of thermodynamic for all processes. The target gas's current produced at the sensing or working electrode is measured as the sensor signal, which can be recorded at either a constant or changing electrode potential.
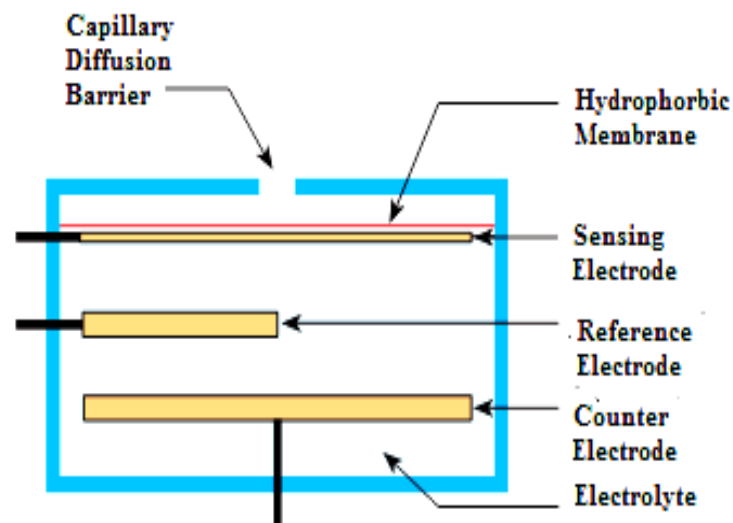
Figure 1.19 The electrochemical gas sensor [83].

By altering the electrolyte, different gases may be detected using amperometric sensors described the use of amperometric gas sensors for hydrocarbon monitoring in exhaust pipes [84].

1.8.4 Potentiometric gas sensor

The analytical concentration of various analyte gas components is determined using potentiometric gas sensors. They can keep an eye on an electrode's electrical potential even when there is no current flowing. The signal is measured by the potential difference between the working electrode and the reference electrode. For the detection of oxygen, potentiometric sensors have been employed.

The source electrode is in touch to a measured oxygen partial pressure, whereas the working electrode is in contact with an unmeasured unidentified oxygen partial pressure. The sensor produces an EMF when the electrodes are separated from one another and in touch with two distinct oxygen partial pressures. The most common materials used to make electrodes are

29

palladium, platinum, gold, and silver. For the detection of various gases, several electrolytes or a mixture of two compounds have also been employed [85-86].

1.8.5 Metal Oxide gas sensor

Since a very long time ago, it has been understood that the presence of impurities in a semiconductor's volume or on its surface greatly affects how resistant it is to electricity. This result was proved for Ge in 1953 [87-89]. The conductivity of ZnO thin films heated to about 300°C was later demonstrated to be sensitive to air's exposure to reactive gas traces. SnO_2 was claimed to have more stable but similar characteristics. These findings inspired the creation of new industrial gas sensors. Earlier metal oxide-based detector materials suffered from high cross-sensitivity, humidity sensitivity, long-term signal drift, and poor sensor response. Metal-oxide semiconductors were tested to increase sensor performance. Due to a lack of sensor response mechanism understanding, trial and error was required to find a suitable material.

The most well-understood oxide-based gas sensor is SnO_2 sensor prototype decades after its original publication. It was known that crystal structure, doping agents, manufacturing technology, operating temperature, etc. might influence sensor characteristics. Nanotechnology has increased academics and engineers' interest in gas sensitive materials. CuO, NiO, TiO_2, WO_3, and SrO are examples of metal oxides (MO) that can exhibit a gas detection sensitivity due to changes in conductance and resistance [90]. The diversity of metal oxides is split into the following categories because the electrical structure is the primary consideration when choosing a metal oxide for a sensor.
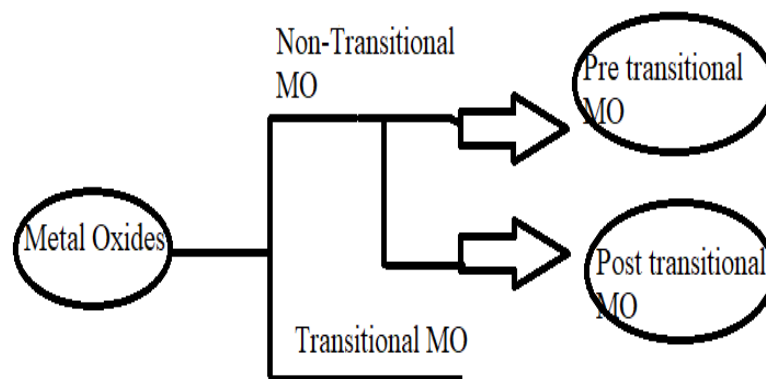
Figure 1.20 The classification of metal oxides.

Transition MOs are not suitable for gas sensing applications, mostly because of structural instability. Large bandgaps are present in pre-transition metal oxide semiconductors (MOS). Therefore, selecting a pre-transition MOs is inappropriate since electron-hole formation is difficult. Hence to measure the conductivity or charge in resistance of pre-transition metal oxides is challenging. For gas sensing applications, the best suitable MOs are post-transition metal oxides [91].

1.9 Principle of MOS gas sensor

Utilizing the chemi-resistance concept, the metal oxide gas sensor operates. The gas molecule can either behave as an acceptor or a donor when it contacts surface of metal oxide. This alters the thin film's resistance or electrical conductivity. The degree to which a gas molecule is reduced or oxidized at room temperature, as well as the percentage of carriers in the thin film, both have an impact on the metal oxide semiconducting thin film's resistivity [92]. Adsorption sites on the surface make sure that gas molecules interact with the substance in the right way.

When it comes to n-type, the advent of oxygen ion species often causes the surface to become depleted of electrons. When these species are exposed to a detecting gas, the gas molecules react with them to return an electron to the surface, boosting conductivity. The p-type, which has a hole as the main carrier, experiences comparable challenges. The chemiresistive behaviour of these gas sensors is explained by the receptor function mechanism in conjunction with the transduction function [93-95]. The metal oxide sensors might be thick or thin sheets, or sintered pellets. The receptor and transduction functions are specifically determined by the shape of the crystallites in the produced crystals and their connection between crystallites.
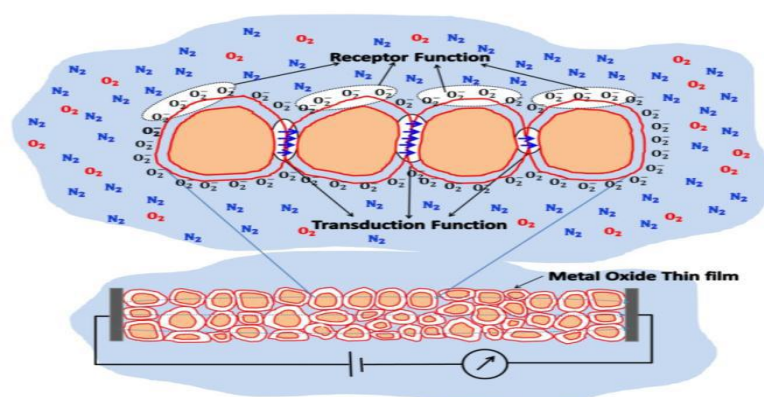
Figure 1.21 The diagram of metal oxide thin film gas sensor.

1.10 (REDOX) mechanisms for reducing gas molecules

When reducing gases come into contact with the surface of a metal oxide, these gases serve as electron donors. By observing the chemical changes that follow the REDOX reaction, the fluctuation in the material's resistance may be utilized to measure the concentration of reducing gases such SO_2, C_2H_5OH, CO, NH_3 and H_2S.

1.10.1 Sulphur dioxide (SO_2)

One of the most toxic gases, sulphur dioxide bonds with the metal layer's strong electron pairs to render it non-resistant. SO_2 and water molecules react in the atmosphere to generate the acid shown in below Eq.

$$2SO_2 + 2H_2O + O_2 \longrightarrow 2H_2SO_4 \quad (1.8)$$

Hydroxide ions and SO_2 increase the acidity of a surface in a moist environment, which severely corrodes the substance. The SO_2 molecules mix with the oxygen adsorbed on the surface to create sulphate (SO_4) ions, which enhances the conductivity of the n-type material in low humidity or dry environments. The continual contact of SO_2 molecules immediately bind with metal sites by entirely desorbing the adsorbed oxygen from the surface and replacing the lattice oxygen from the first layer, maintaining its resistance after integration.

Chemical kinetics of SO_2 molecules causes the concentration of carriers in n-type materials to grow, and this is because sulphate molecules have taken the position of oxide molecules on the surface [96].

1.10.2 Hydrogen (H_2)

H_2 molecules interact with the thin film surface again as hydroxyl ions after being adsorbed as protons and desorbed as water vapour [97]. Hydrogen and water vapor may entirely develop over 300 °C [98]. Proton adsorption on the surface increases the electron concentration, as seen in below Eq.

$$H_2 \longleftrightarrow 2H + e^- \quad (1.9)$$

Using p-type CuO metal oxide, Hao et al. [99] demonstrated how to detect hydrogen; the process is shown in Eq. 28.

$$2H_2 + O_2{}^-_{ads} \longleftrightarrow 2H_2O + e^- \quad (1.10)$$
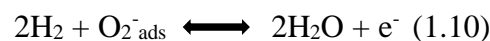
1.10.3 Carbon monoixide (CO)

As a reducing agent, carbon monoxide oxidation raises surface electron concentration. Carbon monoxide and chemisorbed oxygen generate carbon dioxide in dry air. Metal oxide does not react to lower carbon monoxide concentrations in moist atmospheres. The metal oxide surface formed formate (HCO_2) ions, an intermediate in CO oxidation.

$$CO + OH^- \longleftrightarrow HCO^-_2 \longleftrightarrow H^+ + CO_2 + 2e^- \quad (1.11)$$

$$CO + H_2O \longrightarrow CO_2 + H_2 \quad (1.12)$$
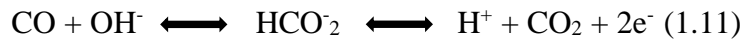
Weimer group used work function computation and experimental work to study the interaction between p-type CuO and CO in humid and dry conditions. Humidity enhanced metal oxide reaction [100]. The REDOX process follows Eqs. 1.13 [101] and 1.14 [102] for temperatures below and above 250 °C. Both equations demonstrate that operational temperature figures out material detection limits.

$$2CO + O^-_2 \longrightarrow CO2 + e^- \quad (1.13)$$

$$CO + O^- \longrightarrow CO_2 + e^- \quad (1.14)$$

1.10.4 Ethanol (C_2H_5OH)

Ethanol is the most significant ambient organic molecule since it is employed in many laboratories and companies for research and applications. The adsorbed ethanol's functional group breaks down as water vapours or hydrogen molecule depending on metal oxide's acidity or basicity. Cyclobutadiene (C_2H_4) and acetaldehyde (CH_3CHO) formed during dehydration or dehydrogenation caused carbon dioxide gas molecules and water vapor to desorb. The ambient oxygen partial pressure determined ethanol desorption.

$$C_2H_5OH \longrightarrow C_2H_4 \uparrow + H_2O \uparrow \quad \text{(Acidic oxide)} \quad (1.15)$$

$$2C_2H_5OH \longrightarrow CH_3CHO + H_2 \uparrow \quad \text{(Basic oxide)} \quad (1.16)$$
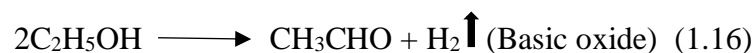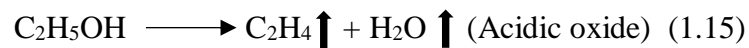
The metal oxide's oxygen-adsorbed surface can be acidic or basic by adsorbing dissociated H and OH ions. Infrared spectrum study showed that 50% RH did not influence sensor response [103].

1.10.5 Hydrogen Sulphide(H_2S)

H_2S vapor significantly interacts with metal oxides to create elemental sulphur. Oxygen adsorption on metal oxide surfaces enhances H_2S vapor response which is stated by below Equation. The above Eq. also describes the significant reduction behaviour in thick oxygen atmospheres with sulphur dioxide and water vapor by products. At low partial pressure of oxygen, H_2S immediately interacts with lattice oxygen to make SO_4 and creates an oxygen vacancy on the metal oxide surface, increasing conductivity.

$$2H_2S + 3O^-_{2(ads)} \longrightarrow 2H_2O + 2SO_2 + 3e^- \quad (1.17)$$

Adsorbed oxygen was totally desorbed as a result of H_2S's ongoing contact with the surface, which caused it to directly interact with the surface and produce elemental sulphur [104-105]. The process that results from this sulphur's ability to replace the lattice's oxygen is known as a sulfurization reaction, and it is described as follows.

$$MO + H_2S \longrightarrow MS + H_2O \quad (1.18)$$
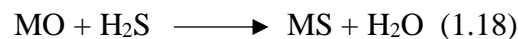
Where MO is the metal oxide and MS is the metal sulphide.

1.11 Features associated with gas sensor materials

1. Sensitivity: Sensitivity refers to a sensor's ability to detect changes in its physical or chemical properties as a result of exposure to the test gas. The proportion of air resistance to presence resistance of the test hazardous gas is used to determine the sensor's operational sensitivity. It is expressed mathematically as

$S = \dfrac{Rg}{Ra}$ (1.19) for oxidizing analyte.

$S = \dfrac{Ra}{Rg}$ (1.20) for reducing analyte.

2. Selectivity: Sensor selectivity refers to a gas-sensor device's capacity to perceive a combination of gases. The gas sensors' selectivity is a serious issue that needs to be fixed. The sensor's selectivity is too broad and it reacts to all reducing test gases that mix with oxygen on the sensor surface, which is inappropriate. Here, catalytic dopants can increase the sensor's sensitivity, and the right catalytic dopant can alter how the sensor material reacts to the desired test gas. Changes in a number of factors, such as catalysts, dopants, grain size, etc., are compatible with discrimination. Under similar operating conditions, the majority of metal

oxide sensors often display a relatively high value of sensitivity for various gases. As a result, this parameter of a sensor towards an analysing gas is assessed by contrasting the response magnitude of many gases examined at the same concentration in a similar environment.

3. Operating temperature: Any semiconductor metal oxide-based sensor's response is probably temperature-dependent. For various gas sensors and various test gases, the operating temperature varies. Resistance and conductance take comparatively more time to reach the steady state when there are fewer sensors, typically at lower temperatures. From this point forward, the measurement must be finished once a sufficient amount of time has passed at a particular temperature for the resistance to achieve the stable value. Although these are operated at normal temperature, semiconductor metal oxide-based gas sensors operate at a higher temperature.

In order to characterize a sensor and determine the ideal operating temperature at which sensitivity is greatest, it is common practice to use the fluctuation of sensitivity with different temperature. Any semiconductor metal oxide-based sensor's response is probably temperature-dependent. For various gas sensors and various test gases, the operating temperature varies. Resistance and conductance take comparatively more time to reach the steady state when there are fewer sensors, typically at lower temperatures. From this point forward, the measurement must be finished once a sufficient amount of time has passed at a particular temperature for the resistance to achieve the stable value. Although these are operated at normal temperature, semiconductor metal oxide-based gas sensors operate at a higher temperature. It is common practise to characterize a sensor by looking at how its sensitivity changes with operation temperature in order to determine the ideal temperature at which sensitivity is greatest.

4. Stability: The primary need for the gas sensors is stability. The gas sensors must therefore frequently operate in challenging settings. Another crucial metric for assessing the efficiency of gas sensors is stable performance without displaying a drift.

5. Response and Recovery times: When exposed to the test gas, the sensor's response time is the is the time taken by sensor to change its resistance value. Similarly, recovery time is the amount of time needed to lower the resistance by 9 to 10% of the permeation value after the gas sensor has been exposed to a dry air environment. The characteristics of a good sensor are indicated by smaller values for recovery and reaction time.

6. Repeatability and Reproducibility: The two components of precision are reproducibility and repeatability. Repeatability, which identifies differences that happen when conditions are

constant and the same operator uses the same instrument within a short period of time, describes the least variability of precision. Reproducibility, on the other hand, refers to the maximum range of accuracy variation when variations take place across extended time periods with various instruments and operators.

7. Limit of detection: The minimum gas concentration at which the signal from noise might be separated is known as the limit of detection.

These variables are all used to describe the device's characteristics [106-107]. High sensitivity, selectivity, and stability, minimum response time and a long-life cycle are all aspects of the perfect chemical sensor. Most of the time, investigators focus on only a few of these desirable qualities while ignoring the others. One reason for this is because it is exceedingly difficult, if not impossible, to develop the perfect sensor for specific gases. However, real-world applications typically do not need sensors with all best feature properties at once. The detection limit requirements can be substantially greater in environmental monitoring applications because the quantities of contaminants often move slowly, although a reaction time of a few minutes can still be acceptable.

1.12 Techniques to improve sensitivity and selectivity

There are five ways to increase the semiconductor gas sensor's sensitivity and selectivity which are discussed as below:

1.12.1 Usage of promoters and catalysts

Another effective method to raise the selectivity of the gas sensor element is the insertion of a catalyst. The primary job of a catalyst is to speed up chemical reactions while avoiding self-precipitation. In gas sensor elements, catalysts such as Pd and Pt are frequently utilized. Low catalyst atom concentrations minimize the impact of the catalysts on the conductance of the sensor element. The activation energy of chemical reactions is decreased by the catalyst atoms. On the basis of fermi level control, the impact of the catalyst on the semiconductor sensor element's response characteristics may also be explained. A higher potential barrier results from a lower fermi level and vice versa. The height of the potential barrier and the volume conductivity of the ceramic grains both affect the sensor resistance.

In general, the catalyst always lowers the temperature at which the sensor element is most sensitive. The nature of the gas to be detected has a significant impact on how sensitive the sensor elements are to them. In addition to catalytic promoters, a sensor element's selectivity

toward various types of gases can be further improved. A promoter favours the promotion of the active phase and raises the electron exchange rate while stabilizing a balancing state [108-109].

1.12.2 Granular surface with an affixing additive

These additives are added to the original mixture that is being prepared to make ceramics. These are distinct metal oxides from the type of grains found in ceramics. Their behaviour is influenced by where they are on the grain surface. The influence of different metals and their oxides on a gas sensor's sensitivity depends on the grain size of those materials [110-112].

1.12.3 Utilization of Filters

Another strategy that holds promise for improving the selectivity of the sensor elements towards a certain gas is the use of filters. If filters are utilized, just one gas can pass through to the sensor element while the rest are adsorbed. For instance, silica can be utilized to improve hydrogen sensitivity when there are hydrocarbons present. this is due to the fact that hydrogen molecules may more easily pass through the surface layer of silica than hydrocarbon molecules. Consequently, silica serves as a filter for molecules of hydrocarbons.

1.12.4 Sensor element's thermal cycling

To provide some selectivity to the gas sensor element, thermal cycling can also be used. The joules law of heating serves as the foundation for the thermal cycling of sensor elements. This law states that heat is produced whenever current passes through the sensor element. The heater voltage wave is generated by a unique function generator. In cyclic variations, the heater voltage wave alternates between three randomly selected heater voltage levels. Measurement of both the current flowing across the sensor element and the dc voltage drop at the same time yields the sensor resistance. The dependency of sensor resistance on time is established after the heater voltage wave has been delivered.

By doing this, we are able to produce a voltage wave curve with two distinct peaks. One peak is associated with heating, whereas another peak is associated with cooling. At the temperature where the sensor element is most sensitive to a particular gas, the heating peak is present. At the same temperature as the heating peak, the cooling peak also appears, but its magnitude is smaller. The peak caused by cooling is not present in the limiting case, where the conductance and heater voltage peaks overlap. The maximal sensitivity to a certain gas is now visible. It has

also been found that if the voltage wave period is larger than roughly a half minute, the sensor element's sensitivity to a particular gas drop.

1.12.5 Regulating the sensor element's operating temperature

The rate of a chemical reaction on grains and gas molecule diffusion to that surface determines how the sensor element reacts to a gas. and gas molecule diffusion to that surface. Chemical reaction limits sensor element response at low temperature. As a result, the sensor element's response to gases at high temperatures was minimal. The responses from the two processes were practically identical at any intermediate temperature (this particular operating temperature has the greatest sensor response for a specific gas). Therefore, there is a specific temperature at which the sensitivity of the sensor element is at its peak for each gas.

The temperature of greatest sensitivity for reducing gases depends on the temperature at which they ignite. For instance, due to its high burning temperature, methane exhibits maximum sensitivity at higher temperatures as compared to hydrogen and carbon monoxide. By choosing the operating temperature of the sensor, the selectivity to a specific gas is achieved in this manner. Therefore, by varying the working temperature, the same sensor element may be used to detect different gases [113-114].

1.13 Model for describing the metal oxide surfaces

Space charge layers, the impact of oxygen molecule adsorption, and the impact of various gases on various types of sensor components are models that are widely used to characterize metal oxide surfaces. Below, these models are thoroughly explained.

1.13.1 Layers of Space Charges

When electrons are taken out or injected by a surface donor or acceptor, the space charge layer is produced. The density and the amount of surface donor or acceptor occupancy affect the electron concentration close to the semiconductor surface. Surface reactivity with gases affects the density of surface states in the context of a gas sensor element. The bulk is considered to contain a homogeneous donor concentration. Surface donors or acceptor are produced by hydrogen and oxygen gases, respectively.

The charge that is positive of a double layer would be present in the ionized bulk donor if oxygen were to chemisorb to the surface. A band banding of around 1 electron volt results from this. When oxygen or hydrogen vacancies are adsorbed, electrons are injected to create a

negative space charge. This causes banding in the opposite direction up to a depth of approximately 10^{-6} cm. The oxygen to tin ratio is decreased when ion bombarded SnO_2 is heated in vacuum at 600 kelvins. An accumulation layer's band banding, which was concurrently seen by ultraviolet photoemission spectroscopy (UPS), was accompanied by an increase in surface conductivity. The surface density of ionosorbed oxygen rises along with the banding of the depletion layer. The number of surface acceptors thus rises over the fermi level [115].

1.13.2 Oxygen Adsorption

While the absorbed oxygen ions serve as the surface acceptor on an oxide surface, the oxygen vacancies function as donors to increase surface conductivity. The deposited oxygen ion joined the electron and decreased the surface conductivity as a result. The following reactions occur on the SnO_2 surface when the temperature rises.

$$O_{2adb}^- \ + \ e^- \ \longleftrightarrow \ 2O_{adb}^- \quad (1.21)$$

This transition causes an increase in surface charge density with constant oxygen coverage, along with a corresponding change in band banding and surface conductivity. This changeover proceeds gradually. The species that are adsorbed assault the carbon bond and release electrons. On the other hand, activated hydrogen or hydrocarbon molecules are the targets of the nucleophilic O_2^- ions reaction. The adsorbed oxygen species emerge from the lattice site as well as the gas phase.

It is possible to think of this procedure as a preliminary stage in the thermal breakdown of the oxide. On the surface, it is believed that there coexists a certain amount of adsorbed species and vacancies. As a result, surface donors and acceptors receive some compensation. Oxidation of reducing gases can also cause oxygen vacancies in the oxide layer of gas sensors. Chemisorption occurs at the working temperature due to a larger charge density. Ionosorbed oxygen alters the oxide's surface in this way [116].

1.13.3 Impact of Different Gases on the Conductivity of the Sensor Element

The reciprocal of resistance, which is determined by the equation below, is the conductance of samples.

$$G = \frac{I}{V} \quad (1.22)$$

Where G is conductance, I is current and V is voltage.

Changes in the concentration of electrons close to the oxide surfaces as a result of reactions with gases produce the signal for metal oxide sensor. The many oxide-related processes are detailed here.

In step one, a surface donor either a reducing molecule or an atom is adsorbed onto the surface. It injects electrons into the semiconductor as a surface donor. This adsorption is followed by breakdown or dissociation.

In step two's nitrogen oxide scenario, the adsorbed acceptor binds electrons, resulting in a decrement in film conductance. Since their levels are deeper due to the additional acceptors originating from more electronegative molecules.

Step three allows for the possibility of changing the surface's stoichiometry through oxidation/reduction reactions with gases. The most straightforward illustration is provided by donors that produce hydrogen by removing oxygen from the lattice. In contrast, vacancies can also be filled with oxygen from the target gas as well as oxygen from the ambient air through ionosorbed oxygen species.

In step four, if the temperature is high enough, donors diffuse initially perpendicular to the surface; later, the concentration of donors near the surface changes. A state of equilibrium can then be attained, where the oxygen partial pressure at the surface controls the donor concentration throughout the bulk. The diffusion of donors from the surface of the zinc oxide crystal into the bulk is brought about by the heating of hydrogen in the environment. The initial conductivity returns to its original value when the earlier mentioned sample is heated without the presence of hydrogen.

In step five, oxygen ionosorbate and reducing gases may react, transferring electrons into the oxide and increasing conductivity [117-119].

1.14 Hydrogen sulphide gas occurrence

Natural gas, anaerobic bacteria, rotting vegetation, volcanoes, waste water of industrial area, flooded ground, salt mines contains hydrogen sulphide. Bacterial sulphide reduction creates H_2S in soil. H_2S emissions commonly include additional hazardous chemicals as So_2, No_2, and others. In many different production processes, such as sulphur-oil exploration, drainage systems, cleaning of marshes, production of sugar and rubber and tunnels, hydrogen sulphide

is produced naturally as a by-product of specific chemical reactions, protein, and impurities [120-121].

In laboratories, dilute acid reacts with metal sulphides to produce hydrogen sulphide. H_2S gas is produced when dilute HCl combines with ferrous (II) sulphide which is given by below reaction

$$FeS\ (s) + 2HCl\ (aq) \longrightarrow FeCl_2\ (aq) + H_2S\ (g) \quad (1.23)$$

In keeps generator, this process occurs. In steel tanks or bottles, this gas may be commercially generated under pressure. The primary impurity in the previously mentioned reaction is hydrogen produced by the acid's interaction with the uncombines iron in a ferrous sulphide sticks. When concentrated HCl combined with antimony sulphide then pure hydrogen sulphide gas obtained which is shown by below reaction

$$6HCl + Sb_2S_3 \longrightarrow 2SbCl_3 + 3H_2S \quad (1.24)$$

1.15 Toxic Effects of Hydrogen Sulphide Gas

When H_2S gas level is 4-50% volume, it instantly ignites at 260 degrees Celsius and mixes with air to generate an explosive combination. It accumulates in low-lying sections of installations because it is heavier than air. Steel can be embrittled by it. Before the harmful threshold concentration of 50-100 ppm is achieved, a person intoxicated with H_2S no longer recognizes its distinctive smell of rotten egg [122-124].

One of the main issues with sewage networks is hydrogen sulphide (H_2S) emissions. This gas, which has a distinct stench of rotten eggs, is extremely hazardous and causes sewer infrastructure to corrode. Sewers are often observed using H_2S gas sensors to safeguard cities and sewer personnel. The health of humans is negatively impacted by hydrogen sulphide. Humans' sense of smell can be harmed by hydrogen sulphide in even small quantities. Olfactory nerves can become paralyzed by hydrogen sulphide in high quantities [125-126].

1.16 Physical Properties of H_2S gas

Table 1.6 The physical properties of hydrogen sulphide gas.

Name	Hydrogen sulphide
Chemical Formula	H-S-H (H_2S)
Solubility	0.4% in cold water, hydrocarbon
Molecular Mass	34.08 g/mol
Odour	Rotten egg like
Appearance	Colorless Gas
Reactivity	High
Dielectric Constant (at -60°C)	10.02
Boling point	212.9 K
Melting point	190.9 K
Nature	Highly Flammable, toxic
Vapor pressure	394.59
Dipole moment	0.97D
Specific gravity	1.2

1.17 Chemical Properties of H_2S gas

H_2S is a reactive substance in chemical terms.

1. Combustion: It burns with a light blue flame and is a flammable gas. It does not advocate for combustion. It burns to produce sulphur and water when there is a shortage of oxygen or air.

$$2H_2S + O_2 \longrightarrow 2H_2O + 2S \quad (1.25)$$

It burns when there is too much oxygen or air, producing sulphur dioxide and water.

$$2H_2S + 3O_2 \longrightarrow 2H_2O + 2SO_2 \ (1.26)$$

2. <u>Reducing properties</u>: Due to how quickly it breaks down into hydrogen and sulphur, hydrogen sulphide is a powerful reducing agent. The following are some significant hydrogen sulphide reduction reactions:

- The impact of halogens: - Halogens lose their colour when H_2S is combined with them, and sulphur is subsequently deposited.

$$H_2S + Cl_2 \longrightarrow 2HCl + S \ (1.27)$$

$$H_2S + Br_2 \longrightarrow 2HBr + S \ (1.28)$$

- The impact of sulphur dioxide: - On combining the hydrogen sulphide with SO_2 it reduces sulphur dioxide to sulphur.

$$2H_2S + SO_2 \longrightarrow 2H_2O + 3S \ (1.29)$$

- The impact of sulphuric acid: - when H_2S react with H_2SO_4 it reduces sulphuric acid to sulphur dioxide.

$$H_2S + H_2SO_4 \longrightarrow 2H_2O + S + SO_2 \ (1.30)$$

- The impact of HNO_3: - in this case nitrogen dioxide is formed.

$$H_2S + 2HNO_3 \longrightarrow 2H_2O + S + 2NO_2 \ (1.31)$$
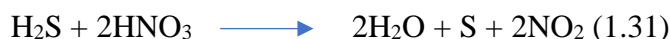
3. <u>Decomposition</u>: When heated, it breaks down into its component parts, which are hydrogen and sulphur. At 310 degrees Celsius, the first stage of decomposition begins, and it lasts until 1700 degrees Celsius.

$$H_2S \longrightarrow H_2 + S \ (1.32)$$

4. <u>Acidic properties</u>: The naturally acidic gas causes the blue litmus paper to become red when it is exposed to moisture. Because of the presence of H_3O^+ ions, the aqueous solution of H_2S has an acidic nature.

$$H_2S + H_2O \longrightarrow H_3O^+ + HS^- \ (1.33)$$

$$HS^- + H_2O \longrightarrow H_3O^+ + S^- \ (1.34)$$

The subsequent reactions provide credence to the gas's acidic character.

- Action of ammonia: - when hydrogen sulphide gas combines with ammonia, ammonium sulphide is formed.

$$2NH_3 + H_2S \longrightarrow (NH_4)_2S \quad (1.35)$$

- Action of metals: - when H_2S react with metal, metal sulphide formed and hydrogen gas release.

$$2Ag + H_2S \longrightarrow Ag_2S + H_2\uparrow \quad (1.36)$$

1.18 Necessity of Hydrogen sulphide gas sensor

Sensors for toxic and hazardous gases play an essential part in the research that is conducted in fields such as human health, ecological preservation, and emissions control. The most significant of these factors is air pollution, which is linked to a variety of diseases and adversely affects human health. The primary pollutants in the air are carbon dioxide (CO_2), nitrogen oxides (NO_2), H_2S and volatile organic compounds (VOCs). Permissible Exposure Limits (PELs) to H_2S gas are defined as 50 parts per million for a period of ten minutes by the Occupational Safety and Health Administration (OSHA). As a result, there is an increasing need for active H_2S gas sensors to monitor and control the emissions of hydrogen sulphide gas into the atmosphere. As a result, the researchers are attempting to build sensors for the detection of H_2S at temperatures and concentrations below the threshold of detection.

Because of high humidity and toxicity of hydrogen sulphide, sewer atmosphere monitoring is difficult. H_2S gas sensors must be durable and satisfy the following requirements: Low monitoring limits, rapid testing, fast setup, simple operation, and low power consumption.

1.19 Challenges for gas sensors based on Nano-thin films

For a safe existence, the need for trustworthy sensors for hazardous gases and VOCs is rising quickly. In order to efficiently use sensing qualities, a lot of development has been achieved in the production of sensors, particularly in the form of thin films. The manufacturing of homogenous nanostructures with respect to thickness, shape, and morphology is difficult for these devices. Additionally, the process is rather pricey. All of these sensors for gas detection have concerns regarding their sensitivity. The reliability of being noticed, specificity, response and recovery times, repeatability, and robustness are all factors that are affected by temperature. Sensors have numerous constraints that must be carefully addressed throughout optimization processes. The ability to obtain all these features of sensor materials evenly will determine how these nanostructure sensors are produced commercially on a big scale. On one

positive note, high-quality and reasonably priced sensor devices will soon be accessible on the market, thanks to the level of complexity in technologies and materials engineering.

The aim of the present thesis is the investigation of pure and doped CuO thin films prepared by sol-gel spin coating technique for hydrogen sulphide gas sensing. Investigations shows that homogeneous grains were formed in CuO films, and all synthesized samples are discovered to be relatively oxygen-enriched. At 400ºC of calcination temperature, obtained films are more crystallize and shows high sensitivity for H_2S gas. To optimize the best sensing response of the prepared samples, various concentration of H_2S gas at different operating temperature was used. To determine the reproducibility, prepared thin films were tested of H_2S gas over a period of 1-3 years and found it stable. Hence, the present work is suitable for hydrogen sulphide gas sensing applications. A systematic study of the influence of various spinning speed related to sol-gel spin coating technique on film properties for gas sensing will be carried in the present.

1.20 Framework of the thesis

The thesis is organized into five chapters, each of which contains the following specifics:

Chapter-1 Introduction

The first chapter provides a general introduction thin films, experimental information on film deposition and their characterization procedures, as well as an understanding of their numerous properties and applications. This chapter also provide a broad overview of sensors along with their classifications, characteristics and promoters to improve those characteristics, mechanism for reducing gases, hydrogen sulphide gas and sensor to monitor this gas.

Chapter-2 Literature survey

A overview of the various deposition methods for nanostructured thin films will be given, with special emphasis on the methods employed in this chapter for the applications of solar cells and gas sensors. At the conclusion of the chapter, the primary objective and structure of the thesis have been provided.

Chapter-3 Result and Discussion of un-doped CuO thin films

The focus of this chapter is the deposition and characterization of CuO thin films to explore the possibility of the CuO thin films for solar cell applications by recording their UV-VIS spectrographs. solar cell applications. This chapter provides a description of the H_2S gas detecting setup along with mechanisms.

Chapter-4 Result and Discussion of doped CuO thin films

The fourth one describes the Sn doping on CuO thin films.

Chapter-5 Summary

This chapter summarizes the results obtained on nanostructured doped and un-doped CuO thin films prepared by sol-gel spin coating technique.

1.21 References

[1] E.H. Nicollian & J.R Brews. (1982). MOS Physics and Technology. Wiley, New York.

[2] A. Goswami. (2003). Thin Film Fundamentals. New Age International (P) Ltd.

[3] F.J. Arregui. (2008). Sensors Based on Nanostructured Materials. Berlin Springer.

[4] R. Padyath, J. Seth & S.V. Babu. (1994). Thin solid Films. 239, 8-15.

[5] T.J. Richardson, J.L. Slack & M.D. Rubin. (2000). Proceedings of the 4th International meeting on Electro-chromism, Uppsala.

[6] R. Chandra, P. Taneja & P. Ayuu. (1999). Nanostructured Materials. 11(4), 505-512.

[7] T.J. Richardson. (2003). Solid State Ionics. 165, 305-308.

[8] V.F. Drobny & D.L. Pulfrey. (1979). Thin Solid Films. 61, 89-98.

[9] R. Kita, T. Hase, R.Itti, M.Sasaki, T. Morishita & S.Tanaka. (1992). Applied Physics Letters. 60, 2624-2630.

[10] K. Kawaguchi, R. Kita, M. Nishiyama & T. Morishita. (1994). Journal of Crystal Growth. 143, 221-226.

[11] K.P. Muthe, J.C. Vyas, S.N. Narang, D.K. Aswal, S.K. Gupta, D.Bhattacharya, R. Pinto, G.P. Kothiyal & S.C. Sabharwal. (1998). Thin solid films 324, 37-43.

[12] K.S. Wanjala, E. Makori & J.M. Ngaruiya. (2016). J. Condens. Matter Phys. 6(1), 1.

[13] T. Dimopoulos, A. Pei, S. Abermann, M. Postl, E.J.W. List-Kratochvil & R. Resel. (2014). EPJ Photovolt. 5, 50301.

[14] A. Bhaumik, A. Haque, P. Karnati, M.F. Taufique, R. Patel & K. Ghosh. (2014). Thin Solid Films. 572, 126.

[15] Y. Aoun, M. Marrakchi, S. Benramache, B. Benhaoua, S. Lakel & A. Cheraf. (2018). J Chem Mater Res 5(6), 119–122.

[16] M.H. Mamat, N.N. Hafizah & M. Rusop. (2013). Mater. Lett. 93, 215–218.

[17] J. Dong, Y. Ozaki & K. Nakashima. (1997). Macromolecules. 30,1111.

[18] T. Tomida, K. Hamaguchi, S. Tunashima, M. Katoh & S. Masuda. (2001). Ind. Eng. Chem. Res. 40, 3557.

[19] H. Absike, H. Labrim, B. Hartiti, M. Tahri & H. Ez-Zahraouy. (2020). Mol. Cryst. Liq. Cryst. 711(1), 18–31.

[20] C. Luyo, I. Fabregas, L. Reyes, J.L. Solis, J. Rodriguez, W. Estrada & R.J.Candal. (2007). Thin Solid Films. 516, 25.

[21] I. Singha & R.K. Bedi. (2011). Applied Surface Science. 257, 7592.

[22] W. Shockley & H. J. Queisser. (1961). J. Appl. Phys. 32, 510.

[23] L.S. Huang, S.G. Yang, T. Li, B.X. Gu, Y.W. Du, Y.N. Lu & S.Z. Shi. (2004). J. Cryst. Growth. 260, 130.

[24] K. L. Chopra & I. J. Kaur. (1983). Thin Film Device Applications. Plenum Press, New York.

[25] D. M. Mattox. (1994).Vacuum Deposition, Reactive Evaporation and Gas Evaporation. ASM Handbook. Surface Engineering (ASM International). (5) 556.

[26] T. Guo, P.Nikolaev, D. Rinzler, D. T. Tomanek, D. T. Colbert & R. E. Smalley. (1995). Journal of Physical Chemistry. 99, 10694.

[27] Y. Cho & J. R. Arthur. (1975). Molecular beam epitaxy. Progress in Solid State Chemistry. 10, 157.

[28] W. A . Bryant. (1977). Journal of Material Science.12, 1285.

[29] R. N. Ghoshtagore. (1978). Journal of the Electrochemical Society. 125,110.

[30] C. J. Brinker, A. J. Hurd, G. C. Frye, K. J. Ward & C. S. Ashley. (1990). Journal of Non-Crystalline Solids. 121, 294.

[31] C. C. Chen, M. M. Nasrallah & H. U. Anderson. (1993). Journal of Electro chemical Society. 140, 3555.

[32] C. J. Brinker, G. C. Frye, A. J. Hurd & C. S. Ashley. (1991). Thin Solid Films, 201(1), 97.

[33] G. Carcano, M. Ceriani & F. Soglio. (1993). Hybrid Circuits. 32, 12.

[34] A. Emslie, F. Bonner & L. Peck. (1958). J. App. Phys. 29, 858.

[35] M. J. Buerger. (1942). X-ray Crystallography. Wiley, New York.

[36] A. Taylor. (1942). X-ray Metallography. Wiley, New York.

[37] Y. Vijayakumar, P. Nagaraju, V. Yaragani, S. R. Parne, N. S.Awwad & M.V. Ramana Reddy. (2020). Physica B: Physics of Condensed Matter. 411976.

[38] P. Bhat, N. Kumar, S. K, P. Nagaraju. (2019). Physica B: Condensed Matter. 570, 139–147.

[39] D. Oatley, M. Mullan & K. C. A. Smith. (1985). Advances in Electronics and Electron Physics Suppl. 16 (London: Academic Press). 443- 482.

[40] P. E .J. Flewit & R. K. Wild. (2003). Physical methods for material characterization, second edition, IOP publishing, London.

[41] G.R. Chatwal & S.K. Anand. (2002). Instrumental methods of chemical analysis, Fifth Edition, Hymalay Publishing group.

[42] M. Pinczlits, G. Spingholz & G. Bauer. (1998). Appl. Phys. Lett. 73, 250.

[43] F.Urbach. (1953). Phys. 92, 1324.

[44] G. A. Khan & C.A. Hogarth. (1991). J Mater Sci. 26, 412.

[45] Y.Singh. (2013). International Journal of Modern Physics: Conference Series. 22, 745-756.

[46] A. Mittiga, E. Salza, F. Sarto, M. Tucci & R. Vasanthi. (2006). Appl. Phys. Lett. 88, 163.

[47] S. Asbrink & L. J. Norrby. (1970). Acta Crystall. B. 26, 8.

[48] B. Balamurugan & B.R. Mehta. (2001). Thin solid films. 396, 90.

[49] Y.S. Gong, C. Lee & C.K. Yang. (1995). J. Appl. Phys. 77, 5422.

[50] J. Wu. (2010). Engineering and Applied Science. 154, 233.

[51] K. El-Khamisy, H. Abdelhamid, S. Elagooz & E.S. El-Rabaie. (2021). Journal of Computational Electronics, 20(5), 1807-1814.

[52] T. Iqbal, M. Ijaz, M. Javaid, M. Rafique, K. N. Riaz, M.B. Tahir, G. Nabi, M. Abrar & S. Afsheen. (2019). Plasmonics. 14,147-154.

[53] Tabrizi, A. Asgariyan & A. Pahlavan. (2020). Optics communications. 454, 124437.

[54] B. Yousif, M.E.A. Abo-Elsoud & H. Marouf. (2020). Plasmonics. 15(5), 1377–1387.

[55] A. Pahuja, M.S. Parihar & D. Kumar. (2019). IEEE Transactions on Nanotechnology. 18, 626-634.

[56] K. Ishaque & Z. Salam. (2011). Solar energy, 85(9), 2217-2227.

[57] RASHEED, Mohammed, O. Alabdali, S. Shihab & Taha Rashid. (22021). Journal of Al-Qadisiyah for Computer Science and Mathematics. 13 (1), 34.

[58] Abdelhamid, Hamdy, A. El-Deib, K. El-Khamisy, K. El-Shekh & Z. Memon. Optical and Quantum Electronics. 54 (7), 424.

[59] A, Kowsar, S.F.U. Farhad, M. Rahaman, M.S Islam, A.Y. Imam, S.C. Debnath, M. Sultana, M.A. Hoque, A. Sharmin & Z.H. Mahmood, Z.H. (2019). International Journal of Renewable Energy Research (IJRER). 9(2), 579-597.

[60] B. Yousif, MEA. Abo-Elsoud & H. Marouf. (2019). Optical and Quantum Electronics. 51(8), 276.

[61] R. Bučík, G.M. Mason, R. Gomez-Herrero, D. Lario, L. Balmaceda, N.V. Nitta, V. Krupař, N. Dresing, G.C. Ho, R.C. Allen & F. Carcaboso. (2021). Astronomy & Astrophysics, 656, 11.

[62] A. Luque, A. Martí & C. Stanley. (2012). Nature Photonics, 6(3), 146-152.

[63] M. Zhu, X. Liu, S. Liu, C. Chen, J. He, W. Liu & J. Zhang. (2019). ACS applied materials & interfaces. 12(2), 2566-2571.

[64] M.H/ Muhammad, M. F. O. Hameed & S. S. Obayya. (2017). IEEE Photonics Journal, 9(3), 1-14.

[65] H.C. Lee, W. Lee, J. H. Moon & D. Kim., D. (2019). Multiscale Science and Engineering, 1, 161-166.

[66] R. P. Wejisundera. (2010). Ceramics Silikáty. 54,19.

[67] B. J. Stanbery. (2002). Crit. Rev.Solid Stat. 27,73.

[68] T. Ishihara, K. Kometani, Y. Nishi & Y. Takita. (1995). Sens. Actuators B. 28,49.

[69] Y. Zeng, T. Zhang, H. Yang, L. Qiao, Q. Qi, F. Cao, Y. Zhang & R. Wang. (2009). Appl. Surf. Sci. 255, 4045.

[70] S. Aygun & D. Cann. (2005). J. Phys. Chem. B. 109, 7878.

[71] L. Presmanes, A. Chapelle, F. Oudrhiri-Hassani, A. Barnabé & P. Tailhades. (2011). Applied Surface Science. 4715, 256.

[72] D. H. Trinh, T. Kubart, T. Nyberg, M. Ottosson, L. Hultman & H. Högberg. (2008). Thin Solid Films. 23, 8352.

[73] V. Saravanakannan & T. Radhakrishnan. (2014). Mater. Res. Bull. 6, 306.

[74] T. Seiyama, A. Kato, K. Fujiishi & M. Nagatani. (1962). Anal. Chem. 34, 1502.

[75] A. Hulnnicki, S. Clab & F. Ingman. (1991). Pure & Appl. Chem. 63, 1247.

[76] T. Hübert, L. Boon-Brett, G. Black & U. Banach. (2011). Sensors and Actuators B: Chemical. 157 (2), 329–352.

[77] S. Okazaki, H. Nakagawa, S. Asakura, Y. Tomiuchi, N. Tsuji, H. Murayama & M. Washiya. (2003). Sensors and Actuators B: Chemical. 93 (1-3), 14-147.

[78] N. Kasai, C. Tsuchiya, T. Fukuda, K. Sekine, T. Sano & T. Takehana. (2011). NDT & E International. 44 (1), 57-60.

[79] H. Okajima, S. Kakuma, K. Uchida, Y. Wakimoto & K. Noda. (2006). In Proceedings of the International Joint Conference SICE-ICASE, Busan, 1656–1659.

[80] C. Lim, W. Wang, S. Yang, and K. Lee & K. Lee. (2011). Sensors and Actuators B: Chemical. 154 (1), 9–16.

[81] W. H King. (1964). Analytical Chemistry. 36, 1735–1739.

[82]. T. Hübert, L. Boon-Brett, G. Black & U. Banach. (2011). Sensors and Actuators B: Chemical. 157 (2), 329–352.

[83] X. Lu, S. Wu, L. Wang, & Z. Su. (2005). Sensors and Actuators B: Chemical. 107 (2), 812–817.

[84] A. Dutta, H. Nishiguchi, Y. Takita & T. Ishihara. (2005). Sensors and Actuators B: Chemical. 108 (1-2), 368–373.

[85] C. Lee, S. A. Akbar & C. O. Park. (2001). Sensors and Actuators B: Chemical. 80 (3), 234–242.

[86] R. Radhakrishnan, A. V. Virkar, S. C. Singhal, G. C. Dunham & O. A. Marina. (2005). Sensors and Actuators B: Chemical. 105 (2), 312–321.

[87] C. G. B. Garrett & W. H. Brattain. (1955). Phys. Rev. 99, 376.

[88] W. H. Brattain & C. G. B. Garrett. (1954). Physica. 20, 885.

[89] W. H. Brattain & J. Bardeen. (1953). Bell Labs Tech. J. 32, 1.

[90] A. M. Azad, S. A. Akbar, S. G. Mhaisalkar, L. D. Birkefeld & K. S. Goto. (1992). Journal of the Electrochemical Society.139, 3690-3704.

[91] G. Korotcenkov. (2007). Mater. Sci. Eng.B. 139,1-23.

[92] T. Seiyama, A. Kato, K. Fujiishi & M. Nagatani. (1962). Anal. Chem. 34,1502.

[93] T. Seiyama & S. Kagawa. (1966). Anal. Chem. 38, 1069.

[94] N. Taguchi. (1972). US Patent 3, 695, 848.

[95] J. A. Rodriguez, T. Jirsak, S. Chaturvedi, M. Kuhn & A. Rodriguez. (1999). Surf. Sci. 442, 400.

[96] O. Wurzinger & G. Reinhardt. (2004). Sens. Actuat. B.103, 104.

[97] G. Jiménez-Cadena, J. Riu, F. X. Rius & G. Jime. (2007). Analyst.132, 1083.

[98] M. J. S. S. Spencer. (2012). Prog. Mater Sci. 57, 437.

[99] N. D. Hoa, S. Y. An, N. Q. Dung, N. Van Quy, D. Kim & N. V. Quy. (2010). Sens. Actuat. B.146, 239.

[100] M. Hübner, C. E. E. Simion, S. Pokhrel, N. Bârsan, U. Weimar & A. Tomescu-Stănoiu. (2011). Sens. Actuat. B. 153, 347.

[101] B. M. Matin, Y. Mortazavi, A. A. Khodadadi, A. Abbasi, A. A. Firooz, B. Mehrabi Matin & A. Anaraki Firooz. (2010). Sens. Actuat. B. 151, 140.

[102] A. Fort, M. Mugnaini, S. Rocchi, V. Vignoli, E. Comini, G. Faglia & A. Ponzoni. (2010). Sens. Actuat. B. 148, 283.

[103] Z. Bai, C. Xie, M. Hu, S. Zhang & D. Zeng. (2008). Mater. Sci. Eng. B.149,12.

[104] R. Kumar, A. Khanna & V. S. Sastry. (2012). Vacuum. 86, (2012) 1380.

[105] T. W. Capehart & S. C. Chang. (1981). J. Vac. Sci. Technol. 18, 393.

[106] Criindler. (2007). Chemical Sensors: An Introduction for Scientists and Kngineers. Springer, Berlin.

[107] C. Cantalini, M. Post, D. Buso, M. Guglielmi & A. Martucci. (2005). Sens. Actuat B.108,184.

[108] S. Kannan, L. Rieth & F. Solzbacher. (2010). Sens. Actuat. B. 149,8.

[109] G. Korotcenkov. (2005). Sens. Actuat. B. 107, 209.

[110] N. Yamazoe, Y. Kurokawa & T. Seiyama. (1983). Sensors Actuators. 4, 283.

[111] N. Yamazoe. (1991). Sensors Actuators B. 5,7.

[112] C.Xu, J. Tamaki, N. Miura & N. Yamazoe. (1991). Sensors Actuators B. 3,147.

[113] S.R. Morrison. (1987). Sensors Actuators. 12, 425.

[114] J. R. Huang, C. P. Gu, K I,. Meng, M. Q. Li & J. H. Liu. (2007). Smart Mater. Struct. 16, 701.

[115] P.B. Weisz. (1953). J. Chem. Phys. 21, 1531.

[116] A. Bielanski & J. Haber. (1979). Catal. Dev. Sci. Eng. 19 (1), 1.

[117] S.C. Chang. (1979). IEEE Transactions on Electron Devices. 26, 1875.

[118] G. Heiland. (1982). Sensors Actuators. 2,343.

[119] A.D. Brailsford & E.M. Logothetis. (1985). Sensors Actuators. 7,39.

[120] Y.Y. Wang, G.T. Duan, Y.D. Zhu, H.W. Zhang, Z.K. Xu, Z.F. Dai & W.P. Cai. (2016). Sens. Actuators B. 228, 74-84.

[121] N.M. Vuong, N.D. Chinh, B.T. Huy & Y.I. Lee. (2016). Sci. Rep. 6, 26736.

[122] Oil and Hazardous Materials, Technical assistance data system, (U.S. Environmental protection agency, Oil and Special Materials Control Division, Washington, 1980)

[123] Inflammabillite et Explosivite Des Gaz, Liquides et Solides Usuees. (1971). Institut National de Recherche et de la Securite, Note no. 740-63-71.

[124] B. Elvers, S. Hawkins & G. Schulz, Eds. (1989). Ullmann Encyclopedia of Industrial Chemistry (VCH, Weinheim). A13, 467.

[125] G. Sberveglieri, S. Groppelli, P. Nelli, C. Perego, G. Valdre & A. Camanzi. (1993). Sensors Actuators B. 15-16, 86.

[126] Dangerous Properties of Industrial Materials. (1979). Van Nostrand, New York.

CHAPTER 2

LITERATURE REVIEW

2.1 Literature review

S.Saito et.al., 1985 have studied the gas sensing performance of pure and doped tin oxide ceramic. It was found that both undoped and platinum doped ZnO ceramic shows chemical changes and change in resistivity for reducing gases. It was observed that Pt doped sensor increase the surface of oxidation at 300°C temperature. Dc four probe technique was used to measure electrical resistivity within the range of temperature from 200°C to 400°C. Xrd confirmed the presence of Pt with particle size of 20-30nm. It was noted that highest sensitivity of 18.6 obtained for reducing gases such as CO, CO_2, C_3H_8 and CCl_4 at 4000 ppm concentration [1].

E. Traversa et. al., 1995 investigated the brilliant ceramic material for chemical sensors. He found the electro ceramic materials was most functional ceramic in field of sensor. Material used in chemical sensor field suffer from many of problems such as poor gas selectivity, no gas detection at low concentration and many more. To overcome all of these problems require solution is project materials with significant detection mechanism. In this study various of brilliant ceramic material for humidity and gas sensor were studied. At constant voltage change in current was measured by varying concentration of reducing gases. It was found that selectivity of CO gas sensor was improved by using La_2CuO_4/ZnO and Au/ZnO for Schottky barriers [2].

A. Chaturvedi et, al., 2000 have studied the selectivity and sensitivity of gas sensor based on tin oxide thick films. In this paper various no of gases such as LPG, methane, CCl_4 and many more exposed on sensor and found that sensitivity is high at room temperature. it was observed that features of gas sensor were improved by using plasma treated film. It was noticed that O_2 plasma treated sensor have best sensitivity toward the exposing gases and Ar_2. Plasma treated sensor have highest selectivity. [3].

J. Santos-cruz et. al., 2005 have studied that low properties of CdO films change with annealing temperature. sol gel method was used to deposit thin films of CdO and their various properties were studied at 200 to 450°C range of temperature. it was found from XRD that all prepared films have polycrystalline nature.it was noted that grain size increase from 20 to 27 A^0 as the annealing temperature increases. In this paper films prepared at 350°C temperature

have highest mobility and lowest resistivity. It was noted that as the annealing temperature increases then absorption edge shifts toward higher wavelength [4].

D. jundale et. al., 2011 have studied the CuO thin films for monitoring H_2S gas. In this paper spin coating technique was used to deposited films of CuO on glass substrate. XRD revealed that all of sample were oriented along (111) plane and have monoclinic crystal structure. These prepared films were tested for H_2S gas of concentration 20ppm to 100 ppm. It was found from the obtained results that highest response of 24 % were obtained for low ppm of gas. It was concluded that CuO films have good response toward H_2S gas. [5].

M.F. Nurfazliana et.al., 2014 have studied the CuO thin films synthesized and characterized by chemical bath deposition technique. Two sample of molar concentration 1mM and 5mM prepared by using $(Cu(NO_3)_2)$ and HMT as precursor and stabilizer respectively. To acquire the deposition of CuO films, gold catalyst deposited at 20 mA for half minute on 2 cm $\times$ 2.5 cm glass slide. Aqueous solution was stream into reagent bottle in which glass substrate attach horizontally by using a rubber tape. This bottle was put in annealing furnace at $80^{\circ}C$ for 3hr and then glass substrate taken out. To remove the residual impurities, sample was preheated at $60^{\circ}C$ for 5 min. It was concluded that a plane and dense surface of films produced when precursor concentration increase [6].

S.S. Shariffudin et.al., 2015 have studied the characterization of thin films of CuO synthesized from sol-gel dip coating. No. of samples of 0.25M concentration with variable thickness were prepared by varying the deposition layers. The obtained films were of thickness 87.14 nm - 253.58 nm measured by surface profiler. FESEM revealed the surface morphology and it was noticed that as the thickness of films increases, films became less porous and denser. Energy gap of these films was in range of 1.9eV to 2.35eV measured by UV spectroscopy. Due to increase of thickness, films get improved and as a result band gap decrease. Two probe set-ups measure the electrical resistivity, conductivity and ohmic nature by making gold contact and concluded that thickest films have less resistivity with highest conductivity [7].

H. Hashim et.al., 2016 have studied the characterization of CuO films synthesized with different molar concentration using sol-gel spin coating method. It was examined that as the concentration of precursor increase, current gets increase and band gap gets decrease. The highest and lowest value of conductivity (0.07S/m) and resistivity (12.76Ω/m) was achieved at 0.5 M between 0.3M-0.5M concentration. FESEM shows that films have smoother surface

with uniform grains. It was concluded from this research that molar concentration play a good role for the formation of good thin films [8].

Jing Wu et.al., 2016 have evaluated the effect of doping concentration of Sn (0.5-2%) to optical, structural and electrical properties of CuO thin films synthesized by facial sol-gel technique. It was noticed that as the Sn concentration increase then band gap reduces from 2.0 eV to 1.95 eV. SEM was used to calculate grain size and found that it decreases from 84.1nm to 61.8nm as the concentration of Sn increases which specify that growth of grain was suppressed by Sn doping. To measure the effect of Sn concentration on electrical properties, Hall effect measurements was carried out and noticed that resistivity decrease as Sn content increase. When Sn content increase then 2 more free electrons were release because Sn^{4+} ions occupied the Cu^{2+} ion sites [9].

S. Muthukrishnan et.al., 2017 have synthesized and characterized CuO thin films by spray pyrolysis method at 300°C annealing temperature. XRD technique confirmed that synthesized sample have FCC structure with crystallite of 3.48 nm. SEM analysis examine the morphology of CuO thin films and revealed that particles were formed with different shape and size. UV analysis found the transmission of 70%-90% in range of 800-900 nm wavelength. Optical band gap of this synthesized sample was found to be 2.43 eV from Tauc plot. It was concluded from electrical properties that these films have lower resistivity and higher mobility which makes it suitable for synthesize device [10].

B. Troudi et. al., 2017 have studied the CuO crystals implants in thin films of PVC. In this paper, first CuO particles have been synthesized from hydrothermal method and then thin films sample was deposited on glass substrate by using colloidal solution of PVC and CuO nanoparticles. It was found from XRD that CuO particles have monoclinic phase in amorphous PVC. From the observed peak position and intensity, it was concluded that there was good crystallization of CuO nano particles. FTIR revealed the vibration mode due to formation of Cu-O band at 605 cm^{-1}. PL spectra shows the green and red emission at 500 nm and 605 nm respectively. UV analysis shows higher absorbance in ultraviolet region and band gap of Cuo-PVC was 3.5eV calculated from tauc-plot [11].

D. Nandhini et. al., 2017 have synthesize and characterized CuO nanoparticle doped with nickle using precipitation method. FTIR was used to confirm the formation of single-phase Ni doped CuO nanoparticles. Sphere shape of CuO nanoparticle was found from SEM analysis. It was found from the EDAX spectrum that peak intensity of Cu increase with decrease of dopant

concentration. It was also noted from EDX analysis that no other peaks except Ni, O, Cl and Cu found which confirm the formation of pure nanoparticles of CuO **[12].**

D. R. Bhowmik et.al., 2018 have studied how various features of CuO thin films changed on changing parameters such as spinning speed and solution concentrations. It was observed that energy band gap increases on increasing spinning speed and decrease on increasing concentration. Nano-electrometer was used to measure electrical resistivity and observed that it increases with increasing spinning speed. XRD revealed that synthesized films have single CuO phase and monoclinic structure. With increasing spinning speed and molar concentration, crystallinity of films decreases and increase respectively. It was analyzed from SEM that films prepared with 0.75M concentration at 1200 rpm have good quality and more suitable for solar cell conversion **[13].**

Hu. Xiaobing et.al., 2018 have studied that CuO microspheres modified with $CuFe_2O_4$ nanoparticles synthesized with facile two step method. These modified microspheres were used for gas sensing toward H_2S gas and found 20 times higher response in comparison of initial CuO microspheres at 240^oC. XRD revealed the purity of CuO microspheres by providing no more crystalline phases except monoclinic phase. FESEM showed the particles were spherical, dense and uniform in shape. Electronic state of element of CuO microspheres and their chemical compositions were examined with XPS. From this research a highly sensitive gas sensor was developed for H_2S gas from p-CuO and n-$CuFe_2O_4$ heterostructure **[14].**

M. Dhaouadi et.al., 2018 have studied the physical properties of CuO thin films prepared by varying precursor concentration and annealing temperature. UV analysis showed that as the concentration increases, band gap decreases which makes it suitable for solar cell applications. At 555^oC, higher absorbance and good crystallinity of films were found. Van-der-Pauw method. Measured the electrical resistivity which increases 84 Ω/cm to 124 Ω/cm w.r.t increment in molar concentration. In future, CuO films of lower resistivity prepared by doping of suitable metals **[15].**

A. Rydos et. al., 2018 have discussed use of CuO thin films for gas sensing application from various research, it was investigated that CuO thin films used to detect gases like Co_2, No_2, H_2S, NH_3, and many more organic compounds. Best gas sensor was revealed by parameters such as sensitivity, selectivity and stability. It was analysed that sensitivity of gas sensor improved by using doping. It was noted that sensing mechanism of gas sensors works on change in resistance. The author reviewed that sensors fabricated with CuO thin films have low cost, high repeatability and easily portable **[16].**

J. M. Rzaij et. al., 2018 have studied the CuO films applicable for H_2S gas sensor. In this study spray pyrolysis technique was used to form CuO film doped with samarium oxide. XRD revealed that as the concentration of Sm_2O_3 increase more than 5% then CuO and SmO have mixed phase of monoclinic and cubic symmetry respectively. It was noticed that CuO and SmO have orientation along (11-1) and (111) plane respectively. It was revealed from optical analysis that energy band gap increase with increasing doping concentration and high transparency was noticed in visible region. When H_2S gas exposed on sensor then fast response was achieved for the film with 3% dopant. It was observed from this paper that CuO based gas sensor have less response time of 9 second with 138% high sensitivity at 152^oC operating temperature [17].

R. Singh et. al., 2019 have examined the change of properties of CuO films on changing annealing time from 15 minutes to 1 hr. As the annealing time increase crystallite size increase and grains of nano size uniformly spread. UV-spectroscopy measure the variance of band gap with annealing time and found that n-CuO/p-si thin film annealed at 15 min were suitable for photonic device. It was noticed that annealed films have most of reflectance in visible region [18].

N.Touka et. al., 2019 have studied that various properties of CuO thin films on varying annealing temperature. As the temperature increases from 350^oC to 550^oC, crystallite size increases because of merging process bring out from thermal annealing. It was observed from this paper that films synthesized at 350^oC have best crystallinity. As the annealing temperature increases, optical band gap increases which shows that CuO thin films worthy for solar cell applications [19].

H. Zare Asl et.al., 2019 have studied the effect of cobalt doping (0% to 10%) on different properties of CuO thin films. XRD & FESEM revealed that crystallite size and grain size decrease respectively with increase of doping concentration. It was noticed from this research that conductivity of CuO films changed from p to n by carried out 10% doping. As the doping increase band gap decrease from 1.67 eV to 1.62 eV. It was observed that un-doped CuO thin films show absorption in visible region and doped CuO films have absorption in IR region [20].

S. Horzum et.al., 2019 have examined the impact of precursor concentration on TiO_2 films synthesized by sol gel dip coating. It was analyzed from XRD that extra compound (Cu-TiO_2) form when concentration of added Cu increased. Raman spectra showed that synthesized films have uniform homogeneity up to 12.5% doping. It was noted from optical measurement that band gap decreases on increasing Cu concentration from this research, it was concluded that structural and optical properties of thin films modify by heavily incorporation of Cu [21].

H.Lec et.al., 2019 have investigated that how characteristics of CuO TFTs affected on varying annealing time (30 min and 3 hrs.). Position of Raman peaks of same sample was found to be different for 3 min and 3 hr. It was observed that as annealing carried for longer period then crystallinity of CuO films improve. FWHM decrease on increasing annealing time and reverse effect on peak intensity. Drain current increase on increasing annealing time. It was concluded from this research that good performance sensor can be synthesized with films annealed at 3 hr. **[22].**

L.Benharrat et.al., 2019 have synthesized and characterized $YPO_4:Eu^{3+}$. Prepared films show good emission efficiency, low symmetry of crystal field and light extraction ratio. It was observed from SEM analysis that synthesized films have uniform morphology with different particle shapes. Orange red colour emission shown by UV excitation. As the solution used for prepare films changing then particle size vary. These films would be used for fabrication of many optoelectronics devices and photovoltaic application by using dopants **[23]**.

N.F.Q.Fahmi et. al., 2019 have investigated the influence of zinc doping (0-2 %) on various properties of NiO thin films. XRD revealed the amorphous structure of all undoped and doped samples. It was observed from the optical properties that transmittance increase and absorption decrease on increasing doping concentration. These synthesized films were used for humidity sensing and found that sensor response decrease with increasing doping. It was noted that as the doping concentration increase up-to 2% sensor response start increasing **[24]**.

A. Khaled et.al., 2019 have synthesized CuO films on stainless steel substrate by sol-gel dip coating technique. Four samples were prepared by varying PEG Wt% (5%- 20%). UV spectroscopy revealed that absorptivity and band gap change on changing weight percentage of PEG. SEM shows that thickness of films increases on increasing PEG content. This paper shows that prepared samples were used for solar cell application. It was found from selectivity of coat analysis that sample of higher PEG content was best candidate for solar cell application **[25]**.

A.Amri et.al., 2019 have studied the various properties of CuO films synthesize by facile one step sol gel dip coating on aluminium substrate. XRD was used to identify phase and crystallinity of synthesized sample. Chemical composition and electronic state of bonding at surface of films was analysed by XPS. FESM revealed the porous structure of sample and states that those films can be used for absorber and catalyst applications. AFM shows the rough surface of films around coating's surface which makes these films suitable for solar absorber. UV analysis was used to calculate band gap (2.7 eV) prepared CuO films **[26]**.

A. H. shukor et. al., 2020 have synthesized two types of single phase CuO films by varying sputtering power from 10 W to 40 W. single phase of CuO and Cu_2O was formed at 10W and 30W power respectively. AFM revealed that large roughness of surface at 10 W and 20 W and it start decreasing as the sputtering power increase beyond 20 W. XPS also confirm two phases of films by providing binding energy and peak position. Hall effect was used to measure resistivity of thin films and found that resistivity decreases with increasing of sputtering power. Films fabricated at 10 W, 20 W, 30 W and 40 W have band gap of 1.7, 2.0, 2.5, and 2.55 eV respectively. From this band gap we conclude that n-type CuO phase with 2.0 eV and p-type Cu_2O phase with band gap 2.5 eV **[27]**.

B.Seddik et.al., 2020 have studied the SnO_2 films doped with Cu for gas sensing applications. At operating temperature 150°C to 300°C, LPG gas exposed to the sample which kept inside the gas chamber. Synthesized films have tetragonal phase with 3.89 nm crystallite size confirmed by XRD. High transmittance of 73.98 % of thin films with 3.9 eV band gap examine by optical analysis, when LPG gas was injected inside chamber then maximum sensitivity obtain at 250°C with 11 sec and 20 sec of response and recovery time respectively. In this work sensitivity of gas sensor was investigated with number of gases such as NH_3, H_2S, CO_2 and LPG. It was found from selectivity analysis that Cu doped SnO_2 films was promising for LPG gas sensing applications **[28].**

Y. Zhao et. al., 2020 have studied the CNT/ SnO_2 films coated with Cu for H_2S gas sensing. The reaction and recuperation times of fabricated sensors were 240 sec and 600 sec respectively. In this work 10 ppm of H_2S was detected by synthesized sensor. Number of gases such as NH_3, CO_2, H_2SO_4 and SO_2 was injected on sensor and found that sensor have best selectivity toward H_2S gas. It was observed from the obtained data of this research that fabricated sensor has good repeatability and stability for 40 ppm H_2S gas **[29]**.

T. Amakali et. al., 2020 have compared the various properties of ZnO films synthesized from molecular precursor and sol-gel method. XRD shows that three films synthesized via sol-gel method have growth in different direction but films synthesized using precursor method oriented along one direction. The surface roughness was high of films fabricated from MPM in comparison of sol-gel method. It was observed from optical analysis that all of films have high transmittance and best suitable for optoelectronics device. Tauc plot was used to calculate band gap. The obtained band gap of ZnO film synthesized by MPM and sol-gel method was 3.75 and 3.25 eV respectively **[30].**

L. Castaneda et. al., 2020 have studied the optical features of ZnO films. This paper reveals nanostructured films of ZnO synthesized by using plant extract. Number of samples of different

thickness were prepared by varying spinning speed form 500 rpm to 3000 rpm. Synthesized films were characterized by using FTIR and UV technique. FTIR shows the Zn-O group at lower wavenumber and UV analysis found the absorption spectrum at 230 nm to 300 nm of wavelength. From optical analysis, it was concluded that films fabricated at 500 rpm have highest absorbance and lowest transmittance [31].

A. Aktar et. al., 2020 have studied the CuO films applicable for solar hydrogen production in solar water splitting. Different phase of synthesized films was analysed from XRD and EDX technique. It was observed that films fabricated at 250, 300 and 350°C have Cu_2O, mixed and pure CuO phase respectively. This study revealed that films have best crystallinity along with smooth morphology of surface. These synthesized films were used as photocathode for PEC system. It was concluded from this study that photocathode retained 85 % for their initial photocurrent for 30, 34 and 39 minutes annealed at 250, 300 and 350°C respectively [32].

F.Baynsal et. al., 2020 have examine the impact of different concentration of Li on CuO films. SEM revealed that with increasing Li concentration, particle size of films decreases and surface became uniform. XRD examined that with increasing Li concentration crystallite size decrease. It was revealed by Raman Spectra that CuO change into Cu_2O after high concentration doping. It was noted that Li doping increase transmittance and band gap. It was investigated from mechanical properties that Li doping improve mechanical strength of films. SPM shows the homogeneity of films by measuring depth of CuO films [33].

C. Yao et. al., 2020 have examined the resistance and magnetization switching properties. Sol-gel method was used to synthesize $Y_3F_5O_{12}$ thin films on pt substrate. XRD found poly-crystalline structure of YIG film without any impurities. From SEM analysis porous structure of films was examined which prevent formation of stacks. XPS was used to analyse chemical composition and found that YIG films have oxygen vacancies. Data retention test was used to investigate stability and reproducibility of thin films and found that resistance of HRS and LRS sustain up to 10 years for memory device applications [34].

A. M. Laera et. al., 2020 have studied the ZnS/ TiO_2 films for NO_2 gas sensing. Three steps facile method was used to synthesize TiO_2 films with nanocrystals of ZnS. Different size of XRD shows that all of samples have same phase structure. Sensor fabricated from these films shows high response time and low recovery time toward NO_2 gas at 270°C. XPS analysed chemical composition and revealed that prepared films have no impurity. It was noted that fabricated sensor has good reproducibility and high stability [35].

B. N. Q. Trinh et. al., 2020 have examined the influence of concentration on CuO films. SEM verify that with increasing solution concentration, grain size of CuO thin films increased. XRD

revealed that lattice imperfection reduced as the solution concentration increase from SEM analysis, it was found that porosity of films decreases by increasing solution concentration from 0.15 M to 0.30 M. conductivity of films increase with increasing concentration. Four-probe measure the electrical property and found that from this study, it was concluded that synthesized films can be used for fabrication of electronic devices [36].

H. Absike et. al., 2021 have studied the variance of spinning speed on CuO film's physical properties. In this study, films were deposited on glass substrate using sol-gel spin coating method by varying spinning speed from 2000 rpm to 4000 rpm. It was confirmed by that films synthesized at 3000 rpm have best crystallinity. It was noted from this study that with increasing spinning speed dislocation density decrease, consequently quality of films improves. Optical analysis shows decrease in value of transmittance with increase of spinning speed. Four-point probe measured the value of resistivity and found that it gradually decreases with increasing of spinning speed [37].

M. Saryac et. al., 2021 have investigated the various properties of CuO thin films doped with Tin. Optical analysis shows that band gap decreases on increasing concentration of Sn as dopant and as a result prepared samples can be used in solar spectrum. SEM and XRD both examine that synthesize films have good crystallization and surface of films was free from contamination. It was found from XRD technique that crystallite size increase with increasing of Sn ratio. It was also noted that intensity of peak increase with increasing of concentration of dopant. Drop cast method was used to form Sn doped CuO films deposited on glass substrate and prepared films was annealed at $550^{o}C$ temperature for two hours [38].

M. H. Kabir et. al., 2021 have examined the effect of stabilizer on aging behavior of sol for CuO films. It was observed from the study that aging time increase when molar ratio of precursor to stabilizer. XRD confirm the monoclinic structure of synthesized films. It was found that with increasing of crystallinity, dislocation density decreases. It was noted that films synthesized at $555^{o}C$ have good crystallinity, optical analysis shows decrease of band gap with increasing annealing temperature which exhibit films have less defect. Homogenous films were synthesized from 1:3 molar solution of precursor to stabilizer rather than 11:1. This study shows that optoelectronics properties improve when long period aging was used [39].

L. zhao et. al., 2021 have synthesize Wo_3 thin films applicable as hole-injection layers in QLEDs. These films were synthesized by using sol gel method and calcinate at $420^{o}C$ for 1 hour. TEM confirmed the polycrystalline nature of films. It was noted that due to uniform quantum size, synthesized films applicable in QLEDs. It was observed that QLEDs based on

Wo$_3$ have less leakage current and enduring carrier transportation light efficiency of quantum dot LEDs was improved by using nanocrystals of tungsten **[40].**

E. C. Nwanna et. al., 2021 have studied the green synthetic approach for synthesis of CuO films applicable in solar cells. In this study, allium cepa was used as reducing agent during fabrication of CuO films. SEM and EDX revealed that prepared films have spherically shaped particle and O$_2$ as well as Cu element respectively. FTIR shows the Cu-O and O-H stretching which reveals pure phase of CuO and no absorption of H$_2$O molecules respectively. UV analysis revealed that both absorbance and transmittance occur in visible region. The energy band gap of fabricated films was 1.48 eV and films have applications as an absorber layer of solar cell **[41].**

M. H. Rajeev et. al., 2021 have studied the thin films of Zirconium Titanate synthesized by sol-gel methods. The ellipsometer revealed that the thickness was in the range of 44 nm to 40 nm when the spinning speed varied from 4000 rpm to 6000 rpm. It was noted that synthesized films have uniform coating, less porosity with minor cracks. FTIR shows the formation of Zr-O vibration bond of Zr TiO$_2$ films and O-H bending mode of absorbed water. Leakage current was measured by dielectric constant and concluded that obtained leakage current was lower than reported leakage current. XRD analysed that synthesized films were of amorphous in nature and more suitable for MOS capacitor applications **[42].**

D. Kaya et. al., 2021 have examined the different properties of NiO films synthesize by thermal evaporation method on various substrates. When these films were annealed at 450°C then Ni ions diffuse into InP, GaAs and sapphire substrate, consequently Ni$_2$InP, Ni$_2$GaAs and NiAl respectively. It was concluded from XRD that NiO films at silicon substrate have high purity. It was found from the UV analysis that films fabricated at sapphire substrate have more transmittance in comparison of films at other substrate. Electrical properties of synthesize films was measured by Hall effect and found that films synthesized at glass and sapphire substrate reveal p-type semiconductor behavior **[43].**

Q. M. Al-Bataineh et. al., 2021 have studied the synthesis and optical characterization of polymethylene methacrylate. PMMA was synthesize by using nanoparticle of metal oxide such as CuO, SiO$_2$, ZnO and TiO$_2$. Different shape of nanostructure was analysed by SEM at 10 KV operating voltage. It was found from UV analysis that PMMA embrace with MOS exhibit low transmittance and reduction in band gap due to shifting of absorption edge toward lower energy. In this study, Wemple- Di Domenico (WDD) model was used to calculate optical parameters and found that value of band gap obtained from WDD and Tauc method was in good agreements **[44].**

R. K. Jain et. al., 2021 have studied H_2S gas sensor fabricated from Wo_3 thin films doped with CuO. To study gas sensing properties, electron beam evaporation method was used to deposit doped and undoped Wo3 films on alumina substrate. These prepared samples were characterized by FESEM and found that Wo_3 films doped with 3% CuO have large improvement of H_2S gas sensing. It was noticed from this paper that response of films toward H_2S gas was increased with increasing temperature from 200^oC to 300^oC. the response and recovery time were also improved by using doping of CuO to Wo_3 thin films. It was concluded from this research prepared films have excellent performance for H_2S gas sensing **[45]**.

Z. Huang et. al., 2021 have investigated CuO films for use as a gas sensor at ambient temperature. In this study, CuO nanomaterial was synthesized using hydrothermal method to detect H_2S gas. The peak of Cu, Al and oxygen was analysed by using energy dispersive spectrometer, consequently pull sample of CuO was formed. SEM analysed that sample prepared by using growth time of more than two hours. It was found from this paper that sensor based on SACNAS manifest high stability, repeatability, good response time at low detection time and excellent performance of gas sensor toward H_2S gas **[46].**

B. Salah et. al., 2021 have fabricate H_2S gas sensor from nanoparticles of SnO_2-Fe_2O_3 nanoparticles. To fabricate sensor device, nanoparticles were deposited on substrate with interlink electrode. Impedance spectroscopy revealed that synthesize nanocomposite were semiconducting in nature. It was found that sensor fabricated from SnO_2-Fe_2O_3 nanocomposite was highly sensitive towards H_2S gas at room temperature. It was observed that nanoparticles keep their crystallinity after executing sensing test of H_2S. XRD revealed the tetragonal and hexagonal structure of SnO_2 and Fe_2O_3 respectively. SEM analysis show that nanoparticles were of semi-circular in shape **[47]**.

P. Devi et. al., 2021 have studied the sensitive colorimetric gas sensor fabricated from In_2O_3 nanoparticles for hydrogen Sulphide gas. Sol-gel method was used to synthesize nanostructure of In_2O_3 on glass substrate using spray coating method. FESEM revealed the spherical morphology and HRTEM was used to analyse the crystallinity and purity of pristine. It was noticed that absorbance and reflectance increase and decrease respectively with increase of exposer time of H_2S gas, synthesized samples show excellent response toward H_2S gas by exhibiting colour change with exposure of H_2S gas due to formation of In_2S_3 layer on top of In_2O_3 films **[48]**.

AI. Ayesh et. al., 2022 have studied the nanoparticle of Fe_2O_3 / CuO as gas sensor for H_2S gas. The chemical composition and semi-circular shape of nanoparticles was revealed by EDS and SEM respectively. It was analysed by XRD technique that Fe_3O_4 and CuO have cubic and

monoclinic structure respectively. Impedance measurement was used to analyse electrical properties of synthesized nanoparticles at different temperatures. In this work selective gas sensor was fabricated at low temperature for low concentration of gas. It was noticed that fabricated sensor has good sensitivity, less response time, low power and good repeatability **[49].**

K. R. Sinju et. al., 2022 have studied the nano-wires of ZnO based on e-nose for discernment toxic gases such as H_2S and NO_2. In this work surface of ZnO wires improved by using sensitizers named as Cu, Ni, MgO and Au for the fabrication of multiple sensor. It was observed that sensor response improves by using the sensitizer for a selective gas and ZnO nanowires-based sensor shows a remarkable response toward NO_2 and H_2S. It was noticed that multiple sensor exhibits good reproducibility with high stability. Elovich model was used for investigating absorption kinetic response for NO_2 and H_2S gas **[50].**

A. Kumar et. al., 2022 have studied the role of acoustic device for gas sensing applications. It was noticed that because of high sensitivity, small scale size, strength and integration with field of electronics acoustic device have wide application in biological and chemical sensing. The resonance frequency of SAW based sensor was found in range between few M-Hz to G-Hz. It was concluded from this paper that SAW sensor suffers from high devitalization of high wave in humid condition **[51].**

M. JIANG et. al., 2022 have studied $CaCu_3-Ti_4O_2$ films doped with magnesium. These films were prepared using modified sol-gel method on silicon wafer. It was revealed by XRD analysis that lattice size became lower as the concentration of dopant increase from 0 to 0.2%. It was observed that when concentration of magnesium increases then it replaces the Cu^{2+} species and CuO phase was produced. The morphology of synthesized films was analysed by SEM and found that grain size decreases with increase of doping concentration. From this research it was concluded that the synthesize films have a significant potential in the fabrication of functional devices **[52].**

X-Yi SHEN et. al., 2022 have studied the removal of heavy metal ions by spherical flower like hydroxide of Mg. In this study magnesium sulphate was used to synthesize flower like magnesium hydroxide. The effect of Mg^{2+}/NH_4OH molar ratio was analysed on structural and morphological properties of Mg hydroxide. As the molar ratio increased then synthesized sample shows uniform and regular flower like structure. XRD and SEM shows the images of magnesium hydroxide at different temperature and found that uniform flower like structure was formed at high temperature. It was concluded that to fabricate spherical flower like magnesium hydroxide, we require 0.5 molar ratio of Mg^{2+}/NH_4OH at 120^oC temperature with

2 mol/L concentration of Mg^{2+}. Due to excellent absorption ability it became a promising candidate for removal of heavy metal ions **[53].**

T. Chommaux et. al., 2022 have investigated in-situ electrical and mechanical properties of Indium and TiO_2. Ion beams sputtering technique was applied ITO thin films on polyimide substrate. Four samples of ITO films were fabricated by various parameter such as with or without oxygen at room temperature and 100^oC temperature. it was revealed by in-situ XRD test that polycrystalline ITO films have very low elastic anisotropy from in-situ electrical measurement, it was analysed that prepared films have cracks onset strain corresponding to applied stream which was delayed by introducing oxygen flow and decreasing the deposition temperature **[54].**

E. Guaus et. al., 2022 have studied the characterization of Zinc phthalocyanine thin films for solid electrodes. In this paper, thin films were formed on carbon electrode of ZnPc. The electrochemical behaviour of deposited films and effect of deposition technique in this behaviour was analysed. Cyclic voltammetry technique was used to characterize the electrochemical behaviour. It was analysed from UV spectra that plot of absorbance and concentration was linear and consequently no aggregation in concentration. It was noticed from this paper that characteristics of spreading solution effect the film formation. It was observed from the AFM that Emmerson films shows a uniform granular structure. Cyclic voltammetry technique shows that the behaviour of Emmerson and LB thin films deposit on carbon electrode was same **[55]**.

S. BAKHTIARNIA et. al., 2022 have investigated the influence of pressure and substrate on $BiVO_4$ thin films. Reactive magnetron sputtering was used to form nano-porous thin films of $BiVO_4$ for obtaining rapid deposition, dc power supply was applied to Bi and V metallic targets. It was found that films deposited on silicon substrate have highest photoactivity. It was analysed from FESEM that films deposited at 4.5 pa have nano porous morphology with highest porosity and lowest band gap. XRD found that films deposited on silicon and alumina substrate have monoclinic scheelite structure without any contamination **[56]**.

A. Alagh et. al., 2022 have studied the NO_2 sensing at room temperature. In this work tungsten oxide nanowires were loaded with nanoparticles of PtO and PdO. FESEM, XRD, XPS and TEM was used to analyse morphological, structural and chemical characteristics. It was found from this paper that fabricated sensor have significant response toward WO_2 gas at room temperature. It was found that response of PtO loaded sensor decrease and response of PdO loaded sensor increase in humidity environment **[57].**

X. Ning et. al., 2022 have studied the electrospinning technology on ceramic tube to improve the response of H_2S detectors. In this paper sub millimeter fibre was deposited on ceramic tube by electro spinning method. Copper oxide doped SnO_2 fibre H_2S detector was fabricated by using this technique. The principle of H_2S gas sensor was based on the decrease of resistance on exposing H_2S gas. It was analysed that SnO_2 based sensor with 10% copper oxide have best performance at 150^oC operating temperature, response time of sensor reduced 70% and recovery time reduced by half for 1 ppm gas **[58].**

A. Al-Sarraj et. al., 2022 have studied the monetization of H_2S gas from WO_3 based sensor. In this paper, microwave assisted chemical route was used to synthesize nanoparticle of tungsten oxide loaded with silver. It was found that WO_3 films loaded with 3% silver shows highest sensitivity towards H_2S at low concentration and less temperature. TEM was used to analyse morphology of nanoparticles thin films. It was noted that nonannealed films have best response toward H_2S gas sensor. It was observed that response time decrease with increasing the temperature because of the reaction rate between gas and sensing material **[59]**.

H. R. Shwetha et. al., 2022 have studied metal oxide-based gas sensor for CO_2 gas sensing. In this paper, $BaTiO_3$- CuO with 1% Ag applied as a sensing material for CO_2 gas sensing. XRD was used to analyse the structure and found that $BaTiO_3$, CuO and Ag have tetragonal, monoclinic and cubic system respectively. XPS analyse the chemical composition and revealed that sensing films have contamination of only low intense carbon. It was found from SEM that films surface made with fine crystallite with higher porosity. When this fabricated sensor used for CO_2 gas sensing then capacitive based sensitivity was 70% for 1000 ppm. It was concluded that capacitive based measurement gave best results **[60]**.

L. Guanglu et. al., 2022 have studied the thin films of tungsten for triethylamine detection. Vacuum thermal evaporation technique was used to deposited tungsten oxide thin films. It was noticed from this research that films annealed at 555^oC temperature shows good response toward triethylamine. XRD analysis found that the WO_3 films were amorphous in nature. It was noted from SEM analysis that grain size increase with increasing of annealing temperature. It was concluded from this research that WO_3 films have great potential in detection of chemical compounds **[61]**.

J.A. Oke et. al., 2022 have studied the various technique of thin films deposition. In this paper, number of techniques were discussed along with mechanism advantage and disadvantage. Thin films fabricated from evaporation technique have best properties at high annealing temperature. it was noted that films prepare from molecular beam epitaxy have good structural, magnetic and optical properties for optoelectronic devices. High quality films were produced by using

pulsed laser deposition and sputtering techniques. Spin coating technique was very suitable at high deposition temperature. it was concluded that properties of films were based on various parameters such as precursors, deposition temperature and type of substrate [62].

M. shkir et. al., 2022 have studied the MoO_3 thin films doped with rare earth metal by spray pyrolysis technique. It was revealed by XRD technique that Pr doped MoO_3 films have monoclinic crystal structure with high purity and 59 nm crystal size. It was found from FESEM analysis that MoO_3 films have reticulated nano-fibrous morphology and doped films have tiny rod-shaped morphology. Highest response toward NH_3 gas was possessed by doped MoO_3 films. It was noted that fabricated films have 54 sec responding time and 12 sec restoration time for 250 ppm NH_3 gas [63].

Li. Chunyan et. al., 2022 have studied the acetone gas sensor applicable for efficient ultrathin nanosheet of NiO. Facile solvothermal method was used to synthesize porous nanosheet of NiO. It was noted that thickness of sheets controlled by varying the ethanol content in solvent. XRD revealed the hexagonal phase of NiO nanosheets. The growth of thin nanosheets structure on substrate was confirmed by TEM and HR- TEM. These fabricated nanosheets were used as sensing material in detection of acetone. It was found that NiO based gas sensor shows low limit of detection, high sensitivity because of the change in carrier concentration and oxygen distribution [64].

J. Chang et. al., 2023 have studied the NO_2 gas sensor fabricated with SnS_2 modified with nanoparticles of Au. Solvothermal and subsequent-in-situ reduction method was used to synthesize sample. XRD found the hexagonal structure of both doped and undoped sample. SEM was used to analyse the morphology of prepared films and found that films have flower like structure. The chemical composition of synthesized films was analysed by XPS technique. It was noted that sensitivity toward NO_2 gas was improved on adding dopant to SnS_2 [65].

A. M. Al-Fa'ouri et. al., 2023 have scrutinize the various properties of nanocomposite of CuO polyvinyl alcohol for solar cell applications. In this paper solution casting method was used to deposit nanocomposite thin films of CuO- PVA. UV analysis shows 2.74 eV band gap of prepared sample. It was observed from electrical measurement that DC conductivity increase by increasing temperature and concentration of CuO nanofiller. It was concluded that these films were suitable for optoelectronic applications. Consequently, synthesized nanocomposite of CuO-PVA was suitable in electronics and solar cell devices [66].

M. Imran et. al., 2023 have researched the impact of annealing on the physical characteristics of CuO films. These films were deposited on glass substrate using chemical bath deposition method. have studied the effect of annealing on physical properties of CuO thin films.

Chemical bath deposition technique was used to deposit thin films of CuO on glass substrate. The annealing temperature was varied between 300 to 500°C and effect of this temperature was investigated on distinct physical properties. It was revealed by XRD that size of crystallites increases on increasing annealing temperature. According to UV spectroscopy, the band gap shrinks from 1.52 to 1.45 eV as the annealing temperature rises. Synthesized films' conductivity was measured using the hot probe technique, and p-type conductivity was verified. **[67]**.

A. K. Vishwakarma et. al., 2023 have studied the gas sensor based on titanium oxide thick film for propanol. In this paper undoped and doped (2 wt% cadmium sulphide) thick films was deposited on alumina substrate at room temperature, the concentration of propanol from 0 to 5000 ppm was exposed on synthesized sample and response of propanol was noted. It was observed that as the concentration of propanol increase then resistance decrease. It was noted that cadmium sulphide doped films have excellent response in comparison of pure films of titanium dioxide. It was found that CdTO films have response and recovery time of 62 second and 195 second respectively **[68]**.

S. R. Sriram et. al., 2023 have studied the Wo_3 and Cu doped Wo_3 films for gas sensing applications. Pyrolysis technique was used to deposit tungsten-based films on glass substrate. XRD revealed that prepared samples have crystalline structure oriented in (200) plane. Tauc relation was used to calculate optical band gap and found that it reduces with increasing dopant concentration. It was noted from this study that fabricated sensor from Cu doped Wo_3 films have excellent response toward lower concentration of NH_3 gas **[69].**

F. O. Oluyemi et. al., 2023 have investigated the interrelationship between properties and molar concentration of CuO films. Pyrolysis method was used to deposit solution of copper oxide varying between 0.1 M to 0.25 M on glass substrate. XRD revealed that films synthesize by 0.1 M, 1.0, 1.5, 0.2 and 0.25. It was observed from optical characterization that films of 0.1 M concentration have lowest band gap in comparison of other concentration. SEM analysis was used to analysing the surface structure and found that 0.1 M films have spherical morphology and films of other concentrations have dense and irregular shape morphology **[70]**.

K. Rajesh et. al., 2023 have studied the NiO films to detect ultrasensitive formaldehyde. Spray pyrolysis method was used to deposit nickle oxide films at different substrate temperature. it was revealed by XRD that synthesized samples have polycrystalline nature with cubic structure. It was found from SEM analysis that as the temperature of substrate increase then synthesize films have nonuniform surface morphology. Optical analysis revealed that films synthesize at highest temperature have excellent response toward lowest concentration of

formaldehyde. It was concluded that films synthesize at 400ºC have good porosity, lowest band gap and highest response toward formaldehyde [71].

D. Rajkumar et. al., 2023 have studied the tin oxide thin films for formaldehyde gas sensor at room temperature. Pyrolysis technique was used to deposit films of TiO_2 at 375ºC to 450ºC temperature. It was found that films fabricated at 400ºC temperature manifest crystalline anatase phase. It was noticed from the optical analysis that films prepared at highest temperature shows less band gap. It was found that films prepared at 400ºC temperature have maximum transparency of 8% in comparison of the films prepared at other temperature. it was noticed from this research that titanium oxide films have a excellent sensor. It was confirmed by FESEM that there was existence of Ti and O element. It was observed that response, recovery time and sensitivity for films was excellent toward 200 ppm [72].

G. Mamtmin et. al., 2023 have studied Zinc oxide films for optical wave guide sensor to monitor sulphide gas. In this paper sensor was fabricated from Zinc oxide films synthesized by spin coating and immersion method. The sensor response was compared and found that sensor fabricated by immersion method have excellent sensitivity. It was noted from this paper that arrangement of molecule of porphyrin on surface of Zinc oxide films prepared from immersion and spin coating method was different. XRD found that Zinc oxide films have hexagonal wurtize structure. It was observed from this paper that COWG sensor have good reproduce ability toward 100 ppm of H_2S and SO_2 gas at room temperature [73].

A. Amri et. al., 2023 have studied the influence of Al doping on various characteristics of ZnO thin films. Sol-gel dip coating method was used deposit films at glass substrate. The change in electrical, optical and structural properties was noticed by varying the doping concentration (0.1% to 3.5%) of aluminium. It was observed from this study that films synthesized with 1% aluminium have best electrical and optical properties. XRD shows that synthesize films were of polycrystalline nature and hexagonal wurtzite structure. It was noted that the peak intensity of (0 02) plane decrease with increasing of doping concentration and crystallite size decrease. It was found that films doped with 1% aluminium have 90% transmission [74].

M. F. Naief et. al., 2023 have synthesized the fullerene for monitoring H_2S and NO_2 gases. To characterize fullerene, various technique such as TEM, FESEM and EDX was used. It was found from TEM analysis that hollow carbon balls of fullerene was formed. EDX examined the presence of O/C ratio. Thin films of fullerene were used to detect gases at various operating temperature. It was noticed that fullerene-based sensor has best sensitivity at 25ºC and 200ºC temperature for Wo_2 and H_2S gas respectively. It was concluded that fullerene sensor has less response time for NO_2 gas at room temperature [75].

V. Kumar et. al., 2023 have studied the Zinc oxide thin films for optoelectronics applications. In this study ion beam approach applied to improve the properties of Zinc oxide films. XRD revealed that ion beam implanted Zinc oxide films have hexagonal wurtzite structure oriented along C axis. Atomic force microscopy revealed that Ag implanted films have rough surface with 48 nm grain size. As the implantation of silver ion increased, then roughness of surface was high. It was noted that conductivity of Zinc oxide films was change from n to p type on implantation of ion. It was observed that luminescence intensity and conductivity was improved by using selected annealing steps. It was concluded from this paper that p-type zinc oxide films prove a promising candidate for optoelectronics devices **[76].**

J. G. Cuadra et. al., 2023 have studied the silver coated titanium dioxide films for antimicrobial and photocatalytic applications. In this paper pulsed laser and spray pyrolysis technique was used to synthesize TiO_2 films coated with silver nanoparticles. These prepared films proved best candidate for photocatalytic application because of the high transmittance value (> 80%). These prepared films were used to determine the antibacterial activity and it was found that 93 % bacteria were killed when UV light irradiated for four hours. It was observed that removal efficiency of RhB reached twice in comparison of pure TiO_2. It was noted that silver coated films have strong antibacterial activities **[77].**

V. A. Owoeye et. al., 2023 have investigated the consequence of precursor concentration of nickel oxide films. In this paper spray pyrolysis technique was applied to form nickel oxide thin films on soda lime glass substrate. The precursor concentration was varied between 0.1 molar to 0.4 molar and effect on optical properties was noticed. EDX was used to examine the elemental composition. It was found that thickness of films increases from 43 nm to 49 nm as molar concentration increases from 0.2 molar to 0.4 molar. It was observed from this paper that transmittance and band gap of nickel oxide films decreases on increasing molarity. Consequently, these prepared films were used as a window layer in solar cell **[78].**

S. K. J. Vigitha et. al., 2023 have studies the indium doped cobalt oxide films for electrochemical applications. This study gives the information of thin films of Co_3O_4 were deposit on glass substrate by applying spray pyrolysis technique. The concentration of indium was varied between 0.025 to 0.1% and effect of variation was noted on various properties of films. XRD found that as doping concentration increase, crystallite size was obtained small due to weak crystallization and line boarding. It was analysed from the SEM that growth of particle of increase with increasing indium concentration. EDAX analysis shows that pure doped and undoped films of cobalt oxide was formed because of the presence of O, Co, and In element.

Band gap reduced with doping and these prepared films can be employed for electrochemical application [79].

K. Hosomi et. al., 2023 have studied the ZnO films for chemical composition, surface morphologies and luminescent properties. XPS revealed that during ion irradiation, change in stoichiometry of ZnO was noticed. It was found that surface roughness and ion beam fluence have strong correlation. It was analysed by monte carlo simulations that oxygen deficient ZnO films surface change into stoichiometric surface. It was concluded that flat surface ZnO films and homogeneous el emission makes promoting candidate for nanometric light source [80].

K. C. Nwambaekwe et. al., 2023 have studied the thin films of kesterite with cd substituent for photovoltaic applications. On soda-lime glass, kestaite films were deposited using the spray pyrolysis method. To study the various properties of films, prepared films were pist annealed at 525°C. It was found that crystallite size of annealed and unannealed films vary from 5-27 nm and 13-25 nm respectively. SEM analysis revealed the morphology of films and noted that annealed and unannealed films have uniform morphology with cube- shaped nano-particles respectively. It was observed that as cd ratio increase then red-shift absorption exhibited by both annealed and unannealed films, because of the optical band gap. Films were suitable for photovoltaic device [81].

D. Bingsheng et. al., 2023 have studied the gas sensor for anti-humidity fabricated from Bi_2Se_3. Solvo-thermal method was used to fabricate bismuth selenide sheets. It was noticed that nano sheets of Bi_2Se_3 shows good response toward NO_2 for low concentration due to of Se vacancies. It was found that Bi_2Se_3 have rhombohedral crystal structure. The thickness of sheets was analysed from SEM and found that prepared sheets were of ultrathin thickness of 3 nanometre. Various gases such as NO, NO_2, NH_3, ethanol, methane and acetone were exposed on gas sensor and found that fabricated gas sensor found selective for NO_2 gas with 93% sensitivity. In presence of humidity of range 0 to 80%, sensor response was found good with volatility of only 3.63% [82].

M. W. Vande Putte et. al., 2023 have studied the thin films of tin selenide for thermoelectric energy generation devices. Electron beam evaporation method was used to grown SnSe films on $DyScO_3$ substrate. It was noticed from AFM that surface roughness of films reduced with increment in temperature because of the diffusion. XRD was used to determine the arrangement of crystals, domain formation, and film alignment and found SnSe films have orthorhombic structure oriented in (110) plane with two SnSe domain types. These prepared films were used in TEG for wireless gas sensor and also to improve the thermoelectric performance [83].

G. V. A. Reddy et. al., 2023 have studied CeO_2 coated tungsten oxide thin films for electrochromic applications. Hydro thermal method was used to fabricate nanorods of cerium oxide and DC magnetron sputtering technique used for synthesis of Wo_3 films. It was noticed from SEM analysis that synthesized films have nonporous morphology. XRD revealed the amorphous structure of Wo_3 films. It was found from optical analysis that Ce_2O_3 coated Wo_3 films have high transmittance. These prepared films were used to improve the electrochemical performance of films for smart window applications **[84]**.

S. Rani et. al., 2023 have studied the NO_2 gas sensor and photodetector fabricated from hetro-junction thin films of $SnSe_2$/ SnO. Thermal evaporation method was used to synthesize thin films of different thickness. For gas sensing, silver electrode distant at 0.5 mm were deposited on thin films. XRD and Raman spectroscopy was used to identify the phase of synthesized films and found that films have four phase $SnSe_2$, SnO_2, SnSe and SnO. FESM was used to analyse the surface and found that films have rice like nanostructure. It was noticed from optical analysis that optical band gap and thickness were inversely proportional. It was concluded from this research that lowest thickness films show good response toward NO_2 gas at room temperature **[85]**.

K. G. -N$_\lambda$ecek et.al, (2023) analyse the ca doped films for the application of hetro-junction solar cell. In this study, low resistivity CuO films were synthesized by using doping of calcium from 1-10wt%. TEM was used for morphological analysis and found that prepared samples have smooth layer. Dopant atoms were found to exert a resistive force against the development of CuO films based on XRD analysis. It was found that films prepared by 4wt% has lowest resistivity. They produced hetro-structure with maximum efficiency of 2.38% **[86].**

M.Abdelfatah et.al. (2023) use an inexpensive electrodeposition technique to synthesizes K doped Cu_2O thin films on conductive FTO substrates. The n-type semiconductor behavior of the generated thin films was demonstrated by the photocurrent measurements. Moreover, increasing the doped concentration increases the photocurrent; a maximum value of 0.1 M K ions was obtained. For doped Cu_2O thin films at 0.1 M K ions, the density of the photocurrent has the greatest value of 0.047 mA/cm2, indicating an improvement in the mobility of charge carriers and a decreased recombination rate. Based on the results, K-doped Cu2O thin films seem to be a great option for solar cell applications **[87]**.

Ahed M. Al-Fa'ouri et.al., (2023) use the solution casting process to make thin films of CuO-PVA nanocomposite, ranging in weight from 13wt% to 51wt%. They also manufacture pure polyvinyl alcohol (PVA). With an increase in CuO nanofiller concentration, DC conductivity

progressively rises. This suggests that spreading CuO nanofiller significantly improves electronic conduction by acting as fillers that are conductive in the PVA host matrix. The optical band gap values for CuO-PVA composite films was found decreasing as the weight percentages rise. This indicates that the doped films' optical band gap increased their ability to absorb visible light. The generated samples can be used to provide a good candidate material for photoactive layers in solar cell applications, according to the work's results **[88].**

K. ElKhamisy et.al., (2024) have surveyed the problems and new advances in silicon thin-film solar cells. The earliest solar cells were made of crystalline silicon. Silicon materials are useful in photovoltaics, however their low energy conversion efficiency (27.6%) and high manufacturing cost are drawbacks. The foundation of the third generation of solar cells is the use of novel materials and technologies that are not yet on the market but should offer the highest theoretical efficiency and lowest manufacturing costs. On the other side, thin-film solar cells result in faster results, lower resource requirements, and higher efficiency **[89].**

A.M. Oni et al. (2024 have researched methods for increasing photovoltaic cell efficiency and the thorough assessment of solar cell technologies. The efficiency of solar cells based on silicon (Si) has almost achieved its maximum value, at about 25%. Thin film solar cells are advantageous since they use less material and are becoming more efficient. A highly promising method for achieving exceptional sunlight-to-electricity conversion efficiency is the multi-junction (MJ) solar cell. These cells are more efficient because they use a range of absorber materials with various bandgaps, which enables them to efficiently absorb a greater range of solar wavelengths and improves efficiency overall and spectrum utilization. **[90].**

D. Motai et.al., (2024) use co-evaporation method to fabricate thin films of $(Ge_x Sn_{1-x})S$ for a multijunction solar cell. XRD and Raman spectroscopy confirmed that a Ge, Sn and S solid solution was formed in the prepared thin films. The solar cells made with the (Ge- 0.42 Sn-0.58) S thin film had the following characteristics: 0.29 V for open circuit voltage (Voc), 6.92 mA/cm^2 for short circuit current density (Jsc), 0.34 for fill factor and 0.67% for PCE. It was analyzed that photo-voltaic characteristics of solar cells fabricated from thin films of Ge doped SnS was better in comparisons of SnS thin films **[91].**

Researchers examine how solar cells behave at temperatures between 15 (288 K) and 50 (323 K) and higher [92]. The first type of solar cell was the monocrystalline one, which required less area to produce the same amount of performance. It costs twice as much as crystalline silicon and more than thin-film solar cells. These solar cells operate poorly at high temperatures (down 10-15%) [93]. Midway through the 1980s, a number of highly cited academic publications on CuO ignited interest in the topic. The primary focus of early research in the

2000s was on the mechanics of growth and how it drives the deposit of thin films for a variety of applications. [94].

2.2 Issues with Gas Sensors Based on Semiconductors

The use of semiconductor materials as sensing materials for many types of oxidizing and reducing gases is widely recognized. When low concentrations of gas are exposed to semiconducting material, the gas sensor suffers from issues including poor selectivity, low sensitivity, and low repeatability. Due to this process, it is challenging to identify a specific gas of interest in a mixture of other gases from the sensor signal. Additionally, the gas sensor component has poor sensitivity, especially at 10 ppm in the ambient, which is a relatively low concentration. At such low gas concentrations, the sensor response is hardly acceptable.

According to the literature, copper oxide thin film sensor elements exhibit outstanding characteristics for sensing hydrogen sulfide gas. Since copper oxide is very selective and exhibits very low sensitivity to other reducing gases like water or ethanol. Therefore, it has been acknowledged as a special promoter of sensitivity toward H_2S gas. However, there are several drawbacks to these thin film sensor elements. The major issue occurs at low operating temperatures when the sensor element is subjected to a lower H_2S concentration. It has been shown that sensor response and recovery times get longer, particularly when H_2S gas is present in the air at low concentrations (a few ppm). In order to create effective and trustworthy gas detecting devices, these issues with semiconducting-based gas sensors must be resolved.

From the literature survey it has been found that the CuO thin films can be used as a sensing material for H_2S gas sensing at high operating temperature in the range of $150^{o}C$ to $300^{o}C$. But despite numerous successful attempts to synthesize CuO nanostructure with various methodologies for gas sensing applications, the issue of low responsiveness and high operating temperature persists. Keeping in view the above facts, an attempt has been made on synthesis of CuO thin films for gas sensing at temperature ($25^{o}C$ to $150^{o}C$). Best response was achieved at lowest temperature and this response was increase by using Sn as dopant.

2.3 Objectives of the Research

In accordance with the information mentioned above, an effort has been undertaken to create nanostructured doped and undoped thin films using simple, affordable synthetic techniques. Investigations have been done into how the characteristics of synthetic materials are affected by varying spinning speeds and used for solar cell applications. For gas sensor applications, thin films of polycrystalline nanoparticles are the best choice. They have a high surface-to-volume proportion because to their small crystallite size, inexpensive price, and great stability.

As a result, effective research was developed in the fabrication and characterization of CuO thin films in this present investigation.

The goal of this study is to pinpoint the elements necessary for the synthesis and creation of CuO-based nanostructured thin films with low operating temperature sensing capabilities. In this context, our work focuses on the synthesis, characterization, and gas sensing behavior of sol gel spin-coated nanostructured CuO thin films. Variations in spinning speed were used to manufacture the samples, and these variations are anticipated to provide variable structural, electrical, optical, and gas sensing capabilities. X-ray Diffraction Analysis, Scanning Electron Microscopy, UV-Visible spectrophotometer, and two probes were used to investigate the microstructural, optical, morphological, and gas sensing features of the films. This is essential for examining the thin film properties for uses in solar cells and gas sensors, among other things.

2.4 References

[1] S. Saito, M. Miyayama, K. Koumoto & H. Yanagida. (1985). Journal of the American Ceramic Society. 68 (1), 40-43.

[2] E. Traversa. (1995). Journal of intelligent material systems and structures. 6, 861-868.

[3] A. Chaturvedi, V.N. Mishra, R. Dwivedi, S.K. Srivastava. (2000). Microelectronics Journal. 31, 283–290.

[4] J. S. Cruz, G. Torres-Delgado, R. Castanedo-Perez, S. Jime´nez-Sandoval, O. Jime´nez-Sandoval, C.I. Zu´n˜iga-Romero, J. Ma´rquez Marı´n & O. Zelaya-Angel. (2005). Thin Solid Films. 493, 83 – 87.

[5] D. Jundale, S. Pawar, M. Chougule, P. Godse, S. Patil, B. Raut, S. Sen & V. Patil. (2011). Journal of sensor technology. 1, 36-46.

[6] M.F. Nurfazliana, S.A. Kamaruddin, N. Nafarizal, H. Saim, & M.Z. Sahdan. (2014). IEEE-ICSE2014 Proc. 978 (1), 4799-5760.

[7] S. S. Shariffudin, S. S. Khalid, N. M. Sahat, M. S. P. Sarah & H. Hashim. (2015). Material Science And Engineering. 99, 012007.

[8] H. Hashim, S. S. Shariffudin, M. S. P. Sarah & N. I. Nasir. (2016). IEEE-ICSE2016 Proc. 978 (1), 5090-2383.

[9] J. Wu, K. S. Hui, K. N. Hui, L. Li, H. H. Chun & Y. R. Cho. (2016). Journal of Materials Science: Materials In Electronics. 27, 1719-1724.

[10] S. Muthukrishnan, V. Subramaniam, T. Mahalingam, P. Sumathi, S. J. Helen, V. S. Kumar, B. Janarthnan & C. Thirunavukarasu. (2017). IJARIIE. 3 (3), 2684-2690.

[11] B. Troudi, O. Halimi, M. Sebais, B. Boudine & A. Djebli. (2017). International Journal of Mechanical and Production Engineering. 5 (2).

[12] D. Nandhini & S. Subashchandrabose. (2017). International Journal of Current Engineering and Scientific Research. 4 (10).

[13] D. R. Bhowmik, A. N. Ahmed, M. A. Gafur, M. Y. Miah & D. Islam. (2018). Materials Science and Engineering. 438, 012001.

[14] X. Hu, Z. Zhu, Z. Li, L. Xie, Y. Wu & L. Zheng. (2018). Sensors And Actuators. 264, 139-149.

[15] M. Dhaouadi, M. Jlassi, I. Sta, I. B. Miled, G. Mousdis, M. Kompitsas & W. Dimassi. (2018). American Journal of Physics and Applications. 6 (2), 43-50.

[16] A. Rydosz. (2018). Coatings. 8, 425.

[17] J. M. Rzaij, I. M. Ibrahim, M. A. Alalousi & N. F. Habubi. (2018). Optik. 172, 117-126.

[18] R. Singh, L. Yadav & S. T. Shrey. (2019). Thin Solid Films. 19, 30395-5.

[19] N. Touka, D. Tabli & K. Badari. (2019). Journal of Optoelectronics and Advanced Materials. 21 (11-12), 698-701.

[20] H. Z. Asl & S. M. Rozati. (2019). Journal of Electronic Materials.1-7

[21] S. Horzum, S. Gürakar, & Tülay Serin. (2019). Thin Solid Films.

[22] H. Lee, X. Zhang, E-j. Kim & J. Park. (2019). Sensors and Materials. 31 (2), 501-507.

[23] L. Benharrat, L. Guerbous, D. Bradai, A. Boukerika, A. Manseri, N. Selmi & B. Rahal. (2019). Thin Solid Films. 137738.

[24] N. F. Q. Fahmi, M. H. Mamat, A. S. Zoolfakar, A. H. A. Razak & M. Rusop. (2019). International Journal of Recent Technology and Engineering (IJRTE). ISSN: 2277-3878, 8 (4).

[25] A. Khaled, N. El-Mahallawy, M. Shoeib & M. R. A. Atia. (2019). Journal of Al-Azhare University Engineering Sector. 14 (50). 245-257.

[26] A. Amri, K. Hasan, H. Taha, M. M. Rahman, S. Herman, A. E. Awaltanova, I. wantono, H.Kabir, C.Y. Yin, Khalil, I. S. Bahri, N. Frimayanti, M. A. Hossain, & Zhong-Tao Jiang. (2019). Ceramics International.

[27] A. H. Shukor, H. A. Alhattab & I. Takano. (2020). Journal of Vacuum Science & technology. 38, 012803.

[28] B. Seddik, B. Salima, G. houda & F. Abdelhakim. (2020). Journal of Atomic, Molecular, Condensed Matter & Nano Physics. 7 (3), 145-154.

[29] Y. Zhao, J. Zhang, Y. Wang & Z. Chen. (2020). Nanoscale Research Letters. 15, 40.

[30] T. Amakali, L. S. Daniel, V. Uahengo, N. Y. Dzade, & N. H. de Leeuw (2020). Structural and Optical Properties of ZnO Thin Films Prepared by Molecular Precursor and Sol–Gel Methods. Crystals.10, 132.

[31] L. Castaneda. (2020). Biomedical Journal of Scientific & Technical Research. 31 (1), 23876-23883.

[32] A. Aktar, S. Ahmmed, J. Hossain, & A. B. Md. Ismail (2020). Solution-Processed Synthesis of Copper Oxide (CuxO) Thin Films for Efficient Photocatalytic Solar Water Splitting ACS Omega. 5, 25125−25134.

[33] F. Bayansal, O. S. ahin, & H. A. Ç etinkara (2020). Thin Solid Films. 137839.

[34] C. Yao, A. Hao, S. K. Thatikonda, W. Huang, N. Qin, & D. Bao (2020). Thin Solid Films. 137889.

[35] A. M. Laera, L. Mirenghi, G. Cassano, L. Capodieci, M. C. Ferrara, S. Mazzarelli, M. Schioppa, D. Dimaio, & A. Rizzo. (2020). Thin Solid Films. 138190.

[36] B. N. Q. Trinh, N. V. Dung, N. Q. Hoa, N. H. Duc, D. H. Minh & A. Fujiwara (2020). Solution-Processed Cupric Oxide P-type Channel Thin-Film Transistors. Thin Solid Films. 704, 137991.

[37] H. Absike, H. Labrim, B. Hartiti, M. Tahri & H. Ez-Zahraouy. (2020). Molecular Crystals and Liquid Crystals. 711 (1), 18-31.

[38] M. Sayrac & E. Sert. (2021). Journal of The Australian Ceramic Society. 58, 93-100.

[39] M. H. Kabir, H. Ibrahim & M. M. Billah. (2021). AIP Conf. Proc. 2324, 030007.

[40] L. Zhao, Z. Zhang, X. Luo, Z. Liu & Y. Zhang. (2021). Thin Solid Films. 730, 138722.

[41] E. C. Nwanna, P. E. Imoisili, S. O. Bitire & T-C. Jen. (2021). Coatings. 11 (12), 1545.

[42] M. H. Rajvee, S.V. J. Chandra, P. Rajesh Kumar, C.H.V.V. Ramana, K. Neelama, & R. S.Dubey. (2021). Biointerface Research in Applied Chemistry. 11 (5), 12761 – 12768.

[43] D. Kaya, H. S. Aydinoglu, E. S. Tuzemen & A. Ekicibil. (2021). Thin Solid Films. 732, 138800.

[44] Q. M. Al-Bataineh, A. A. Ahmad, A. M. Alasad & A. D. Telfah. (2021). Heliyon. 7, e05952.

[45] R. K. Jain, & A. Khanna (2021). CuO-doped WO3 thin film H2S sensors. Sensors & Actuators: B. Chemical 343, 130153.

[46] Z. Huang, X. Wang, F. Sun, C. Fan, Y. Sun, F. Jia, G. Yin, T. Zhou & Bo Liu (2021). Super response and selectivity to H2S at room temperature based on CuO nanomaterials prepared by seed-induced hydrothermal growth. Materials and Design, 201, 109507.

[47] B. Salah & A. I. Ayesh. (2021). Materials Chemistry and Physics. 266, 124597.

[48] P. Devi & J. P. Singh. (2021). IEEE Sensors Journal. 21 (17), 18512-18518.

[49] A. I. Ayesh & Belal Salah. (2022). Materials Chemistry and Physics. 125934.

[50] K.R. Sinju, B. Bhangare, A. Pathak, S.J. Patil, N.S. Ramgir, & A.K. Debnath. (2022). Materials Science in Semiconductor Processing. 137, 106235.

[51] A. Kumar, & R. Prajesh. (2022). Sensors and Actuators: A. Physical. 113498.

[52] M. Jiang, Z. Cheng, D. Zhao, L. Zhang & D. Xu. (2022). Transaction of Nonferrous Metals Society of China. 32, 1589-1597.

[53] X-y. Shen, Y-x. Huang, H-m. Shao, Y. Wang, Q. Han, J-i. Chen, B-c. Li & Y-c. Zhai. (2022). Transaction of Nonferrous Metals Society Of China. 32, 3149-3162.

[54] T. Chommaux, P. O. Renault, D. Thiaudiere, P. Godard, F. Paumier, T. Girardeau, S. Hurand & PH. Goudeau. (2022). Thin Solid Films. 741, 139035.

[55] E. Guaus & T. Burgues. (2022). Thin Solid Films. 747, 139145.

[56] S. Bakhtiarnia, S. Sheibani, A. Billard, E. Aubry & M. A. P. Yazdi. (2022). Transaction of Nonferrous Metals Society of China. 32, 957-971.

[57] A. Alagh, F. E. Annanouch, K. A. Youssef, C. Bittencourt, F. Guell, P. R. Martinez-alanis, M. Reguant & E. Liobet. (2022). Sensors and Actuators: B. Chemical. 364, 131906.

[58] X. Ning, D. Tang & M. Zhang. (2022). Nano Materials Science. 4, 376-382.

[59] A. Al-Sarraj, B. Salah, A. I. Ayesh, K. M. Saoud, A. A. E. Mel, A. U. Rehman, A. Bermak & Y. Haik. (2022). Sensors and Actuators: A. Physical. 333, 113256.

[60] H. R. Shwetha, S. M. Sharath, B. Guruprasad & S. B. Rudraswamy. (2022). Micro and Nano Engineering. 16, 100156.

[61] G. Lei, Z. Li, G. Lu, J. Hu, H. Shang, X. Zhang, X. Liu, J. Zhang & X. Guo. (2022). Journal of Materiomics. 8, 408-416.

[62] J. A. Oke & T-c. Jen. (2022). Journal of Materials Research and Technology. 21, 2481-2514.

[63] M. Shkir, A. B. G. Trabelsi & F. H. Alkallas. (2022). Journal of Material Research And Technology. 20, 4556-4565.

[64] C. Li, P. G. Choi, K. Kim & Y. Masuda. (2022). Sensors and Actuators: B. Chemical. 367, 132143.

[65] J. Chang, C. Qin, W. Guo, L. Zhu, Y. Zhang, Y. Wang & J. Cao. (2023). Sensors and Actuators B: Chemical. 385, 133633.

[66] A. M. Al-Faouri, O. A. Lafi & H. H. Abu-Safe. (2023). Arabian Journal of Chemistry. 16, 104535.

[67] M. Imran, G. Asghar, G. H. Tariq, A.W. Faridi, S. Bano, M. S. Shifa & S. Ullah. (2023). Results in Optics. 10, 100331.

[68] A. K. Vishwakarma, A. K. Sharma, A. K. Mishra & L. Yadava. (2023). Materials Letters: X. 17, 100184.

[69] S. R. Sriram, S. R. Parne, N. Pothukanuri & D. R. Edla. (2023). Applied Surface Science Advances. 15, 100411.

[70] F. O. Oluyemi, E. D. Ogunmola & A. A. Ajayi. (2023). Results in Optics. 11, 100416.

[71] K. Rajesh, N. Pothukanuri, S. G. Dasari & M. V. R. Reddy. (2023). Journal of Alloys And Metallurgical Systems. 2, 100009.

[72] D. Rajkumar, H. Umamahesvari & P. Nagaraju. (2023). Results in Chemistry. 5, 100946.

[73] G. Mamtmin, P. Nizamidin, R. Abula & A. Yimit. (2023). Chinese Journal of Analytical Chemistry. 51 (7), 100260.

[74] A. Amiri, L. Arab, A. Meftah & A. Latif. (2023). Results in Optics. 11, 100426.

[75] M. F. Naief, S. N. Mohammed, Y. N. Ahmed, A. M. Mohammed, S. N. Mohammed & S. N. Mohammed. (2023). Results in Chemistry. 5, 100924.

[76] V. Kumar, J. Prakash, D. Pathak, D. P. Sharma, L. P. Purohit & H. C. Swart. (2023). Chemical Engineering Journal Advances. 15, 100501.

[77] J. G. Cuadra, S. M. Prados, G. M. Vega, A. C. Estrada, T. Trindade, C. Oliveria, M. P. Seabra, J. Labrincha, S. Porkar, R. Cadena, D. Fraga & J. B. Carda. (2023). Applied Surface Science. 617, 156619.

[78] V. A. Owoeye, S. A. Adewinbi, A. O. Salau, A.N. Orelusi, A. E. Adeoye & A. T. Akindadelo. (2023). Heliyon. 9, 13023.

[79] S.K. J. Vijitha, K. Mohanraj & R.P. Jebin (2023). Chemical Physics Impact. 6, 100143.

[80] K. Hosomi, W. Inami & Y. Kawata. (2023). Results in Surfaces And Interfaces. 11, 100105.

[81] K. C. Nwambaekwe, V. P. Batir, L. Dermenji, N. D. Curmei. (2023). Material Chemistry and Physics. 301, 127594.

[82] B. Du, W. Kang, Y. He, Y. Wang, X. Yang, G. Meng, Z. Zhu, X. Lin, Y. Tan, C. Liang, X. Guo, J. Jian, Y. Guo & M. Zhou. (2023). iScience. 26 (4), 106387.

[83] M. W. Van de Putte & M. Huijben. (2023). Applied Surface Science. 623, 157034.

[84] G. V. A. Reddy, K. N. Kumar, R. Naik, V. Revathi K. M. Girish & K. Munirathnam. (2023). Applied Surface Science. 16, 100417.

[85] S. Rani, M. Kumar, P. Garg, R. Yadav, Y. Kumar, A. Kumar, B. Govind, U. Deshpande, S. Hausale & V. N. Singh. (2023). Journal of Science Advanced Materials and devices. 100583.

[86] K. N¸ecek, Z. Starowicz, J. Wo´zny, P.M. Nuckowski, M. Musztyfaga-Staszuk & P. Panek. (2023). Molecules. 28, 7324.

[87] M. Abdelfatah, N. Darwesh, M.A. Habib, O.K. Alduaij, A. El-Shaer & W. Ismail. (2023). Nanomaterials. 13, 1272.

[88] A. M. Al-Fa'ouri, O. A. Lafi, Hu. H. Abu-Safe & M. Abu-Kharma. (2023). Arabian Journal of Chemistry.16, 104535.

[89] K. ElKhamisy, H. Abdelhamid, El-S. M. El-Rabaie, N. Abdel-Salam. (2024). Plasmonics. 19, 1–20.

[90] A. M. Oni, A. S.M. Mohsin, Md. M. Rahman & M. B. H. Bhuian. (2024). Energy Reports 11, 3345–3366.

[91] D. Motai & H. Araki. (2024). Materials. 17, 692.

[92] Bertolli M (2008) Solar cell materials. Course: Solid State II. Dep. Physics, Univ. Tennessee, Knoxv.

[93] Sze SM, Li Y, Ng KK (2021) Physics of semiconductor devices. John Wiley & Sons

[94] F.J. Arregui. (2008). Sensors Based on Nanostructured Materials. Berlin Springer.

CHAPTER 3

GROWTH AND CHARACTERIZATION OF PURE CuO THIN FILMS.

In this chapter, we present the synthesis and characterization of pure CuO thin films for solar cell and gas sensing applications.

3.1 Introduction

CuO have monoclinic crystal structure with C2/c space group and lattice parameters a = 4.6837 Å, b =3.4226 Å and c = 5.1288 Å [1]. In recent years, the electrical, optical and mechanical properties of copper oxide films have found number of applications in technological areas. Semiconducting thin films of CuO have been prepared by using number of techniques such as evaporation, sputtering and many more. The dependence of electrical resistivity of a semiconducting oxide films particularly copper oxide layers on external atmosphere is well known phenomena. It is this property of CuO films which has tremendously exploited for the fabrication of solid-state gas sensor [2-4].

Utilizing the straightforward and affordable sol-gel spin coating process, thin layer is deposited which affects the thickness of films on varying the spinning speed. Precursor solution, which is used for depositing is very essential and it affects the properties of a thin film. The nature of the precursor, type of salt (nitrate, halide, etc.), the volume of the solvent and concentration will critically affect the physical characteristics of the thin films. When a sol- gel come out from the dropper, the fine droplets put at center of substrate which is placed in spin coater. After applying few rpms, the droplets reached to the surface of the substrate and expand homogenously on substrate by using principle of centrifugal force. The volume and momentum of the droplet determine its size and form [5-8].

No of gases existed in the air in low quantity in the range of ppm also harmful to the atmosphere in addition to the effect on human health [9]. H_2S gas is very dangerous due to its corrosive and explosive nature [10]. When hydrogen sulphide gas come in contact of water then acidic solution form which create corrosion in pipeline and may result in failure of structure [11]. The sources of production of this gas are paper mills, oil-field and power station, tannery, water sewages and also through food processing [12]. Sensors synthesized from metal oxide semiconductors sensitively respond to various gases by providing the change in conductivity [13]. The various gas sensors synthesized by both p-type and n-type metal oxides are ZnO [14-15], In_2O_3 [16-17], SnO_2 [18], CeO_2 [19], WO_3 [20], NiO [21]. CuO is an exceptional promoter

of H_2S sensing owing to its conversion from p-type semiconducting CuO to CuS. This conversion of CuO makes it a degenerate semiconductor due to ion vacancies (Cu or S) [22-23].

Recognition of these toxic gases in the atmosphere is an essential task due to their intricate behavior. Therefore, considerable thoughtfulness has been specified by the scientific society to design and improve gas sensors with the best quality for the sensing of these gases.

Various precursors have been utilized by different researchers across the world. Commonly, distilled water or de-ionized water will be used as an ideal solvent in this technique. In general, the thin films which are deposited at low spinning speed will be thickest, while at high spinning speed, films with lesser thickness was observed. As a result, altering the deposition conditions allows for customization of the produced thin film's structural characteristics and crystallinity. The impact of these deposition parameters on structural, morphological properties of CuO thin films are systematically discussed.

3.2 Chemicals Used

Highly pure stannous chloride di-hydrate ($SnCl_2.2H_2O$), Copper acetate dehydrate (Cu ($CO_2CH_3)_2 \cdot 2H_2O$), isopropyl alcohol, polyethylene glycol $HO(C_2H_4O)_nH$, ethanol (C_2H_5OH), acetone (C_2H_6CO) and di-ethanloamine have been purchased from Sigma-Aldrich. All the chemicals have been used as received. Deionized water used in the experiments has been purified by a millipore simplicity, water purification system.

3.3 Preparation of Substrate

The substrate serves as the framework for the thin film components. The substrate's characteristics have a big impact on how well the device works. In this experiment, a diamond cutter was used to cut a glass slide into a 2×2 cm square. All substrates were sterilized in an acidic solution consisting of nitric acid, acetone, methanol, and de-ionized water in order to achieve nice and clean surfaces.

3.4 Cleaning of Glassware

The borosilicate glassware (flasks, measuring cylinders and beakers) and corning glass materials used for the experiments were washed with laboratory detergent teepol solution and with distilled water.
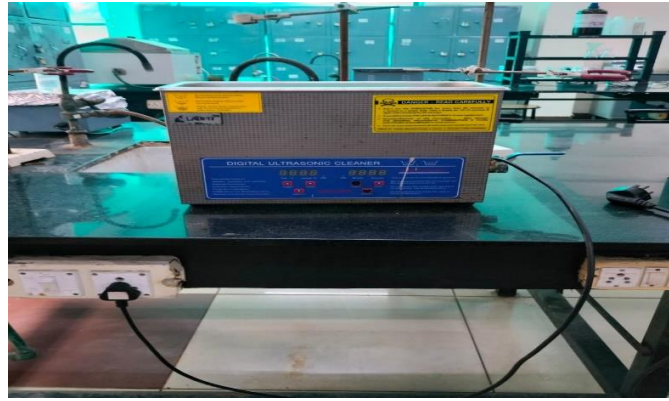
Figure 3.1 The ultrasonic cleaner

For chemical cleaning the substrates were treated with dilute alkaline solution of NaOH and later with dilute nitric acid. The glassware was then washed with distilled water and then finally ultrasonically cleaned in isopropyl alcohol using an ultrasonic cleaner. The cleaned glass substrates were kept in desiccator for further use.

3.5 Experimentation for synthesis of nanostructured CuO thin films

Nanostructured thin films of CuO have been fabricated by non-aqueous sol gel method using copper acetate dehydrate and iso-propyl alcohol as precursors. The deposition system for copper oxide thin films used for this study is shown in below figure.

Figure 3.2 The above figure shows the spin coater for fabrication of thin films.

Spin coating [24-25] is a process which is used for depositing thin films on the metal substrate. In this method, very few amounts of the material which is to be coated is applied on middle of the substrate, after which quickly rotate the substrate at 1000 times of rpm. This material is spread by centrifugal process and the thin films are formed at the surface of the substrate. Spin coating process have followings stages: -

❖ Deposition of coating material on the substrate.
❖ Substrate is rotated with constant speed and the thickness of the films is measured by viscous force. Substrate is accelerated so that coating material is spread uniformly on it [26-27].
❖ Solvent is evaporated and a thin fluid layer develops at the substrate.

A typical spin process entails four steps: a high-speed spin step to thin the fluid, a drying stage to remove extra solvents from the film and a dispense step in which the solution fluid is applied to the substrate surface. Vacuum is then used to hold the substrate securely. There are two typical distribution techniques. One is Static dispense and another is Dynamic dispense.

Simply placing a little quantity of fluid on the substrate's center or close to it is known as static dispensing. Depending on the solution's viscosity and the size of the substrate, it can be anywhere between 1 and 10 cc. Generally speaking, a larger puddle is needed to achieve complete covering of a larger substrate or one with a higher viscosity.

The method of dispensing while the base material is moving slowly is known as dynamic dispense. This stage of the operation typically uses a speed of 500 rpm. This is a useful technique because it may fill any gaps that may arise even if the fluid or substrate itself has poor wetting properties. For the substrate to accelerate sufficiently after the dispensing process in order to achieve the necessary film thickness.

In the spin coating process, vacuum is crucial. Vacuum must be produced using a vacuum pump. It firmly retains the substrate, preventing it from slipping. It firmly retains the substrate during spinning, protecting the sample from any form of fracture.

For this stage, typical spin speeds vary from 1500 to 3000 rpm. This process might take ten seconds or several minutes. In general, thinner films are produced by greater spin speeds and longer spin times. The amount of radial (centrifugal) force given to the liquid solution as well as its velocity depend on the substrate's speed (rpm). The ultimate film thickness is typically determined by the high-speed spin stage. At this point, very small fluctuations of 50 rpm can result in a 10% difference in thickness. Programming is able to control it.

The characteristics of coated films can also be impacted by the substrate's acceleration toward the ultimate spin speed. It's crucial to precisely manage acceleration because during the initial portion of the spin cycle, the solution starts to dry. The substrate surface has to be smooth for a coat to adhere evenly [28-30].

3.6 Preparation of Sol-gel

To prepare CuO solution by sol-gel process, copper acetate dehydrates, di-ethanolamine, iso-propanol and poly ethylene glycol were used as materials. Copper acetate dehydrates and iso-propanol have been used as starting precursors for sol-gel synthesis. For preparation of precursor solution calculated amount of $Cu\ (CO_2CH_3)_2.2H_2O$ is dissolved in 9 ml of iso-propanol for obtaining a solution of different concentration. The mixture is stirred for 15 mins on hot plate cum magnetic stirrer at room temperature in a closed vessel for initial dissolution. Then 0.5ml of di-ethanolamine was added to the solution and stir again for 15 minutes. Finally, 0.5 ml of polyethylene glycol added to solution and continuously stir for half hour and we obtain a transparent dark blue solution of required molarity.

Solution of two different concentration i.e. 0.75M and 1M were prepared by dissolving 0.75g and 1g copper acetate dehydrate respectively in isopropanol. A dark blue solution of 0.75M and 1M (called as sol-gel) without any suspension of particles were obtained after 2hr and 4hr respectively.

3.7 Fabrication of Thin films

Thin films of CuO have been fabricated for conducting electrical, solar cell and gas sensing studies.

Figure 3.3 The muffle furnace used for annealing of thin films.

For this sol-gel of different molar concentrations was prepared. A few drops of this sol-gel are then deposited onto pre-cleaned glass substrates. To ensure that the paste is distributed evenly, the films are then spun over substrates made of glass using a spin coater for 10s at 1500–3000 rpm. Coated substrates are subjected to heat treatment which is required to evaporate the binder and convert the applied solution into a dense inorganic film. Thermal annealing at 400°C for two hours has been performed on freshly produced CuO thin films.

To avoid quick cooling fractures, films have been kept inside the furnace until room temperature is reached. The block diagram representing the step wise approach to deposit CuO films by utilizing the sol-gel spin coating method in various laboratory conditions is shown as below.
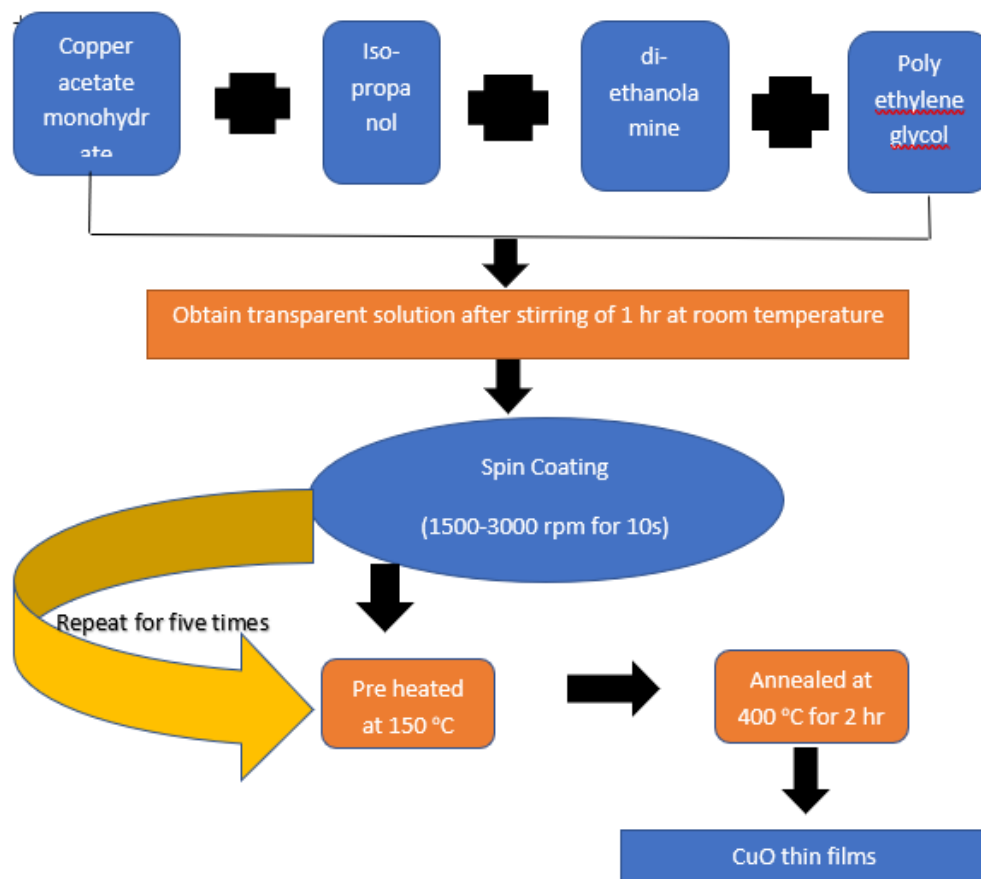
Figure 3.4 Procedure of synthesis of thin films.

In this way, number of samples of different thickness were synthesized by changing the spinning speed and molar concentration of solution. These samples are shown by given table.

Table 3.1The prepared samples (thin films of pure CuO)

Concentration of prepared solution	Name of sample	Spinning speed (RPM)	Deposition temperature	Thickness (nm)
0.75M	0.75M1	3000		239
	0.75M2	3500		115
	0.75M3	4000		89
	0.75M4	4500		75
	0.75M5	1500		470
	0.75M6	2000	400ºC	370
	0.75M7	2500		157
1M	1M1	2500		378
	1M2	2000		411
	1M3	1500		435
	1M4	1000		721

3.8 Characterization of CuO thin Films

Several methods were utilized to characterize the films' thickness, structure, morphology, optical properties, and electrical properties; these methods are discussed below.:

3.8.1 Thickness Measurement

In this work, thickness of some samples was measured by cross-sectional SEM and thickness of some sample was measured by gravimetric method. Even though it necessitates a certain level of attention and physical dexterity on the side of the operator, the cross-section technique is widely used and rather straightforward to apply. It involves dividing the sample in half and looking at it transversely along the layer profiles that need to have their thicknesses measured. As a result, this method enables accurate ruler-based direct measuring of the film's thickness.

The whole analysis procedure is divided into three stages: sample preparation, microscopic examination and data processing using specialized software to scale the picture dimensions from pixels to length. [31-32].

Cross-section SEM analysis was used to look into the thickness of CuO films (0.75M1-0.75M4). Thickness of films analysed from cross section SEM which is stated as below.
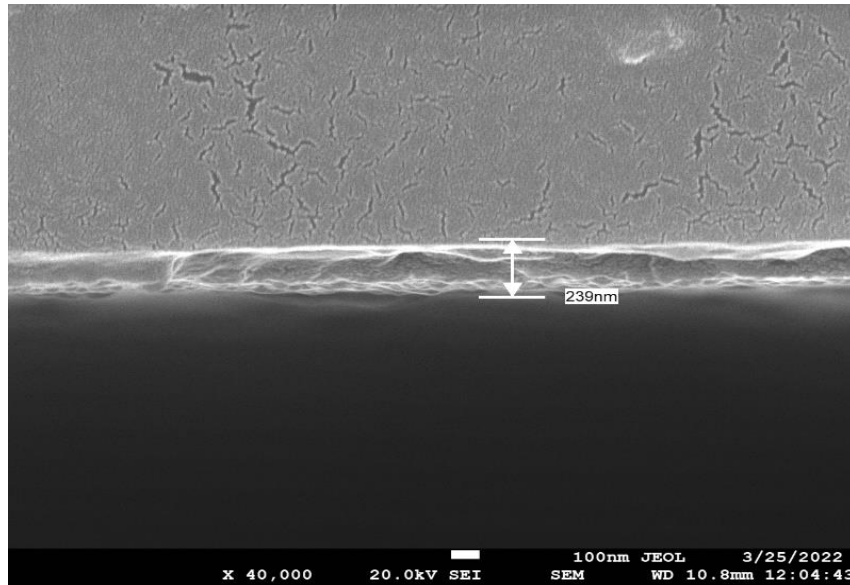
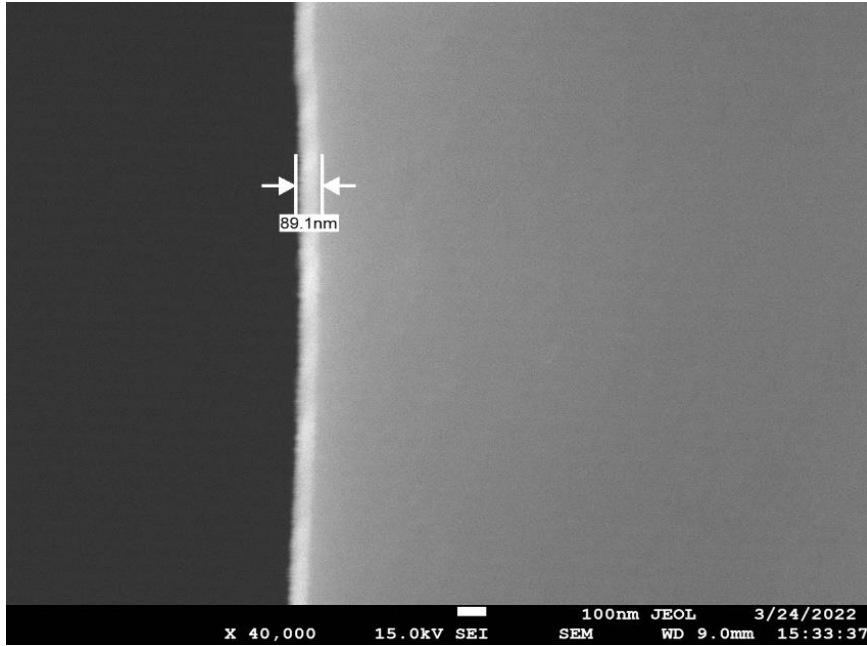Figure 3.5 (a) Cross-section SEM of sample 0.75M1.
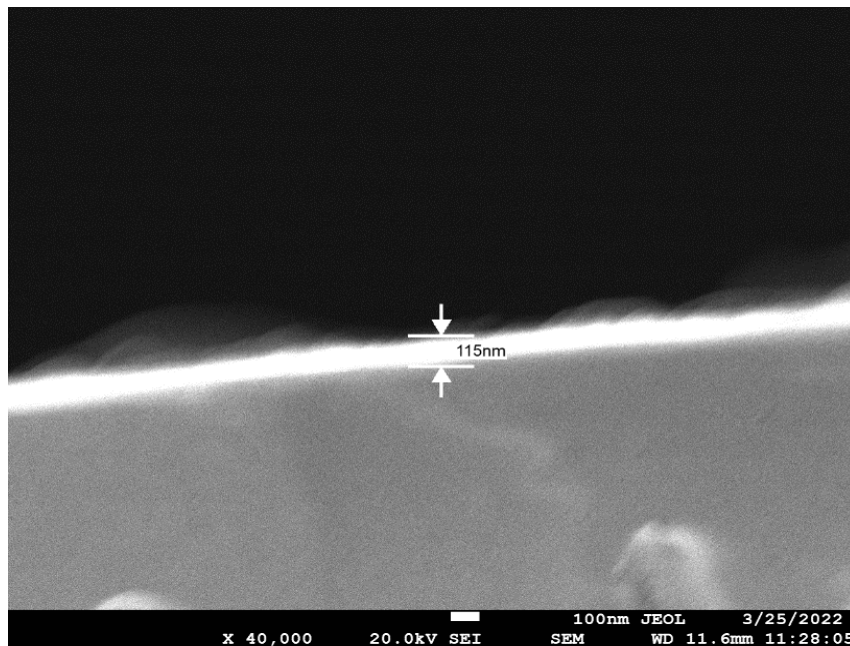
Figure 3.5 (b) Cross-section SEM of sample 0.75M2.

Figure 3.5 (c) Cross-section SEM of sample 0.75M3
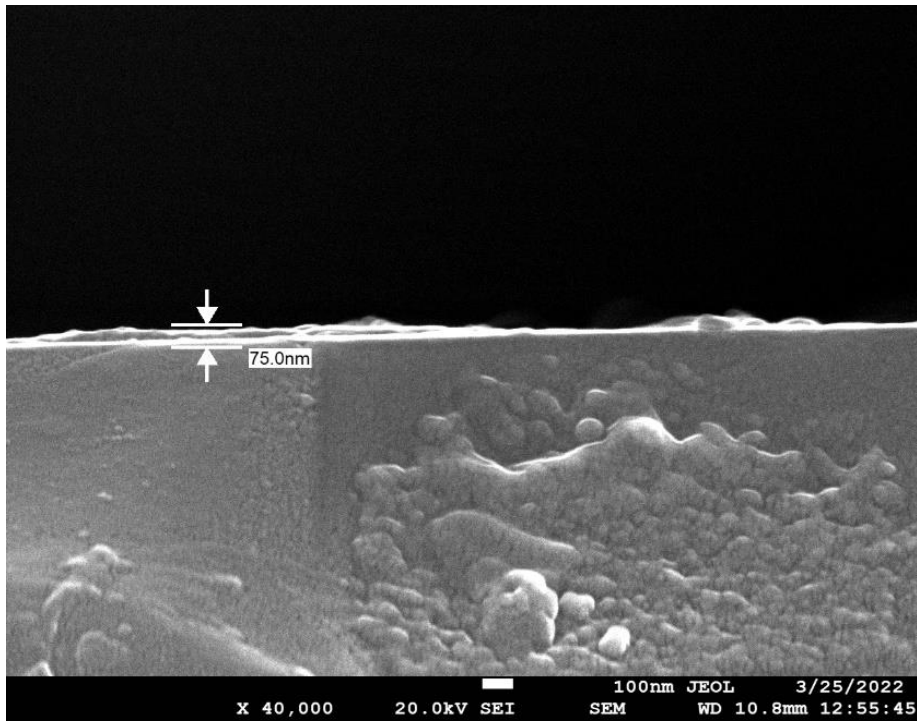
Figure 3.5 (d) Cross-section SEM of sample 0.75M4.

To obtain the thickness of remaining samples, weight difference technique was used. The weight difference method is given by the following relation (3.1), [33-34].

$$t = \frac{W2 - W1}{\rho \times A} \quad (3.1)$$

Where t is thickness of films, ρ is density i.e. 6.31g cm^{-3}, A is the area, w_1 and w_2 are the weight of substrate before and after deposition of material.

3.8.2 Structural properties

The XRD pattern of deposited CuO films at variable spinning speed (between 1000rpm to 4500 rpm) and annealed at 400°C for 2hr was taken out. The 2Θ value was adjusted from 20 to 80 degrees while the diffractometer reflections were recorded at room temperature. The XRD pattern is used to assess the structural properties of each CuO film that has been deposited. The following formulae are used to compute the size of crystallite, lattice strain, dislocation density, and number of crystallites:

The crystallites size was calculated from Debye Scherer's formula which is given as below equation (3.2) [35]:

$$D = \frac{K \times \lambda}{\beta \times \cos\Theta} \quad (3.2)$$

The strain is equal to the slope of the plot of β cos (θ) / λ vs. sin (θ) / λ of different peaks. Strain is given by equation (3.3) [36]

$$\varepsilon = \frac{\beta \times \tan\Theta}{4} \quad (3.3)$$

The dislocation density (δ) is calculated using this equation

$$\delta = \frac{1}{D^2} \quad (3.4)$$

Where β stand for FWHM (full width at half maximum) of diffraction peaks.

θ and δ is used for the Bragg angle and dislocation density respectively.

λ and D denote the wavelength of the used X rays and crystallite size respectively [37-38].
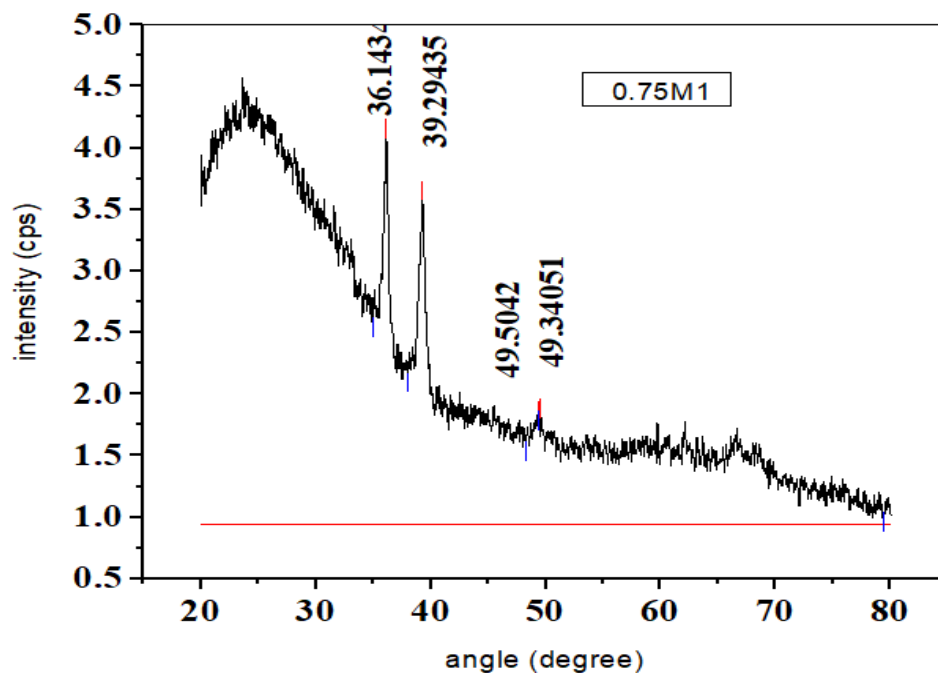
Figure 3.6 (a) XRD pattern of 0.75M1 sample of thickness 239nm.
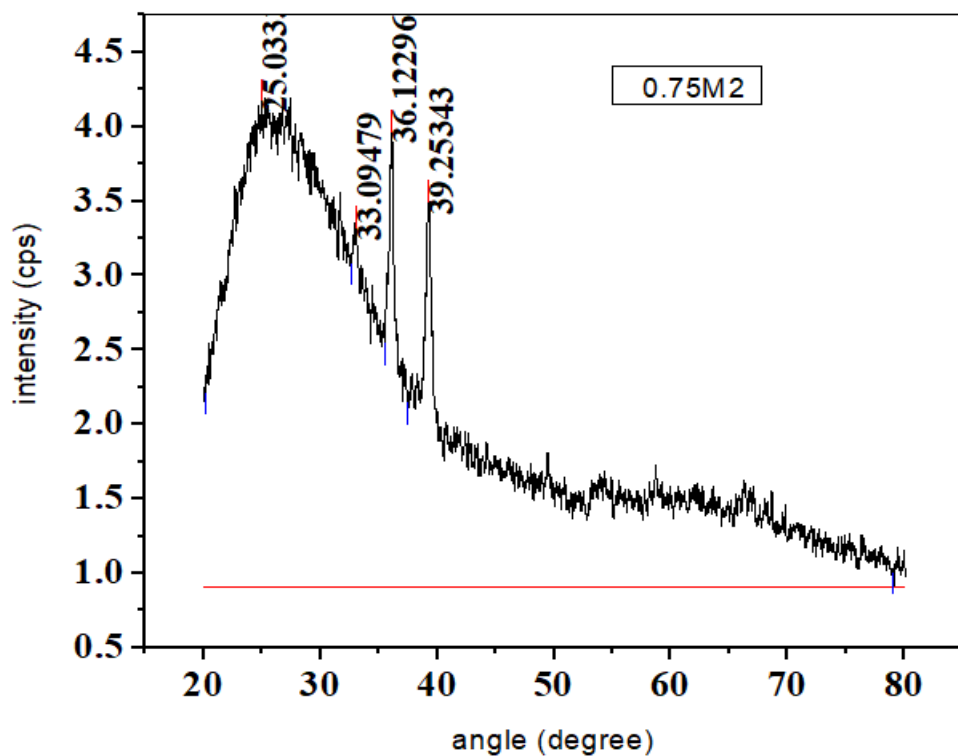
Figure 3.6 (b) XRD pattern of 0.75M2 sample 0.75M of thickness 115nm.
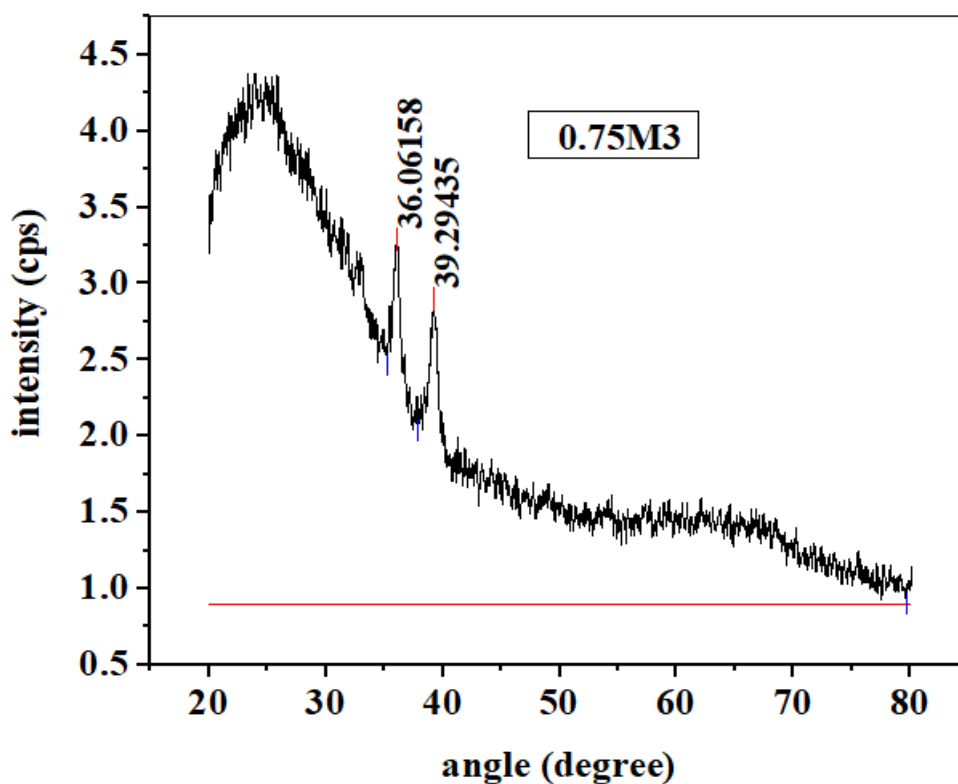

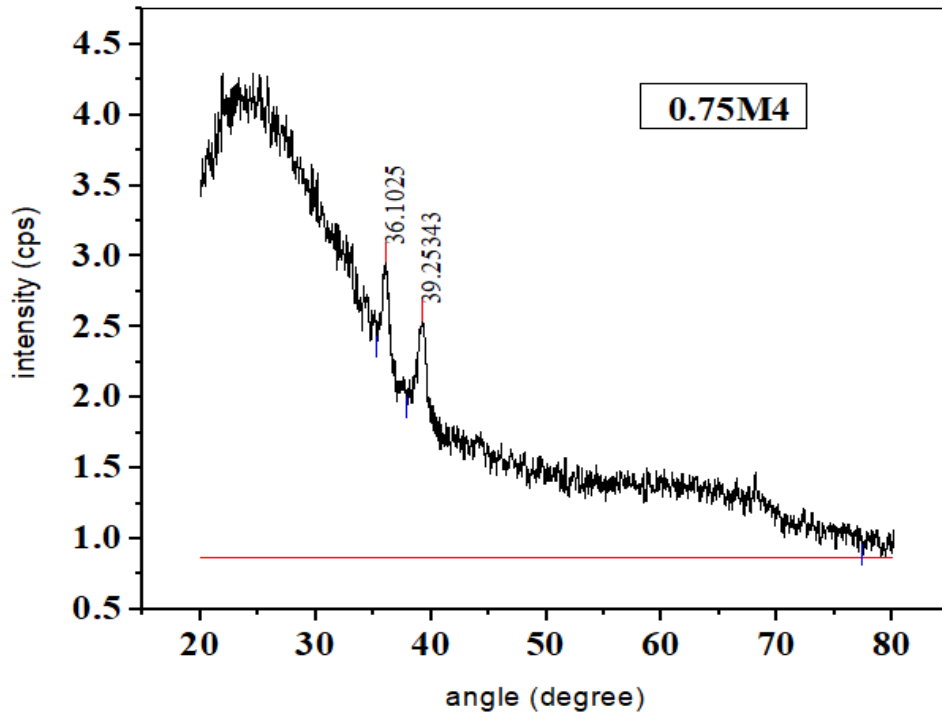Figure 3.6 (c) XRD pattern of 0.75M3 sample of thickness 89nm.

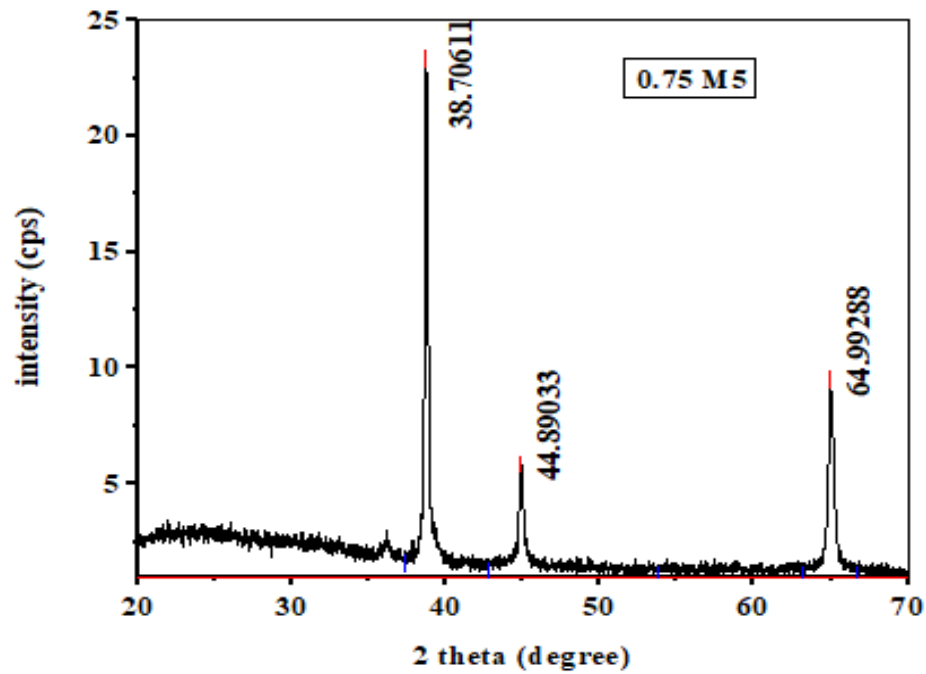Figure 3.6 (d) XRD pattern of 0.75M4 sample of thickness 75nm.

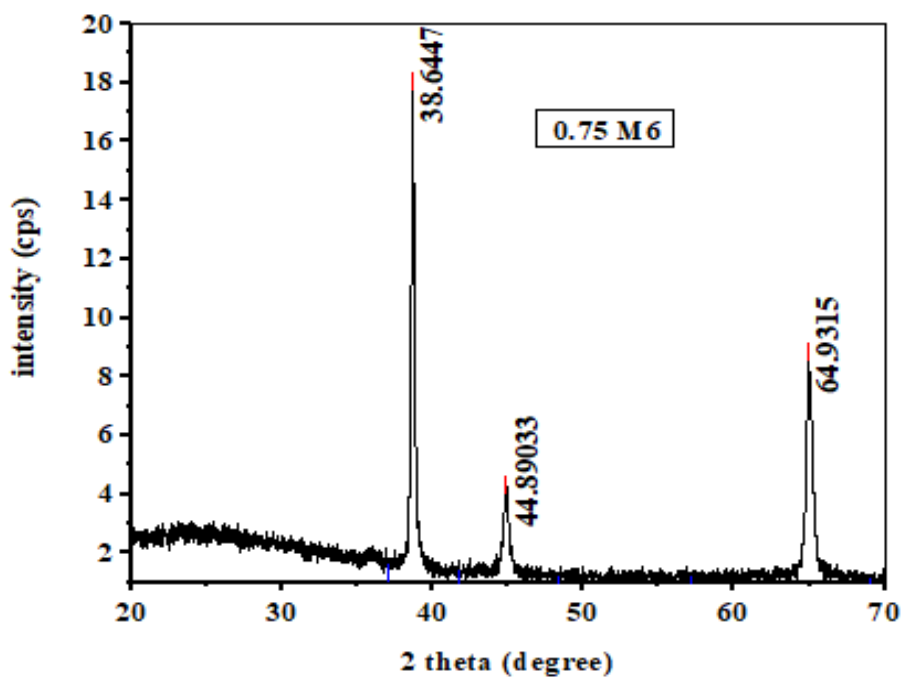Figure 3.6 (e) XRD pattern of 0.75M5 sample of thickness 470nm.

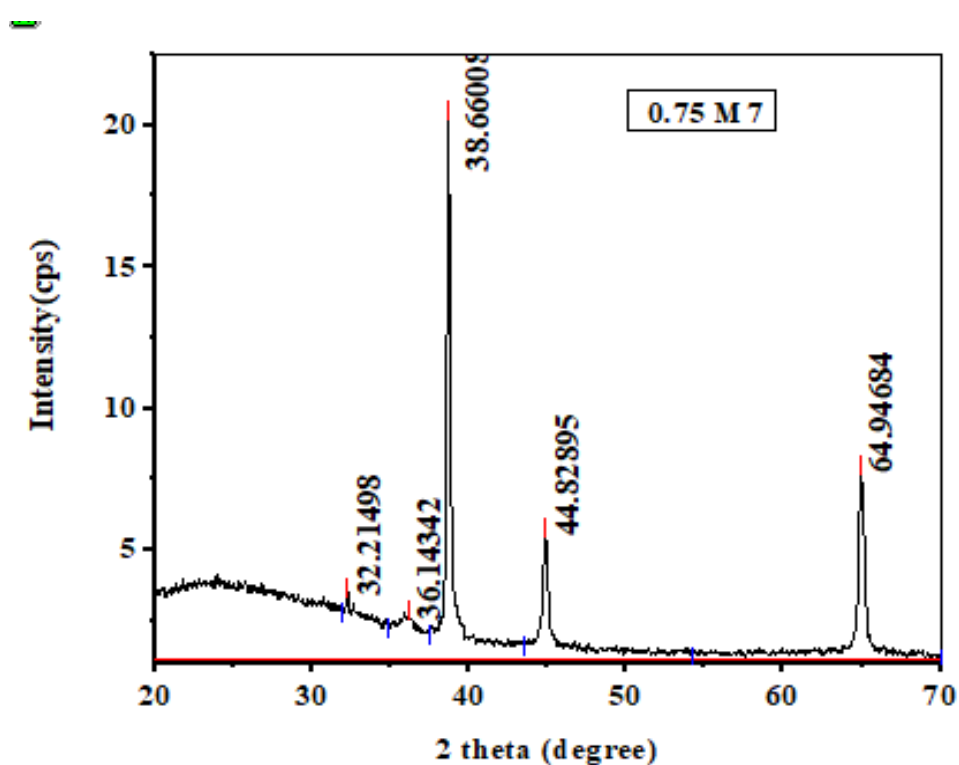Figure 3.6 (f) XRD pattern of 0.75M6 sample of thickness 370nm.

Figure 3.6 (g) shows the XRD pattern of 0.75M7 sample of thickness 157nm.

In figure 3.6 (a) – (g), the distinct films of 0.75M concentration, XRD diffraction patterns have been reorganized. It is evident how changing spinning speed affects thickness on the films, indicating how sensitive this parameter is to the structural characteristics of the films. When

compared to typical JCPDS values (80-0076), the samples' XRD patterns exhibit a fine crystalline structure with distinct peaks of the monoclinic CuO phase. The fact that the as-prepared films are polycrystalline may be seen from minor characteristics of other atomic planes that are located at large diffraction angles. For all of the produced films of varying thickness, the diffract-grams reveal notable (200) and (111) atomic planes situated at 2 values of 36° and 38.6°.

Figure 3.6.2 (a) to (d) analysis revealed that the produced films are polycrystalline in nature, and the pure phase of CuO films was recognized. When compared to other films, it can be seen that the film produced at 4500 rpm has the highest crystallinity. As the spinning speed rises, the peak at 36.14° becomes more intense. Applying the Debye-Scherrer relation revealed that crystallite size decreased as spinning speed increased [34, 35]. Other structural parameters also calculated by using equation (3.2) to eq. (3.4) which is given by below table

Table 3.2 The structural parameters of sample 0.75M1 – 0.75M4.

Name of sample	Thickness (nm)	Spinning speed (rpm)	Crystallite size (nm)	Strain (m)	Dislocation density (10^{16} m^{-2})
0.75M1	239	3000	6.95	0.00515	2.073
0.75M2	115	3500	6.13	0.00698	2.661
0.75M3	89	4000	3.77	0.00983	7.035
0.75M4	75	4500	3.28	0.01059	9.295

As the spinning speed is greater than the fluid's rate of spin-off, CuO thin films crystallize more effectively at the sample's surface. As the thickness grows, the width reduces, which causes the reduction in lattice imperfections. As a result, size of the crystallites increase and microstrain decrease [39- 43].

It was observed from the figure 3.6 (e)- (g) that there were many reflection peaks identified from XRD pattern with strong intensity at 38.7° and low intensity peak at 32.21°, 36.14°, 44.89° and 64.93° associated with plane (200), (110), (-111), (-112) and (-312) respectively confirmed from the JCPDS card no – 05-0661. The micro structural parameters such as crystallite size (D), micro strain (ε) and dislocation density (δ) were calculated and shown by given table

Table 3.3 Structural parameters of CuO films, 0.75M5 – 0.75M7.

Name of sample	Thickness (nm)	Spinning speed (rpm)	Crystallite size D (nm)	Micro strain ε (m)	Dislocation density δ (10^{15}m^{-2})
0.75M7	157	2500	18.14	0.0048	3.03
0.75M6	370	2000	25.09	0.00147	1.58
0.75M5	470	1500	27.48	0.00132	1.32

It was noted from the calculated parameters that crystallite size goes on increasing as the thickness of films increasing. This is due to the reason as we increase thickness, dislocation density and strain decrease which improves the high quality of thin films (more regular will be the crystalline structure when imperfection is decrease) and consequently increase the size of crystallite size. Similar type of result (variation of crystallite size with thickness of prepared films) has been reported by literature [44]. The results of obtained dislocation density agree well with findings of literature [45].
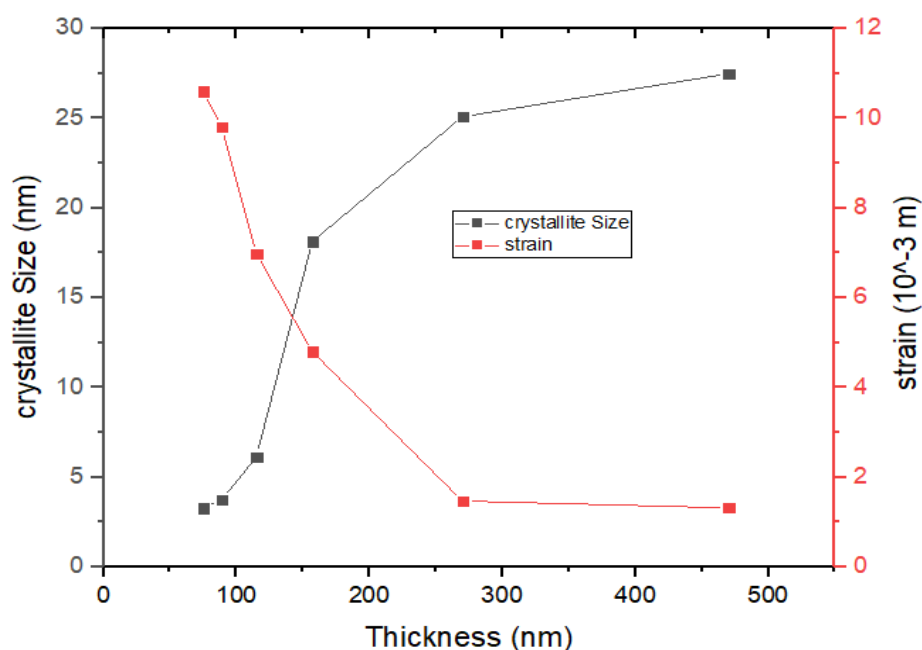
Figure 3.7 The variation of crystallite size and strain with thickness of sample.

Following is an illustration of the XRD pattern of a sample made from a solution at a single molar concentration employing the sol-gel spin coating technique with spinning at various speeds. According to the JCPDS file [89-5899], it was clearly determined from XRD data that CuO exhibits a monoclinic phase with lattice parameters of a = 4.689 Å, b = 3.420 Å c = 5.130

Å, and = 99.57º. Different XRD peak at 36.15, 38.76, 44.92 and 65.31º were assigned to (002), (111), (200) and (220) planes respectively. It was observed from the graph that obtained peaks are sharp and peak intensity is large at (111) plane which confirm that obtained films have good crystallinity.
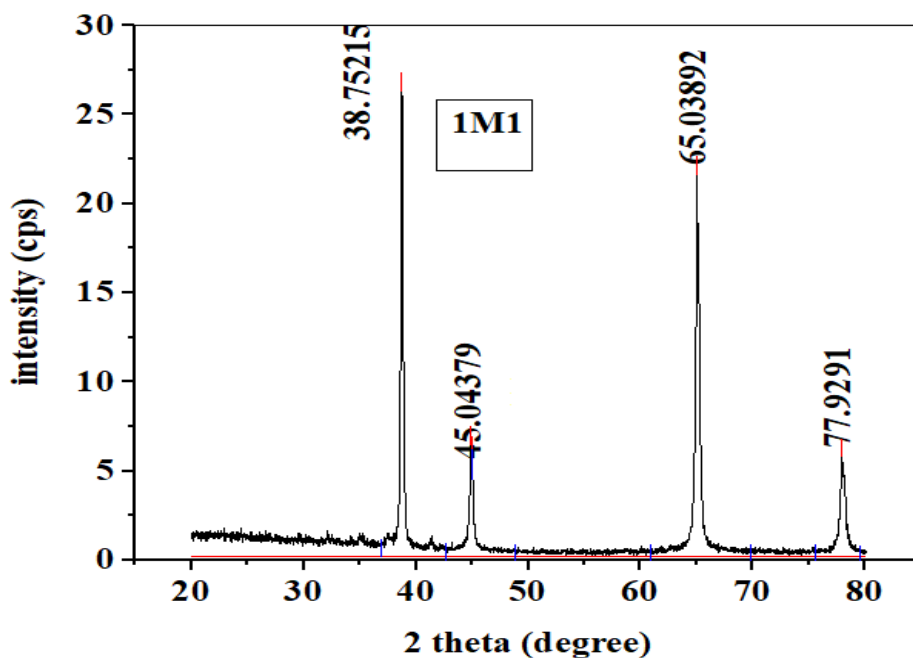

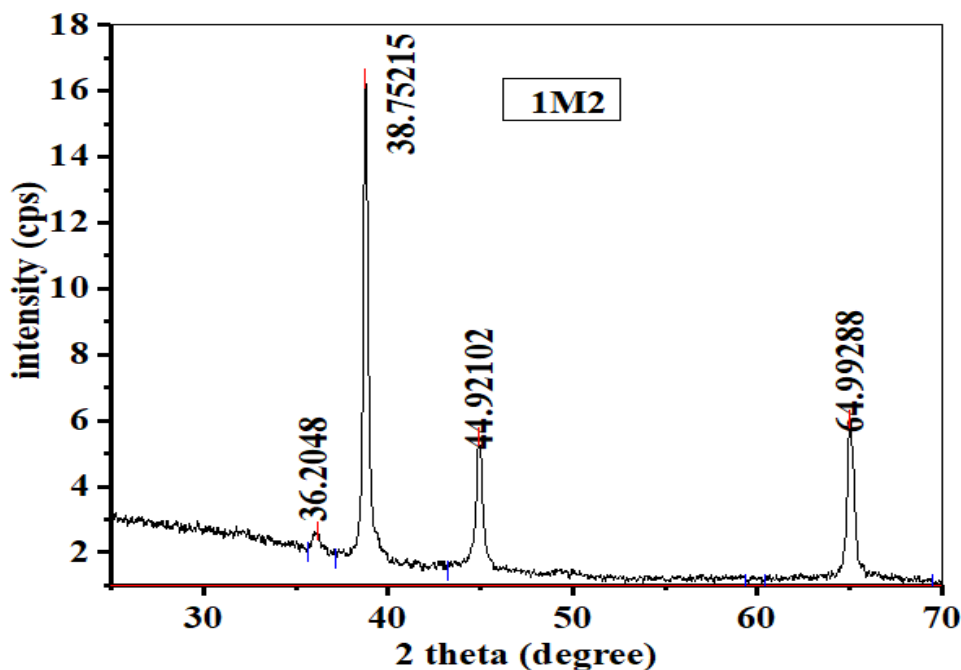Figure 3.8 (a) XRD pattern of 1M1 sample of thickness 378nm.

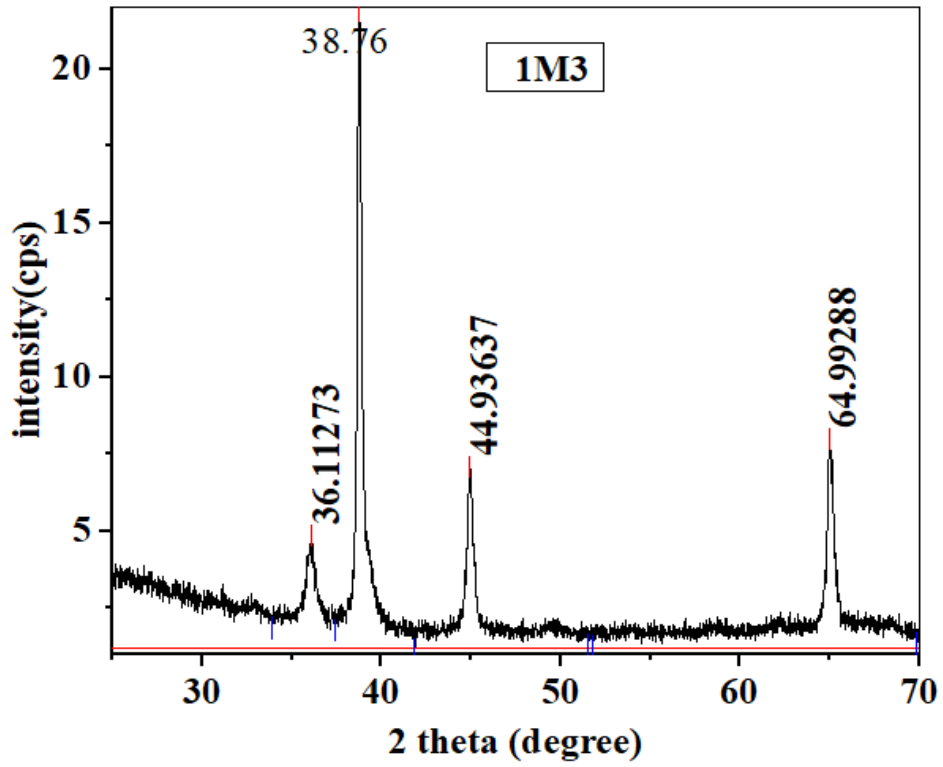Figure 3.8 (b) XRD pattern of 1M2 sample of thickness 411nm.
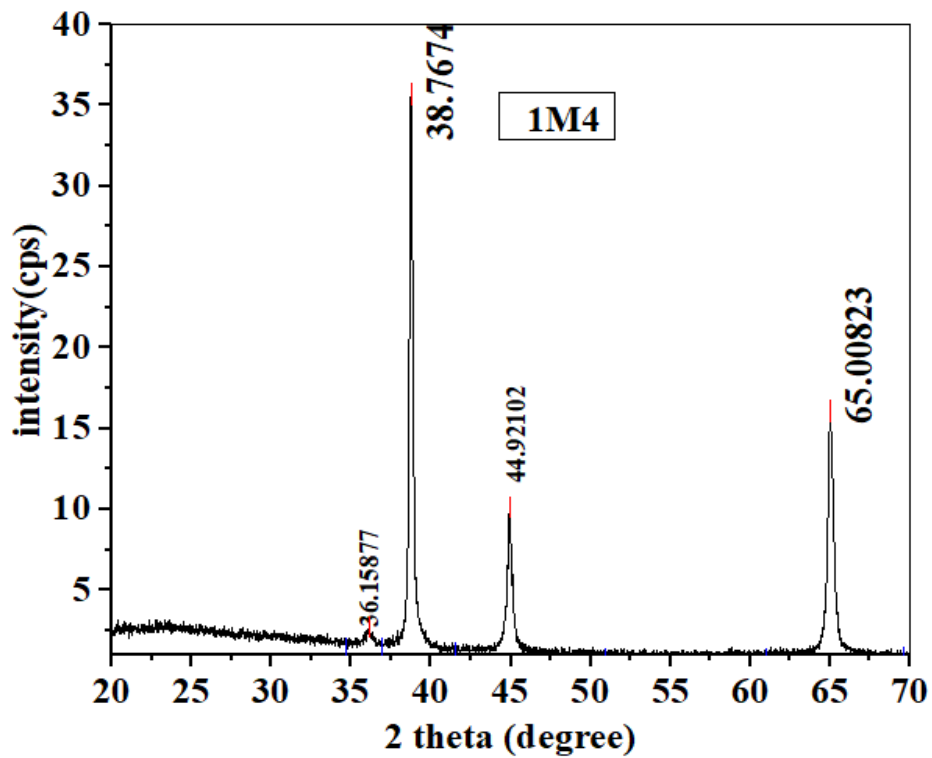
Figure 3.8 (c) XRD pattern of 1M3 sample of thickness 435nm.

Figure 3.8 (d) XRD pattern of 1M4 sample of thickness 721nm.

Table 3.4 Structural parameters of CuO films, 1M1 – 1M4.

Name of sample	Thickness (nm)	Spinning speed (rpm)	Crystallite size D (nm)	Dislocation density δ (10^{15}m^{-2})
1M1	378	2500	10.18	9.64
1M2	411	2000	19.64	2.59
1M3	435	1500	21.14	2.23
1M4	721	1000	23.29	1.84
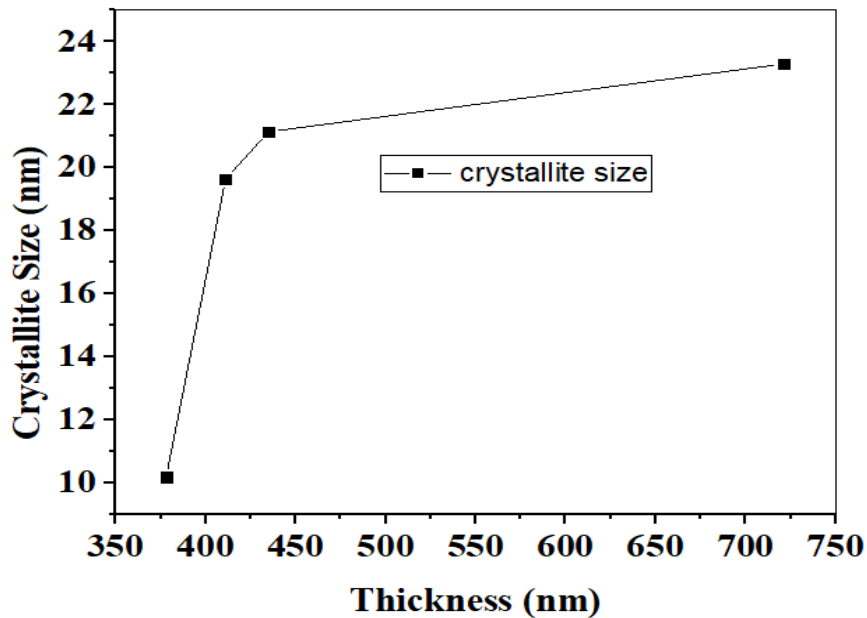
Figure 3.9 The variation of crystallite size with thickness of sample.

From this graph, it was observed that crystallite size gets increase as thickness increase. As the thickness increases, dislocation energy decreases which shows that there is more regular crystalline structure occur because of reduction of number of imperfections [46].

In the XRD pattern of films of 1M concentration formed at various spinning speed, we note that no peak due to Cu_2O has been seen. Although it has seen from the literature that spray-deposited CuO films contain both the CuO and Cu_2O phases [47-48]. It is significant to note that copper oxide thin films with a predominant CuO phase have been successfully produced with spinning speeds of 1000–4500 rpm. According to analysis, the spinning speed should range from 1000 to 3000 rpms in order to produce pure crystalline films of CuO.

3.8.3 Morphological Properties

In this work, morphological study of surface of thin films was doing by FESEM technique. It was observed that as the thickness of films reduced from 370nm to 157nm then there is reduction in grain size from 45nm to 41nm respectively. Morphological analysis reveals that reduction in thickness will shrink the grain size. These results agree well with findings of Ala'eddin A. Saif et.al. [49]. Below figure shows that grain size obtained from SEM was large as in comparison of the grain size obtained from the XRD. This is due to reason that grain size measured from SEM by measuring the distance between visible grain boundaries.
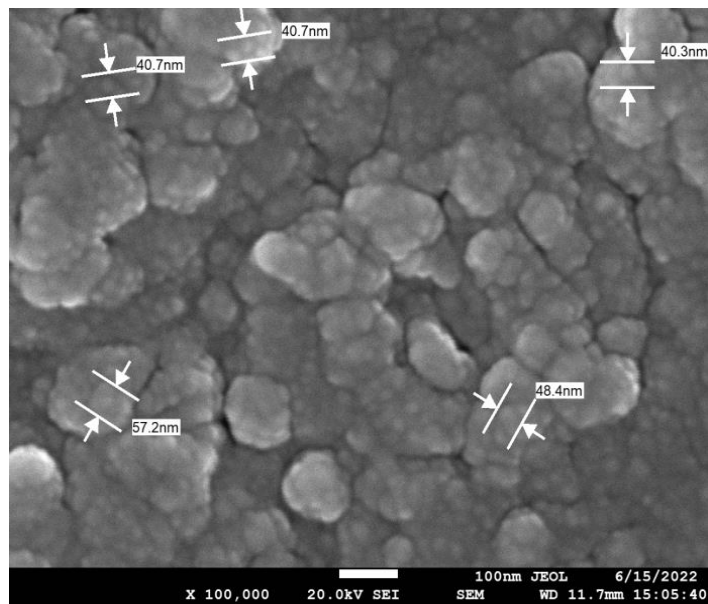

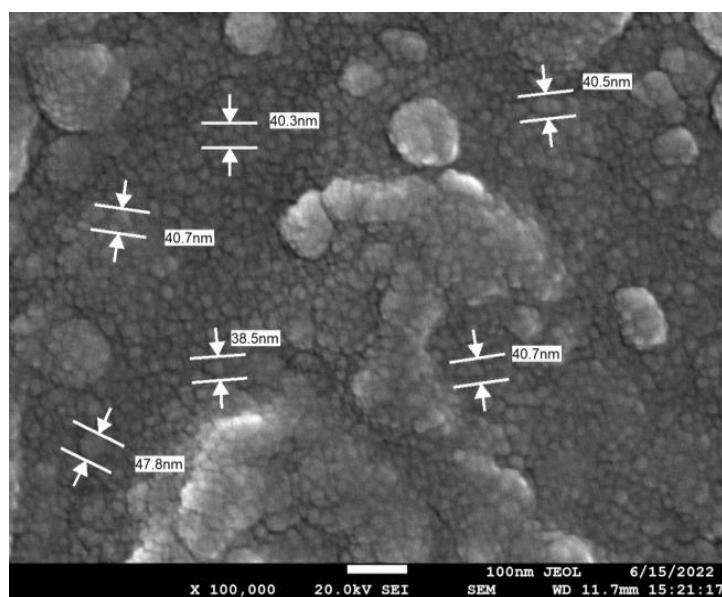Figure 3.10 (a) FESEM images of CuO films for 0.75M6.

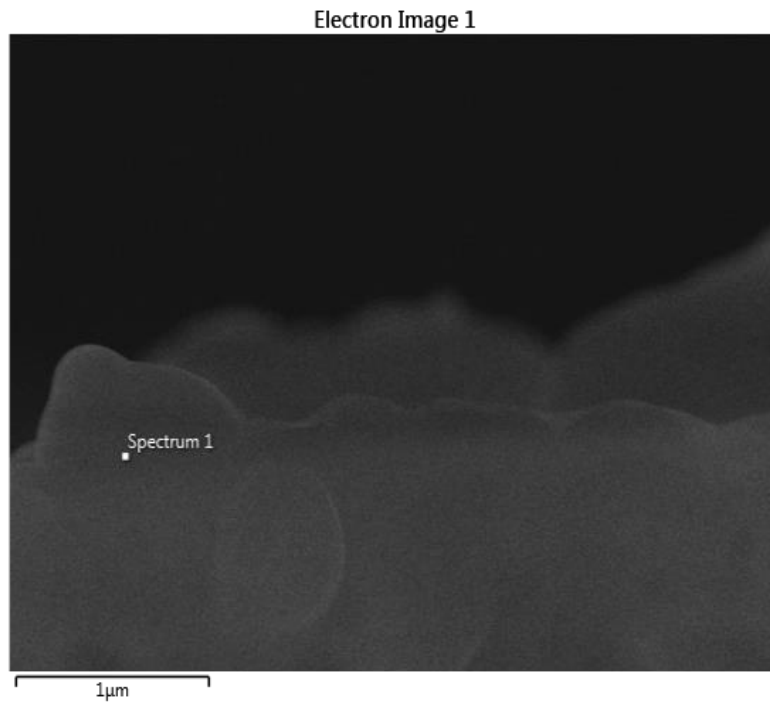Figure 3.10 (b) FESEM images of CuO films for 0.75M7.

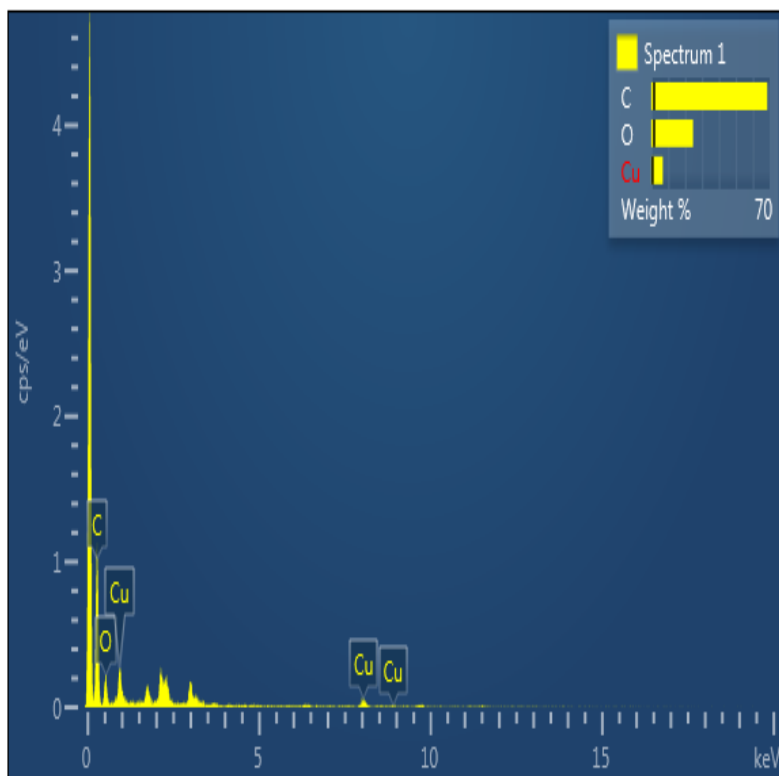Figure 3.11 (a) SEM images of CuO films for 1M1 sample.

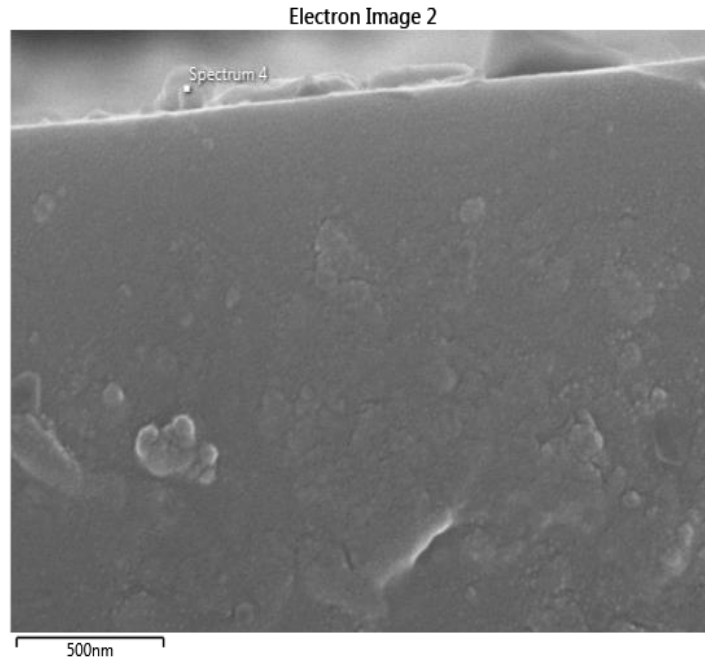Figure 3.11 (b) EDS of CuO films for 1M1 sample.

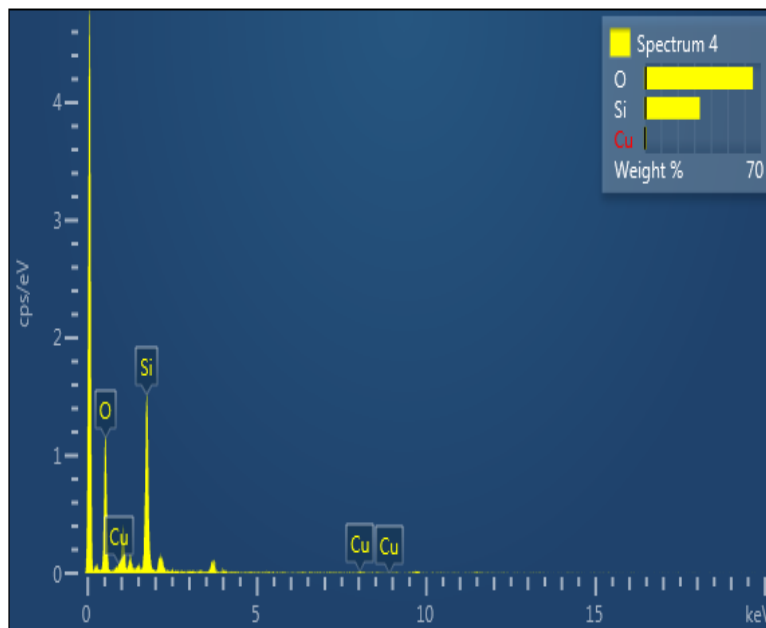Figure 3.12(a) SEM images of CuO films for 1M2 sample.

Figure 3.12 (b) EDS of CuO films for 1M2 sample.

3.8.4 Optical Properties

The optical band gap of CuO thin films samples has been determined from absorbance studies carried out in the wavelength range of 300-800 nm. For thin films samples a two slide of glass was taken out of which one is plane glass and other is covered with material (in form of film) and put in the cuvette inside the spectrometer. This plane glass slide has been used as a reference. The light emitted from the source passes through a grating monochromator and is then split into two beams, one passes through the sample and the other through the reference

sample. After passing through the sample the monochromatic beams are converged and converted to electrical signal by a detector. The absorption spectra of the sample are then obtained by collecting the absorbance as a function of wavelength at room temperature [50]. Absorption coefficient (α)is determined with the absorbance (A) value calculated for a definite wavelength and the thickness (t) with the following equation

$$\alpha = \frac{2.303\ A}{t} \quad (3.5)$$

The transmittance spectra of CuO thin films prepared from 0.75M and 1M concentration by varying the spinning speed between 1000-4500 rpms in air atmospheric condition are recorded. From the figure 3.13, it is seen that transmission spectra are extremely transparent in the visible and near infrared range. Due to the beginning of fundamental absorption, optical transmission drops extremely sharply in the immediate vicinity of the UV area. Additionally, when the spinning speed increases, the basic absorption edge shifts to the shorter wavelength side.

The enhanced crystallinity and greater carrier concentration may be responsible for the spectral shift toward the UV region. This transmission spectrum led to the conclusion that transmission diminishes with thickness. As the film thickness rises from 75 to 239 nm in this study due to an increase in film density, transmission decreases by up to 15%. Since many more photons are absorbed as film thickness rises, films become less transparent. It became apparent that films are transparent at the greatest wavelength value and opaque at lower wavelength values.
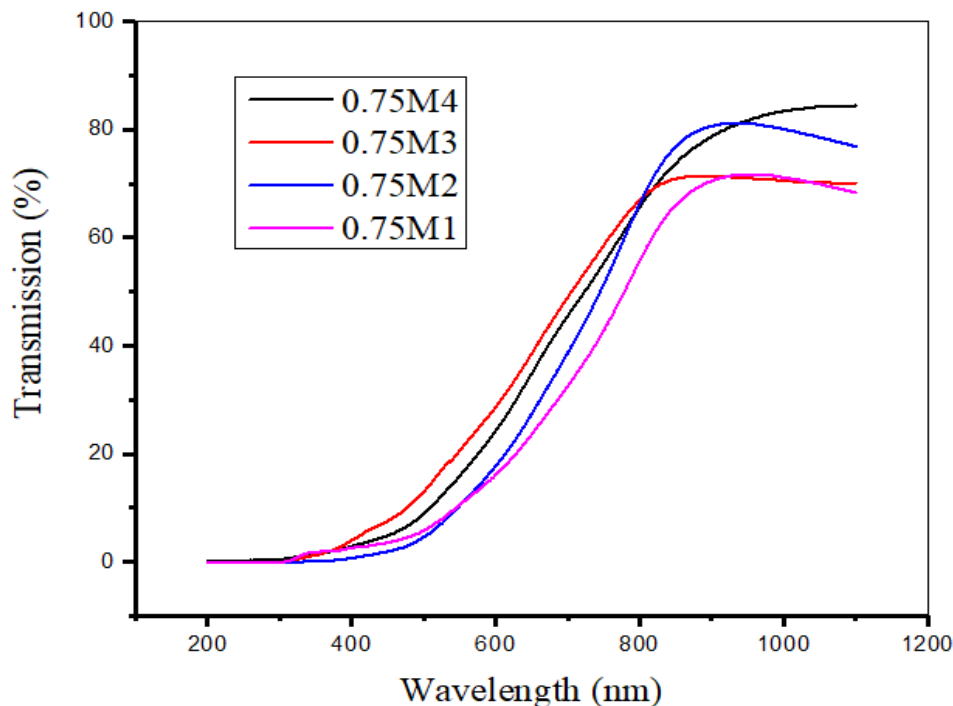

Figure 3.13 Transmission spectra of CuO films by varying the thickness.

The transmittance of CuO thin films was measured using a UV-VIS spectrophotometer across the wavelength range (200-1100 nm). The produced samples were discovered to be extremely sensitive to film thickness. According to the findings, a film with a thickness of 75 nm (0.75M4) has the maximum transmission of 83.59%, while a film with a thickness of 239 nm (0.75M1) has the lowest transmission of 68.51%. The transmittance/absorbance of a material offers adequate way to conclude the absorption edge and energy gap of the material.

By using Tauc relationship, we can obtain the direct band of CuO thin films. E_g was calculated by extrapolating the linear region of graph of $(\alpha h\upsilon)^2$ on y-axis and photon energy (hυ) on x-axis.

$$\alpha h\upsilon = A\,(\,h\upsilon - E_g\,)^2 \quad (3.6)$$

where α is the absorption coefficient, h is planck's constant and v is the photon energy [51].

Figure 3.14 (a, b, c and d) shows the spectral variation of $(\alpha h\upsilon)^2$ under direct allowed transitions for CuO thin films samples. The band gap value is obtained by extrapolating the straight-line part of the plot to the energy axis and found to lie between 2.02 eV- 2.23 eV.

Figure 3.15 (a, b, c and d) shows the spectral variation of $(\alpha h\upsilon)^{1/2}$ under indirect allowed transitions for CuO thin films samples and band gap is found to lie between 0.98 eV – 1.46eV.
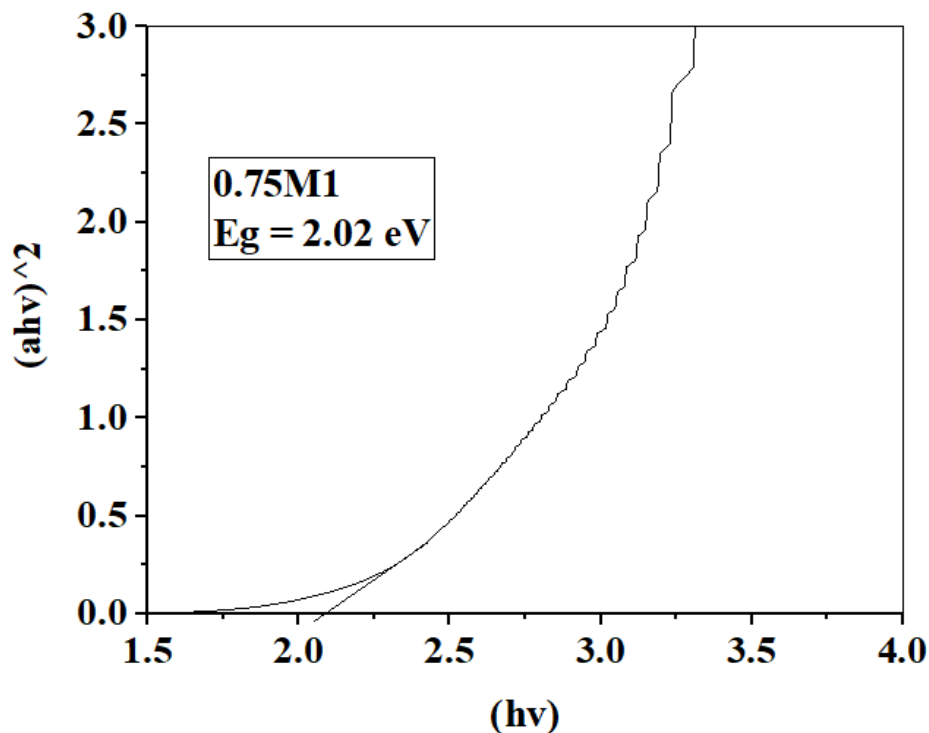

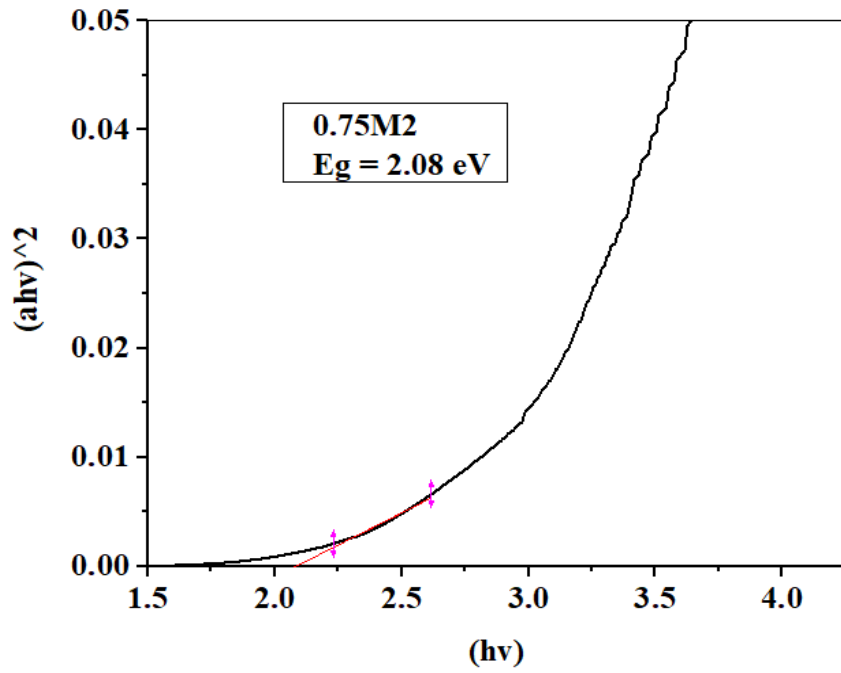Fig. 3.14 (a) Direct band gap of 0.75M1sample of CuO films.

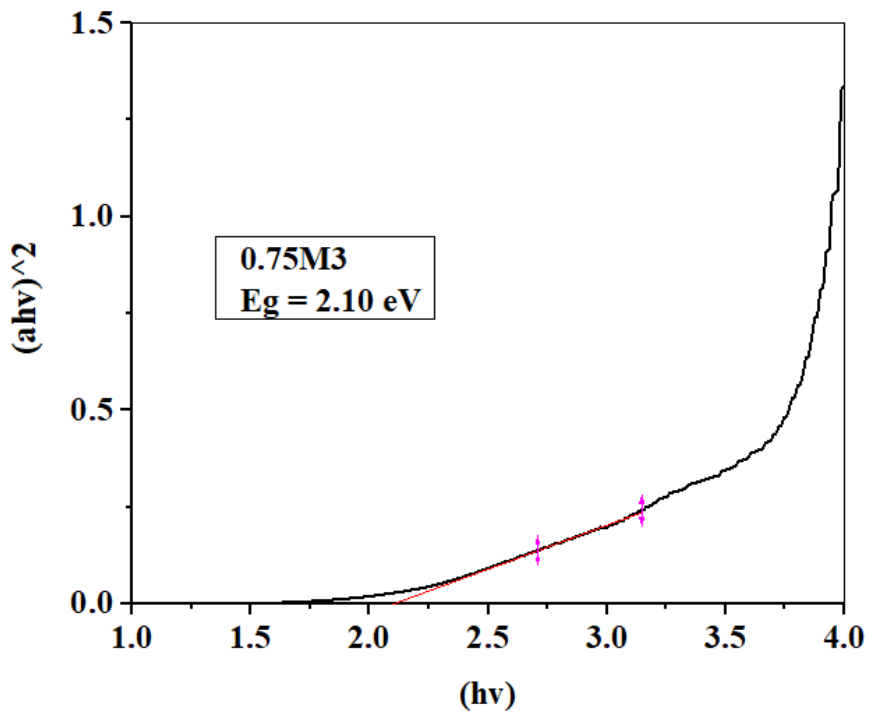Fig. 3.14 (b) Direct band gap of 0.75M2 sample of CuO films.

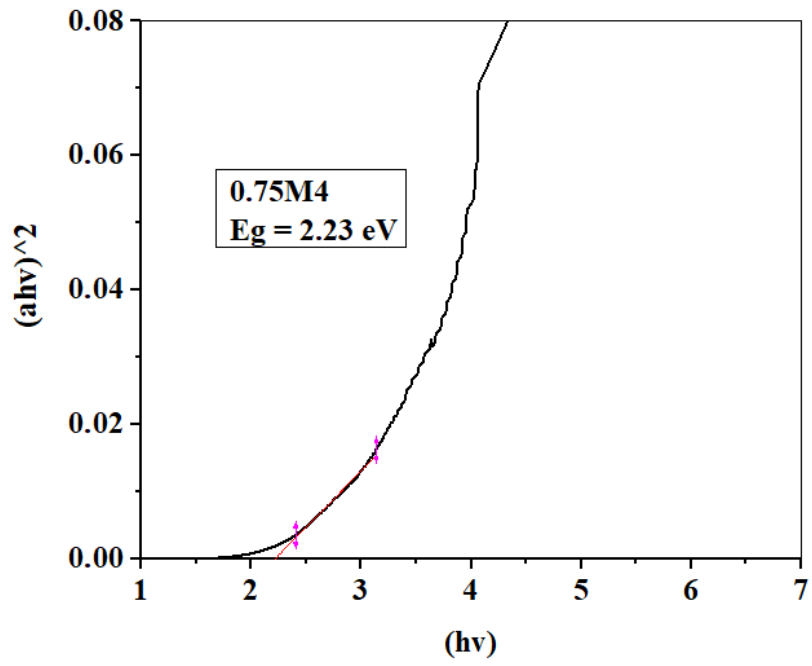Fig. 3.14 (c) Direct band gap of 0.75M3 sample of CuO films.

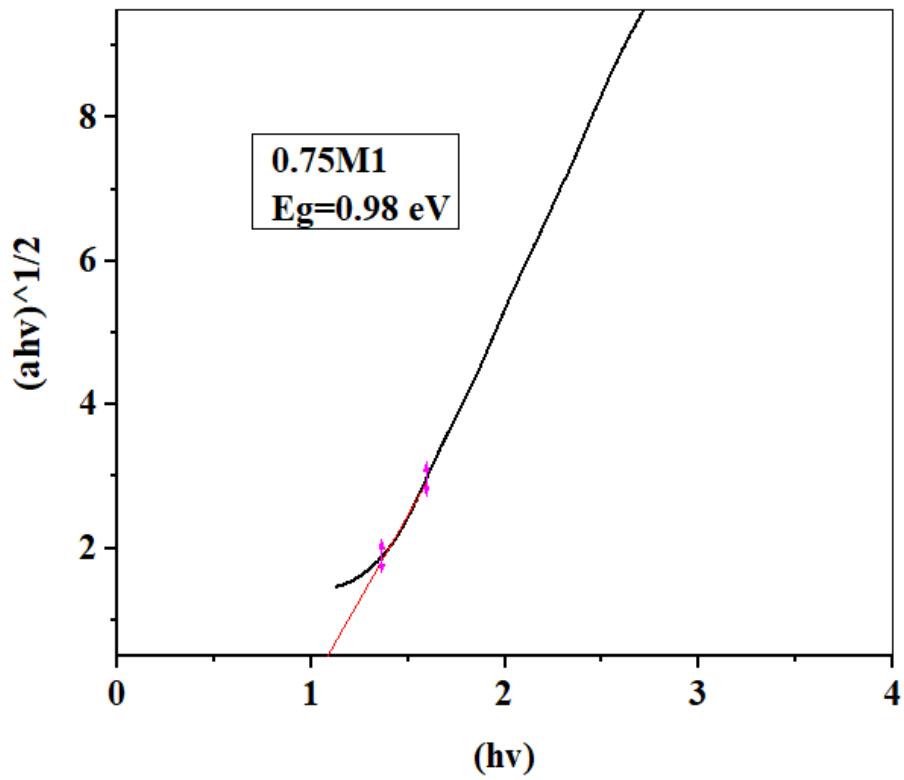Fig. 3.14 (e) Direct band gap of 0.75M4 sample of CuO films.

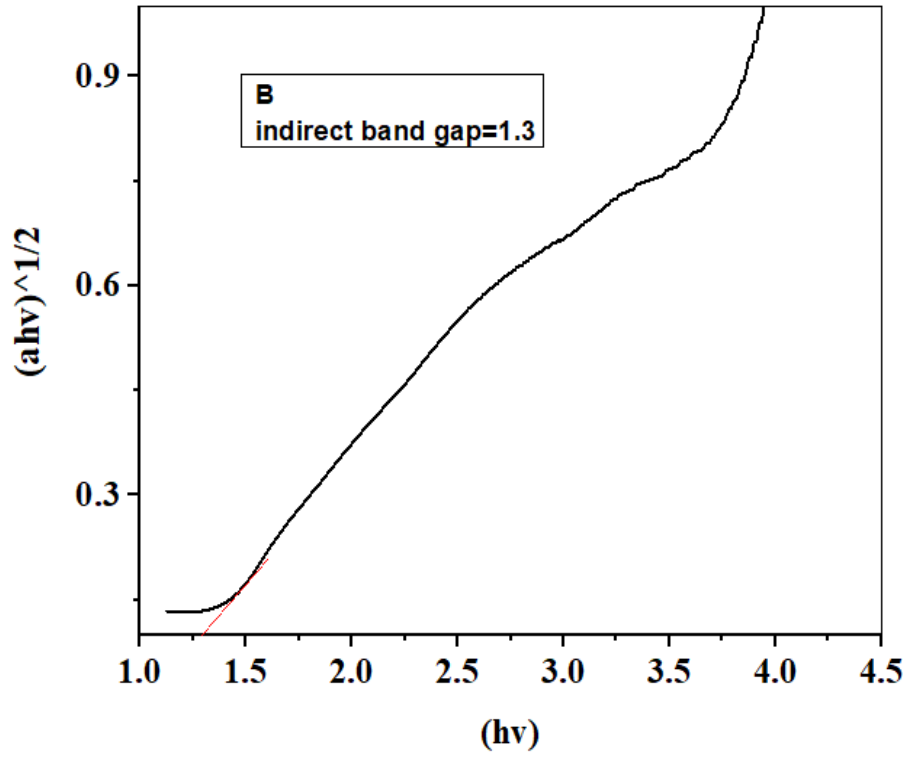Figure 3.15 (a) Indirect band gap of 0.75M1 sample of CuO films.

Figure 3.15 (b) Indirect band gap of 0.75M2 sample of CuO films.
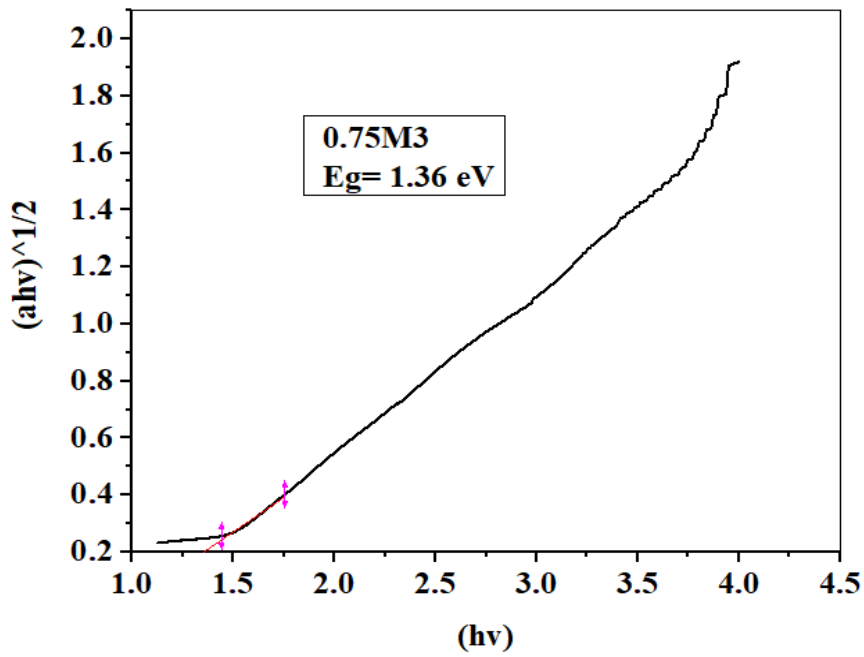

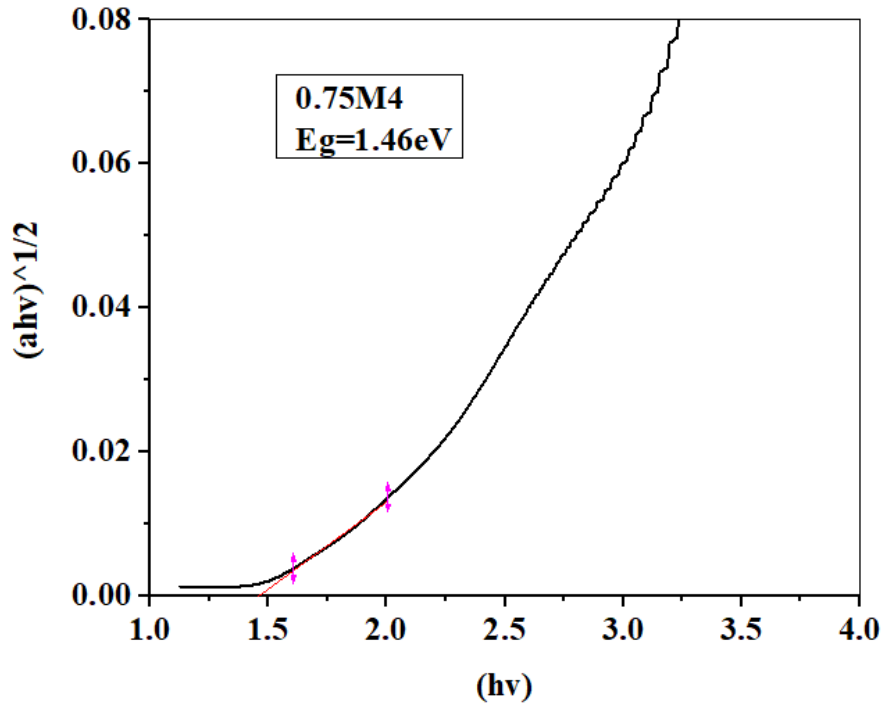Figure 3.15 (c) Indirect band gap of 0.75M3 sample of CuO films.

Figure 3.15 (d) Indirect band gap of 0.75M4 sample of CuO films.

From the Figure 3.14 (a) – (d), it is noted that lowest direct band gap of 2.02 eV and indirect band gap of 0.98 eV of sample named as 0.75M1 which has highest thickness of 239 nm.

Table 3.5 The variation of band gap of sample 0.75M1 – 0.75M4 on varying thickness.

Name of Sample	Spinning Speed (rpm)	Thickness (nm)	Direct Band Gap (eV)	Indirect Band Gap (eV)
0.75M1	3000	239	2.02	0.98
0.75M2	3500	115	2.08	1.3
0.75M3	4000	89	2.10	1.36
0.75M4	4500	75	2.23	1.46

It was found that indirect band gap in range between 0.98 to 1.46 eV which shows that prepared samples were very suitable for application in solar cell. The highest value of both direct and indirect band gap was at 3000 rpm. After increasing the spinning speed beyond 3000 rpm then band gap starts decreasing. The reduction in band gap indicates the improvement of films on increasing thickness. The variation of band gap is due to decrease in defects in thin films [52]. Our results are comparable to the band gap analysed from the literature review [52-55].

Figure 3.16 (a) Band gap of sample 0.75M5 having thickness 470nm.

Figure 3.16 (b) Band gap of sample 0.75M6 having thickness 370nm.
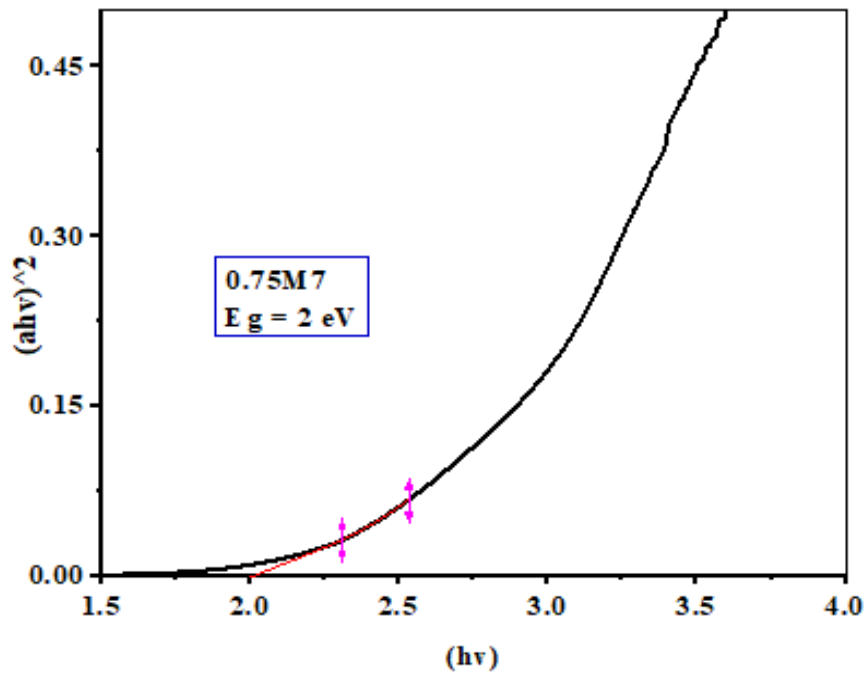
Figure 3.16 (c) Band gap of sample 0.75M7 having thickness 157nm.

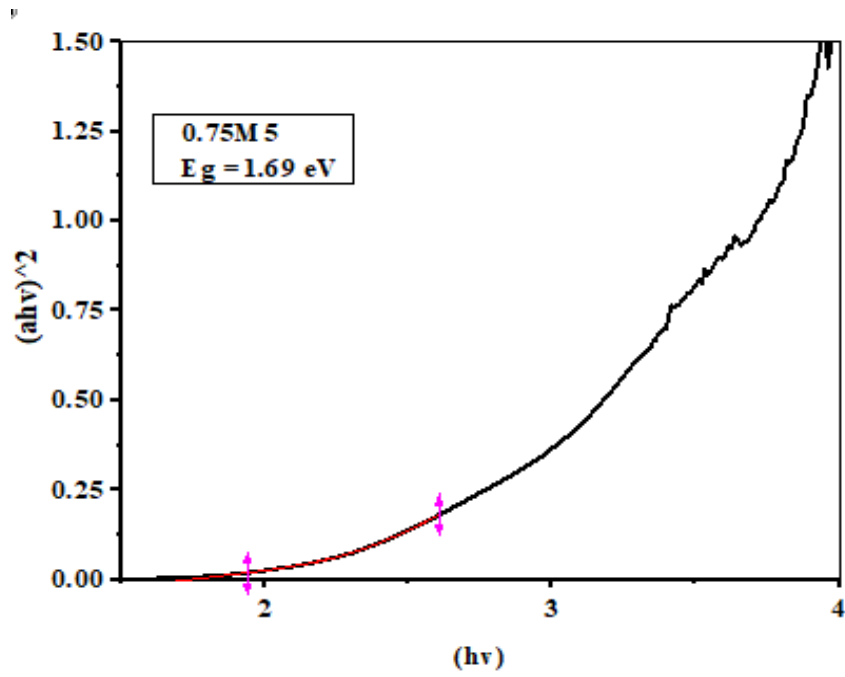The optical band gap of sample prepared by solution of 1 molar is shown as below

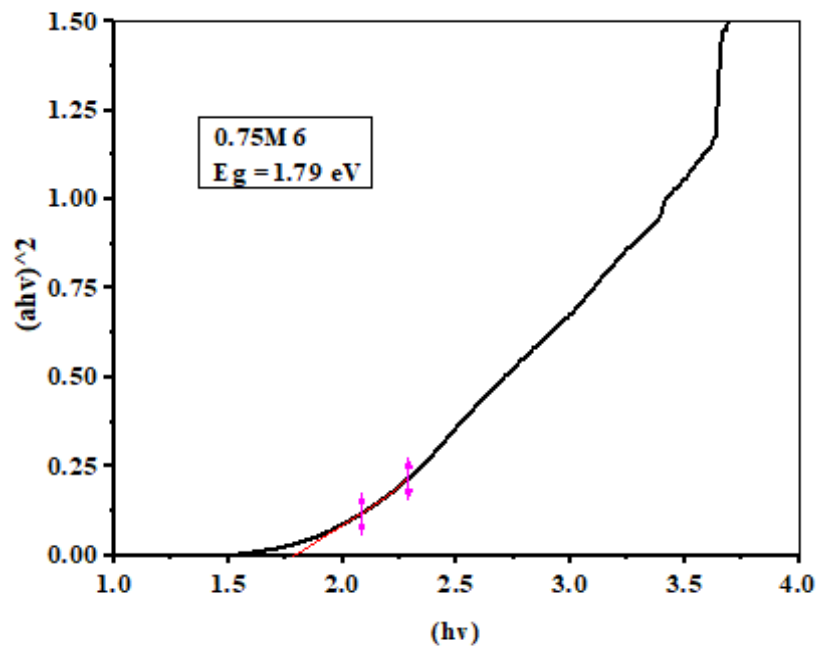Figure 3.17 (a) Band gap of sample 1M1 having thickness 378 nm.

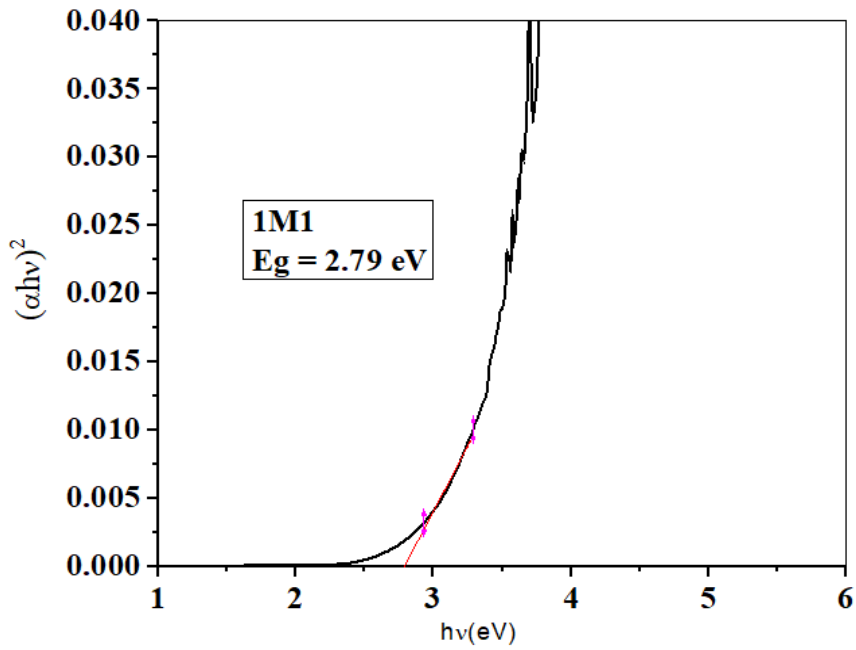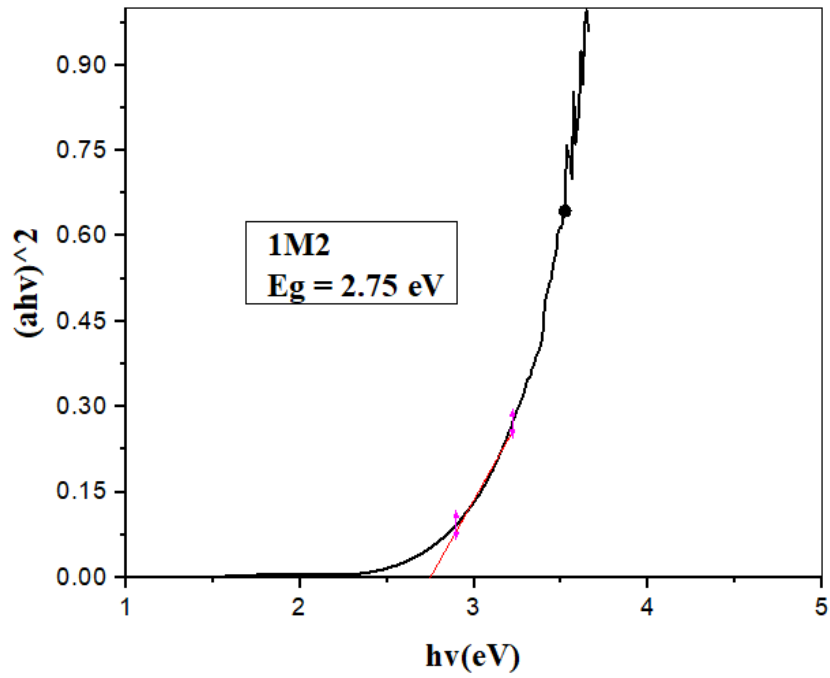Figure 3.17 (b) Band gap of sample 1M2 having thickness 411 nm.
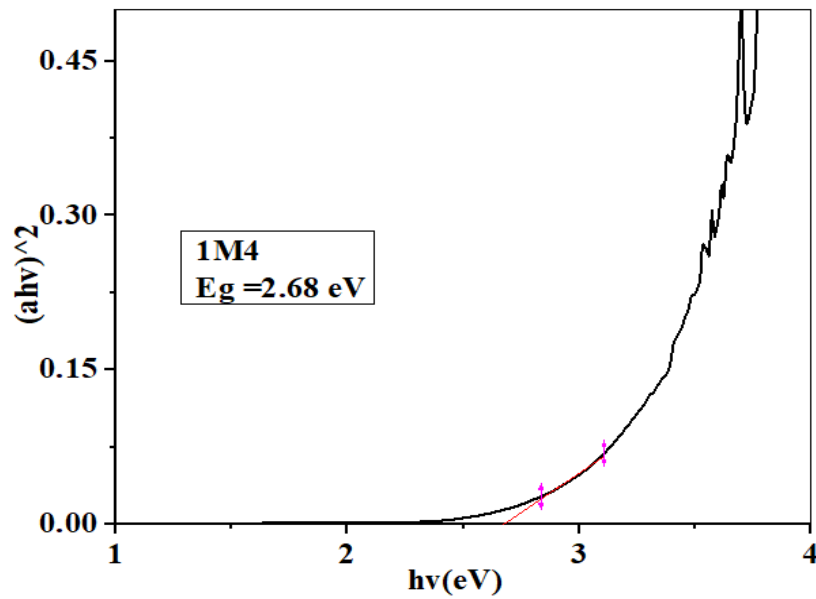

Figure 3.17 (d) Band gap of sample 1M4 having thickness 721 nm.

The calculated band gap of various sample prepared by 0.75M and 1M concentration solution is tabulated in below table

Table 3.6 The variation of band gap of sample of 0.75M and 1M concentrations on varying thickness.

Name of Sample	Spinning Speed (rpm)	Thickness (nm)	Optical band gap (eV)
0.75M5	1500	470	1.69
0.75M6	2000	370	1.79
0.75M7	2500	157	2
1M1	2500	378	2.79
1M2	2000	411	2.75
1M4	1000	721	2.68

It is evident from table 3.6 and 3.7 that the optical band gap of CuO film is appropriate for use as a selective absorber in solar cell cells. The increase in carrier concentration and enhanced crystallinity are responsible for the band gap fluctuation, which causes the fermi level to rise within the conduction in degenerate semiconductors.

3.8.5 Electrical Properties

The electrical resistance of CuO thin film samples has been determined using standard two probe technique by measuring current at two points of the film under variable dc power supply of 1V-10V. For each sample under study, silver electrodes have been placed on top of the film samples with a set spacing between electrodes and electrode length of 1 and 0.5 cm. The needles of the probe must make a strong contact with the surface in order to produce accurate data. [56].

 The room temperature electrical resistance of films is observed to lie between 12.5×10^8 Ω to 1×10^9 Ω. Compared to 0.75M2, 0.75M3, and 0.75M4 films, 0.75M1 films exhibit much reduced resistance, which can be attributed to the growth in crystallite size and decrease in porosity of the films.

Also, the resistance of 0.75M5 is found to be comparatively lower than 0.75M6 and 0.75M7. The electrical resistance of these samples observed in range between 2.5×10^6 Ω to 2.5×10^7 Ω. Further variation of resistance with temperature in investigated range confirms the semiconducting nature of films. This decrease in resistance with increasing of thickness can be attributed to increase in value of charge carriers. The electrical resistance of sample 1M1 is

higher in comparisons of 1M2 and 1M4 because of the highest and lowest thickness of 1M4 and 1M1 respectively. It is clear from the figure 3.18, 3.19 and 3.20 that all of films show ohmic behaviour with linear I-V curve.
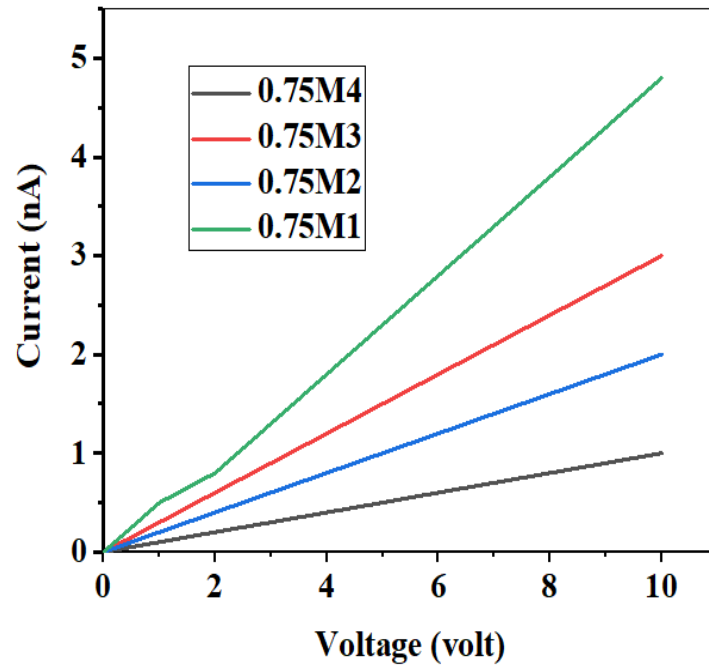
Figure 3.18 I-V dependence of CuO Films (0.75M1- 0.75M4).
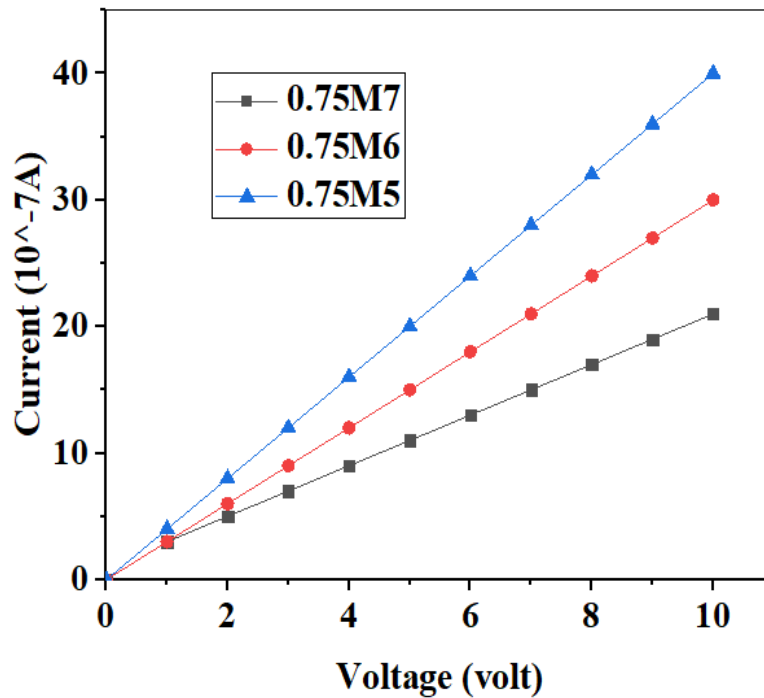
Figure 3.19 I-V dependence of CuO Films (0.75M5- 0.75M7).
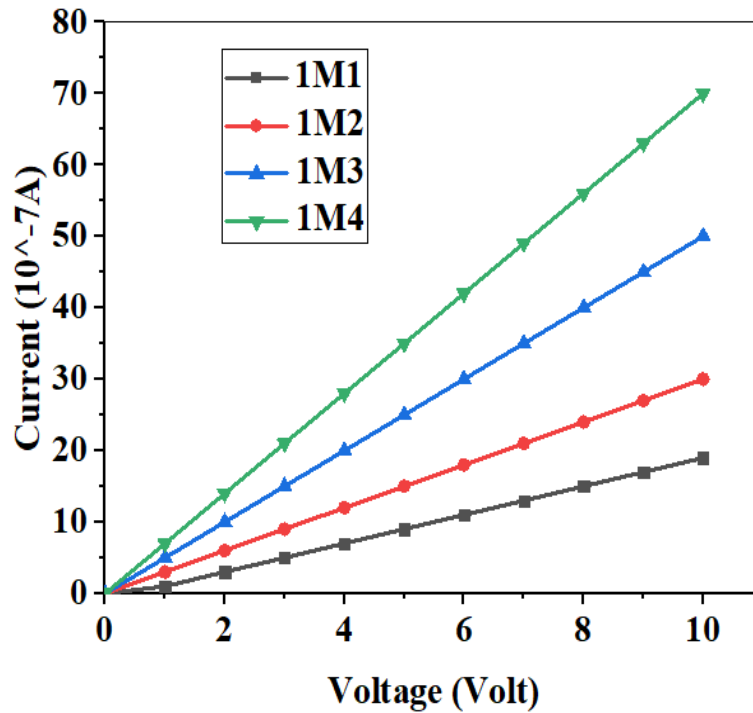
Figure 3.20 I-V dependence of CuO Films (1M1- 1M4).

It was observed that current varies linearly as we change voltage continuously. The studied voltage was kept 1 V to 10 V and obtained current was in nano-ampere to micro-ampere. It was noted that spinning speed has a great influence on I–V characteristics of CuO thin films and found that current goes on increasing as the thickness of film increases. It could be said that the current values at fixed voltage decreased due to decreased of thickness of the copper oxide thin films.

Increase in film thickness results in increase the number of electrons and holes (so called sheet resistance and conductivity), while the bulk concentration may remain the same. The electrical resistivity and conductivity measure by 2- probe set-up for CuO deposited films. We passed a voltage through one probe and reported the current through second probe. The resistivity and conductivity are calculated by following equation (3.7), [45].

$R = \frac{\pi \times V}{ln2 \times I}$ (3.7)

$\rho = R \times t$ (3.8)

$\sigma = \frac{1}{\rho}$ (3.9)

Where R is the average resistance of thin film, V is the voltage applied, I is the obtained current on applying voltage, σ is conductivity of thin films, ρ is resistivity of thin film and t is the thickness of thin film.

The resistivity was determined to be maximum at 3000 rpms and is approximately 239 Ω-cm. As the spinning speed increases, resistivity first falls and then increases. The highest resistivity was roughly 58.67 Ω-cm at 4500 rpm, whereas the lowest resistivity was 37 Ω-cm at 3500 rpm. The increase in carrier concentration of holes and electrons is what causes the resistivity to decrease. After 3500 rpm, resistivity begins to rise as a result of a large reduction in crystallite size brought on by an increase in deposition rate. This decrease in carrier mobility causes resistivity to rise as a result.

Electron and hole were transferred to the active area in order to acquire the superior electrical characteristics. In agreement with B. L. Anderson et. al. [57], a lower resistivity value would improve the conductivity of films. The below figure 3.21 illustrates how changing the spinning speed affects the resistivity and conductivity of CuO thin films with varied thickness.
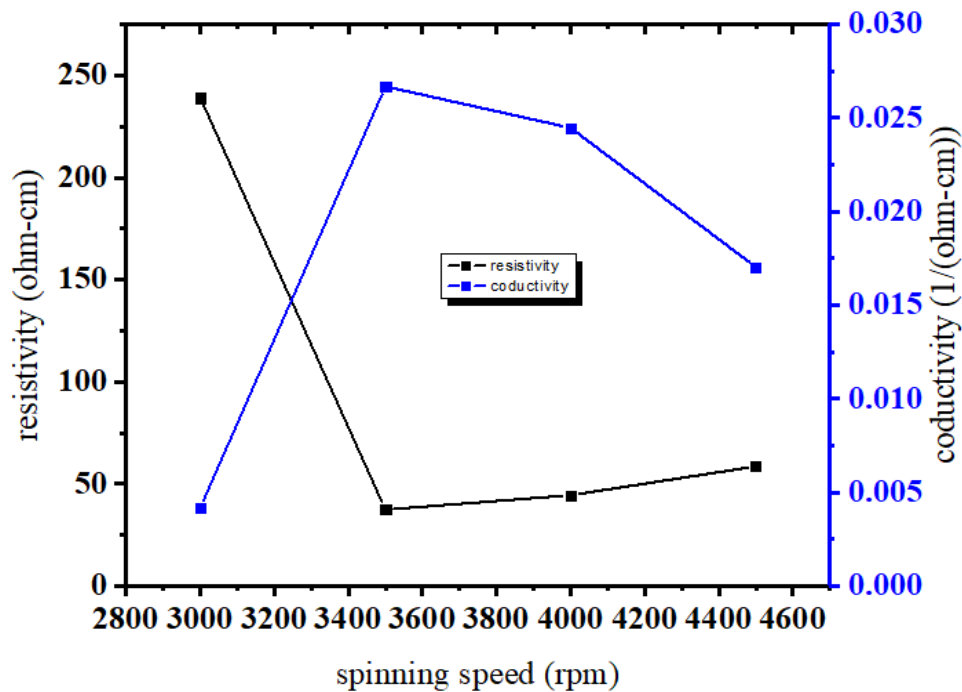
Figure 3.21 CuO thin films (0.75M1- 0.75M4) with resistivity and conductivity variations as a function of spinning speed.

It was noted that a thin coating of CuO had lowest resistivity for 0.75 M7 sample and highest resistivity for 0.75 M5 sample. This resulted from an increase in the concentration of carriers like as electrons and holes, which reduced the resistivity. As the resistivity decrease, electrical conductivity gets increase.
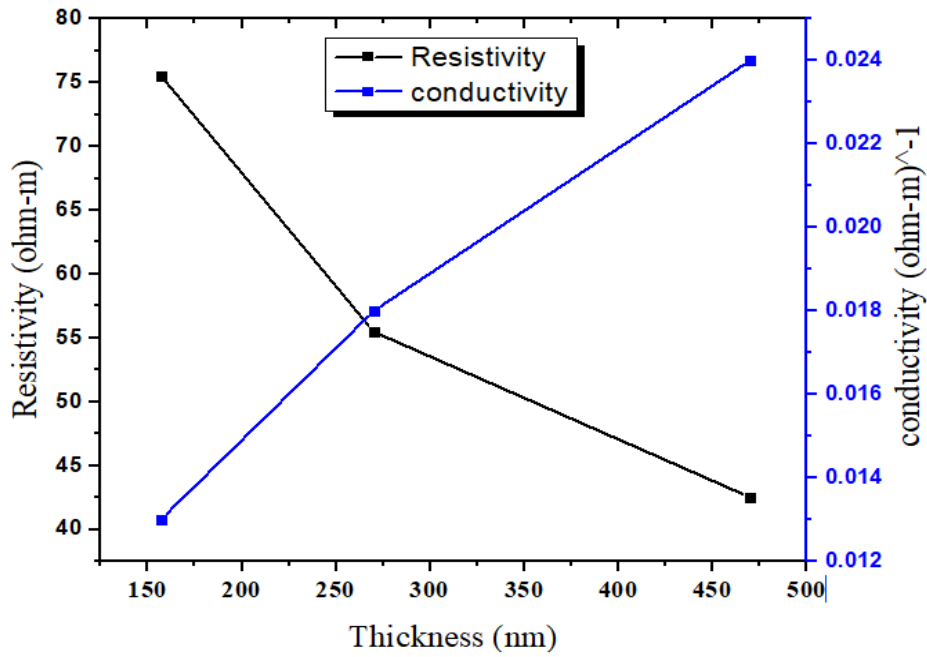
Figure 3.22 The variation of resistivity and conductivity on varying the thickness of films for sample 0.75M5 to 0.75M7.
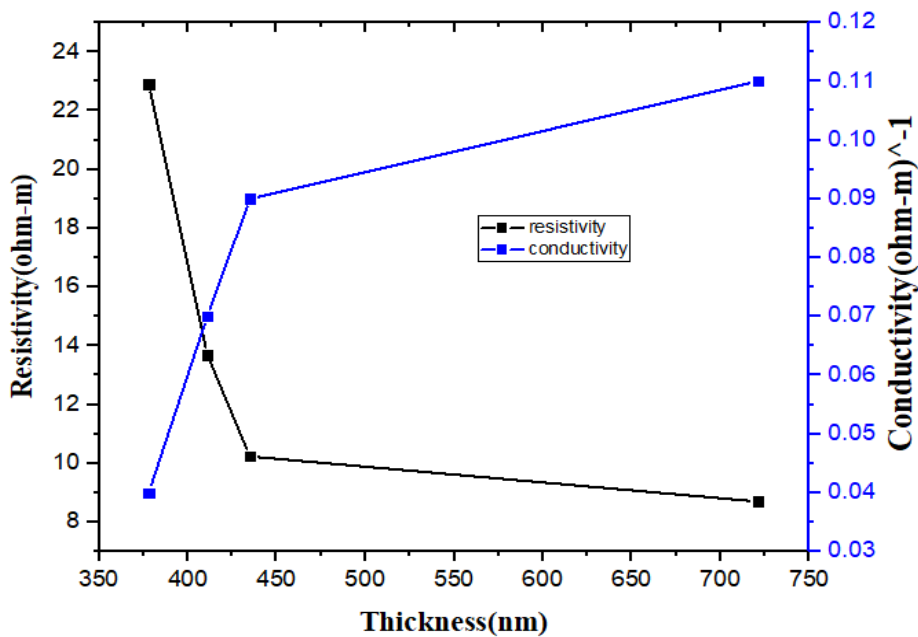
Figure 3.23 The variation of resistivity and conductivity on varying the thickness of films for sample 1M1 to1M4.

It was found that CuO thin films prepared from one molar concentration of solution have lowest resistivity for 1M4 sample of thickness 721nm and highest resistivity for 1M1 sample of thickness 378nm. The value of lowest and highest resistivity was 10.23 ohm-m and 22.9 ohm-m respectively.

3.9 Fabrication of Gas Sensor

Figure 3.7 shows the schematic for the manufactured gas sensor. First, CuO thin films were created on glass substrates using the sol-gel spin coating process, with spinning speeds ranging from 1000 to 4500 rpm. After this process, films annealed at 400°C annealing temperatures for 2 hours. These films were prepared by using copper acetate dehydrate as precursor with 0.75M and 1M molar concentrations. CuO thin films have been studied for their gas sensing behaviour towards reducing gases at different operating temperatures. To analyse the gas sensing parameters of the films, gas sensor was fabricated at our laboratory.

Figure 3.24 Experimental set-up of thin film gas sensor for measuring response toward H_2S gas.

The gas sensing performance was analysed in stainless-steel home-made test chamber with volume 1.5L. By using two-probe electrical resistivity system (SES Instruments Pvt. Ltd., Roorkee, Model: DPM-111 of digital pico-ammeter and Model: EHT-11A of high voltage power supply) in a test chamber, sensitivity of thin films samples of CuO were studied. To control the operating temperature between range of 25°C- 200°C, oven (Pid controlled oven, Model: PID-TZ) was used. The gases are introduced in test chamber with the help of syringe containing desired ppm of test gas and obtained resistance has been used to calculate the gas response of films sample.

At 10V voltage, sensor resistance was measured by digital pico-ammeter. To measure the resistance of each sample before and after exposing the H_2S gas, two electrodes at distance 1cm were made with the help of silver paint. Sensitivity of these samples toward H_2S gas was

measured by taking the ratio of resistance of thin film element in air to the resistance of thin film element in gas atmosphere. At different operating temperatures, 1ppm to 4ppm concentration of gas was passed through syringe and sensitivity was noted. From 25°C to 100°C working temperature, response and recovery time of each sample was measured.

3.10 Mechanism of Gas Sensor

The sensing mechanism of CuO thin films towards reducing gas such as ethanol, Sulphur dioxide, acetone and hydrogen sulphide can be explained on the basis of redox reaction with adsorbed oxygen species on CuO surface as discussed below:

$$O_{2\,(gas)} \longrightarrow O_{2\,(adb)} \quad (3.10)$$

$$O_{2\,(adb)} + e^- \longrightarrow O^-_{2\,(adb)} \quad (3.11)$$
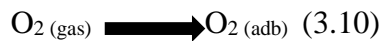
At ambient air conditions, different negatively charged surface oxygen species (O^-_2, O^{2-}) are formed due to chemisorption of molecular oxygen from air on the surface of CuO films as explained by above equations. It is assumed that species creates a barrier to tap surface charge carrier and results in increase of films resistance. The redox reaction of test gas with oxygen species leads to consumption of oxygen adsorbate, accompanied by a corresponding variation in barrier height and bring a change in the sensor resistance.

Both adsorption and desorption of gas molecules caused a change in electrical resistance, which served as the basis for the gas sensor's process [58]. When an airborne thin film gas sensor is exposed, oxygen molecules adsorb on the sensor's surface and create O- ions [59]. When H_2S gas was injected on CuO thin films sensor then it reacts with adsorb O^- ions and reacting equation is given as below

$$H_2S + CuO \rightarrow CuS + H_2O \quad (3.12)$$
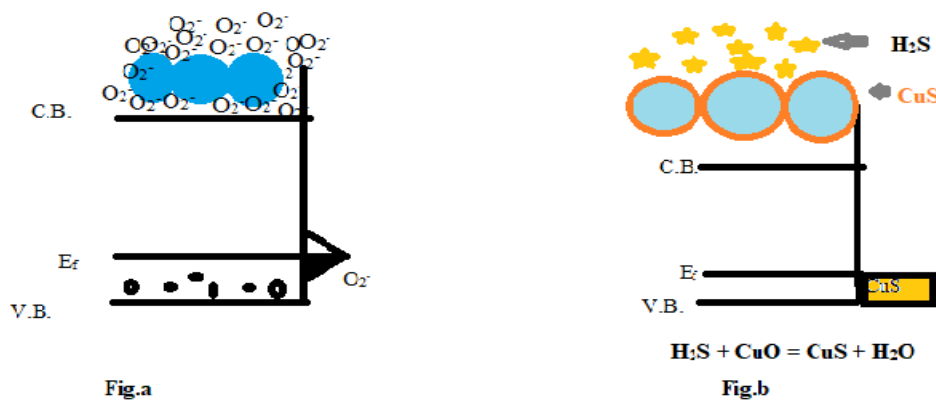
Figure 3.25 Gas sensing mechanism of CuO thin films; (a) in presence of air and (b) in presence of H_2S gas.

3.11 Gas Sensing Performance

The outcomes of the actualized gas sensor, which is based on CuO thin films, are shown. These thin films were created by altering the thickness and molarity of solution. The characteristics of various samples' CuO-based sensors are shown below.

3.12 Operating temperature

The operating temperature has a significant impact on the response of semiconductor-based sensors. In actuality, the sensor layer's operating surface temperature has a direct impact on the adsorption of gases. Figure 3.26 displays the responses that were obtained after the sensor was subjected to 40 ppm of hydrogen sulfide at various temperatures ranging from 25 to 150 °C in order to figure out this temperature. It is frequently known in the literature that a standard operation temperature corresponds to the maximal response.

In our situation, the progression of the response from the sensors shows that this maximum is situated about 25 °C. Comparatively, this operating temperature (25°C) is lower than earlier reported working temperatures for sensing H_2S, which ranged from 200 to 400°C [60-61]. In addition, we observe that the CuO-based sensor performs well at lower operating temperatures of 25 °C. This low working temperature may result in reduced sensor consumption of electricity, improving device reliability, profitability and durability.

Figure 3.26 CuO-based sensors' response towards H_2S gas (40ppm) at

different operating temperatures.

119

3.13 Gas Response Measurement of CuO thin films of 0.75M concentration toward H₂S

The relative change in the signal being monitored during gas exposure is the film sensitivity. The formula for the gas response of the sensor states t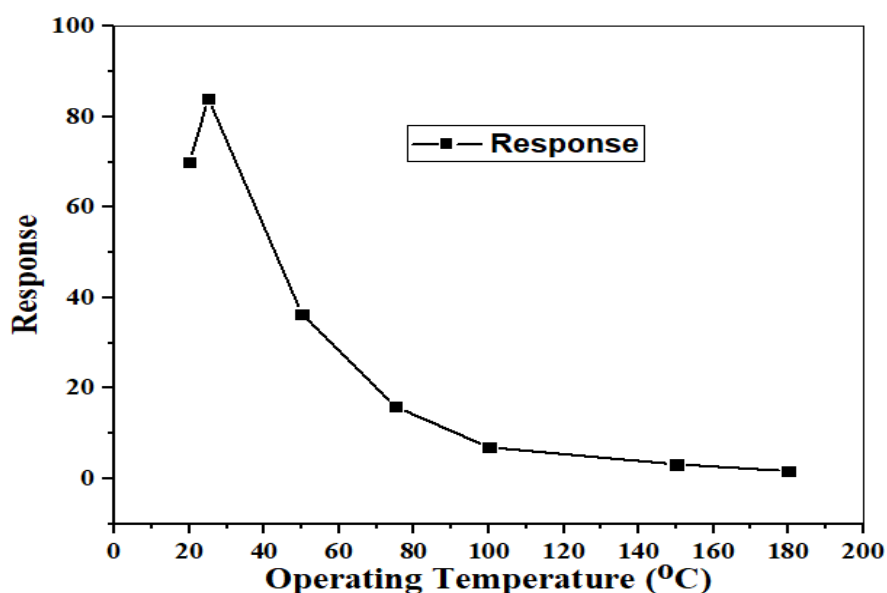hat it is the ratio of the change in the sample's resistance when tested with target gas on the resistance it experiences in air:

$S = \frac{R_a}{R_g}$ (3.13)

Where R_a and R_g are the resistance in presence of air and gas respectively [62].

The sensitivity factor (S%) is calculated using equation:

$(S\%) = \frac{R_g - R_a}{R_a} \times 100\%$ (3.14)

The gas response of CuO based samples towards the H₂S gas has been studied. For this various concentration of gas is introduced in the chamber and the change in resistance is recorded on a digital pico-ammeter connected in series to the sample. Upon resistance stabilization, the lid of the chamber is opened for gas exit and the sample is allowed to recover to its original resistance value. The studied temperature range for measuring the response of a gas has been selected in the range 25-100°C and found best response at 25°C temperature. Oxygen atoms or molecules adsorb and desorb on the surface of the sensor film, changing the electrical resistance.

Among various sample of 0.75M and 1M concentration, some of sample were optimized to detect the sensitivity. The higher sensitivity may be due to the largest surface area and the optimum surface roughness. Thin films based on sample 0.75M4 are high sensitivity to H₂S gas was discovered at 25°C temperature and shows a comparatively lower response time towards the gas at higher operating temperatures. The response towards tested gases is observed to be suppressed for 0.75M5,0.75M6 and 0.75M7 due to their comparatively larger grain size and reduced porosity. The increase in grain size decreases the surface-to-volume ratio, consequently sensitivity decrease.

Response time is the amount of time it takes for the sensor to modify its resistance by 90% of its maximum after being exposed to gas. Recovery time is the amount of time it takes for the sensor to regain 90% of its initial resistance once the target gas has been removed. The various parameters of samples at different operating temperature on exposing H₂S gas is show by given table.

Table 3.7 The sensitivity toward H_2S gas, response time and recovery time for sample 0.75M4 as a function of gas concentration and operating temperature.

Concentration of Gas	Response Parameters	Operating Temperature (^{o}C)			
		25	50	75	100
10 ppm	Sensitivity (R_a/ R_g)	28.37	26.62	20.92	12.18
	R_t (s)	30	30	28	20
	Re_t (s)	120	115	115	110
20 ppm	Sensitivity (R_a/ R_g)	40.18	35.72	28.06	22.44
	R_t (s)	20	20	15	12
	Re_t (s)	140	137	130	128
30 ppm	Sensitivity (R_a/ R_g)	72.03	66.41	62.52	58.03
	R_t (s)	15	14	12	10
	Re_t (s)	150	140	135	122
40 ppm	Sensitivity (R_a/ R_g)	102.17	90.02	85.92	78.66
	R_t (s)	10	10	12	10
	Re_t (s)	220	212	200	188

Table 3.8 The sensitivity toward H_2S gas, response time and recovery time for sample 0.75M7 as a function of gas concentration and operating temperature.

Concentration of Gas	Response Parameters	Operating Temperature (^{o}C)			
		25	50	75	100
10 ppm	Sensitivity (R_a/ R_g)	18.51	12.43	5.76	1.27
	R_t (s)	70	70	68	60
	Re_t (s)	180	175	168	160
20 ppm	Sensitivity (R_a/ R_g)	25.55	14.5	9.76	3.35
	R_t (s)	60	60	55	52
	Re_t (s)	420	417	408	388
30 ppm	Sensitivity (R_a/ R_g)	50	25.52	14.22	5.51
	R_t (s)	50	48	42	38
	Re_t (s)	480	470	450	402
40 ppm	Sensitivity (R_a/ R_g)	87	36.44	15.92	6.96
	R_t (s)	20	20	18	15
	Re_t (s)	720	712	700	688

Table 3.9 The sensitivity toward H_2S gas, response time and recovery time for sample 0.75M6 as a function of gas concentration and operating temperature.

Concentration of Gas	Response Parameters	Operating Temperature (^oC)			
		25	50	75	100
10 ppm	Sensitivity (R_a/R_g)	5.13	4.7	1.45	1.25
	R_t (s)	75	75	70	68
	Re_t (s)	180	178	170	160
20 ppm	Sensitivity (R_a/R_g)	12.5	9.66	2.77	1.4
	R_t (s)	70	60	55	52
	Re_t (s)	240	238	228	220
30 ppm	Sensitivity (R_a/R_g)	38	13.6	5.28	1.87
	R_t (s)	60	48	42	38
	Re_t (s)	300	298	290	285
40 ppm	Sensitivity (R_a/R_g)	43	22.3	13.51	3
	R_t (s)	55	20	18	15
	Re_t (s)	660	660	650	630

Table 3.10 The sensitivity toward H_2S gas, response time and recovery time for sample 0.75M5 as a function of gas concentration and operating temperature.

Concentration of Gas	Response Parameters	Operating Temperature (^{o}C)			
		25	50	75	100
10 ppm	Sensitivity (R_a/ R_g)	4.2	3.11	1.23	1.18
	R_t (s)	78	78	76	70
	Re_t (s)	120	120	110	108
20 ppm	Sensitivity (R_a/ R_g)	5.33	3.5	2.4	2.07
	R_t (s)	70	60	55	52
	Re_t (s)	900	880	850	800
30 ppm	Sensitivity (R_a/ R_g)	10	4.32	3.99	2.75
	R_t (s)	60	48	42	38
	Re_t (s)	1500	1498	1490	1485
40 ppm	Sensitivity (R_a/ R_g)	33	6.53	5.4	3.84
	R_t (s)	55	20	18	15
	Re_t (s)	1800	1790	1650	1600

The above table shows that if we decrease the thickness of CuO thin films, the gas response toward hydrogen sulphide gas change. Thinner films could lead to higher sensitivity and faster response due to increased surface area, but it might also affect the overall gas sensing

performance. The effect of different temperature and thickness on sensitivity of sample is also shows by below figures
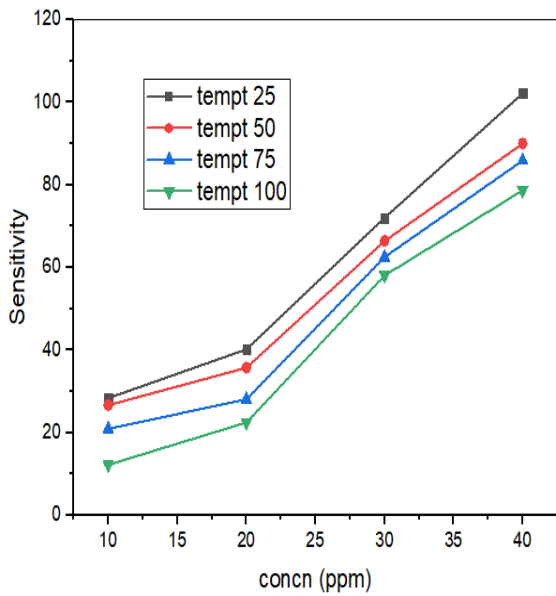

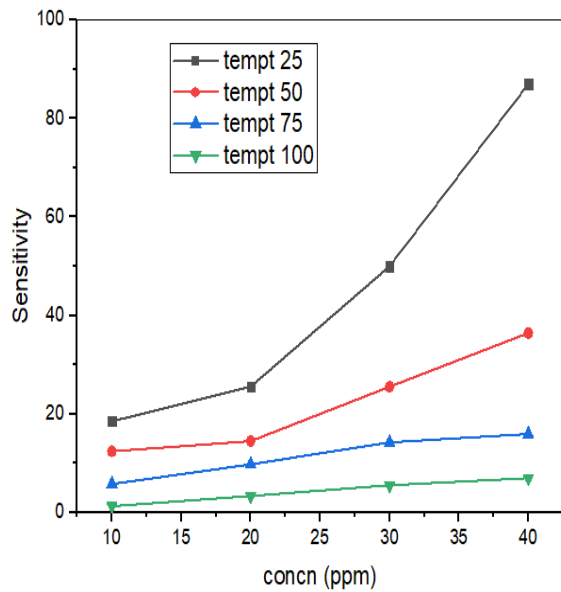Figure 3.27 (a)   Figure 3.27 (b)
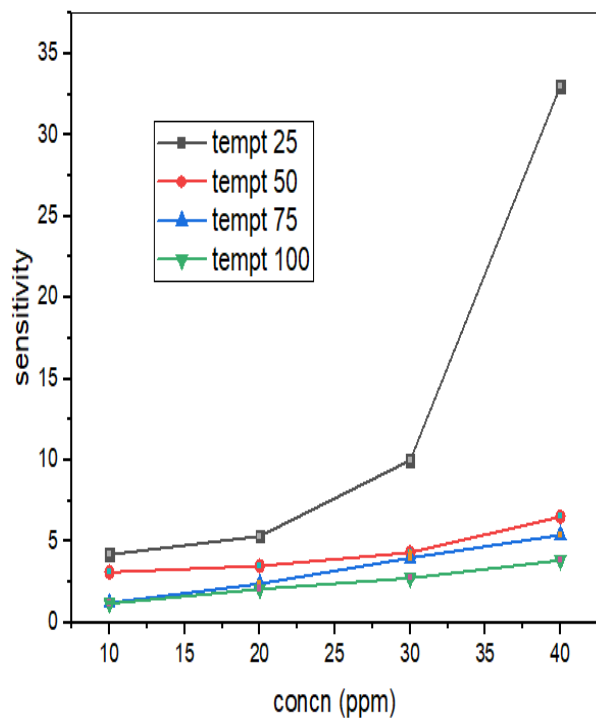
Figure 3.27 (c)   Figure 3.27 (d)

Figure 3.27 variation of sensitivity with operating temperature and concentration of H_2S gas of sample (a) 0.75M4 of thickness 75nm, (b) 0.75M7 of thickness 157nm, (c) 0.75M6 of thickness 370nm and (d) 0.75M7 of thickness 470nm.

3.14 Gas Response Measurement of CuO thin films of 1M concentration toward H_2S

Table 3.11 The sensitivity toward H_2S gas, response time and recovery time for sample 1M1 as a function of gas concentration and operating temperature.

Concentration of Gas	Response Parameters		Operating Temperature (^oC)				
		25	50	75	100	150
10 ppm	Sensitivity (R_a/ R_g)	3.1	2.55	2.39	1.43	1.51
	R_t (s)	40	40	38	34	30
	Re_t (s)	145	142	142	140	136
20 ppm	Sensitivity (R_a/ R_g)	14.66	3.44	3.2	3	2.2
	R_t (s)	38	36	32	30	28
	Re_t (s)	148	148	146	144	142
30 ppm	Sensitivity (R_a/ R_g)	95	14.35	10.3	40	8.4
	R_t (s)	32	30	28	28	25
	Re_t (s)	150	150	148	145	140
40 ppm	Sensitivity (R_a/ R_g)	155	33.55	25.4	64.9	20
	R_t (s)	30	28	26	25	22
	Re_t (s)	170	165	160	155	150

Table 3.12 The sensitivity toward H_2S gas, response time and recovery time for sample 1M4 as a function of gas concentration and operating temperature.

Concentration of Gas	Response Parameters		Operating Temperature (^oC)				
		25	50	75	100	150	
10 ppm	Sensitivity (R_a/R_g)	5.8	2.4	2.3	1.63	1.2	
	R_t (s)	150	148	142	140	130	
	Re_t (s)	210	212	200	190	176	
20 ppm	Sensitivity (R_a/R_g)	11.6	4.1	5.1	2.09	1.79	
	R_t (s)	135	132	122	113	110	
	Re_t (s)	225	222	220	195	190	
30 ppm	Sensitivity (R_a/R_g)	13.7	12	9.4	3.06	1.9	
	R_t (s)	130	128	122	118	112	
	Re_t (s)	270	258	240	210	189	
40 ppm	Sensitivity (R_a/R_g)	24.5	21	14.6	3.72	2.1	
	R_t (s)	125	122	120	115	102	
	Re_t (s)	470	365	310	255	150	

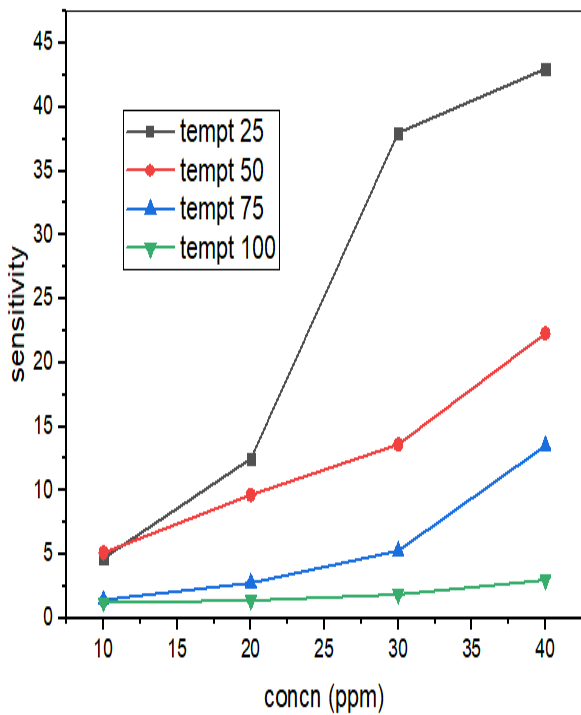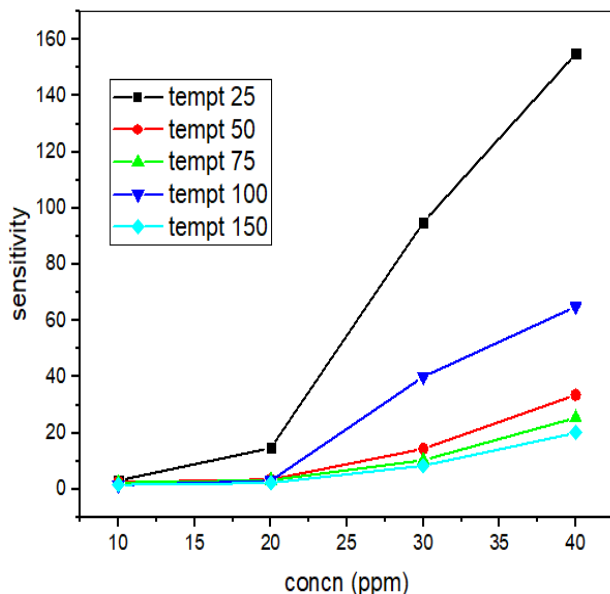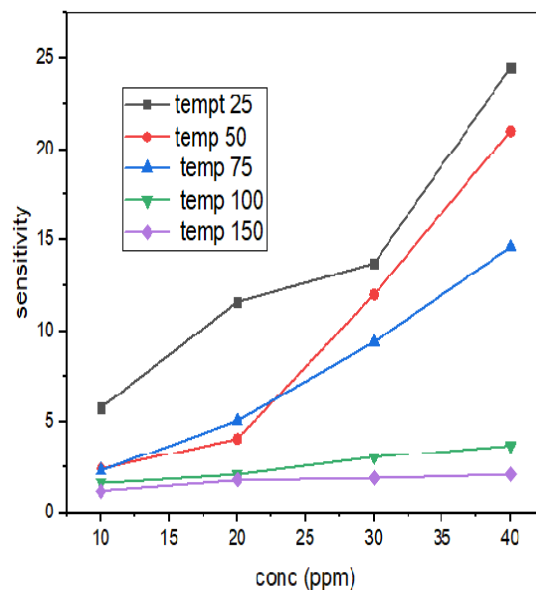|	
Figure 3.28. (a)	Figure 3.28 (b)

Figure 3.28 variation of sensitivity with operating temperature and concentration of H_2S gas; (a) for sample 1M1 and (b) for sample 1M4.

It was analysed from the above tables and graphs that as the precursor concentration increase time of response and recovery reduced because of the Cu concentration. The gas response toward hydrogen sulphide was tested of sample having lowest and highest thickness. It was found from the figures that sample 1M1 of thickness 378nm have high sensitivity in comparison of sample 1M4 of thickness 721 nm.

3.15 Selectivity of gas sensor

An attempt was made to study selectivity of CuO films for 40 ppm concentration of H_2S as compared to the sensitivities of ethanol and NH_3. Below figure shows the bar chart made from data obtained from various gases for selectivity.

It is observed from the figure 3.29 that thin films of CuO have high sensitivity toward H_2S as compared to other gases. This high sensitivity of CuO thin films for H_2S indicates that sensor made from CuO films is selective for this gas. Different interactions between the sensor film and the adsorbed gas can be used to explain this higher sensitivity. CuO is a p-type material that experiences a drop-in charge carrier density when it interacts with reducing gases like H_2S, ethanol, and many others. Conductivity falls as a result, and film resistance rises.

Our work is updated to H_2S gas sensing only. So, other gases we have used just to test the selectivity of our thin films for H_2S gas only.
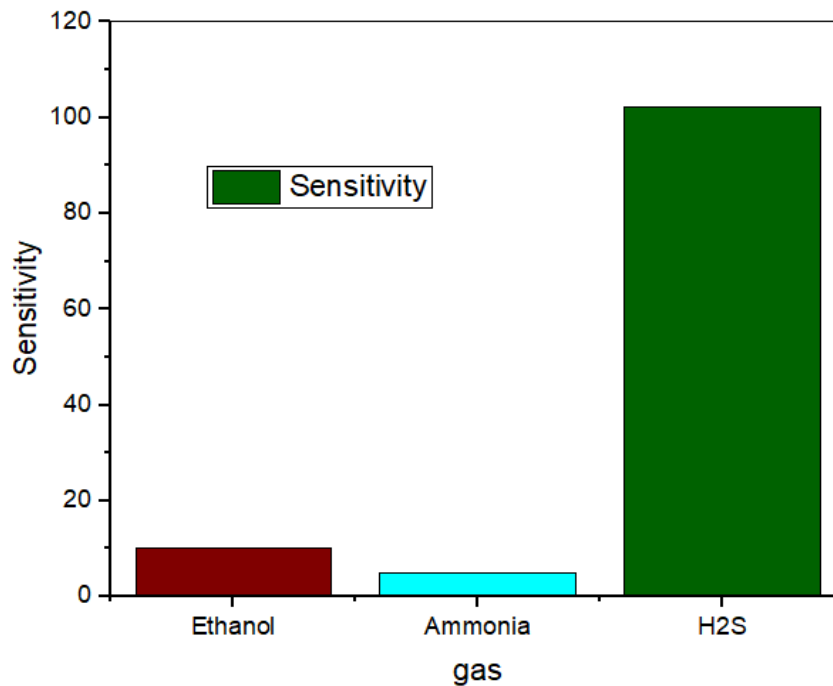
Figure 3.29 Gas responses of CuO sensor film (0.75M4 sample) toward 40 ppm of H_2S, NH_3, and ethanol.

3.16 References

[1] S. Asbrink & A. Waskowska. (1991). Journal of Physics: Condensed Matter. 3 (42), 8173.

[2] R.S. Niranjan, K.R. Patil, S.R. Sainkar & I.S. Mulla. (2003). Mater. Chem. Phys. 80, 250–256.

[3] S. Mridha & D. Basak. (2006). Semicond. Sci. Technol. 21, 928–932.

[4] R.B. Vasiliev, M.N. Rumyantseva, N.V. Yakovlev & A.M. Gaskov. (1998). Sens. Actuators B: Chem. 50,186–193.

[5] T. Kida, T. Oka, M. Nagano, Y. Ishiwata, X.-G. Zheng & J. Am. Ceram. (2007). Soc. 90, 107–110

[6] P. Samarasekara & N. G. K. V. M. Premasiri. (2015). Res. Rev.: J. Phys. (RRJoPHY) 4 (2), 8.

[7] M. Dahrul & H. Alatas. (2016). Procedia Environ. Sci. 33, 661.

[8] H. Z. Asl & S. M. Rozati. (2018). Mat. Res v. 2 (2), e20170754.

[9] K. S. Wanjala, E. Makori & J. M. Ngaruiya, Amer. (2016). J. Condensed Matter Phys. 6 (1), 1.

[10] H. Sawalha, M. Maghalseh, J. Qutaina, K. Junaidi, E. R. Rene. (2020). Bioengineered 11(1), 607-618.

[11] M. N. Hassankiadeh, A. Hallajisani. (2020). Journal of Petroleum Science and Engineering. 190, 107131.

[12] M.J. Priya, P.P. Subha, P.M. Aswathy, K.W. Merin, M.K. Jayaraj, K. R. Kumar. (2021). Materials Chemistry and Physics. 260, 124038.

[13] M. He, L. Xie, X. Zhao, X. Hu, S. Li, Z.G. Zhu. (2019). Journal of Alloys and Compounds. 788, 36–43.

[14] H. Yuan, S. Aljneibi, J. Yuan, Y. Wang, H. Liu, J. Fang, C. Tang, X. Yan, H. Cai, Y. Gu, S. J. Pennycook, J. Tao, D. Zhao. (2019). Advanced Materials. 31, 1807161.

[15] N.M. Hieu, D.V. Lam, T.T. Hien, N.D. Chinh, N.D. Quang, N.M. Hung, C. Van Phuoc, S.M. Lee, J.-R. Jeong, C. Kim, D. Kim. (2020). Materials & Design. 191, 108628.

[16] S. Yang, Z. Song, N. Gao, Z. Hu, L. Zhou, J. Liu, B. Zhang, G. Zhang, S. Jiang, H.-Y. Li, H. Liu (2019). Sensors Actuators B Chemical. 286, 22-31.

[17] K. Zhang, S. Qin, P. Tang, Y. Feng, D. Li. (2020). Journal of hazardous materials. 391, 122191.

[18] J.-H. Kim, A. Mirzaei, J.H. Bang, H.W. Kim, S.S. Kim. (2019). Sensors Actuators B Chemical. 300, 126981.

[19] A. Yang, W. Li, J. Chu, D. Wang, H. Yuan, J. Zhu, X. Wang, M. Rong. (2020). Materials & Design. 187, 108391.

[20] L. Yin, G. Qu, P. Guo, R. Zhang, J. Sun, D. Chen. (2019). Journal of Alloys and Compounds. 785, 367–373.

[21] M.H. Raza, K. Movlaee, S.G. Leonardi, N. Barsan, G. Neri, N. Pinna. (2019). Advanced Functional Materials. 30, 1906874.

[22] F. Peng, Y. Sun, W. Yu, Y. Lu, J. Hao, R. Cong, M. Ge, J. Shi, N. Dai. (2020). Nanomaterials. 10, 1–14.

[23] J. Deng, Z.Y. Zhao. (2019). Materials Research Express 6, 105513.

[24] Y.F. Lim, C. S. Chua, C. J. J. Lee & D. Chi. (2014). Physical Chemistry Chemical Physics. 16, 25928-25934.

[25] S. C. Ray. (2001). Solar energy materials and solar cells. 68, 307-312.

[26] C.J. Brinker & G.W. Scherer. (2013). Sol-Gel Science: The Physics and Chemistry of Sol-Gel Processing, Academic Press.

[27] N. Sahu, B. Parija & S. Panigrahi. (2009). Indian J. Phys. 83 (4), 493-502.

[28] Y. Mouhamad, P. Mokarian-Tabari, N. Clarke, R. A. L. Jones & M. Geoghegan. (2014). Journal of Applied Physics. 116 (12), 123513.

[29] De. Longchamp, D. M. Brandon, M. Vogel, Y. Jung, M. C. Gurau, C. A. Richter, O. A. Kirillov & Jan Obrzut. (2005). Chemistry of materials. 17 (3), 5610-5612.

[30] T. Ishitani, H. Tsuboi. (1997). Scanning. 19, 489–497.

[31] A. A. Tseng. (2004). J. Micromech. Microeng. 14 (4), 15-34.

[32] S. Joo, H. Liang. (2013). In Encyclopedia of Tribology; Springer US: Boston, MA, USA, 2989–2994.

[33] K.M. Greenland. (1952). Vacuum. 2 (3), 216-230.

[34] S. M. Abdulalmohsin & F. Ajeel. (2015). Journal of Applied Physical Science International. 3, 178-184.

[35] Z. Essalhi. (2017.) Opt. Quantum Electron. 49.

[36] G.K. Williamson & W.H. Hall. (1953). Acta Mater. 1, 22.

[37] B. C. Balasingh, A. Abuhasan, & P. K. Predecki. (1990). Powder Differ. 6 (1), 16.

[38] W. B. Wang. (2014). J. Vac. Sci. Technol. 32 (6), 061502.

[39] E.R. Shaaban, N. Afify & A. El-Taher. (2009). J. Alloys Compd. 482, 400–404.

[40] P. Samarasekara & N. G. K. V. M. Premasiri. (2015). Res. Rev.: J. Phys. (RRJoPHY). 4 (2), 8.

[41] M. Dahrul & H. Alatas. (2016). Procedia Environ. Sci. 33, 661.

[42] H. Zare Asl & S. Mohammad Rozati. (2018). Mat. Res v. 21n. (2), e20170754.

[43] L. Armelao. (2003). Thin Solid Films. 442 (1-2), 48.

[44] Sameer Atta. Makki & O. A. Mahmoud. (2017). Journal of Multidisciplinary Engineering Science Studies (JMESS). 4 (7).

[45] H. Absike, H. Labrim, B. Hartiti, M. Tahri & H. Ez-Zahraouy. (2020). Molecular Crystals and Liquid Crystals. 711(1), 18-31.

[46] S.T. Khlayboonme & W.Thowladdab. (2018). Key Engineering Materials. 766, 205 – 210.

[47] M. T. S. Nair, L. Guerrero, O. L. Arenas & P. K. Nair. (1999). Appl. Surf. Sci. 150, 143.

[48] B. Balamurugan & B.R. Mehta. (2001). Thin solid films. 396, 90.

[49] A. A. Saif, , Z. A. Z. Jamal & P. Poopalan. (2011). Zeitschrift für Naturforschung A, 66(12).

[50] F. Yakuphanoglu, M. Sekerci & O. F. Ozturk. (2004). Opt. Commun. 239 (4-6), 275. (2004).

[51] J. Tauc & A. Menth. (1972). J. Non-Cryst. Solids. 8, 569–585.

[52] M.G. Varnamkhasti, H.R. Fallah, M. Mostajaboddavati & A. Hassanzadeh. (2012). Vacuum 86(9), 1318–1322.

[53] D. S. C. Halin, I. A. Talib A. R. Daud & M. A. A. Hami. (2009). Solid State Science and Technology 17.

[54] R. A. Hammoodi, A. P. D. A. K. Abbas & A. K. Elttayef. (2014). International Journal of Application or Innovation in Engineering & Management (IJAIEM). 3, 1-7.

[55] N. Mukherjee, B. Show, S. K. Maji, U. Madhu, S. K. Bhar, B. C. Mitra, et al. (2011). Materials Letters. 65, 3248-3250.

[56] A. H Reshak, M. M Shahimin, N. Juhari & S. Suppiah. (2013). Progress in Biophysics and Molecular Biology. 113, 289-294.

[57] B. L. Anderson & R. L. Anderson. (2005). Mc Graw Hill International Edition.

[88] Y. Wang, J. Chen & X. Wu. (2001). Materials Letters. 49 (6), 361-364.

[59] A.I. Ayesh, A.A. Alyafei, R.S. Anjum & R.M. (2019). Applied Physics A. 125, 1-8.

[60] Y. Guo, B. Liu, Z. Duan, Z. Yuan, Y. Jiang & H. Tai. (2023). Materials Chemistry and Physics. 302, 127768.

[61] Y. Masuda. (2022). Sensors and Actuators B: Chemical. 364, 31876.

[62] A. Z. Sadek, W. Wlodarski, K.Kalantar-Zadeh & S. Choopun. (2005). Proc. IEEE Sensors. 2, 1326–1329.

CHAPTER 4

GROWTH AND CHARACTERIZATION OF Sn DOPED CuO THIN FILMS.

In this chapter, we present the synthesis and characterization of pure CuO thin films for gas sensing applications.

4.1 Introduction

Because of the toxic nature, high flammability and rotten egg like smell, H_2S gas is easily recognized. The main source of production of H_2S gas is decay of organic matters such as human and animal's waste by anaerobic digestion. The other sources of this poisonous gas are paper mills, oil-field and power station, tannery, water sewages and also through food processing [1-2]. A number of studies reveal the harmful effect of H_2S on human health and environmental quality. Therefore, it is very important to monitor its concentration for safety applications.

To detect H_2S gas, there are effective methods such as fluorescent probe [3], gas chromatography [4] and chemical method [5]. Due to their complex detection process and high cost, there is vast demand of simple and portable gas sensors. For domestic as well as industrial applications, it is commanding to develop H_2S gas sensor with fast response and recovery time, long repeatability, low operating temperature and high sensitivity/ stability. Recently, metal oxides have received great attention in gas sensing applications because of their low cost, simple fabrications, portability and compatibility [6-7]. On the basis of their charge carriers these metal oxide semiconductors are categorized into two types i.e. p-type and n-type. The SnO_2-based gas sensor has drawn more attention than other metal oxide semiconductor sensors because of its very high sensitivity [8].

As reported in literature, sensitive materials for H_2S detection are NiO, ZnO, TiO_2, SnO, WO_3, SnO_2 and CuO. The best performance shown by SnO_2 for hydrogen sulphide gas detection [9-12]. It is a wonderful material which is broadly used for gas sensor applications [13-14]. Because of their high operating temperature, poor selectivity, and incapacity to detect tiny concentrations of gas effectively, single metal oxides have been the subject of extensive research in recent decades as semiconductor gas-sensing materials [15-16]. Researchers have suggested using composite nanomaterial technology.

Li-Yuan Zhu et al. [17] produced a heterojunction p-CuO/n-SnO$_2$ core-shell nanowire (NW)-based high-sensitivity and high-selectivity gas sensor. CuO semiconductor is widely used in gas detection due to exhibition of good response toward toxic gases like CO and H$_2$S. CuO thin films achieve appreciable gas sensing response due to change in resistance on changing environmental conditions. Due to its transformation from p-type semiconducting CuO to CuS, a degenerate semiconductor caused by ion vacancies (Cu or S), CuO is a remarkable activator of H$_2$S sensing.

However, SnO$_2$ that is semiconducting n-type and has a large energy band gap of 3.6 eV. SnO$_2$ responded strongly to ethanol [18]. Furthermore, Phouc et al. [19] found that the product had the maximum response to H$_2$S at an operating temperature of 200 °C. They created SnO$_2$ porous nanofibers by electro spinning method. In addition, the porous SnO$_2$ films exhibited a strong reaction to triethylamine due to their abundance of oxygen vacancies [20]. The main problems associated with these sensors is that they can't be used in environments containing very low concentration of H$_2$S gas at low operating temperature. Also, the preparatory techniques of CuO-SnO$_2$ sensor elements as reported in literature are complicated and time consuming. Therefore, an attempt was made to make low operating gas sensor by using Sn doped CuO thin films.

In this work, CuO thin films were prepared by using Sn as dopant. These films were characterized by two-probe set up, UV spectrometer and through X-Ray diffraction. Thickness of samples was analyzed by using gravimetric analysis. The obtained band gap of samples varies from 3.27eV to 3.83eV as the thickness of samples decrease from 570nm to 165nm. These synthesized films were used to detect response of H$_2$S gas at various concentrations and several operating temperatures. Among these prepared films, the highest response was found for thin films of thickness 165nm.

4.2 Experimental procedure for preparation of nanostructured CuO thin films

There were various steps involve during the preparation of doped CuO thin films, including preparing glass substrate, used chemicals and cleaning procedure of glassware discussed in subsection 3.2 to 3.4 in chapter 3. All the chemicals used in present investigation are of high purity obtained from sigma Aldrich and used in the form as received.

Nanocrystalline thin films of CuO have been developed via sol-gel spin coating technique using copper acetate dihydrate and iso-propanol as precursors. Stannous chloride di-hydrate (SnCl$_2$.2H$_2$O) was used as a dopant to form Sn doped copper oxide thin films. To form the

CuO sample, first of all sol-gel have to be formed to deposit on glass substrate. The detail of gel formation and experimental procedure is described as below
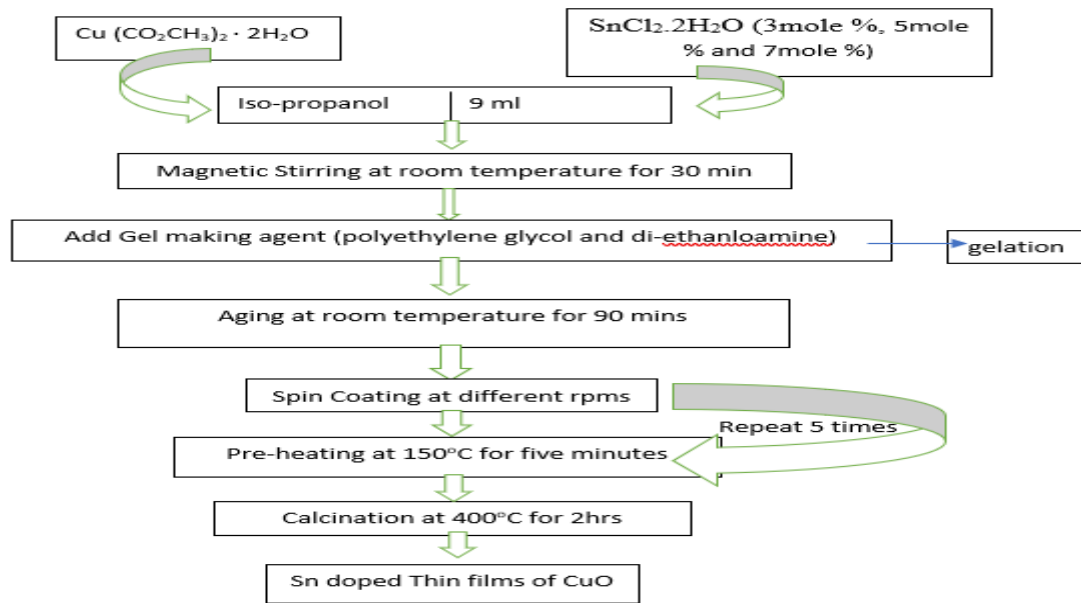

Figure 4.1 The formation of Sn doped thin films.

Table 4.1 The prepared samples of Sn doped thin films of CuO

| Concentration of prepared solution	Name of sample	Spinning speed (RPM)	Deposition temperature	Thickness (nm)
0.75M	0.75MD1	3000		165
	0.75MD2	2500		337
	0.75MD3	2000		461
	0.75MD4	1500		570
1M	1MD1	3000		181
	1MD2	2500	400°C	288
	1MD3	2000		413
	1MD4	1500		528

Various samples were prepared by using different concentration and by varying spinning speed. Four samples of 0.75M concentration was synthesized named as 0.75MD1, 0.75MD2, 0.75MD3 and 0.75MD4 of spinning speed 3000rpm, 2500 rpm, 2000 rpm and 1500 rpm respectively. Similarly, four samples of 1 molar concentration were also prepared by varying spinning speed. The synthesized samples were labelled in the manuscript as 1MD1 for 3000rpm, 1MD2 for 2500rpm, 1MD3 for 2000rpm and 1MD4 for 1500rpm for discussion

4.3 Characterization of Sn doped CuO thin Films

An enumerated number of techniques was employed to explore the structural, optical, morphological and electrical characteristics of the films, presented as below:

4.3.1 Morphological properties

In this work, morphological study of surface of Sn doped CuO thin films was doing by FESEM technique. As seen in figure 4.2 below, the CuO: SnO2 target material's micrograph has a homogeneous distribution with a semi-spherical shape. It displays the deposited films' EDX spectra side by side, confirming the samples' purity. The illustrations below illustrate the investigation and display of both morphology and elemental composition.
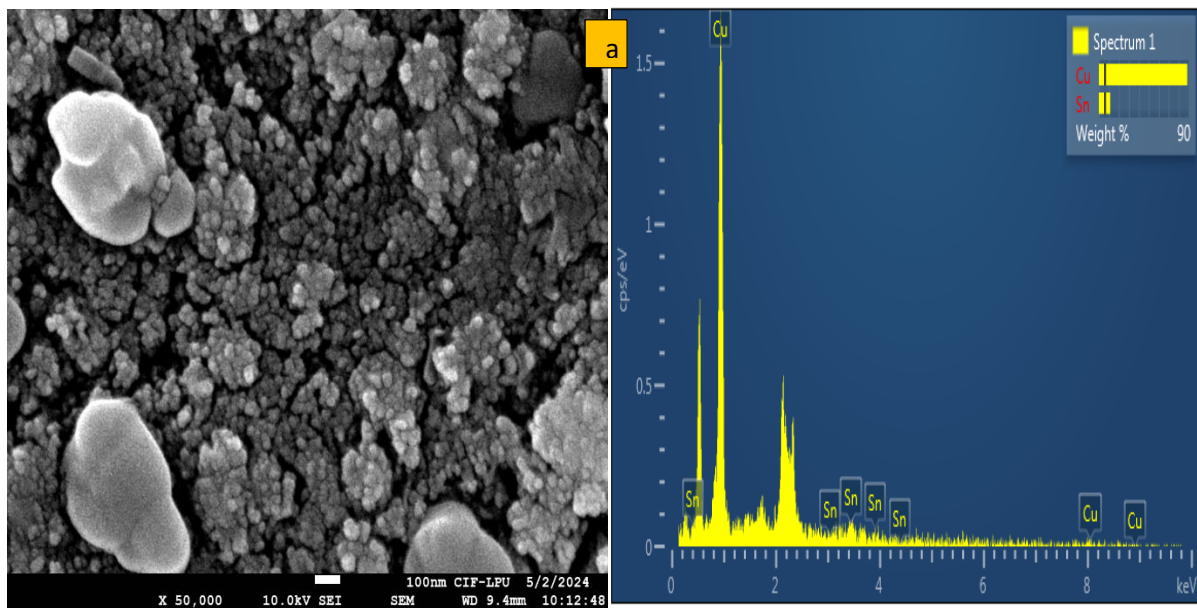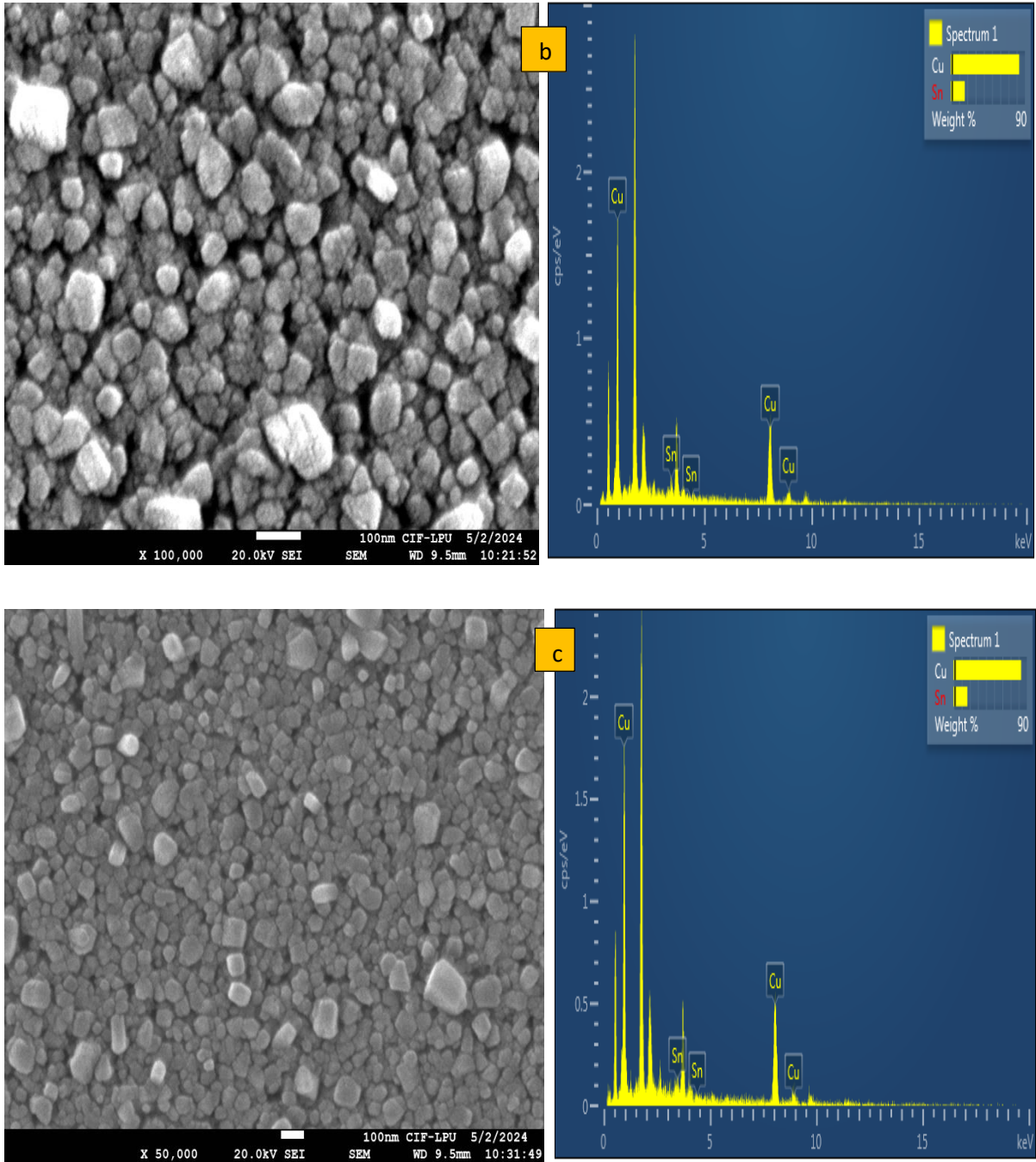
Fig 4.2 SEM micrographs and EDX spectra of (a) 0.75M1 sample of thickness 165 nm, (b) 0.75M2 sample of thickness 337nm and (c) 1M1 sample of thickness 181nm.

The study revealed that there was a corresponding increase in grain size from 50nm to 54nm with an increase in thickness from 165nm to 337nm in films made at a 0.75M concentration. This was probably brought about by the elimination of carbon traces from the particle's surface, which forced nearby particles to aggregate and eventually form massive particles [21]. It can be observed that the rough, net-like shape is changing as concentration rises. Similar growth behavior was reported in Sn-doped ZnO [22] and CuO-doped Wo_3 films [23]. In samples (a)

and (b), the surface grows rougher, whereas in sample (c), the surface becomes smoother with increasing concentrations. Samples with rough surfaces always have more sites available for gas molecules to adsorb onto them. Consequently, for optimal gas sensing performance, the surface of the sample prepared at 0.75M concentration is appropriate.

4.3.2 Structural properties

X-ray diffraction spectra recorded for Sn doped CuO thin films of different molarities prepared by sol-gel spin coating technique.
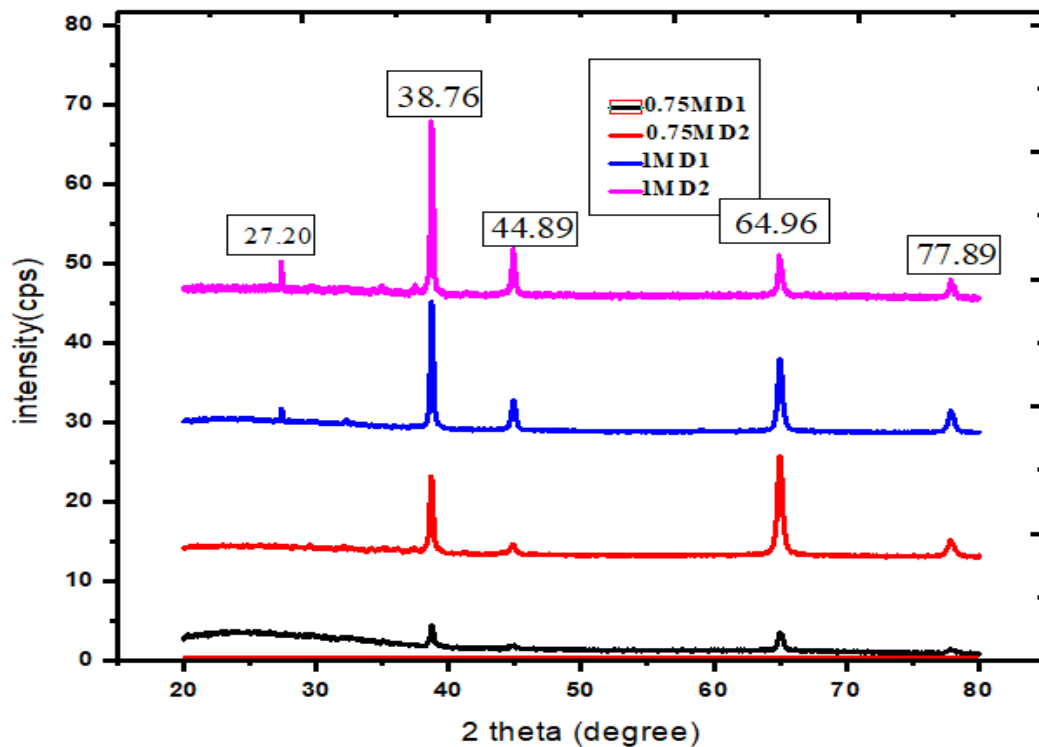

Figure 4.3 XRD pattern of Sn doped CuO thin films.

In figure 4.3, we have reported produced CuO thin films' XRD pattern. These films are of different thickness at a constant annealing temperature of 400°C for different precursor concentrations of 0.75M and 1M. The preferred orientation of the film, seen in the above figure, was along the planes (111) and (200) with diffraction angles of 38.76° and 44.89°, respectively. It has been observed that these peaks exist for all Sn doped CuO films and their intensity increase on increasing the molarity from 0.75 M to 1M. In addition, other low intensity peaks were observed at $2\Theta = 27.20°$, 64.96° and 77.89° corresponding to atomic plane (110), (112) and (321) respectively, (JCPDS card no. 82-087). The obtained peaks resemble with the results obtained by S.R. Cynthia [24] showing that this would make it possible for CuO and SnO_2 to form a p-n heterojunction. The calculated structural parameters are shown by given table.

Table 4.2 Structural parameters of Sn doped CuO thin films.

Name of sample	Thickness (nm)	Crystallite size (nm)	Strain (m)	Dislocation density (10^{15} m^{-2})
0.75MD1	165	14.33	0.00523	4.869
0.75MD2	337	16.83	0.00202	3.531
1MD1	181	23.61	0.00133	1.794
1MD2	288	43.79	0.00057	0.0521

It was noted from the calculated parameters that crystallite size goes on increasing as the molarity of films increasing. The rise in molarity causes an increase in the concentration of Cu, which causes more condensation of Cu atoms and a quicker nucleation rate, both of which result in the formation of larger crystallite sizes. These findings were agreed with Shabu et.al., [25].
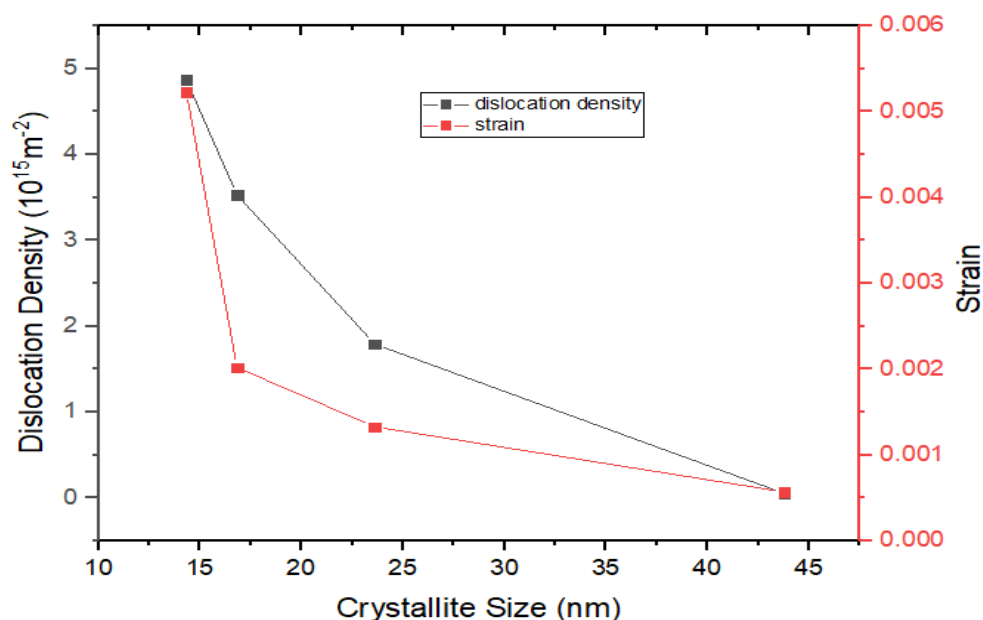

Figure 4.4 Variation of strain and dislocation density with crystallite size.

From figure 4.4, it was found that both dislocation density and strain decrease on increasing crystallite size. This is due to the reason as the crystallite size increases, more regular will be the crystalline structure. The decreasing order of both dislocation density and strain shows the improvement in high quality of thin films.

4.3.3 Optical Properties

By using Tauc relationship, we can obtain the direct band of CuO thin films which is shown by given table.

Table 4.3 The variation of band gap on varying thickness.

Name of Sample	Thickness (nm)	Direct Band Gap (eV)
0.75MD1	165	3.83
0.75MD2	337	3.72
0.75MD3	461	3.66
0.75MD4	570	3.27
1MD1	181	2.36
1MD2	288	2.20
1MD3	413	1.70
1MD4	528	1.45

It was noted from the table that band gap gets reduce on increasing the thickness which demonstrates how films are getting better.
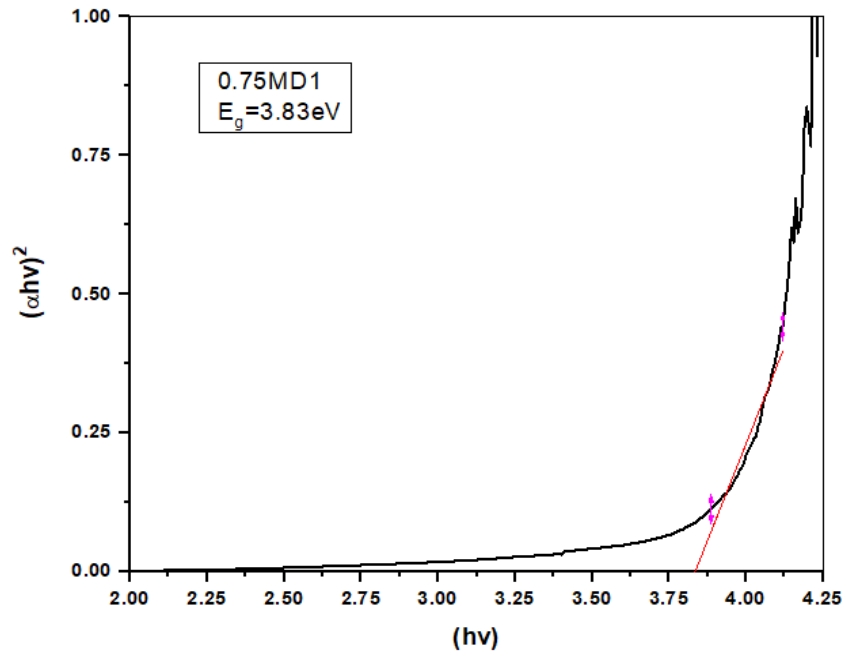
Figure 4.5 (a) Direct band gap of 0.75MD1 sample of Sn doped CuO films.
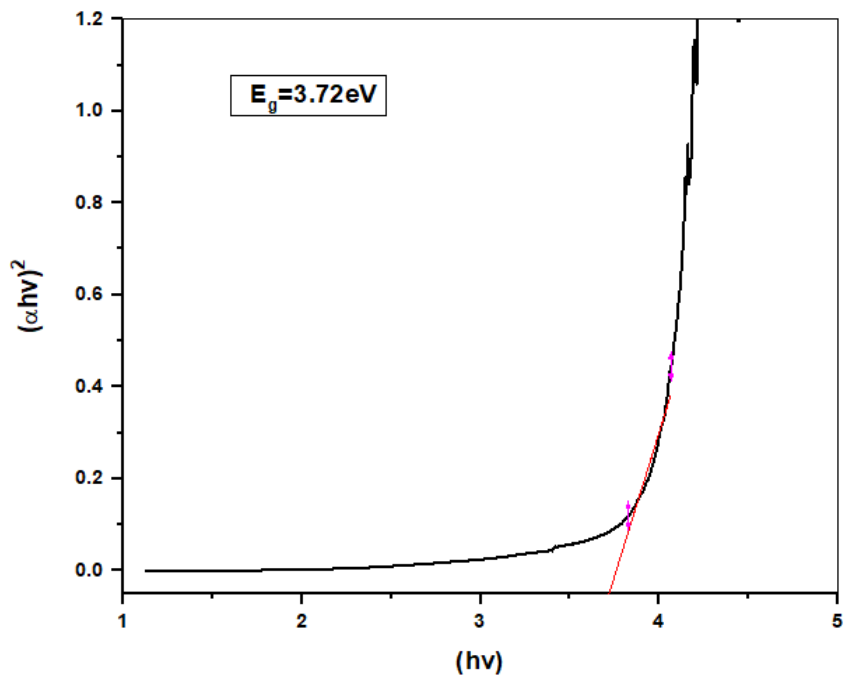

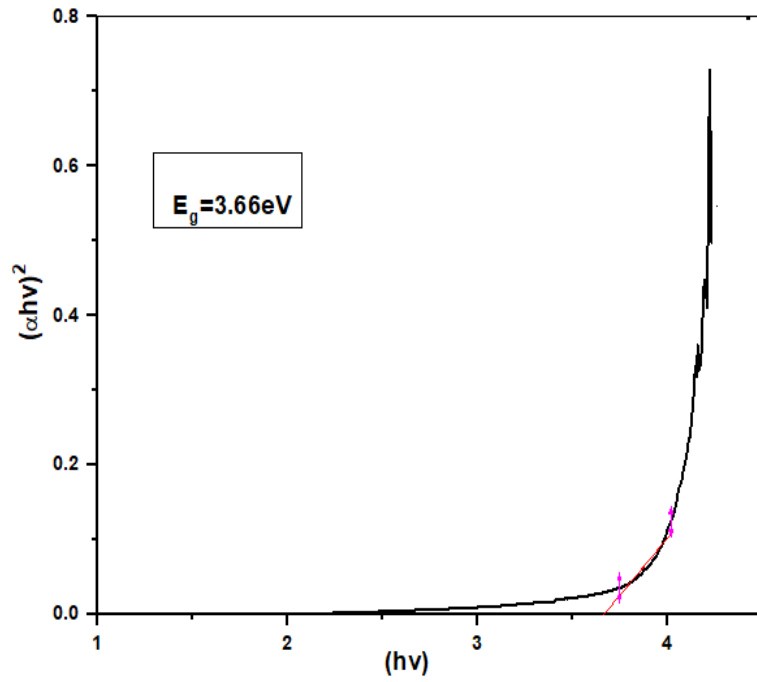Figure 4.5 (b) Direct band gap of 0.75MD2 sample of Sn doped CuO films.

Figure 4.5 (c) Direct band gap of 0.75MD3 sample of Sn doped CuO films.
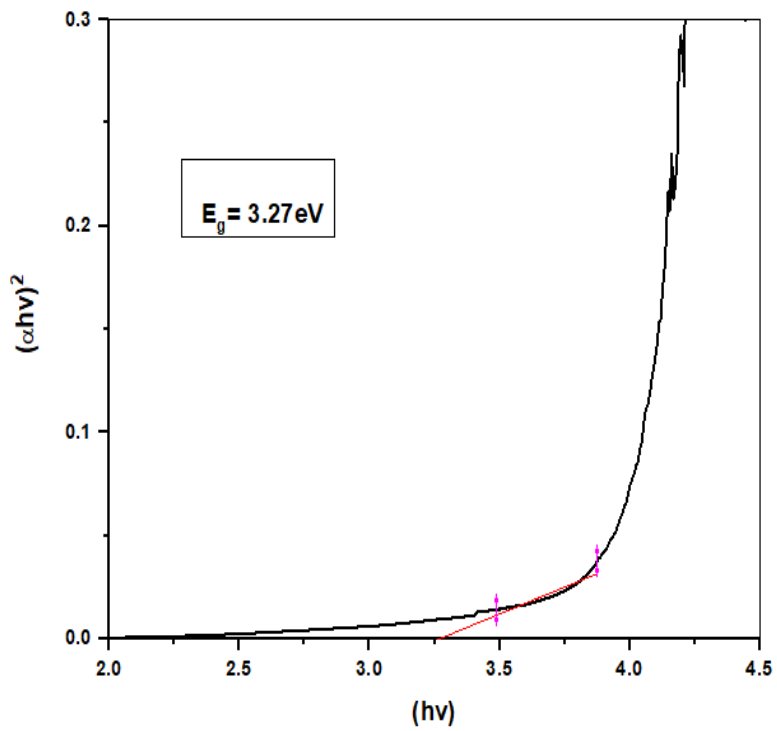
Figure 4.5 (d) Direct band gap of 0.75MD4 sample of Sn doped CuO films.
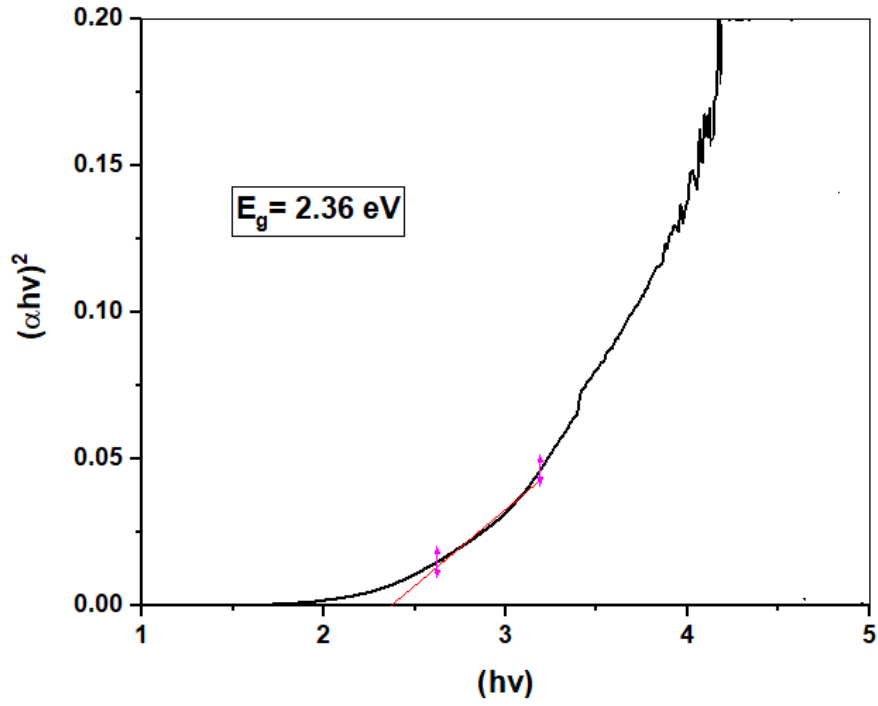
Figure 4.6 (a) Direct band gap of 1MD1 sample of Sn doped CuO films.
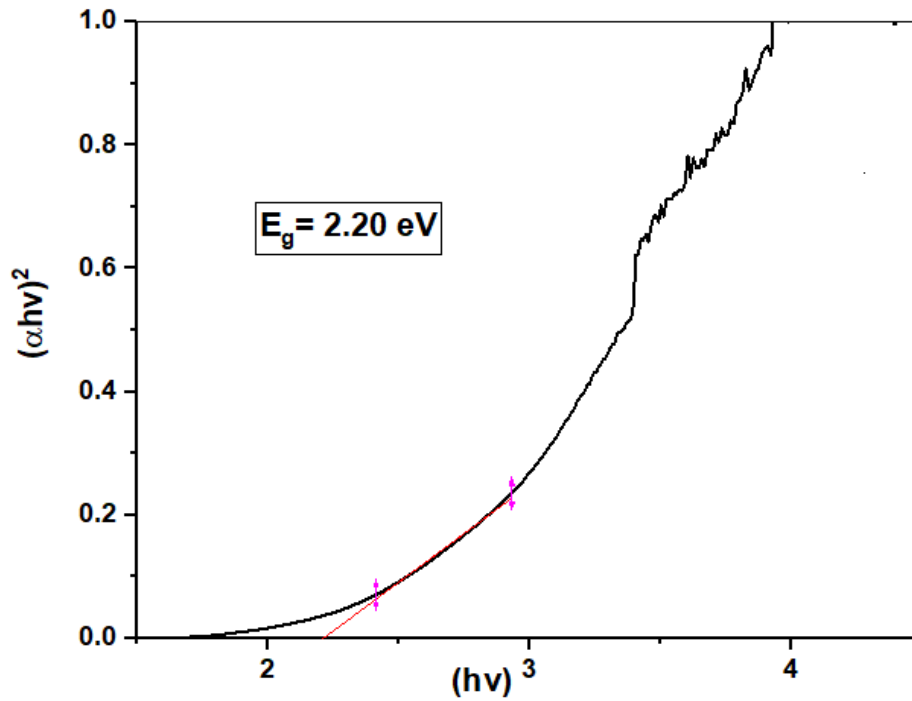
Figure 4.6 (b) Direct band gap of 1MD2 sample of Sn doped CuO films.
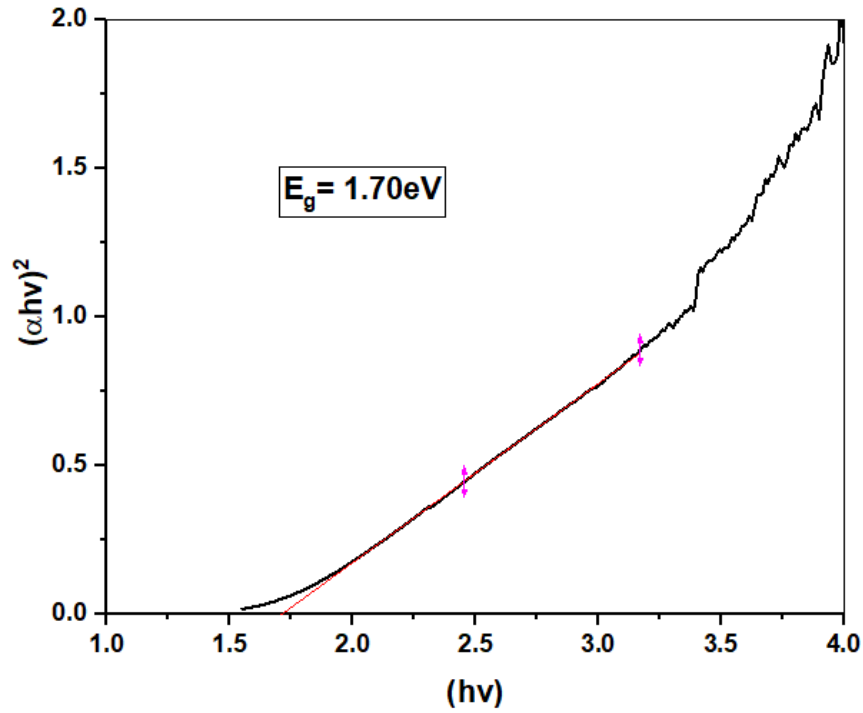
Figure 4.6 (c) Direct band gap of 1MD3 sample of Sn doped CuO films.

Figure 4.6 (d) Direct band gap of 1MD4 sample of Sn doped CuO films.

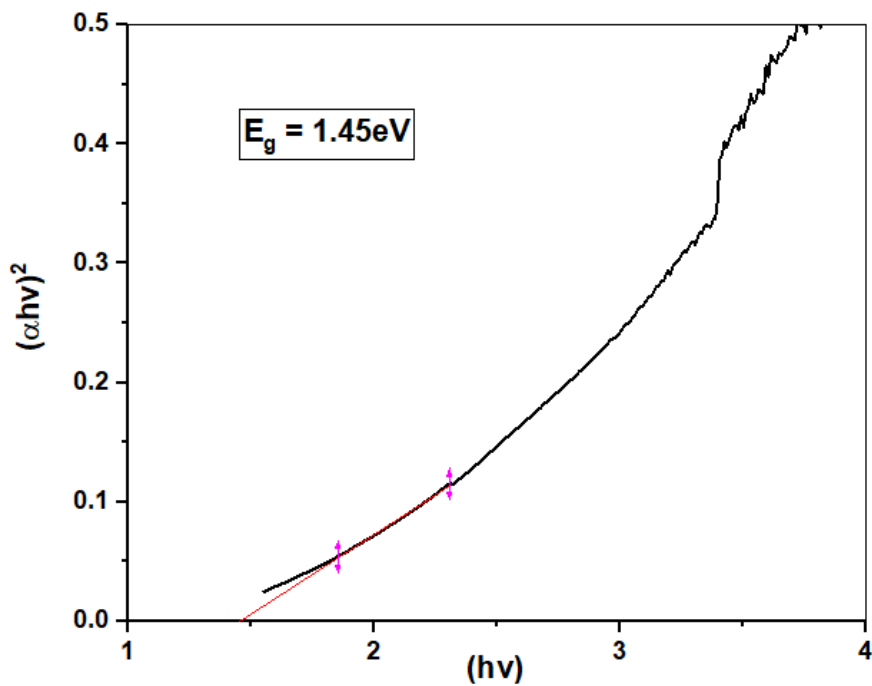As seen from the above graph, band gap of sample has been obtained from the spectral variation of $(\alpha h\nu)^2$. Band gap can be calculated by extrapolating a straight line until it reaches the point where $(h\nu)^2 = 0$. It is found to lie between 3.84 to 3.27eV of sample prepared from 0.75M and

between 2.20 to 1.45eV for sample prepared from 1M. With increasing the molarity concentration of precursor solution from 0.75M to 1M, the optical band gap reduces from 3.84 to 1.45 eV. These values agree with those reported earlier for CuO.

4.3.4 Electrical Properties

To check electrical properties, two electrodes were made on samples by using silver paste through which we can analyse current. It was found that current linearly increase on increasing the voltage which reveals that prepared films were of ohmic in nature.

At room temperature, the electrical resistance of films prepared from 0.75M Sn doped CuO is found to lie between 2.23×10^7 Ω to 1.66×10^6 Ω. The resistance of 0.75MD1 films is found to be comparatively lower than 0.75MD2, 0.75MD3 and 0.75MD4 films. The range of electrical resistance of sample prepared from 1M concentration was in range of 0.5×10^7 Ω to 0.2×10^7 Ω. It was noted from the below graph that lower resistance of sample 1MD4 and highest resistance of sample 1MD1. This variance of resistance might due to thickness of prepared samples from both precursor concentration of 0.75M and 1M.
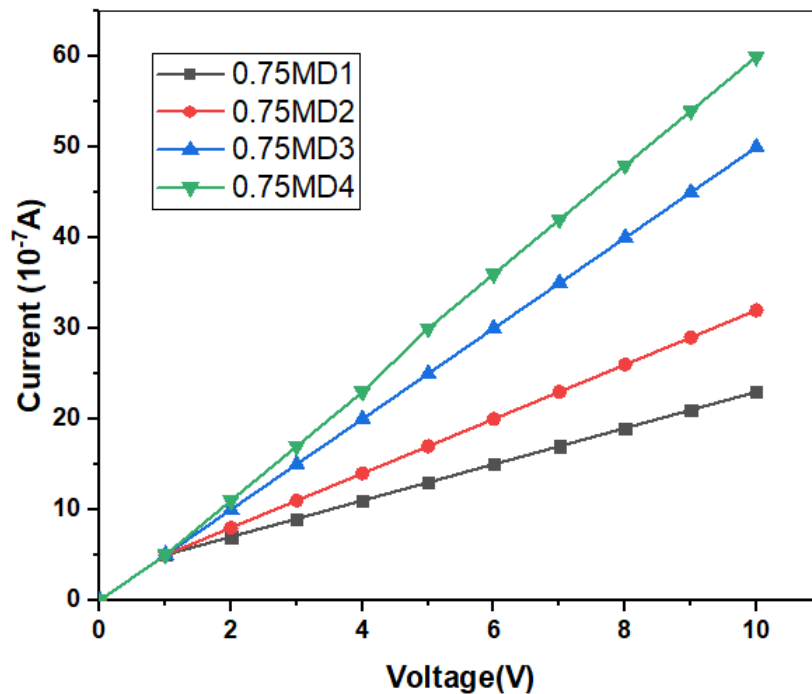

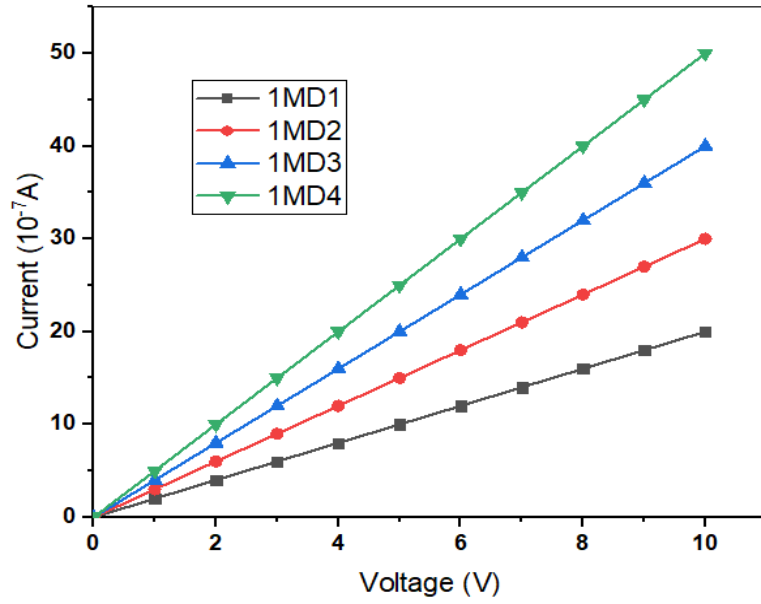Figure 4.7 I-V properties of thin Sn-doped CuO films of 0.75 Molarity.

Figure 4.8 I-V properties of thin Sn-doped CuO films of 1M concentration.
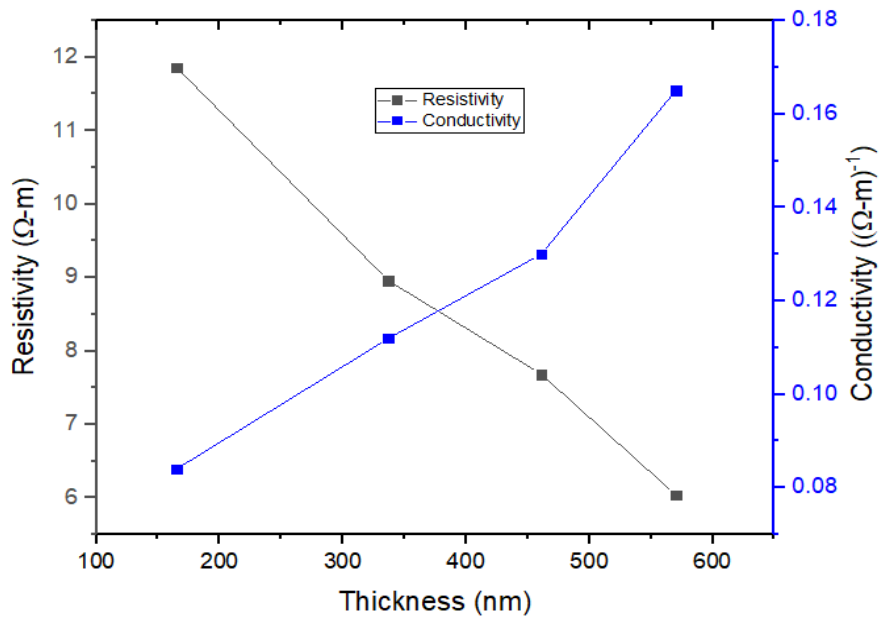

Figure 4.9 Variation of resistivity and conductivity of Sn doped CuO thin films of 0.75M concentration as function of thickness.
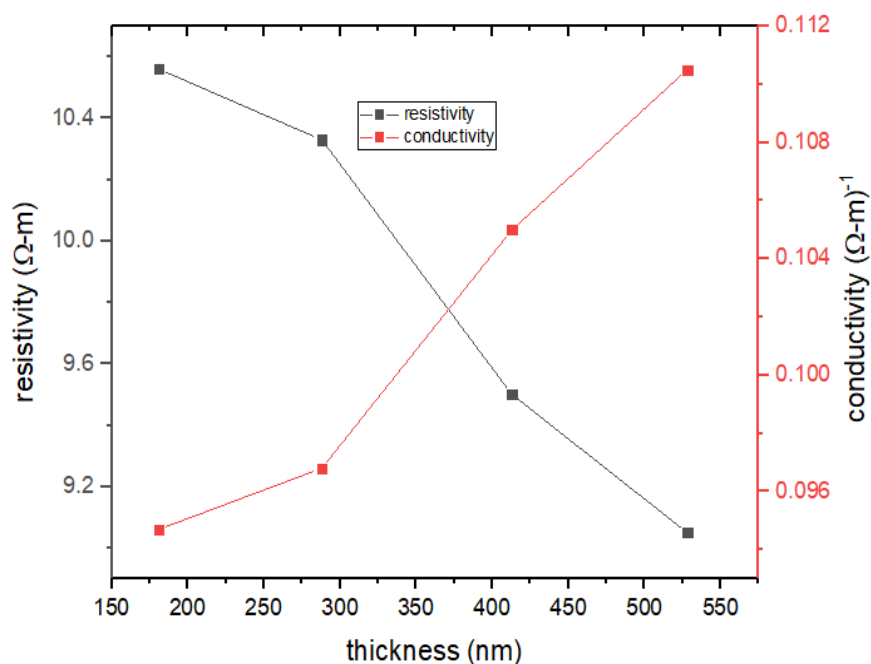
Figure 4.10 Variation in resistivity and conductivity of Sn doped CuO thin films of 1M concentration with thickness.

The lowest resistivity was 6.04 Ω-m at 570nm while highest resistivity was about 11.86 Ω-m at 165nm for sample prepared from 0.75M concentration of Sn doped CuO. The highest and lowest value of conductivity of 1MD sample are 0.1105 $(\Omega\text{-m})^{-1}$ and 0.0947 $(\Omega\text{-m})^{-1}$ respectively. It was noted from the figure 4.9 and 4.10 that resistivity of doped sample decreases on increasing the thickness of films. Due to increased electron and hole carrier concentration, resistance reduced and conductivity increased.

Furthermore, as thin films become thinner, electron scattering at various interfaces becomes more prominent. Grain boundaries, surfaces, and interfaces serve as scattering centers that hinder electron flow. In thicker films, electrons have a higher probability of avoiding these scattering sites due to their greater average distance from them. However, as thickness decreases, electrons encounter these scattering sites more frequently, leading to enhanced scattering and subsequently increased resistivity.

As the thickness of sample increases then conductivity increase due to enhancement in large number of charge carriers. On increasing the molarity of precursor solution, change in resistivity was noted. It was found that resistivity gets reduce on increasing the molarity of solution.

4.4 Gas Sensor

Sn doped CuO thin films of different precursor concentration 0.75M and 1M have been tested for various concentration of hydrogen sulphide gas at 25°C. The sensitivity, response time and recovery time toward hydrogen sulphide gas at different ppm of gas has been described in upcoming section. The fabrication of gas sensor using thin films of CuO has already described in chapter 3, section 3.7. The difference is that here we use Sn doped CuO films as a testing material instead of pure CuO films.

4.5 Mechanism of Gas Sensor fabricated from Sn doped CuO thin films.

CuO films' sensing mechanism relies on changes in their conductivity and resistance after exposure to H_2S gas [26]. It can be understood by the following reaction that occurs when this gas is supplied and it reacts with the adsorbed oxygen at the sensor surface:

$$R + O^- (ads) \rightarrow RO + e- \quad (4.1)$$
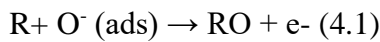
O^- (ads) is the oxygen ion adsorption, R is the reducing gas and e^- are liberated electrons. [27-28]. The CuO/SnCl2 thin film offers more surface area for the gas molecules to adsorb and disperse.

(a)   (b)
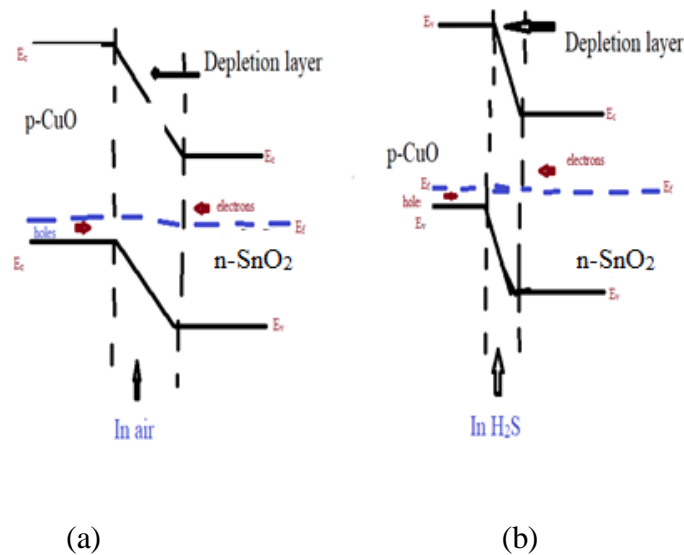
Figure 4.11 Mechanism of gas sensor; (a) in presence of air and (b) in presence of H_2S gas.
The above figure 4.11 (a) shows high resistivity of sensing materials in air is caused by the charge carrier depletion layer that forms at the p-CuO/n-SnCl₂ interface. When H_2S gas is exposed then p-n junction gets break down by transforming CuO to CuS. Due to this junction breakdown depletion layer becomes thin and we obtained low resistance of sensing materials as shown in figure 4.11 (b).

4.6 Gas Sensing Performance

The sensing results obtained from Sn doped CuO based sensor of various samples of different doping (3%, 5% and 7%) are presented below.

4.7 H₂S sensing toward Sn doped 0.75M concentration films of CuO

Gas response of prepared Sn (3%) doped CuO thin sheets from 0.75M concentration has been calculated by using equation (3.13) as described in section 3.12, chapter 3. Figure 4.12. (a) – (d) shows response for different concentration of gas.
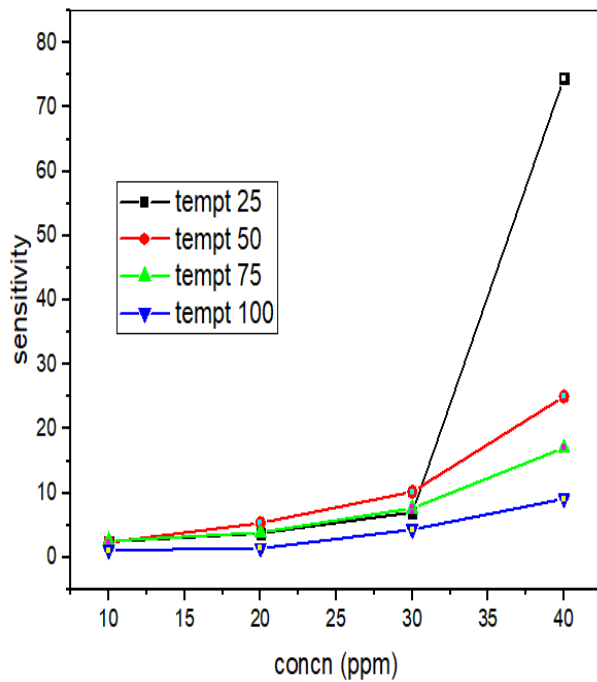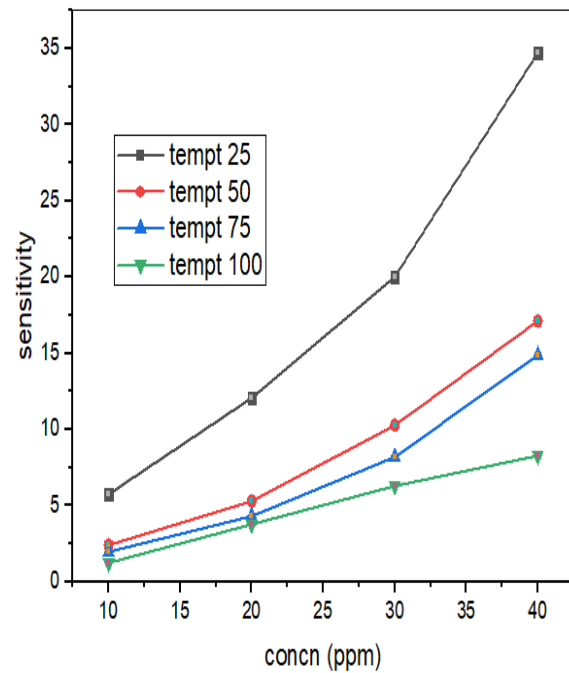
Figure 4.12. (a)   Figure 4.12. (b)
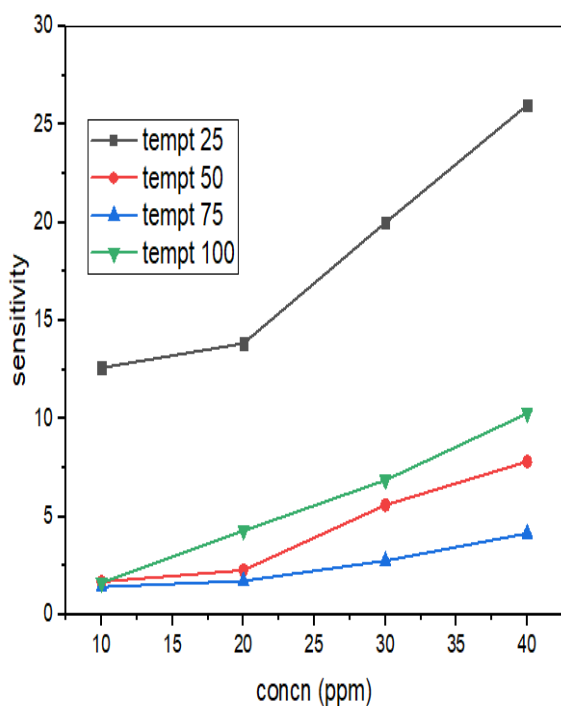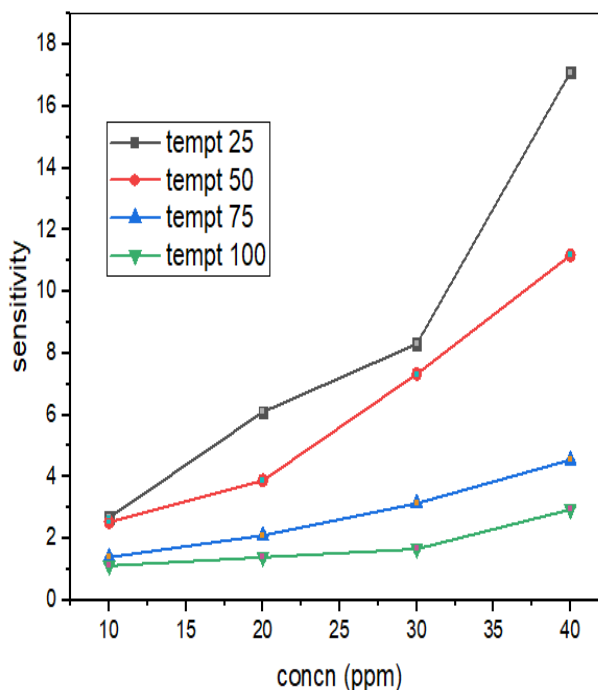
Figure 4.12 (c)   Figure 4.12 (d)

Figure 4.12 (a), 4.6. (b), 4.6. (c) and 4.6. (d) Sensitivity of sample 0.75MD1, 0.75MD2, 0.75MD3 and 0.75MD4 respectively with operating temperature and concentration of H_2S gas.

It was noticed from the above figures that the highest gas response of all samples was achieved at room temperature. It was observed that response of films also starts decreasing as the operating temperature increases which is explained by the phenomena of adsorption and desorption of oxygen. These results are in close agreement with [29-31].

The obtained response time, recovery time and calculated response of different samples are provided in table 4.4. – 4.7. Amongst the samples named as 0.75MD1, 0.75MD2, 0.75MD3 and 0.75MD4, it was found that 0.75MD1and 0.75MD4 sample have highest and lowest gas response of 74.63 and 17.13 respectively. At room temperature, sample 0.75MD1 have lowest response time of 5 seconds and sample 0.75MD4 have highest response time of 50 seconds. The highest sensitivity and lowest response time are due to the reason of lesser thickness of sample 0.75MD1. It has also been noticed that Sn doped CuO thin films fully recovered their resistance due to smaller molecule size of hydrogen sulphide gas. On the basis of obtained results we can conclude that the response time and recovery time can be reduced by doping of Sn to thin films of CuO.

Table 4.4 Fluctuations of sensitivity toward H_2S gas, time of response and recovery of sample 0.75MD1 with concentration of gas and operating temperature.

Concentration of Gas	Response Parameters	Operating Temperature (°C)			
		25	50	75	100
10 ppm	Sensitivity (R_a/R_g)	2.44	2.33	2.53	1.12
	R_t (s)	15	15	14	12
	Re_t (s)	125	125	122	120
20 ppm	Sensitivity (R_a/R_g)	5.33	3.77	3.88	1.39
	R_t (s)	10	10	8	8
	Re_t (s)	140	137	120	120
30 ppm	Sensitivity (R_a/R_g)	7	10.17	7.66	4.33
	R_t (s)	8	7	8	7
	Re_t (s)	150	150	140	142
40 ppm	Sensitivity (R_a/R_g)	74.5	25	17	9.11
	R_t (s)	5	5	5	5
	Re_t (s)	160	160	150	148

Table 4.5 Fluctuations of sensitivity toward H_2S gas, time of response and recovery of sample 0.75MD2 with concentration of gas and operating temperature.

Concentration of Gas	Response Parameters	Operating Temperature (^oC)			
		25	50	75	100
10 ppm	Sensitivity (R_a/ R_g)	5.75	2.41	1.96	1.24
	R_t (s)	18	18	17	16
	Re_t (s)	126	126	120	114
20 ppm	Sensitivity (R_a/ R_g)	12.07	5.3	4.31	3.77
	R_t (s)	16	16	15	12
	Re_t (s)	132	132	130	128
30 ppm	Sensitivity (R_a/ R_g)	20.01	10.27	8.19	6.29
	R_t (s)	14	14	10	10
	Re_t (s)	142	140	140	132
40 ppm	Sensitivity (R_a/ R_g)	34.72	17.12	14.87	8.28
	R_t (s)	12	12	10	10
	Re_t (s)	180	178	170	160

Table 4.6 Fluctuations of sensitivity toward H_2S gas, time of response and recovery of sample 0.75MD3 with concentration of gas and operating temperature.

Concentration of Gas	Response Parameters	Operating Temperature (°C)			
		25	50	75	100
10 ppm	Sensitivity (R_a/R_g)	12.6	1.68	1.42	1.63
	R_t (s)	22	22	21	20
	Re_t (s)	130	125	125	120
20 ppm	Sensitivity (R_a/R_g)	13.84	2.27	1.72	4.28
	R_t (s)	20	20	20	18
	Re_t (s)	136	132	130	128
30 ppm	Sensitivity (R_a/R_g)	20	5.59	2.75	6.86
	R_t (s)	18	18	17	15
	Re_t (s)	140	140	138	132
40 ppm	Sensitivity (R_a/R_g)	26	7.81	4.15	10.27
	R_t (s)	15	15	13	12
	Re_t (s)	150	148	140	130

Table 4.7 Fluctuations of sensitivity toward H_2S gas, time of response and recovery of sample 0.75MD4 with concentration of gas and operating temperature.

Concentration of Gas	Response Parameters	Operating Temperature (^oC)			
		25	50	75	100
10 ppm	Sensitivity (R_a/R_g)	2.68	2.53	1.4	1.12
	R_t (s)	25	25	24	23
	Re_t (s)	135	135	132	130
20 ppm	Sensitivity (R_a/R_g)	6.1	3.88	2.1	1.39
	R_t (s)	22	22	20	20
	Re_t (s)	140	137	132	128
30 ppm	Sensitivity (R_a/R_g)	8.3	7.33	3.14	1.66
	R_t (s)	19	19	18	16
	Re_t (s)	148	145	145	138
40 ppm	Sensitivity (R_a/R_g)	17.11	11.17	4.55	2.94
	R_t (s)	17	16	15	12
	Re_t (s)	160	158	150	138

4.8 H_2S sensing toward Sn doped CuO thin films of 1M concentration

In our work, molarity changes from 0.75M to 1M then thickness increase from 165 to 181nm. Similar type of observation has also been reported by Shabu et al [25]. The sensitivity of sample

155

prepared from 3% doping of Sn to thin films of CuO is shown by given table 4.8- 4.11 and figure 4.13 (a) – 4.13 (d).

Table 4.8 The sensitivity toward H_2S gas, response and recovery time for sample 1MD1 with gas concentration and operational temperature.

Concentration of Gas	Response Parameters	Operating Temperature (°C)			
		25	75	100	150
10 ppm	Sensitivity (R_a/ R_g)	3.1	2.88	1.4	1.2
	R_t (s)	25	25	24	24
	Re_t (s)	120	120	110	108
20 ppm	Sensitivity (R_a/ R_g)	19	17	16.8	4.5
	R_t (s)	22	22	20	19
	Re_t (s)	130	130	120	120
30 ppm	Sensitivity (R_a/ R_g)	89	60	32.8	8.2
	R_t (s)	21	20	20	18
	Re_t (s)	150	149	149	148
40 ppm	Sensitivity (R_a/ R_g)	1036	450	61.6	7.76
	R_t (s)	18	18	18	15
	Re_t (s)	180	180	178	175

Table 4.9 The sensitivity toward H_2S gas, response and recovery time for sample 1MD2 with gas concentration and operational temperature.

Concentration of Gas	Response Parameters	Operating Temperature (^oC)			
		25	75	100	150
10 ppm	Sensitivity (R_a/R_g)	18.6	14	10	5.68
	R_t (s)	28	28	248	27
	Re_t (s)	125	125	122	120
20 ppm	Sensitivity (R_a/R_g)	32	25	20.09	7.33
	R_t (s)	26	26	26	24
	Re_t (s)	130	128	126	124
30 ppm	Sensitivity (R_a/R_g)	364	180	36.09	19.3
	R_t (s)	24	24	22	21
	Re_t (s)	140	149	149	148
40 ppm	Sensitivity (R_a/R_g)	833	340	65.54	24.6
	R_t (s)	18	18	18	15
	Re_t (s)	160	158	158	150

Table 4.10 The sensitivity toward H_2S gas, response and recovery time for sample 1MD3 with gas concentration and operational temperature.

Concentration of Gas	Response Parameters	Operating Temperature (^{o}C)			
		25	75	100	150
10 ppm	Sensitivity (R_a/R_g)	2.5	1.69	1.46	1.16
	R_t (s)	32	32	30	30
	Re_t (s)	138	138	136	136
20 ppm	Sensitivity (R_a/R_g)	52.5	12.85	2.26	1.88
	R_t (s)	30	30	28	27
	Re_t (s)	136	136	132	134
30 ppm	Sensitivity (R_a/R_g)	116.5	53.85	4.4	3.03
	R_t (s)	29	29	28	26
	Re_t (s)	134	133	132	130
40 ppm	Sensitivity (R_a/R_g)	420	100	6.86	4.03
	R_t (s)	25	25	24	22
	Re_t (s)	154	154	150	150

Table 4.11 The sensitivity toward H_2S gas, response and recovery time for sample 1MD4 with gas concentration and operational temperature.

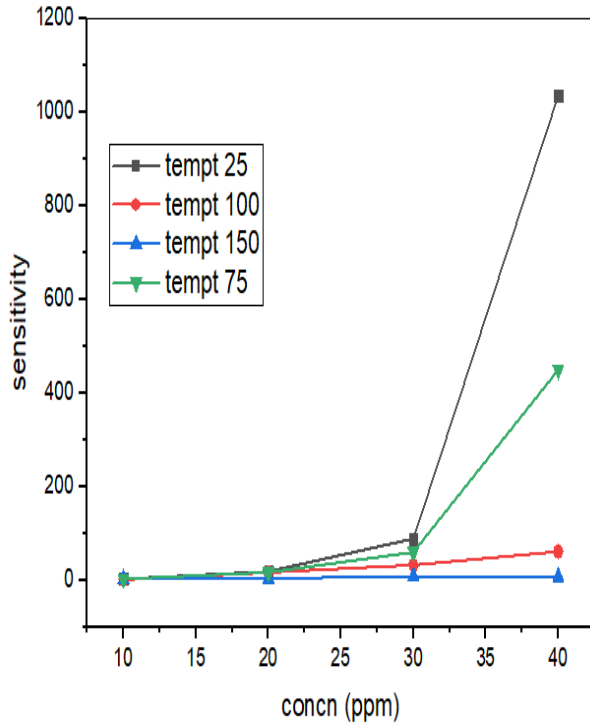| Concentration of Gas	Response Parameters	Operating Temperature (^oC)			
		25	75	100	150
10 ppm	Sensitivity (R_a/R_g)	5.15	3	1.57	1.1
	R_t (s)	35	35	34	34
	Re_t (s)	145	142	140	136
20 ppm	Sensitivity (R_a/R_g)	67	7.5	5.25	1.37
	R_t (s)	33	32	32	31
	Re_t (s)	148	148	144	142
30 ppm	Sensitivity (R_a/R_g)	116.5	53.85	4.4	3.03
	R_t (s)	32	30	30	28
	Re_t (s)	150	150	148	145
40 ppm	Sensitivity (R_a/R_g)	420	100	6.86	4.03
	R_t (s)	30	30	27	25
	Re_t (s)	170	164	160	150

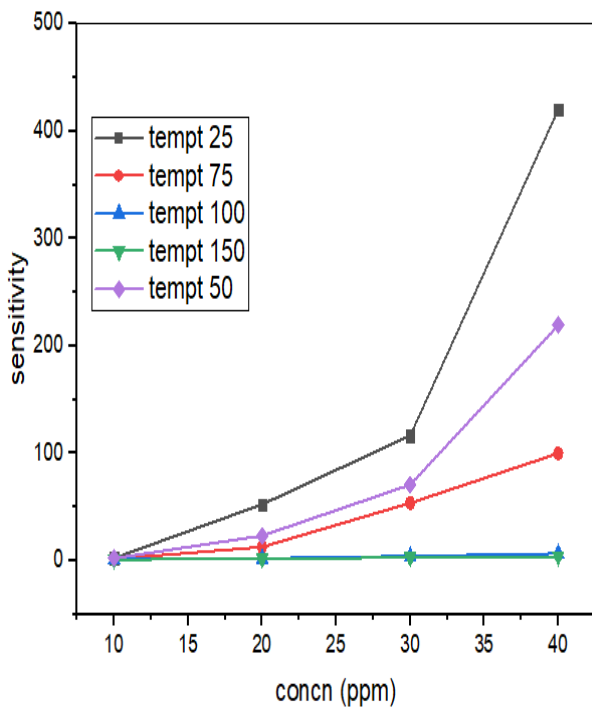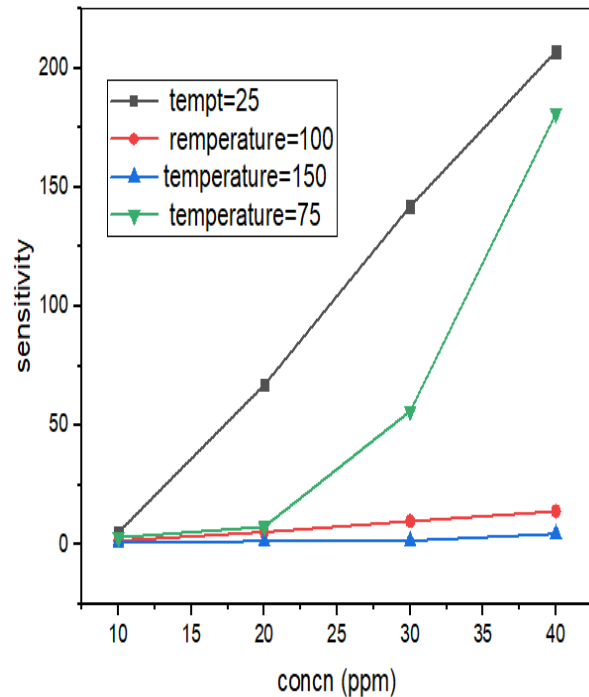Figure 4.13. (a)
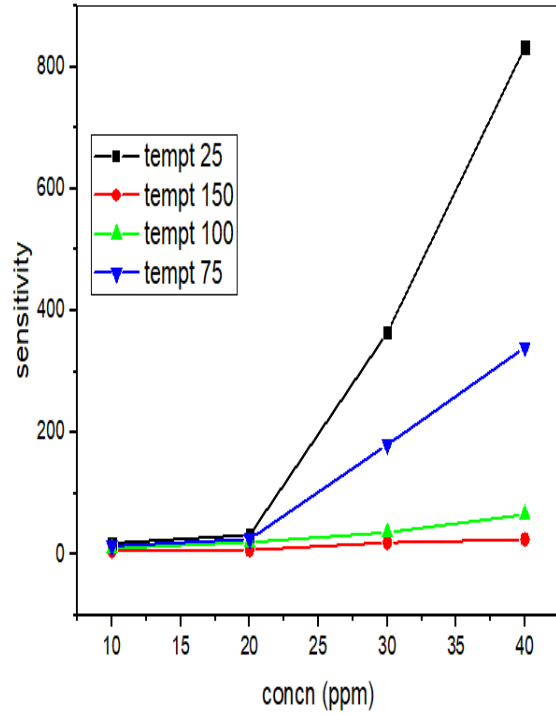
Figure 4.13 (b)

Figure 4.13 (c)

Figure 4.13 (d)

Figure 4.13 variation of sensitivity with operating temperature and concentration of H_2S gas; (a) for sample 1MD1, (b) for sample 1MD2, (c) for sample 1MD3 and (d) for sample 1MD4.

It was concluded from the above obtained data that a 3% doping of Sn enhance the sensitivity of the CuO thin film to target gas i.e. hydrogen sulphide gas. This is due to reason that the presence of Sn atoms increases molecule adsorption in gas and increase sensitivity toward target gas. Response increase due to formation of small dispersed SnO_2 with CuO to form large no of p-n junction, consequently response increase toward H_2S sensing [32].

To check the further effect of doping on sensitivity of sample, doping increase upto 7%. The synthesized samples with 5% Sn doping was classified as 1MD1(5% Sn), 1MD2(5% Sn), 1MD3(5% Sn) and 1MD4(5% Sn) for 3000 rpm, 2500 rpm, 2000 rpm and 1500 rpm respectively.

Figure 4.14 variation of sensitivity of 5% Sn doped CuO films with operating temperature (at 25°C) and various concentration of H_2S gas.

Figure 4.14 shows the variation of sensitivity at 25°C temperature and concentration of H_2S gas of sample 1MD1, 1MD2, 1MD3 and 1MD4 with 5% doping of Sn to films of CuO. It was noticed from the above figure that the highest gas response of all samples was achieved at room temperature by increasing the concentration of target gas. Amongst these four samples, it was found that 1MD4 (5% Sn) and 1MD1(5% Sn) sample have highest and lowest gas response of 100 and 53 respectively.

Similarly, for 7% doping samples codes were given as 1MD1(7% Sn) for 3000 rpm, 1MD2(7% Sn) for 2500 rpm and 1MD3(7% Sn) for 2000 rpm.
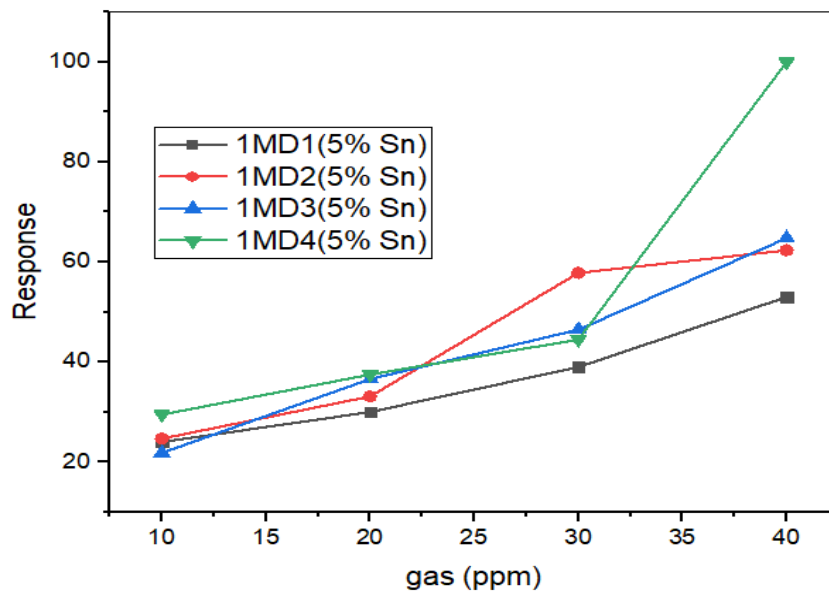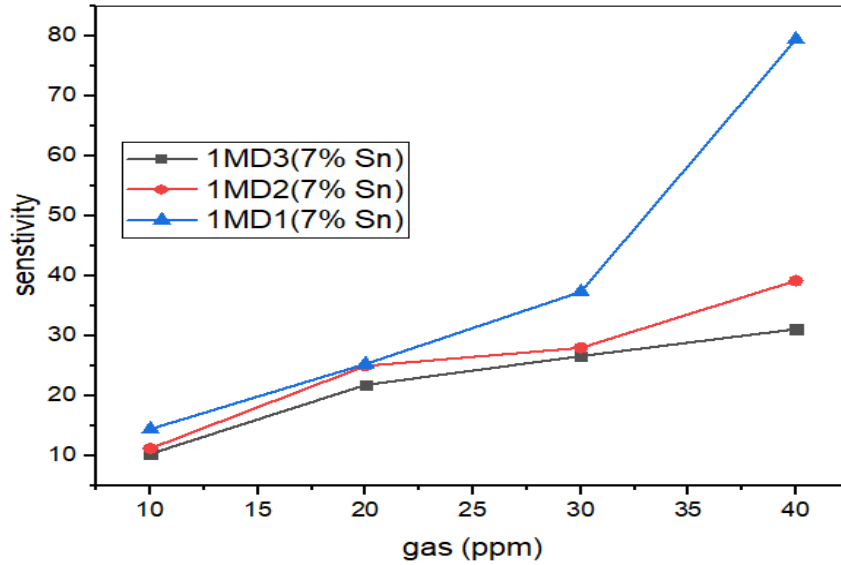
Figure 4.15 variation of sensitivity of 7% Sn doped CuO films with operating temperature (at 25°C) and various concentration of H_2S gas.

It was found from the above figure 4.15 that the highest gas response of all samples was achieved at room temperature and highest gas response of 79.51 achieve for sample 1MD1(7% Sn). CuO thin films are copper oxide films that have been doped with varying percentages of tin (Sn) atoms. The doping of tin into copper oxide can affect the sensitivity of the thin films, particularly in gas sensing applications. As the concentration increase from 0.75M to 1M then surface morphology and structure both were influenced. Surface of films become more porous and sensitivity increase for 3% of Sn dopant. It was observed from the obtained results that high doping (5% and 7%) don't provide an sufficient results of sensitivity because the surface of prepared films become smooth. The effect on sensitivity can vary depending on the dopant concentration. However, there will be a noticeable deterioration in responsiveness at even greater doping of Sn. This is due to the fact that p-n junctions can only be formed by using a portion of tin.

We observed that a moderate concentration of tin doping (5%) could further enhance the sensitivity of the CuO thin film. At this level of doping, the film's surface potentially leading to improved gas interaction and greater sensitivity to hydrogen sulphide gas. We use doping up-to 7% because beyond a certain point, too much doping can lead to the formation of secondary phases or structural changes that could reduce sensitivity or introduce unwanted properties. Overall, the effect of tin doping on sensitivity in CuO thin films depends on a balance between the altered surface chemistry, defects, and potential changes in the film's

structural properties. Proper tuning of the doping concentration is crucial to achieve the desired level of sensitivity for specific gas sensing applications.

4.9 References

[1] M. Nabipoor Hassankiadeh & A. Hallajisani. (2020). J. Pet. Sci. Eng. 190, 107131.

[2] M.J. Priya, P.P. Subha, P.M. Aswathy, K.W. Merin, M.K. Jayaraj & K. R. Kumar. (2021). Mater. Chem. Phys. 260, 124038.

[3] W.H. Li, W. Sun, X.Q. Xu, L.P. Du, M.Y. Li & J. Fluoresc. (2013). 23, 181-186.

[4] N.A. Zaidi, M.W. Tahir, M.J. Vellekoop & W. Lang. (2017). Sensors. 17, 2283–2294.

[5] H.A. Henthorn, M.D. Pluth & J. Am. (2015). Chem. Soc. 135, 15330-1536.

[6] N.S.A. Eom, H.B. Cho, Y. Song, G.M. Go, J. Lee & Y.H. Choa. (2018). Sens. Actuators B Chem. 273, 1054–106.

[7] M. He, L. Xie, X. Zhao, X. Hu, S. Li & Z.G. Zhu. (2019). J. Alloys Compd. 788 ,36–43.

[8] A.K. Elger, C. Hess. (2019). Angew. Chem. (Int. Ed. Engl.) 58,15057–15061.

[9] S.K. Pandey, K.H. Kim & K.T. Tang. (2012). TrAC - Trends Anal. Chem. 32, 87–99.

[10] A. Khanna, R. Kumar & S.S. Bhatti. (2003). Appl. Phys. Lett. 82, 4388–4390.

[11] F. Peng, Y. Sun, W. Yu, Y. Lu, J. Hao, R. Cong, M. Ge, J. Shi & N. Dai. (2020). Nanomaterials 10, 1–14.

[12] J. Deng & Z.Y. Zhao. (2019). Mater. Res. Express 6, 105513.

[13] A.M. Azad, S.A. Akbar, S.G. Mhasalkar, L.D. Birkefeld & K.S. Goto. (1992). J. Electrochem. Soc. 139, 3690.

[14] T.G. Nenov & S.P. Yordanov. (1996). Ceramic Sensors, Technology and Applications (Technomic Publishing Co. Inc. Basel).

 [15] A. Dey. (2018). Mater. Sci. Eng.: B. 229, 206–217.

[16] J. Zhang, S. Ma, B. Wang & S. Pei. (2021). J. Alloys Compd. 886, 161299.

[17] L.-Y. Zhu, K. Yuan, J.-G. Yang, H.-P. Ma, T. Wang, X.-M. Ji, J.-J. Feng, A. Devi, H.- L. Lu. (2019). Respir. Res. 20, 233–241.

[18] B.J. Wang, S.Y. Ma. (2020). Vacuum 177, 109428.

[19] P.H. Phuoc, C.M. Hung, N.V. Toan, N.V. Duy, N.D. Hoa, N.V. Hieu. (2020). Sens. Actuator A. Phys. 303, 111722.

[20] Y. Xu, L. Zheng, C. Yang, W. Zheng, X. Liu, J. Zhang. (2020). A.C.S. Appl, Mater. Inter 12, 20704.

[21] A. A. Baqer, K. A. Matori, N. M. Al-Hada, A. H. Shaari, E. Saion, J. L. Y. Chyi. (2017). Results Phys. 7, 611.

[22] K.J. Chen, F.Y. Hung, Y.T. Chen, S.J. Chang, Z.S. Hu. (2010). Mater. Trans. 51, 1340–1345.

[23] R. K. Jain & A. Khanna. (021). Sen. & Act.: B. Chem. 343, 130153.

[24] S.R. Cynthia, R. Sivakumar, C. Sanjeeviraja, C. Gopalakrishnan & K. Jeyadheepan. (2020). J. of Mat. Sci. Mat. Elect. 31, 18018-18036.

[25] R. Shabu, A. M. E. Raj, C. Sanjeeviraja & C. Ravidhas. (2015). Materials Research Bulletin. 68, 1.

[26] P. Shankar, J. B. B. Rayappan. (2015). Sci. Lett. J. 4, 126.

[27] F.-N. Meng, X.-P. Di, H.-W. Dong, Y. Zhang, C.-L. Zhu, C. Li, Y.-J. Chen, Sensor. Actuator. B Chem. (2013). 182, 197–204.

[28] A.I. Ayesh, A.A. Alyafei, R.S. Anjum, R.M. Mohamed, M.B. Abuharb, B. Salah, M. El-Muraikhi, Appl. Phys. (2019). A 125, 550.

[29] F.I. M. Ali, S. T. Mahmoud, F. Awwad, Y. E. Greish, A. F.S. Abu-Hani. (2020). Carb. Poly. 236, 116064.

[30] Z. Haung, C. Fan, F. Sun, X. Wang, M. Majidi, P. Kumar & Bo. Liu. (2020). J Mater Sci 55, 7702–7714.

[31] A. Kumar, A. K. Shringi and M. Kumar. (2022). Sens. and Actua. B: Chem. 370, 132417.

[32] Z. Chen, Z. Xu & H. Zhao. (2021). Proceedings of the Combustion Institute, 38(4), 6743-6751.

CHAPTER 5

SUMMARY AND CONCLUSIONS

5.1 Summary and Conclusions

Gas sensing technology has a big impact on many different industries, including the healthcare sector, monitoring of the environment, aviation, automotive applications, and spacecraft. Due to the enormous tender range, the need for inexpensive, power-hungry, portable, and dependable gas detecting equipment is becoming increasingly crucial. In all fields of material science and physics application, metal oxides serve as an example of a separate class of materials that includes everything from metals to semiconductors and insulators. It has been discovered, particularly in detection of hazardous gases, that the quantity and configuration of the poisonous gases affect how much electrical resistance can resist a sensing element based on metal oxides.

The introduction chapter begins with description of the peculiar traits of several types of gas sensors, principle of operation for reducing gases, parameters of sensor materials. Various techniques to improve the sensitivity of sensor, occurrence of H_2S gas and necessity of hydrogen sulphide gas sensor is provided. The production of CuO films along with their electrical, optical, structural, morphological and gas sensing characteristics have received the majority of attention. It is also discussed the superiority of spin coating method over all others synthesis methods. The applications of thin films as solar cells and gas sensing toward a target gas have been discussed.

Based on literature, CuO thin films has generated a lot of interest in the study of gas sensors because of its strong catalytic, adsorption, thermal and n-type conductivity abilities. Sol-gel spin coating has produced thin CuO films that can sense tiny reducing gas concentrations at low temperatures. The samples were manufactured using varied spinning speeds and analysis of structural, optical and electrical properties for solar cells and gas sensing characteristics. Brief overview of findings from chapter 3 and 4 which is provided below.

In summary, thin CuO films were grown successfully on glass substrate with the help of the sol gel spin coating technique at $400^{o}C$ annealing temperature. The optimized parameters were spinning speed and precursor molarity. It has been observed that both parameters effect the various properties of thin films used for gas sensing and solar cell applications.

166

XRD revealed that all of prepared samples have (200) and (111) atomic planes at 2 theta value. The monoclinic phase of CuO and polycrystalline nature of prepared films was shown by the XRD measurement. It was found that crystallinity of films increases as the spinning speed increases. The crystallite size and dislocation density increase and decrease respectively which shows that films synthesized at higher spinning speed are of high quality.

It was found that intensity of peak observes at (111) plane increases for sample synthesize by one molar concentration. It confirms that films have good crystallinity as concentration change from 0.75M to 1M. The crystallite size increase with increasing of the molar concentration and lies in the range of 10.18 nm to 3.29 nm. From the obtained results of XRD, it was concluded that pure crystalline films of CuO achieve at spinning speed in range of 1000 to 3000 rpms. Morphological study shows that grain size decrease as the thickness of films decreases.

Optical investigation shows that transmission drops by 15% as film thickness increases from 75 to 239 nm owing to film density. Thinner sheets absorb more photons, making them less transparent. Obtained band gap lies in range from 1.69 eV to 2.23 eV which makes the prepared samples useful for solar cell applications. To verify the ohmic nature of films, silver electrode has been deposited on surface of films and observe that current linearly goes on increasing with increasing voltage. From the calculation of resistivity and conductivity, it was analysed that resistivity falls and conductivity increase on increasing spinning speed. Samples of 1M concentration have lowest and highest resistivity value of 10.23 ohm-m and 22.9 ohm-m respectively.

Doped sample of CuO also prepared by using Sn as dopant with 3 moles %, 5 moles % and 7 mole % using sol-gel method. Transparent solution prepares after aging of 90 minutes. This solution was used to synthesize films on substrate of glass. Debye Scherrer formula was used to calculate the size of crystallite and found that it lies in the range of 14.33 nm to 16.83 nm for Sn doped sample of 0.75M concentration and 23.61 nm to 43.79 nm for Sn doped sample prepared from 1 M concentration. XRD shows that films are oriented along (111) and (200) planes. It was observed from the calculation that dislocation density decreases indicating the more regularity of crystalline structure.

Optical properties of doped films from 1 molar concentration shows the band gap in range of 2.36 eV to 1.45 eV. This obtained band gap makes the samples suitable for absorber layer in solar cell. From I-V characteristics, it was seen that all of doped sample have ohmic nature. It

was analysed from the figure 4.8 and figure 4.9 that resistivity decrease and conductivity increase on doping of Sn material to CuO.

These prepared samples were studied at various temperature and different concentration of H_2S gas for gas sensing applications. It was found that 25°C is the best operating temperature due to high gas response and less time taken for showing change in resistance and also for recovering. 10 ppm to 40 ppm hydrogen sulphide gas was passed to sample and analyse the sensitivity. It was noticed from the figure 3.27 that sensitivity goes on increasing as the concentration of gas increase. It has been found that lowest thickness sample show more sensitivity toward H_2S gas with minimum time taken for responding and recovering. The selective nature of CuO films was also verified by passing ethanol, ammonia and H_2S of 40 ppm at 25°C temperature. It was observed from the figure 3.29 that sensor fabricated from CuO was selective for H_2S gas. Among the testing of pure and doped sample of CuO, it was found that sample minimum responding time taken by sensor was 5 seconds. We can conclude based on the results that doping of Sn to thin CuO films reduces response and recovery time. A moderate dose of tin doping (3%) increase CuO thin film sensitivity.

Besides that, the investigation on the structural and morphological properties of the copper oxide thin films could be performed using different annealing temperature. In future, we can explore the feasibility of incorporating the Sn doped CuO thin films into practical gas sensing devices for real time monitoring of environmental pollutants or industrial gases. Prepared thin films of CuO can also use as absorbing layer in photovoltaic devices for improving their performance and stability.

List of Conferences

- International Conference on "Scientific Developments in the Current Era" (ICSDCE-2021), 9-10 April, 2021, I.B. College, Panipat.

- International Conference on "Recent Advances in Fundamental and Applied Sciences" (RAFAS-2021), 25-26 June, 2021, Lovely Professional University, Punjab.

- International Confrence on " Recent advances in basic and applied Sciences" (ICRABAS-2021) (online), 27-28 August, 2021, BMU, Rohtak.

- International Conference of Emerging Technologies: ICMET-2021, 18-19 Feb, 2022, Lovely Professional University, Punjab.

List of Publication

1. "Investigation of effect of spinning speed on structural, electrical and optical properties of CuO thin films prepared by sol–gel spin coating technique", Jyoti, Rajesh Kumar.

Journal of optics (2022), DOI: 10.1007/s12596-022-00942-9.

2. "Variation In Electrical, Optical and Structural Properties Of CuO Thin Films Prepared By Sol-Gel Spins Coating Technique By Varying Thickness", Jyoti, Rajesh Kumar.

American Institute of Physics (2023), DOI:10.1063/5.0163464.

3. "Effect of Spin Speed on the Physical Characteristics of CuO Films Synthesized with Sol-Gel Spin Coating for H2S Gas Sensing", Jyoti, Rajesh Kumar.

Journal of Electronics and Materials (2024), DOI: 10.1007/s11664-024-11236-0.

4. "Synthesis and characterization of Sn doped CuO thin films for gas sensor toward H_2S gas sensing", Jyoti, Rajesh Kumar, Ashok Kumar.

Journal of Electronics and Materials (2024), DOI: 10.1007/s11664-024-11249-9.

5. "Design and characteristics of various types of gas sensors for hydrogen sulphide gas detection- A review", Jyoti, Rajesh Kumar.

Journal of physics (2022), DOI: 10.1088/1742-6596/2267/1/012008.

6. "SENSOR BASED METHOD TO DETECT AND MONITOR H2S GAS –A REVIEW", Rajesh Kumar, Jyoti,

Poll Res. 41 (1): 286-291 (2022), DOI: 10.53350/PR.2022.v41i01.042.